# Magnetic approaches for tissue mechanics and engineering of the skeletal muscle

Irène Nagle

**THÈSE de DOCTORAT D'UNIVERSITÉ PARIS CITÉ**

Opérée au sein du :

**Laboratoire Matière et Systèmes Complexes, UMR 7057**

**Ecole Doctorale Physique en Ile-de France - ED n°564**

**Spécialité : Physique**

---

# Magnetic approaches for tissue mechanics and engineering of the skeletal muscle

---

Thèse de doctorat de **Biophysique**


## Irène NAGLE


Présentée et soutenue publiquement le 10/02/2023

Devant le jury composé de :

| | | |
|---|---|---|
| **Morgan DELARUE** | Chargé de recherche CNRS | **Rapporteur** |
| **François GRANER** | Directeur de recherche CNRS | **Président du jury** |
| **Myriam REFFAY** | Maîtresse de conférence Université Paris Cité | **Directrice de thèse** |
| **Aurélien ROUX** | Professeur Université de Genève | **Rapporteur** |
| **Marie-Émilie TERRET** | Directrice de recherche INSERM | **Examinatrice** |
| **Claire WILHELM** | Directrice de recherche CNRS | **Directrice de thèse** |

## Titre : Approches magnétiques de mécanique et d'ingénierie du tissu musculaire squelettique

**Résumé**:

La thèse est centrée sur les propriétés mécaniques macroscopiques de tissus modèles. L'incorporation de nanoparticules super-paramagnétiques (maghémite) au cœur des cellules permet à la fois leur manipulation à distance pour créer des agrégats multicellulaires de forme contrôlée et l'application de forces pour mesurer leurs propriétés mécaniques ou induire leur organisation. Les cellules modèles choisies sont des précurseurs de muscle de souris (C2C12), pour une application directe à la mécanique et à l'ingénierie du muscle squelettique.

Les déformations des agrégats formés magnétiquement et soumis par la suite à un gradient de champ magnétique permettent de mesurer leurs propriétés mécaniques macroscopiques (tension de surface, module d'Young). Nous avons ainsi pu étudier l'interaction entre les propriétés de la cellule individuelle (adhésions intercellulaires, structure et tension de l'actine) et les propriétés mécaniques à l'échelle du tissu, mettant notamment en évidence l'importance de la désorganisation de la desmine pour la rigidité et la tension de surface macroscopique. En utilisant des cellules exprimant une desmine mutée (mutation ponctuelle présente chez des patients souffrant de desminopathie), nous avons souligné le rôle fondamental de l'architecture du réseau de filament intermédiaire dans ce tissu modèle 3D.

Les forces magnétiques ont ensuite été utilisées pour aider la différenciation en cellules musculaires en favorisant leur alignement et en permettant leur stimulation mécanique. Pour ce faire, nous avons développé un étireur magnétique qui étire des agrégats multicellulaires de cellules précurseurs de muscles placées entre deux aimants mobiles et favorise leur différenciation en cellules musculaires alignées. Ce dispositif représente un outil innovant pour étudier les déformations cellulaires sous étirement et la différenciation musculaire.

**Mots-clés**: nanoparticules d'oxyde de fer superparamagnétiques, muscle squelettique, myoblaste, agrégat multicellulaire, tension de surface, filaments intermédiaires, étireur magnétique

# Title : Magnetic approaches for tissue mechanics and engineering of the skeletal muscle

**Abstract**:

The thesis is focused on the macroscopic mechanical properties of tissue models. The incorporation of superparamagnetic nanoparticles (maghemite) into the cells enables both their manipulation at distance to create multicellular aggregates of controlled shape and the application of forces to measure their mechanical properties or induce their organization. The cellular model chosen is a mouse muscle precursor cell line (C2C12), for a direct application to tissue mechanics and tissue engineering of the skeletal muscle.

The deformations of the aggregate formed magnetically and then submitted to a magnetic field gradient enable to measure its macroscopic mechanical properties (surface tension, Young's modulus). We could therefore look at the interplay between the individual cell properties (cell-cell adhesions, actin structure and tension) and the mechanical properties at the tissue scale revealing the importance of desmin disorganization in macroscopic rigidity and surface tension. By using desmin-mutated muscle precursor cells (point mutations involved in desminopathies), we enhanced the fundamental role of the intermediate filament network architecture in this 3D tissue model.

Magnetic forces were then used to promote differentiation into muscular cells by first reproducing their alignment and secondly mechanically stimulating them. To that end, we developed a magnetic stretcher to stretch multicellular aggregates of muscle precursor cells trapped between two mobile magnets and induce their differentiation into aligned muscular cells. This magnetic stretcher represents a new tool to study cell deformation under stretching and muscle cell differentiation.

**Keywords**: iron oxide superparamagnetic nanoparticles, skeletal muscle, myoblast, multicellular aggregates, surface tension, intermediate filaments, magnetic stretcher

# Contents

# Preface

Biological tissues are highly complex and organized structures. A better understanding of the processes driving their assembly and organization would be crucial in many fields from disease modelling to development or tissue engineering which aims at recapitulating the function and structure of organs for regenerative medicine or tissue repair. While the role of biochemical cues has been extensively studied for many years, biophysical cues such as mechanical forces and the cell mechanical properties are now admitted as playing an essential role in mature tissue regulation and maintenance as well as in embryonic development.

Studying mechanical properties of biological tissues therefore represents a major issue, both for a better understanding of their properties and for the reproduction of complex organs. Tissues are complex heterogeneous and active materials but their properties can be largely apprehended through concepts from soft matter (viscoelasticity, surface tension...). Their mechanical properties arise from their cellular microscopic properties, however this interplay is still not completely understood.

Multicellular aggregates as tissue models are useful tools both to investigate the role of individual cellular properties on the mechanics of tissues, and to reproduce the tissue complexity. Indeed, standard 2D approaches are far away from the 3D tissular environment, and spheroids and multicellular aggregates help to better mimic the tissue physiological conditions regarding cell-cell and cell-matrix adhesions. While many strategies focused on obtaining 3D tissue models, the ability to stimulate the tissues through external forces is also crucial. First, to measure its mechanical properties, tools to stimulate mechanically the tissue and record the resulting deformation are required. Second, external stimulating forces have been shown to be essential for tissue maturation and regulation in many tissue types, such as in the heart, muscle or intestine. One of the current challenges of tissue engineering is indeed to control spatial organization of cells in 3D while being able to apply mechanical forces. For instance, skeletal muscle presents a multiscale aligned structure and its resulting organization and function are related to the stimulations applied during

maturation.

Magnetic forces are great candidates to remotely control cell organization and apply external forces at will. The team has developed a technique based on the incorporation of iron oxide nanoparticles into the cells to confer them a magnetic moment enabling their manipulation at distance. Iron oxide nanoparticles were first introduced as Magnetic Resonance Imaging (MRI) contrast agents and are now used in many biomedical areas. Most studies have demonstrated their cytocompatibility, legitimizing their use in *in vitro* and *in vivo* applications. Thanks to this magnetic strategy and with no addition of any substrate or external matrix, magnetic multicellular aggregates of unprecedented size and of controlled shape are formed, and can be stimulated thanks to magnetic forces. This PhD aims at stimulating mechanically tissue models thanks to magnetic forces (i) to investigate the mechanical properties of 3D tissues and (ii) to drive tissue differentiation and organization in the context of skeletal muscle engineering.

---

This manuscript is composed of two independent parts. A first chapter of general introduction (**chapter 1**) introduces the elements required and common for both parts. Spheroids and multicellular aggregates as models of 3D biological tissues are presented as well as iron oxide nanoparticles and the skeletal muscle organization.

The first part (**part I**) focuses on the study of static and dynamical mechanical properties of multicellular aggregates formed and stimulated magnetically. First, mechanical and rheological properties of multicellular aggregates are introduced. Then, in **chapter 2**, macroscopic mechanical properties such as the effective surface tension of spheroids are measured and related to microscopic properties of individual cells. The spheroid mechanical properties are measured by flattening and deforming the aggregate thanks to a constant magnetic field gradient. In **chapter 2 section 2.2**, the interplay between the macroscopic surface tension and microscopic properties such as the actin cytoskeleton organization and tension, intercellular adhesions or intermediate filaments is investigated in a model of mouse muscle precursor cell spheroids. The experimental results are presented in the form of an accepted article. Next, **chapter 2 section 2.3**, in a model of human breast cancer cells, tumor-related properties such as invasion, migration or adhesion are correlated to the macroscopic surface tension. The experimental results are presented in the form of a published article. Finally, **chapter 3** presents a magnetic tool to probe the rheology of multicellular aggregates by applying a varying magnetic field thanks to an electromagnet. The experimental results obtained with this magnetic rheometer are cross-validated with parallel-plate rheometry.

The second part of this manuscript (**part II**) presents a magnetic approach to apply mechanical cues to drive organization and enhance differentiation of 3D skeletal muscle constructs. In **chapter 4**, myogenesis and tissue engineering strategies for the skeletal muscle are first introduced. Then, the magnetic stretcher device used to obtain stretchable mouse muscle precursor cell multicellular aggregates between two micromagnets and its optimization are described. The experimental results show that this magnetic stretcher drives cell alignment and favors differentiation into muscular cells.

# Chapter 1

# General introduction

The different projects presented in this thesis are based on the use of magnetic multicellular aggregates as stimulable tissue models. In this general introduction, we will introduce the different common elements to the different projects. First, we will present the structure and key elements of biological tissues, and why spheroids and multicellular aggregates are valuable tools as tissue models for tissue mechanics or biophysics studies, and how they can be obtained. Then, the use of iron oxide nanoparticles to magnetize the cells and their general features will be presented. This thesis will mainly focus on muscle cell mechanics and differentiation; consequently, we will describe the peculiar organization and function of the skeletal muscle.

## 1.1 Biological tissues

Biological tissues can be described as a collection of interconnected cells that together carry out a similar function within an organism. They are composed of two physiological elements : the cells and the extracellular matrix (ECM) but does not sum up as a simple mixing: collective effects play a major role. In living organisms, cells are interconnected through a support matrix (ECM) that consists in a 3D network composed of extracellular macromolecules and proteins. Cells receive external signals either through neighboring cells or through contact with ECM that guides their behavior such as motility or even differentiation. These signals from the external environment are sensed by the cells thanks to their cytoskeleton.

### 1.1.1 The cell cytoskeleton

The ability of cells to change their shapes, divide, migrate or react to their environment, is at least partially controlled by the active assembly and disassembly of cytoskeletal proteins (requiring ATP consumption). The cell cytoskeleton is composed of this dynamical network across the entire cell and its structure is permanently renewed. It is also involved in the intracellular trafficking in combination with molecular motors [1]. The cytoskeleton of eukaryotic cells is made up of three major components that we will briefly introduce : actin filaments, microtubules and intermediate filaments (Figure 1.1).

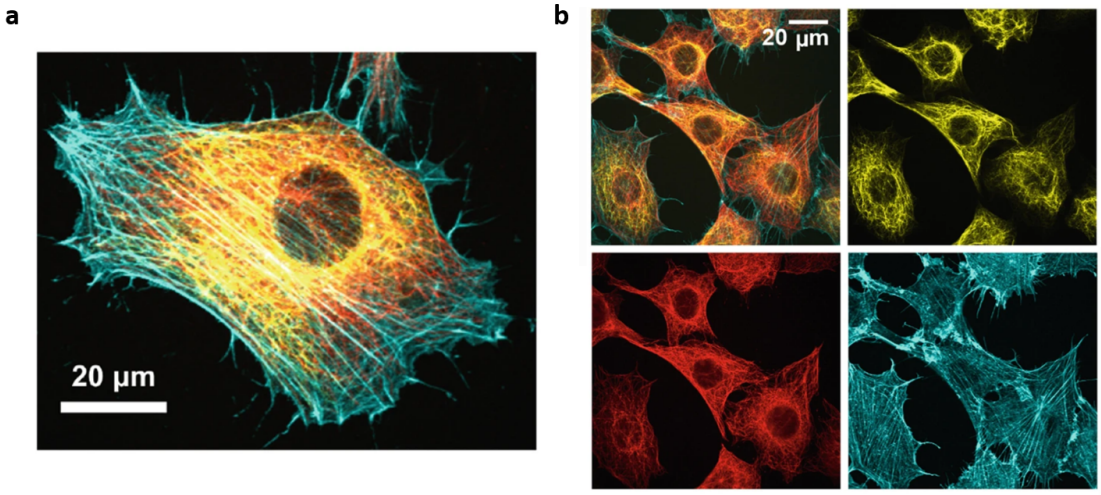


**Figure 1.1 The cell cytoskeleton.** Immunofluorescence images of a single **a)** or several adhering 3T3 fibroblasts **b)**. Vimentin filaments, microtubules and actin filaments are labelled in yellow, red and cyan respectively. Figures are adapted from Schepers et al. [2] and Lorenz et al. [3].

- **Actin filaments** (or microfilaments) are obtained from the polymerization of monomeric G-actin into filamentous actin (F-actin). The resulting filaments are polarized, semi-flexible polymers (persistence length of about 18 µm), which means that the persistence length is of the order of the filament length. Their diameter is about 6 nm. Actin filaments are mainly located in the cell cortex under the cell membrane or in stress fibers across the cell. These filaments are associated with force generation that is necessary for shape changes, focal adhesion or movement. Indeed, myosin molecular motors couple actin filaments together by sliding one set of microfilaments with respect to another. This actin-myosin network provides contractile properties to the cell.

- **Microtubules** are composed of $\alpha$- and $\beta$-tubulin heterodimers and form hollow filaments of about 24 nm diameter with a hole of 12 nm diameter. In comparison to actin

filaments, they are much more rigid since their persistence length is in the range of millimeters. They polymerize from centrosomes and generally reach the plasma membrane. Microtubules play a role in division through positioning of the spindle during mitosis, in migration, in cell shape control or in intracellular trafficking.

- **Intermediate filaments** are made of proteins of a large class encoded by at least 70 genes. The resulting filaments have a diameter of 10 nm. In contrast with actin filaments and microtubules that are found in all eukaryotic cells, intermediate filaments are cell type specific. They are divided into 5 classes. While the first four classes (type I to IV) are cytoplasmic, type V intermediate filaments are nuclear (lamins). Type I and II filaments are heteropolymers consisting of different keratin proteins. Type III are homopolymers such as vimentin or desmin. While vimentin is mainly expressed in fibroblasts, astrocytes or endothelial cells, desmin is specific to muscle cells. Finally, type IV intermediate filaments comprise three neurofilament heteropolymers expressed mainly in the cells of the nervous system. Intermediate filaments can be considered as flexible polymers with a persistence length smaller than 1 µm. They are involved in the mechanical response of cells especially at large strains. Indeed, they are the most extensible, the softest and the most resilient to stress among the three elements of the cytoskeleton. In particular, vimentin is thought to act as a safety belt for cells under strain [4].

As evidenced recently [5], these three networks are interpenetrated, connected and interacting networks. It is therefore hard to disentangle each contribution on the global cell properties and mechanics.

### 1.1.2 The extracellular matrix

Cells are embedded in an extracellular matrix to form biological tissues. The extracellular matrix is composed of a dense meshwork of polymers such as proteins or polysaccharides. Collagen is the most abundant ECM protein, but we can also find laminin, elastin or fibronectin. The ECM structure and specific composition is tissue type dependent and can be secreted by specialized cells such as fibroblasts. The biochemical properties of ECM but also its physical properties such as stiffness are crucial for the cell response [6].

### 1.1.3 Cell adhesions

Through specific transmembrane proteins, cell can probe their microenvironment and adapt to mechanical stimulations. Cells are connected to neighbouring cells through cell-cell adhesion proteins and to the external matrix thanks to cell-matrix adhesion proteins.

### Cell-cell adhesions

Cell-cell adhesions are performed thanks to transmembrane proteins that interact through their extracellular domains. These transmembrane proteins are linked to the cytoskeleton through specific proteins enabling the transduction and propagation of external mechanical stimuli between the cells. We count four main categories of cell-cell adhesion proteins: cadherins, immunoglobulins, selectins and some integrins (see Figure 1.2). The interactions between adhesion proteins can be either homophilic, like for cadherins where the extracellular domains of two cadherins are interacting, or heterophilic, like for integrins where integrins interact with proteins bound to the membrane of another cell.

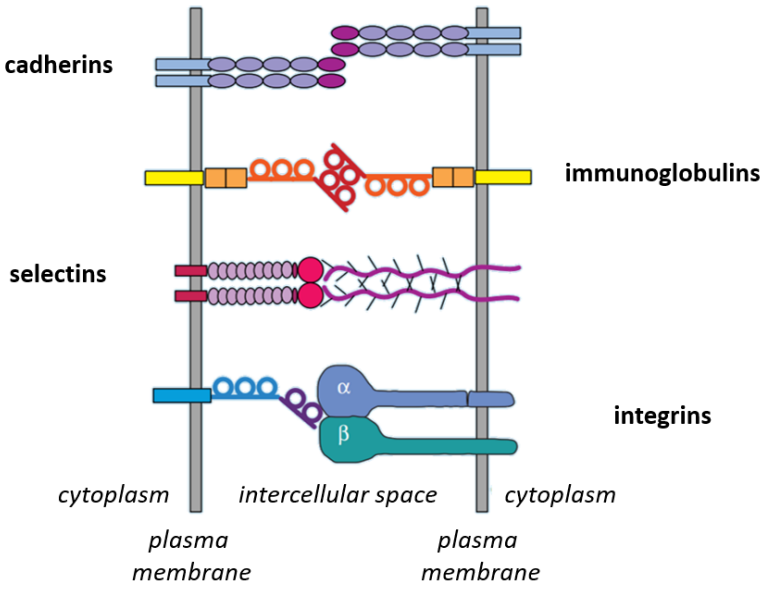


**Figure 1.2 The different types of cell-cell adhesion proteins.** Figure adapted from Hynes et al. [7].

The family of cadherins has been the mostly studied and characterised up to now. They are involved in the formation of adherens junction or desmosomes. Cadherin-cadherin interactions are dependent on extracellular $Ca^{2+}$ that rigidifies the cadherin extracellular domains promoting junctional interactions [8]. Extracellular calcium depletion therefore decreases cadherin adhesion efficiency. Cadherins are linked to the cytoskeleton thanks to specific proteins such as catenins. Several types of cadherins have been identified. While E-cadherins are mainly found in epithelial tissues, N-cadherins are specific to mesenchymal tissues.

### Cell-matrix adhesions

The adhesion between cells and their substrate is ensured by another type of transmembrane proteins called integrins. The extracellular domain of integrins is able to interact with specific proteins of the extracellular matrix (ECM) such as collagen, laminin or fibronectin. Here again, integrins are linked to the cytoskeleton through specific anchoring proteins enabling the cells to receive the external mechanical stimuli from their environment. Integrins are for example involved in focal adhesions, allowing the cells to adapt to the mechanical properties of the ECM.

Figure 1.3 sums up the different elements involved for a cell to sense its environment through cadherin-dependent adherens junctions or integrin-based focal adhesions. Mechanical signals are relayed through cadherins and integrins connected *via* a contractile actin-myosin network enabling the cells to actively adapt to their physical environment.

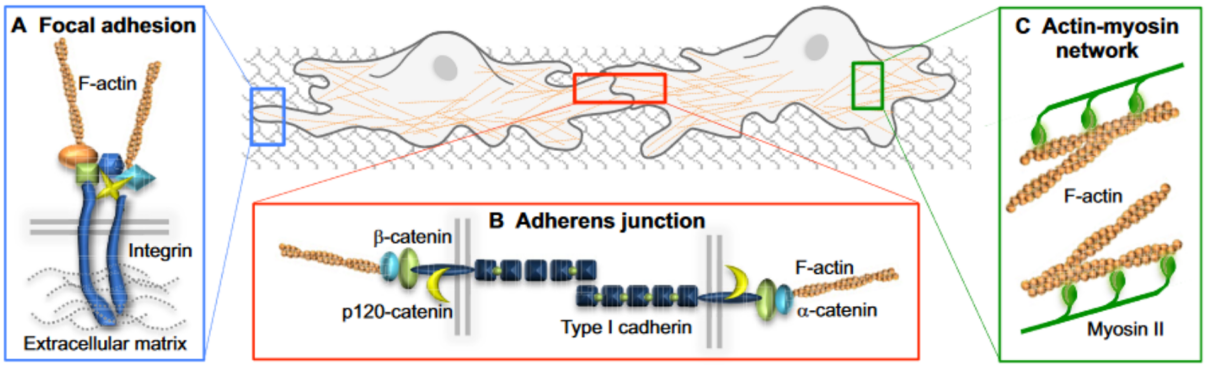


**Figure 1.3 External mechanical signals are transmitted to cells through integrins and cadherins that are linked by the contractile actin-myosin network.** Figure extracted from Mui et al. [9].

Whereas the contribution of biochemical signals has long been studied for guiding complex cell behaviors from migration to differentiation, biophysical and mechanical signals are now widely recognized to also be essential [10].

## 1.2 Spheroids and multicellular aggregates as tissue models

In order to better understand the function of biological tissues, many studies focused on individual cells cultured on 2D substrates. By forming 2D layers, cells can be used as a tissue model mimicking an epithelium for instance. However, these elementary tis-

sue models arising from 2D cell culture, do not reproduce the cell-matrix and cell-cell interactions observed in 3D tissues.

### 1.2.1 Spheroids to bridge the gap between 2D culture and *in vivo* studies

In the last decades, there has been a growing interest for spheroids and more generally multicellular aggregates because of their potential ability to bridge the gap between 2D *in vitro* culture and *in vivo* experiments by reproducing more closely the 3D physiological conditions *in vivo*. In standard 2D culture systems, cells grow on a solid flat substrate and lack cell-matrix and cell-cell interactions that are present in native tissues, while 3D culture systems such as spheroids mimic one step further the complexity of the tissue environment. Spheroids are multicellular aggregates growing as spheres derived from the self-assembly of suspended cells (in biological fluids or in a matrix) (illustrative examples Figure 1.4). They have been studied since the 50's, but they were first called "spheroids" by Sutherland et al. in the 70's [11], [12] who obtained spherical multicellular aggregates from hamster lung cells as a model of nodular carcinomas. While they were initially developed for biomedical and drug screening applications in order to better reproduce 3D tumor environment, they can also be used as models to address many biological questions, from pharmacology and drug screening [13] [14] to biophysics [15] [16] and mechanobiology [17] [18], or tumorigenesis [19] [20] and embryogenesis [21] [22]. Even if spheroids lack vascularization or innervation to perfectly reproduce the physiological environment of tissues, their 3D structure and the potential presence of ECM make them a model of choice at the intersection between 2D cultures and *in vivo* tissues.

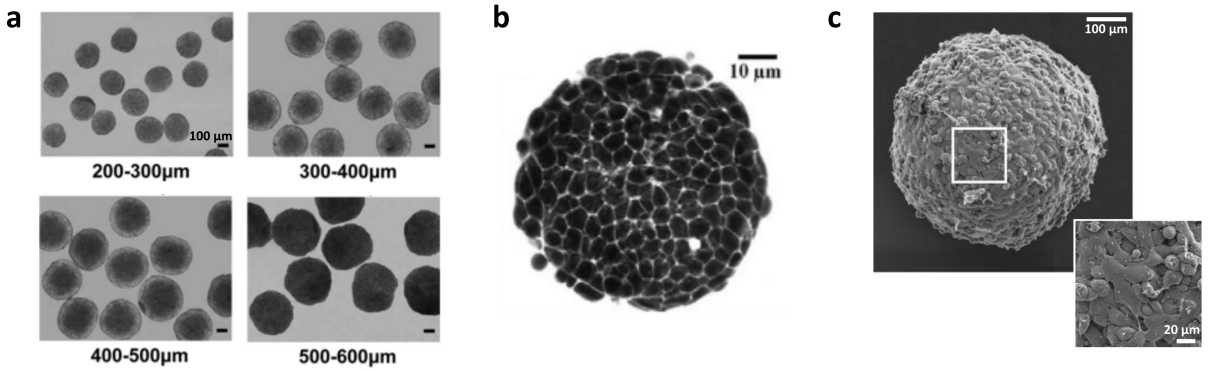


**Figure 1.4 Spheroids to go from 2D to 3D culture.** **a)** Bright field images of MCF-7 spheroids formed with agarose microwells and with a varying number of deposited cells after 3 days of culture. **b)** Two-photon microscopy image of a F9 multicellular aggregate obtained with the hanging drop technique. The intercellular spaces are visualized thanks to sulforhodamine B. **c)** Scanning electron microscopy images of a CHO cell aggregate. Images a, b and c adapted from Gong et al. [23], Stirbat et al. [24] and Jakab et al. [25] respectively.

### 1.2.2 Standard techniques for 3D cell culture

All the techniques that were developed to form spheroids are based on favoring the formation of cell-cell contacts of suspended cells to form a cohesive 3D structure. We can distinguish two main approaches to obtain them as presented in Figure 1.5.

On one hand, **scaffold-free approaches** rely on the aggregation of suspended cells in liquid medium followed by a phase of growth to reach the final size. In the case of the hanging drop technique, suspended cells are aggregated thanks to gravity in liquid drops of a few tens of µL formed on a flipped dish [24] while for the magnetic culture, cells are magnetized with iron oxide nanoparticles and aggregated by the attraction towards magnets. Besides, cell aggregation can be generated by permanent agitation of the suspended cells in spinner or rotating flasks. Cells can also spontaneously aggregate with the liquid overlay technique where suspended cells are put in non adhesive dishes or microwells [23] or with microfluidic systems where cells are trapped into hydrogel capsules such as alginate spheres that are permeable to oxygen and nutrients [26] (Figure 1.5).

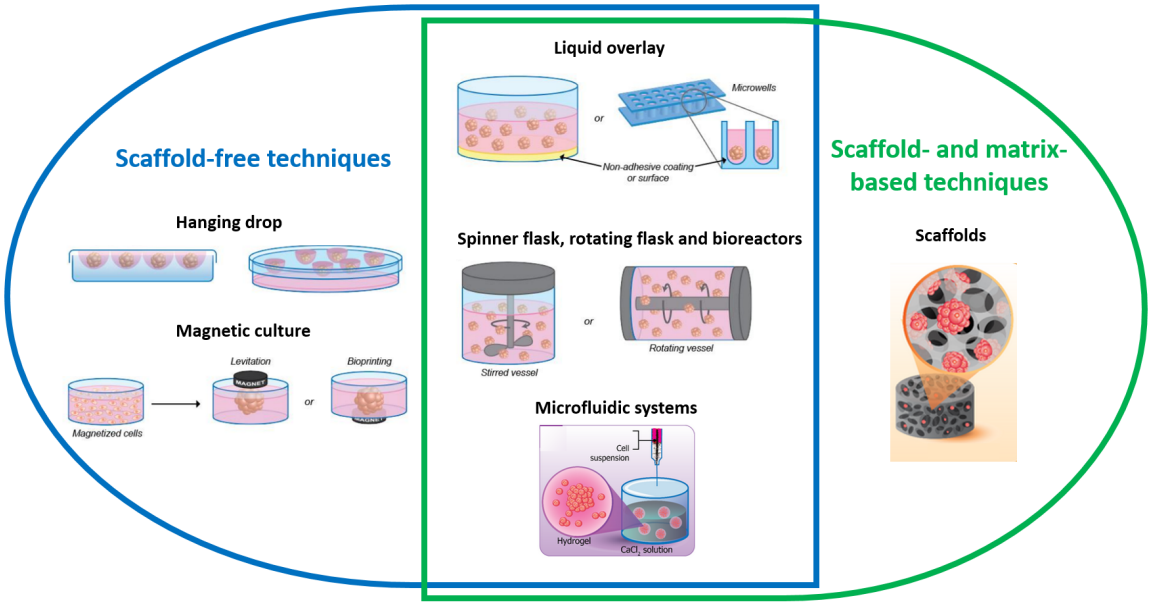


**Figure 1.5 Classical techniques to form spheroids.** Scaffold-free techniques (blue) and scaffold- or matrix-based techniques (green) are both based on the aggregation of suspended cells to generate cell-cell contacts followed by a phase of growth during several days. Techniques in the intersecting region can be performed with or without scaffolds or matrix. For instance, in the liquid overlay technique or for microfluidic systems, culture medium can be replaced by ECM protein matrix or hydrogels, whereas scaffolds can be placed into bioreactors. Adapted from Van Zundert et al. [27] and Chaicharoenaudomrung et al. [28].

On the other hand, **scaffold-based approaches** rely on the use of an external substrate constructed to mimic the extracellular matrix (ECM) into which cells are inserted. Several techniques can also be adapted for scaffold- or matrix-based approaches. First, in the liquid overlay technique or with microfluidic generated capsules, cells can be embedded in ECM protein matrix or hydrogels (such as collagen or Matrigel for example) instead of being suspended in liquid culture medium. Rotating flasks and bioreactors can be combined with scaffolds to allow oxygen and nutrients to be mixed in the media (Figure 1.5).

In the case of scaffold-free approaches or with the liquid overlay technique, the obtained spheroids are typically about a few hundreds of µm diameter after 24 hours and are not larger than 500 µm diameter after about 7 days. The spheroids being formed by successive cell growth and division during several days, access to nutrients and oxygen is limited by diffusion which can lead to a necrotic core for spheroid sizes larger than a few hundreds of µm. Besides, their shape is necessarily spherical.

To circumvent these limitations and to generate reproducible multicellular aggregates of large size with various shapes and no necrotic core, the team has developed a magnetic

molding technique based on the use of agarose molds and on the incorporation into the cells of maghemite iron oxide nanoparticles [29]. These iron oxide nanoparticles will be presented in greater details in section 1.3.

### 1.2.3 The magnetic molding technique

The team has recently developed a technique based on magnetically labelled cells (called magnetic cells) to form large spheroids above 500 µm diameter, in less than a day [29] [30]. The magnetic molding technique takes advantage of the magnetization of cells thanks to the incorporation of superparamagnetic iron oxide nanoparticles ($\gamma - Fe_2O_3$) as in the magnetic culture technique depicted Figure 1.5. However, with the magnetic molding, only the formation of cell-cell contacts is required and no phase of growth is necessary to reach the desired spheroid size.

Cells are first labelled with the superparamagnetic nanoparticles in 2D plates to confer them magnetic properties. Magnetic cells are then detached and the suspended cells are attracted in agarose molds by permanent magnets placed beneath the molds (Figure 1.6 a). After an overnight incubation at 37°C and 5% $CO_2$, multicellular aggregates are removed from the molds by gently pipetting the surrounding medium.

With this technique, we can obtain cohesive multicellular aggregates of unprecedented sizes (up to 2 mm), very fast (in about 10 to 20 hours) and with a controlled geometry defined by the shape and the size of the molds (Figure 1.6 b-c). Since spheroids are formed in less than a day, there is no induction of a necrotic or hypoxic core. Moreover, the incorporation of maghemite nanoparticles has worked efficiently on all the cell types tested up to now ranging from mesenchymal stem cells [29] [31] to immortalized cancer cell lines [18] [30] or embryonic stem cells [32]. This technique of multicellular aggregate formation is therefore universal as long as cells are able to incorporate nanoparticles and to form cell-cell adhesions.

Finally, the resulting multicellular aggregates have a magnetic moment that enables the application of magnetic forces for their mechanical stimulation that is of high interest for many fields of applications as presented in the following section.

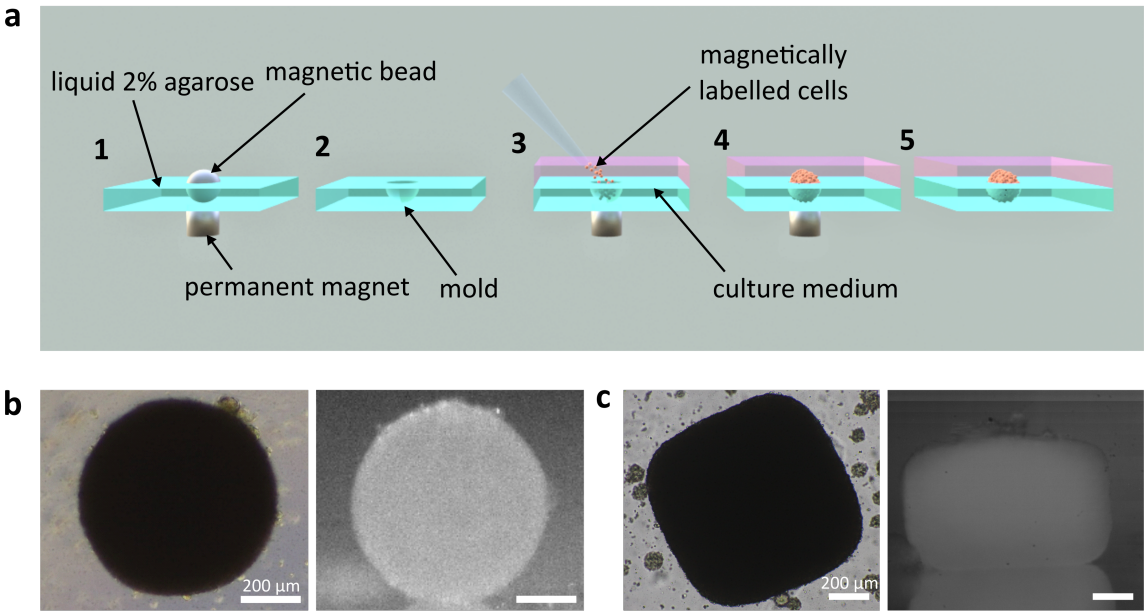


**Figure 1.6 Magnetic molding to form multicellular aggregates.** **a)** Schematics of the magnetic molding technique. Steel beads of calibrated size are deposited in Petri dishes and are held in place by permanent magnets while they are embedded in heated 2% liquid agarose (1). Once the agarose is solidified, beads are removed creating semi-spherical agarose molds (2). At this stage, any other shape can be used instead of spheres. Magnetically labelled cells are then attracted in the molds by permanent magnets placed beneath (3) until the molds are filled (4). The permanent magnet is then removed for overnight incubation at 37°C at 5% $CO_2$ (5). Within 10 to 20 hours, cell-cell contacts develop to form cohesive multicellular aggregate and spheroids can be removed from their molds by gently pipetting the surrounding medium. **b)** Top (left) and side view (right) of a muscle precursor cell spheroid (C2C12) obtained by magnetic molding. **c)** Top (left) and side view (right) of a cuboid of murine carcinoma cells (F9) of 1 mm side length and about 600 µm height.

### 1.2.4 Applications of multicellular aggregates and the need to exert mechanical forces

Multicellular aggregates are relevant models for studies in a wide range of fields, in particular in biophysics and in tissue engineering that both require the application of external mechanical forces.

From a **biophysical standpoint**, they represent simple tissue models whose properties can be controlled. Multicellular aggregates are therefore a great tool to understand the mechanical properties of tissues, and have been extensively used for biophysical studies [33]. By extending the soft matter concepts to biological tissues, an analogy can be drawn between multicellular aggregates and classical fluid, viscous or elastic materials. However, to measure the mechanical properties of such tissue models, multicellular aggregates need to be deformed in a controlled manner through the applications of mechanical forces. This point will be addressed in details in part I.

From a **tissue engineering view**, multicellular aggregates present direct applications in regenerative medicine and disease modelling. The aim is to reproduce a specific organ or tissue function and organization *in vitro*. However, if biochemical cues have been extensively studied for the fate of cells, biophysical cues such as mechanical stimulation are also crucial for the proper differentiation and organization of cells. Nevertheless, tools to apply mechanical forces to such constructs are still missing, and existing techniques are generally based on force application to an external support matrix. This topic will be addressed in part II through an application for the skeletal muscle.

These two different domains of applications highlight the need of strategies to apply remote forces to 3D multicellular aggregates. Magnetic forces appear as well-suited candidates. Indeed, they enable the application of remote and versatile stimulations. The approach proposed in this manuscript is the incorporation of maghemite iron oxide nanoparticles into the cells for the formation of multicellular aggregates but also for the manipulation of cells at distance and the application of remote forces. General properties of iron oxide nanoparticles are addressed in the following section.

## 1.3 Iron oxide nanoparticles

### 1.3.1 Biomedical applications

Iron oxide nanoparticles, generally composed of magnetite ($Fe_3O_4$) or maghemite ($\gamma - Fe_2O_3$), are multifunctional tools for many biomedical applications mainly thanks to their good biocompatibility and their specific magnetic properties. They were initially developed as an MRI (Magnetic Resonance Imaging) contrast agent. In 1996, the first iron oxide nanoparticle based product was approved by the FDA as an oral administrated contrast agent for the gastrointestinal tract [34].

Many applications then emerged based on the cellular uptake of iron oxide nanoparticles. These nanoparticles can be used in combination with **MR imaging** for the *in vivo* monitoring of cell trafficking or cell migration in cell-therapy assays [35]. They can also be useful tools for the targeted destruction of tumour tissues with **hyperthermia**. This strategy is based on the incorporation of the iron oxide nanoparticles into a solid tumor followed by the application of a high-frequency alternating magnetic field generating an increase in temperature leading to apoptosis or necrosis. Multifunctionalization of iron oxide nanoparticles by both targeting agents and drugs, is also a strategy for a **targeted drug delivery** [34] [36].

Iron oxide nanoparticles therefore present a wide range of promising applications from MR imaging, to hyperthermia, drug delivery, or tissue repair and engineering [37]. However, the incorporation of iron oxide nanoparticles into the cells is also of high interest for mechanobiology studies. Through the application of external magnetic fields, remote forces can be applied to the cells thanks to their superparamagnetic properties.

### 1.3.2 Magnetic properties

Indeed, while iron oxide is ferromagnetic, sufficiently small nanoparticles containing one single magnetic domain, have a superparamagnetic behavior. In that case, in the absence of a magnetic field, magnetization randomly flips under the influence of thermal agitation and the average magnetic moment measured is zero. However, the application of an external magnetic field magnetizes the nanoparticles, in a similar way as a paramagnet but with a much larger susceptibility, and a magnetic moment aligned with the magnetic field can be measured.

In the case of MR imaging, the superparamagnetic nanoparticles enhance the contrast

where they accumulate on scales larger than their dimension by creating local magnetic fields under the application of a magnetic field and therefore modifying the magnetization of neighbouring protons [38]. These superparamagnetic nanoparticles can also be incorporated into the cells providing a great tool to manipulate and apply forces to the cells at distance with external magnets.

### 1.3.3 Different types of iron oxide nanoparticles for magnetic labelling

To allow for cell manipulation and force application, nanoparticles need to be incorporated into the cells. The main requirements are to provide the cells with sufficient magnetization to be manipulated but without altering their viability or functionnality. Several methods have been developed to improve the magnetic labelling and uptake for a variety of applications:

- **Iron oxide nanoparticles** can be coated with dextran itself **functionnalized with proteins** such as immunoglobulins that trigger receptor mediated endocytosis. In that case, internalization is cell type specific.

- **Tranfection agents** can be used to facilitate the uptake of nanoparticles. Dextran-coated nanoparticles form large complexes with the transfection agent highly charged macromolecules. By electrostatic interactions, they adsorb to the cell membrane and trigger endocytosis through membrane bending. However, the properties of the formed nanoparticle/transfection agent complex are hard to control and studies evidenced the possible presence of precipitates and adsorption of the complex on the cell membrane instead of internalization.

- **Polymer-free iron oxide nanoparticles coated with anionic monomers** are an alternative strategy. They are coated by anionic monomers such as citrate giving a negative zeta potential providing the stability of the colloidal suspension thanks to electrostatic repulsions. With this approach, nanoparticles are incorporated in the cells by endocytosis in an aspecific manner.

In the following work, we used iron oxide nanoparticles from the last category : $\gamma - Fe_2O_3$ **coated with citrate anions**.

Indeed, these iron oxide nanoparticles coated with anionic monomers present many advantages. First, the incorporation process through endocytosis has been fully described as presented in Figure 1.7. Cells are incubated with a nanoparticles solution and nanoparti-

cles are first adsorbed to the cell membrane. They are then endocytosed and the nanoparticle loaded vesicles fuse with the endosomes where the nanoparticles are stored.

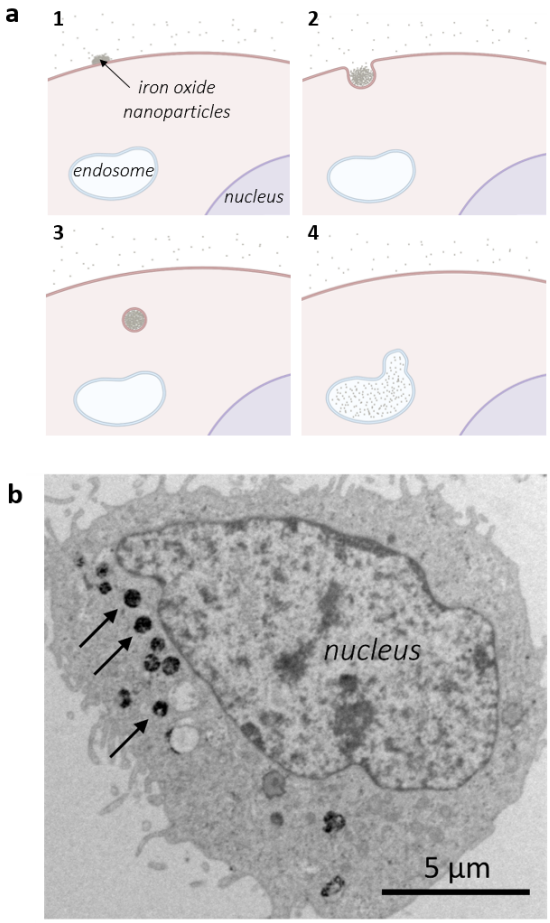


**Figure 1.7 Internalization and cellular fate of iron oxide nanoparticles.** **a)** Internalization of iron oxide nanoparticles by the cells. Nonspecific adsorption of nanoparticles on the plasma membrane (1). Invagination of the membrane (2). Endocytosis, formation of an intracellular vesicle containing the nanoparticles (3). Fusion of the loaded vesicle with the endosome (4). Adapted from Rivière et al. [39]. **b)** Transmission electron microscopy (TEM) image of an adherent mesenchymal stem cell after nanoparticle incorporation. Nanoparticles are stored in the endosomes indicated with black arrows. Image from François Mazuel's PhD thesis [40].

Second, the nanoparticle (NP) synthesis and incorporation is simpler since there is no need for NP functionnalization or addition of transfection agents. Besides, the NP uptake is fast (30 min to 2h) and can be tuned by the incubation time with nanoparticle or the concentration of the NP solution. Finally, since the internalization process is aspecific, it can be adapted to any cell type. The incorporation of maghemite nanoparticles has worked efficiently on all the cell types tested up to now.

### 1.3.4 Synthesis

In the following work, the nanoparticles used are all maghemite ($\gamma - Fe_2O_3$) iron oxide nanoparticles coated with citrate anions. They were synthetized at the PHENIX laboratory (UMR 8234) or by Véronique Thévenet in the laboratory.

First, magnetite nanoparticles ($Fe_3O_4$) are obtained by alkaline coprecipitation of Fe(II) chloride ($FeCl_2$) and Fe(III) chloride ($FeCl_3$) according to Massart's procedure [41]. Then nanoparticles are oxidized into maghemite ($\gamma - Fe_2O_3$) by the addition of boiling iron nitrate ($Fe(NO_3)_3$). After magnetic decantation and several washes with acetone and ether, the precipitate is resuspended in water. Sodium citrate ($NaC(CH_2COOH)_2(COOH)(OH)$) is then added to ensure electrostatic stability of the suspension thanks to the adsorption of citrate anions (negative charges due to the carboxyl groups) to the nanoparticles. Before precipitation with acetone, the solution is heated for 30 min at 80°C in water. After magnetic decantation and several washes in acetone and ether, the precipitate is resuspended in water.

The resulting solution is composed of nanoparticles of about 8 nm diameter (cf Figure 1.8 a) that are superparamagnetic objects as described previously. A typical magnetization curve of the nanoparticle solution is presented Figure 1.8 b.

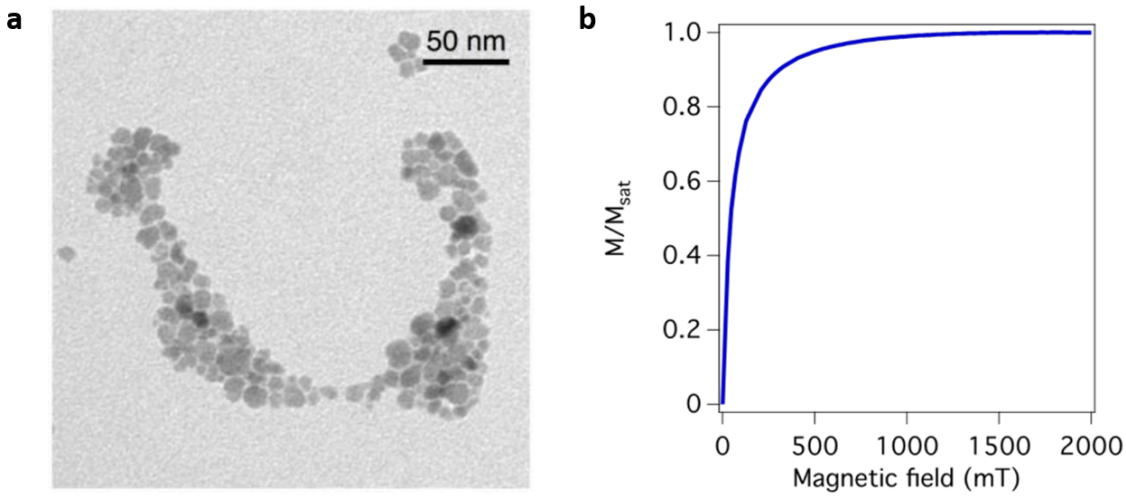


**Figure 1.8 Maghemite iron oxide nanoparticle geometry and magnetization.** **a)** TEM image of iron oxide nanoparticles in solution prepared according to the presented protocol. Image from Mazuel et al. [42]. **b)** Magnetization curve of the iron oxide nanoparticle solution. The plot represents the magnetic moment M normalized by the magnetic moment at saturation $M_{sat}$ as a function of the applied external magnetic field. Curve from Mary et al. [43].

### 1.3.5 Cytocompatibility and intracellular fate

Thanks to the cellular uptake of iron oxide nanoparticles, we can therefore provide magnetic properties to the cells. For each application, the labelling conditions have to be adapted to provide the chosen cell magnetization. However, the cytocompatibility also needs to be carefully checked.

Iron oxide nanoparticles and more generally nanoparticles and nanomaterials raised concerns about their potential toxicity, due to their size and their ability to cross biological membranes and to access cells and tissues. Many studies have been conducted to address this question [44]. If some environmental or food nanomaterials are now controversial, iron oxide nanoparticles are considered biocompatible at low doses.

Several studies have investigated the potential cytotoxic effect of different types of superparamagnetic iron oxide nanoparticles with different coatings showing no or low cyotoxicity associated until exposure to high concentration levels [45]. Besides, differentiation of mesenchymal or embryonic stem cells was shown not to be affected by the internalization of maghemite nanoparticles under a certain threshold by several teams [46] [47] [48] and also in our group [32] [49].

Moreover, iron is taken over by the iron metabolism. Indeed, iron is essential for many cellular processes in all living organisms from oxygen transport to respiration. For example, it is involved in heme that is a precursor of hemoglobin that binds oxygen for transport. Heme is also the active part of cytochromes that are key co-enzymes of the Krebs cycle for electron transport. The iron metabolism therefore enables to maintain iron homeostasis involving many proteins and enzymes. In particular, the ferritin protein enables to store iron on its Fe(III) form. If the ferroxidase enzyme enables to convert Fe(II) into Fe(III) with no reactive oxygen species (ROS), the presence of $Fe^{2+}$ can also lead to the generation of ROS through the Fenton reaction :

$$Fe^{2+} + H_2O_2 \longrightarrow Fe^{3+} + HO\cdot + OH^-$$

causing an oxidative stress [45] that is thought to be the main mechanism of cytotoxicity [44]. In the case of maghemite nanoparticles, iron is in its oxidated Fe(III) form, in contrast with magnetite nanoparticles (containing a mixture of Fe(II) and Fe(III)), reducing this potential damage to the cell proteins, DNA or lipids. Recently, it has been shown by the team that maghemite nanoparticles coated with citrate anions are degraded in the endosomes (lysosomes) and stored in ferritin [42], showing that iron oxide nanoparticles are indeed taken over by the iron metabolism. In the case of mesenchymal stem cell spheroids, 80% of iron oxide nanoparticles are degraded after 10 days. Finally, remagnetization of human stem cells from nanoparticle degradation products in certain conditions

was evidenced demonstrating a possible neosynthesis of magnetic nanoparticles in the cells [50].

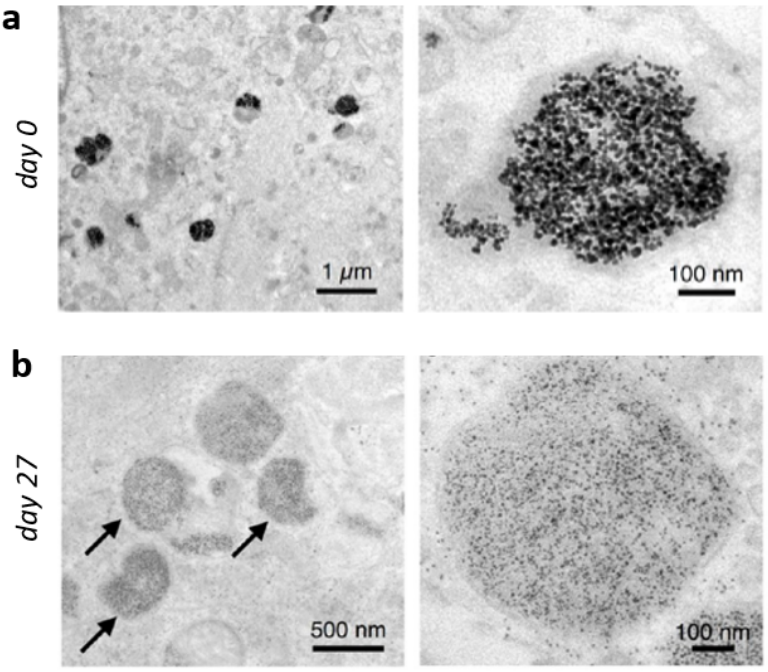


**Figure 1.9 Iron oxide nanoparticles are degraded by the cellular machinery.** TEM representative images of iron oxide nanoparticle degradation in human mesenchymal stem cell spheroids. At day 0 **(a)**, nanoparticles are confined in the endosomes, while after 27 days **(b)**, the endosomes (indicated with black arrows) contain lighter spots identified as ferritin. Ferritin spots are also detected in the cytoplasm outside the endosomes. Images from Mazuel et al. [42].

In the following work, we used as a cellular model mouse muscle precursor cells (C2C12). These immortalized cells are myoblasts, that are able to fuse and differentiate into skeletal muscular cells. In this manuscript, thanks to magnetic forces, we first investigate the mechanical properties of unorganized muscle tissue models (part I chapter 2.2). We then use magnetic forces to favor differentiation and 3D organization of muscular cells (part II). The skeletal muscle structure and function will be presented in the next section.

## 1.4 The skeletal muscle

A muscle is a tissue composed of fibers that can contract to produce a movement or generate a force. This contraction can be either involontary (smooth muscle or striated cardiac muscle) or voluntary as in the striated skeletal muscle. In this manuscript, we will focus on this second category. The skeletal muscle is linked to the bones thanks to tendons. It maintains their position and controls their movement through voluntary contraction.

The striated skeletal muscle is a multi-scale structure with a very complex organization. It is composed of aligned bundles of muscle fibers following the axis of force application. These bundles are called fascicle and have a diameter varying from 1 to 5 mm for lengths up to cm. They are composed of entangled myofibers, or single muscle fibers, corresponding to polynucleated cells. These myofibers, with diameters ranging from 10 to 100 µm originate from the fusion of hundreds of muscle precursor cells, the myoblasts (Figure 1.10). Finally, each myofiber contains hundreds of myofibrils that are composed of elementary contractile protein units in series called sarcomeres of about 2 µm diameter (Figure 1.11). The shortening of each sarcomere leads to the contraction of individual myofibers and consequently of the whole muscle. This strong anisotropy of the muscle determines directly the contractile force (active behavior) and the elasticity (passive behavior) of the muscle.

Sarcomeres are highly organized structures composed of actin filaments (thin filaments), myosin filaments (thick filaments) and other proteins confering its specific organization. According to the widely accepted sliding filament theory, myosin thick filaments slide on actin thin filaments, each filament remaining at a constant length, resulting in muscle contraction. Myofibrillar actin filaments are anchored to the Z-line thanks to support proteins such as $\alpha$-actinin while myosin filaments are anchored to the M line [53] (Figure 1.11). The lighter I band (isotropic) and the darker A (anisotropic) band, named

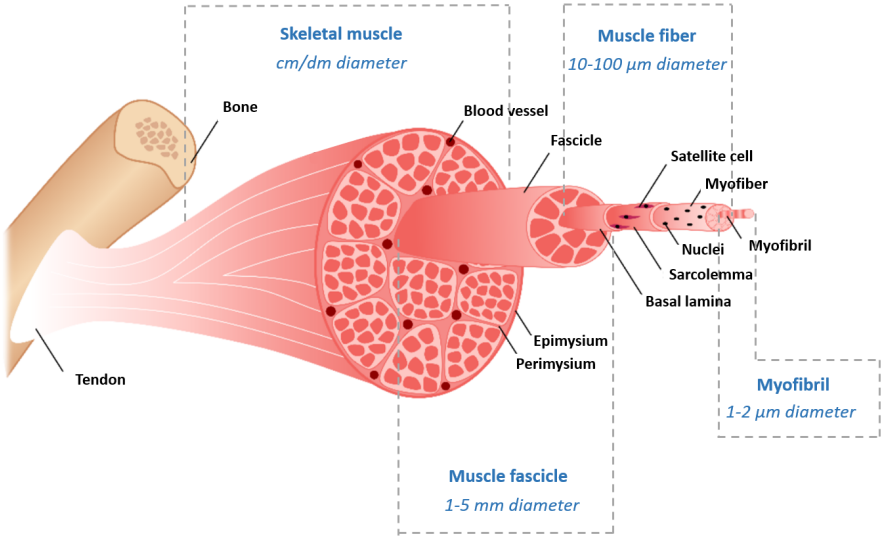


**Figure 1.10 The skeletal muscle and its multiscale aligned structure.** The skeletal muscle is composed of aligned bundles of muscle fibers, the fascicles. Each fascicle contains aligned myofibers : elongated and polynucleated cells that are the individual muscular cells. In each myofiber, myofibrils composed of thousands of sarcomeres (the elementary contractile units of the muscle) are also aligned. Adapted from Beldjilali-Labro et al. [51] and Carnes et al. [52].

after their properties under polarized light microscopy, contain respectively only the actin filaments and the entire length of myosin thick filaments. The darker A band therefore contains both actin and myosin filaments. Finally, the H zone that appears lighter than the A band in polarized microscopy contains only the myosin thick filaments [54]. Intermediate filaments and especially desmin, are essential for the structural integrity of myofibers, connecting myofibrils with each other and attaching the myofibrils to the sarcolemma.

In the sarcomeres, actin filaments are covered with tropomyosin that are hiding the myosin binding sites (Figure 1.11 b). When the sarcoplasmic reticulum surrounding the myofibrils releases calcium ions in response to a motoneuron stimulation, $Ca^{2+}$ ions bind to troponin C located throughout tropomyosin proteins inducing a conformational change of the troponin complex (composed of troponin C, I and T) and uncovering the actin binding site for myosin heads [55]. Thanks to the ATP hydrolysis cycle, myosin heads first change to an extended conformation and bind to actin filaments forming a cross-bridge. Then they change conformation again providing the power stroke and detach from the actin filaments. Myosin heads pull the actin filaments inwards reducing the distance between the two Z lines therefore contracting the myofibril and ultimately the whole muscle [54]. For one myosin head the force generated is of the order of magnitude a few $pN$ [56], while for myofibrils it is around a few tens of $nN/\mu m^2$ [57] [58], resulting in a generated force of

hundreds of $N$ for the whole muscle. The multi-scale aligned organization of the skeletal muscle is essential for this force generation.

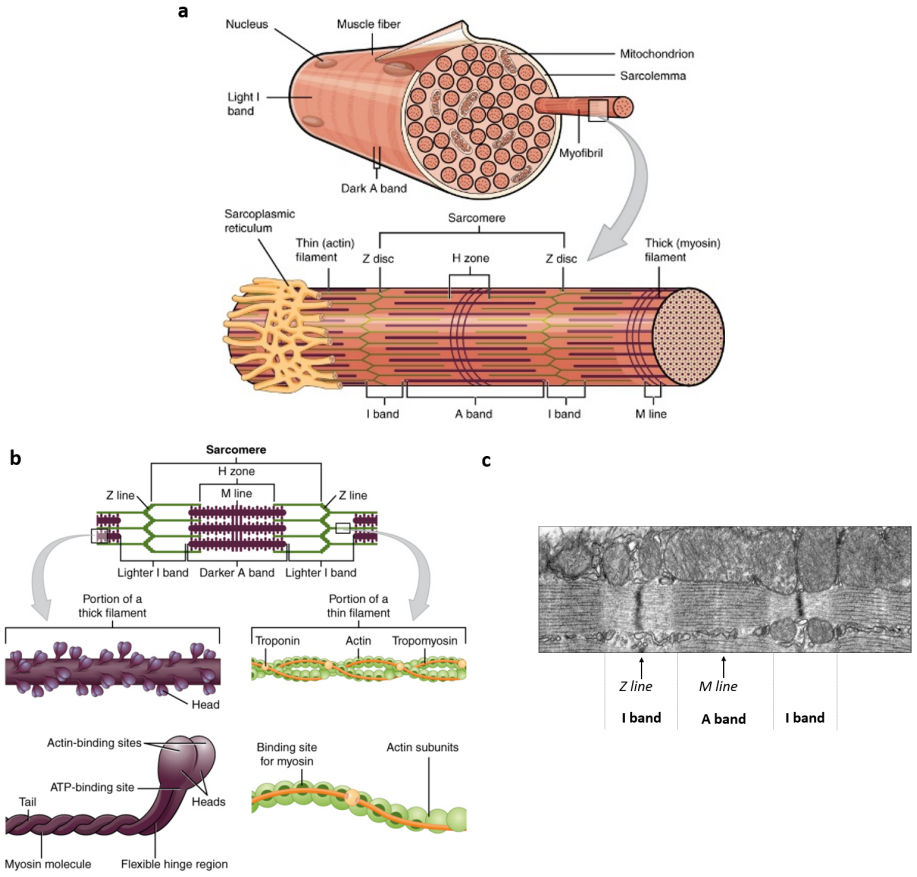


**Figure 1.11 The elementary contractile unit of the muscle: the sarcomere.** **a)** Schematic view of a myofiber composed of aligned myofibrils. **b)** Schematics of a sarcomere and of its two main components: myosin thick filaments and actin thin filaments. Actin filaments are anchored to the Z line. These filaments are covered with tropomyosin hiding the myosin binding sites. Upon $Ca^{2+}$ binding to troponin, the myosin binding sites are revealed enabling myosin heads to bind and pull on actin filaments shortening the sarcomere. The lighter I band corresponds to the sarcomere part containing only actin filaments while the darker A band contains the entire length of the myosin thick filaments. This A band therefore contains both actin and myosin filaments. Finally, the H zone corresponds to the part containing only myosin filaments. The myosin filaments sliding and pulling on the actin filaments, the lighter I band and the H zone length decrease upon contraction while the A band size remains constant. Illustrative schematics from Betts [59]. **c)** Electron micrograph of a striated muscle cut longitudinally. One single sarcomere is visible at the center of the picture. Mitochondria are visible on the top half part while the sarcoplasmic reticulum surrounding the myofibrils is visible on the bottom part between the two myofibrils. Picture extracted from Lange et al. [53].

In conclusion, spheroids and multicellular aggregates are good tools to reproduce the 3D organization of biological tissues. These tissue models have many field of applications in particular in biophysics and in tissue engineering where the application of external mechanical forces is essential. Herein, we use magnetic cells to form and stimulate remotely multicellular aggregates.

In the two parts presented in this manuscript, magnetic forces are used to **i) deform multicellular aggregates and measure their mechanical properties** and **ii) apply mechanical cues to favor differentiation and organization of 3D skeletal muscle constructs**.

# Part I

# Mechanics of 3D tissue models

# Mechanical and rheological properties of multicellular aggregates

Biological tissues, and more specifically multicellular aggregates are composed of a large number of cells. Tissue mechanics can thus be described using a continuum approach, where each elementary volume contains many cells [60]. Therefore multicellular aggregates can be characterized through macroscopic properties by analogy with soft matter objects.

## Response at different time scales

Biological tissues, and in particular multicellular aggregates, present a wide range of mechanical and rheological responses depending on the time scale considered, that we will here briefly introduce.

**At short time scales**, **from seconds to minutes**, and at low deformation levels, multicellular aggregates present an **elastic behavior** upon the application of a constraint. Deformations are reversible and are mainly due to the elasticity of individual cells conferred by their cytoskeleton.

**At intermediate time scales**, **from minutes to an hour**, multicellular aggregates have been shown to experience a **viscoelastic response** [61] [29]. A fast elastic deformation is followed by a slower deformation where internal rearrangements can arise. The aggregates can therefore be described as viscoelastic fluids, characterized by their surface tension, their elastic modulus and their viscosity. The internal rearrangements or reorganisation between cells are conferring the viscous properties to the multicellular aggregates and are enabling the relaxation of internal stresses. These rearrangements upon constraint, relaxing internal elastic stresses at intermediate time scales, have been evidenced for instance by Phillips et al. [62] with embryonic cell aggregates upon prolonged centrifugation or by Tlili et al. [63] with embryonic cell aggregates aspired through constrictions in microfluidic channels with a stress relaxation time scale of about 20 min.

**At longer time scales**, **from several hours to days**, cell division and apoptosis have to be taken into account. For instance, rearrangements caused by cell death and division are thought to fluidize the tissue providing a relaxation time set by the rates of apoptosis and division [64].

In the following work, we will focus on mechanical properties at short and intermediate scales where the effects of cell death and division are negligible.

## Active behavior of biological tissues

In contrary to common inert materials, biological tissues and multicellular aggregates have active properties and their mechanical properties may present spatial or temporal variations in adaptation to their mechanical environment. For instance, a mechanosensing effect was observed by Guevorkian et al. [61] where local surface tension of the aggregates increased with the force of aspiration in a micropipette. Cell proliferation or cell flows can also be modified by global osmotic compressions of spheroids [65] [66].

## Theoretical models

Many theoretical models have been developed to account for these manifold properties of biological tissues. They were described with a variety of models: elastic, viscoelastic [61], fractional viscoelastic [67], or visco-elasto-plastic [68], the latter trying to comprise the plasticity of biological tissues observed in some experimental conditions. However, there is no unified description of biological tissues as each model describes a few of their specific features.

## Relating individual microscopic properties to macroscopic mechanical properties

Understanding the interplay between the properties of individual cells and the global mechanics of biological tissues is now a real challenge to better apprehend the mechanical properties of tissues. If some studies have focused on this interplay at the level of 2D epithelium such as in Moisdon et al. [69], few studies focused on the translation of individual cellular properties at the 3D tissue scale. Besides, tools able to measure deformations at the tissue scale upon force application are developing, opening new possibilities to understand the relationship between microscopic properties and macroscopic mechanical properties of tissues.

In the first chapter of this part (chapter 2), we will focus on surface tension of multicellular aggregates measured thanks to magnetic forces. First, we will study the role of the cell cytoskeleton properties and cell-cell adhesions on the global mechanics of muscle precursor cell spheroids. If the influence of cell-cell adhesions and actin structure and tension have been already evidenced [70] [71] [72], the effect of desmin intermediate filaments, specific of muscle cells, on the 3D mechanics of spheroids is unknown and will be explored in section 2.2. Then in section 2.3, in a model of human breast cancer cells at different

stages of epithelial-mesenchymal transition, tumor related properties of individual cells will be correlated to the global mechanics of spheroids obtained from these cells. Finally, in chapter 3, we will present a new tool based on magnetic forces for the measurement of rheological properties of multicellular aggregates.

# Chapter 2

# Surface tension of 3D tissue models

## Contents

## 2.1 Introduction

### 2.1.1 Surface tension of multicellular aggregates

The study of mechanical and rheological properties of biological tissues, inspired from soft matter concepts was largely initiated by Steinberg. He was the first to notice the liquid behavior in embryonic tissues [73] by noticing the similarities between the spontaneous rearrangement of two different cell types and the behavior of two non-miscible fluids. He then drew an analogy between biological tissues and a viscoelastic fluid [62] (Figure 2.1), introducing the concept of a tissue surface tension governing the shape at equilibrium of multicellular aggregates.

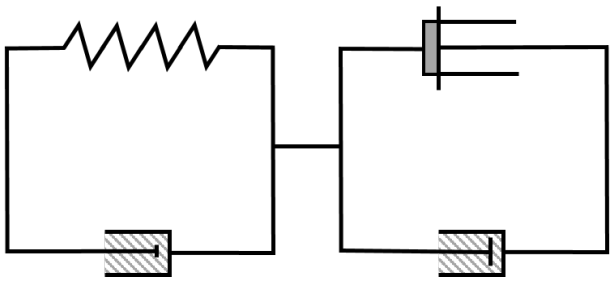

**Figure 2.1 A viscoelastic liquid model for multicellular aggregates.** The left half of the schematics corresponds to the fast-responding (low viscosity) viscoelastic solid modeled by a spring and a dashpot in parallel. The right half corresponds to the viscous liquid component modeled with a dashpot (high viscosity) and a slide wire in parallel (adapted from Phillips et al. [62]). Here in this example model, the plasticity component of a multicellular aggregate is not taken into account and neglected.

In that case, the short time scale mechanical response of the biological tissue to an external deforming force is dominated by the viscoelastic solid response of the individual cells (cell stretch and deformation) and of the extracellular matrix with no cell rearrangements. At longer time scales, the response is dominated by the viscous liquid component corresponding to cells slipping on another and relaxing the internal forces. The viscoelastic liquid model explains many experimental results [25] [74] however the biological identity of each component of the model is not clear.

Several hypotheses have been developed to account for the differences of surface tension in tissues. A simplified view to visualize the concept of tissue surface tension is that similarly to liquids consisting of molecules with attractive interactions, tissues consist of cells with adhesive interactions mediated by cell-cell adhesions molecules such as cadherins. As in liquids, the size of individual cells is much smaller than the characteristic size of a tissue and tissues can be treated as a continuous medium with macroscopic properties such as viscosity, elasticity or surface tension [15]. With this simplified model,

Steinberg first proposed the Differential Adhesion Hypothesis (DAH) that postulates that differences in surface tension are largely determined by differences in expression of cell adhesion molecules [73]. He found experimentally that surface tension was linearly proportional to the cadherin expression level [70]. However, this postulate is still disputed and does not explain the order of magnitudes measured [75]. Another hypothesis was proposed by Harris, the Differential Surface Contraction Hypothesis (DSCH) [76]. The DSCH proposes that surface tension arises from differences in actomyosin-driven cell cortical contractility. Finally, the Differential Interfacial Tension Hypothesis (DITH) [77] combines the DAH and the DSCH to propose that tissue surface tension is governed by the tension along the edges of individual cells or an effective adhesion combining both cell adhesion and cell contractility. The origin of surface tension in cellular aggregates is still an open research subject. This surface tension can however be measured experimentally thanks to different set-ups.

### 2.1.2 Techniques to probe the mechanical properties of multicellular aggregates

#### Surface tension measurements

Few experimental techniques exist to measure the surface tension of multicellular aggregates. They are described in Figure 2.2.

- For **parallel-plate compression**, the aggregate is compressed at constant deformation [72] [78]. Surface tension $\gamma$ is obtained from the aggregate's deformed shape at equilibrium and can be determined as $\gamma = \frac{F}{\pi {R_3}^2} \times \frac{1}{\frac{1}{R_1}+\frac{1}{R_2}}$ (Figure 2.2 a).

- **Micropipette aspiration** enables to measure the local surface tension of the aggregate [79]. Spheroids are sucked in micropipettes as represented Figure 2.2 b. Surface tension can be determined from the spheroid deformation as $\gamma = \frac{\Delta P_c}{2\times(\frac{1}{R_p}-\frac{1}{R_0})}$ with $\Delta P_c$ the critical pressure to aspirate the spheroid. This local sensing does not provide a measurement of the macroscopic surface tension; however above the critical pressure to aspirate the spheroid, it will start to flow inside the micropipette and its viscosity can be deduced from the tongue flow and retraction speed.

- In the **aggregate centrifugation technique**, the aggregate is exposed to an acceleration of about 100 times earth gravity [80]. $\gamma$ is obtained from the aggregate's deformed shape under centrifugation (Figure 2.2 c). The dynamical behavior is not extracted and the samples are fixed to be observed.

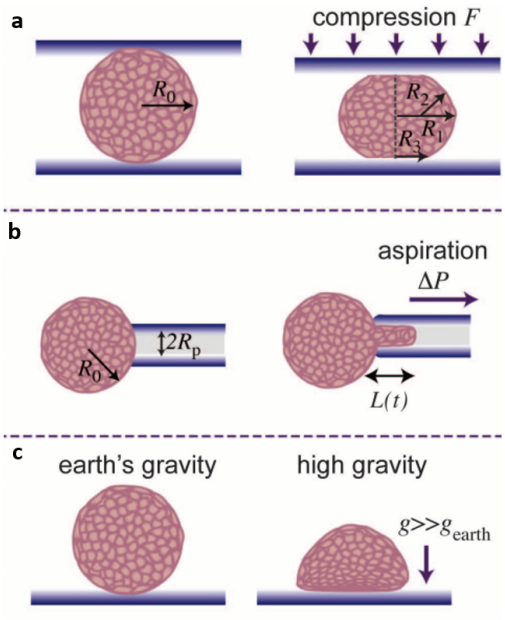


**Figure 2.2 Methods for the measurement of surface tension of multicellular aggregates.** Parallel-plate compression (a), aggregate centrifugation (b) and micropipette aspiration (c). Pictures were extracted from Gonzalez-Rodriguez et al. [15].

These techniques enable to measure the surface tension of spheroids, however other macroscopic properties such as elasticity can be assessed.

### Elasticity measurements

In order to measure the elastic properties of multicellular objects several techniques are available to probe spheroids at the global or local scale (Figure 2.3).

First at the local scale, the micropipette aspiration provides not only information on the surface tension of spheroids but it also gives access to an estimate of the elastic modulus [61]. Atomic force microscopy (AFM) or nanoindentation can also be used to probe the elasticity of the spheroids. By indenting the spheroids with the tip located at the end of the cantilever and analyzing the applied force as a function of the indentation depth, a local Young's modulus can be determined [81]. This technique is probing the spheroid elasticity only at its surface on the first top cell layers and at a very local scale. Finally, elastography-based measurements, such as optical coherence elastography/tomography (OCE/OCT) or Brillouin microscopy [82], provide information on the internal elasticity map. The elasticity distribution is deduced either by measuring the shear wave velocity that depends on the stiffness (shear-wave elastography) or by measuring the displacement field resulting from a compression stimulus (strain-imaging elastography).

At the global scale, isotropic loading can be applied to spheroids thanks to osmo-mechanical stresses by the addition of large non-penetrating molecules to the medium [65], providing compression modulus measurements [66].

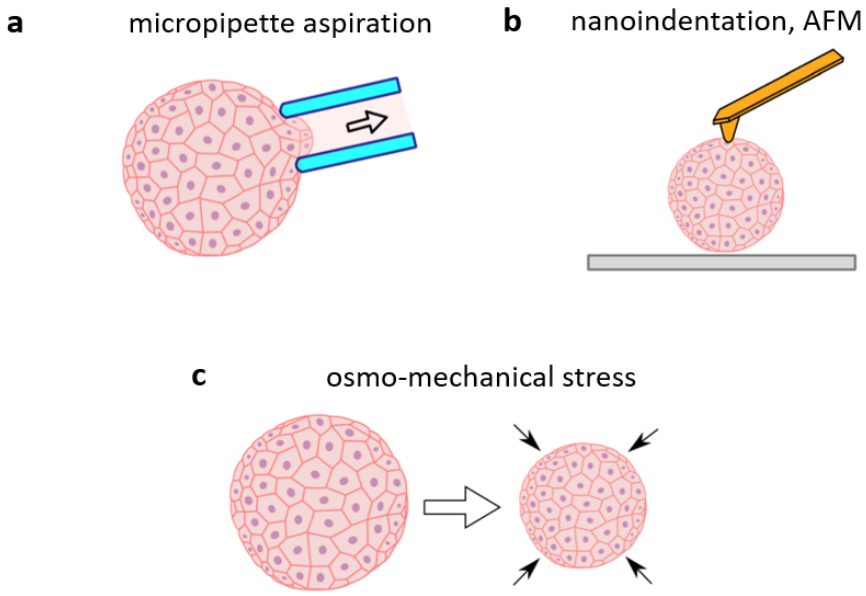


**Figure 2.3 Techniques to measure spheroid elasticity.** Micropipette aspiration **a)**, AFM or nanoindentation **b)** and osmo-mechanical stress **c)** probe the multicellular aggregates elasticity at the micro-, the nano- and the global scale respectively. Pictures were extracted from Efremov et al. [33]

### 2.1.3 The magnetic force tensiometer

All these methods provide various information on the viscoelastic properties of spheroids. However none of them provides a global scale measurement of both their surface tension and elasticity. To overcome this challenge, the magnetic force tensiometer was recently developed in our team [29]. The magnetic tensiometer is an integrated approach to measure multicellular aggregate mechanical properties and especially surface tension. This method is close to the centrifugation method presented Figure 2.2 a since the idea is to impose a "magnetic supergravity" to the aggregate by forming aggregates with cells labelled with magnetic nanoparticles (see chapter 1 section 1.2.3). The main advantages in comparison to centrifugation are: (i) that the aggregate can be visualized during the whole experiment and therefore the dynamical behavior of the aggregate can be extracted, (ii) magnetic molding techniques can be used to obtain aggregates of controlled size, shape and content (see chapter 1 section 1.2.3).

Indeed, spheroids are formed by magnetic molding. Due to iron oxide nanoparticle incorporation, cells acquire a magnetic moment. The assembly of the magnetic cells gives rise to a magnetic spheroid with a given magnetic moment. Therefore, the multicellular aggregate can be magnetized when a magnetic field is applied. Thanks to the presence of this magnetic moment, a magnetic force per unit volume $f_v$ can be applied to the aggregate: $f_v = M_v \times grad(B)$ with $M_v$ the volumic magnetic moment and $grad(B)$ the magnetic field gradient generated by the magnet. A cylindrical neodymium magnet (6 mm high and 6 mm in diameter) was used for the magnetic force tensiometer. It was selected to generate a homogeneous magnetic force per unit volume. Indeed, close to the surface (magnetic field of 0.47 T) and within a cylindrical volume of 1.5 mm high and 1.5 mm in diameter, the magnetic field gradient was uniform ($grad(B) = 170\,/m$) (see Appendix A). In conclusion, spheroids are submitted to an homogeneous force per unit volume equivalent to a gravity around 100 g when putting a permanent magnet under the cellular aggregate. The experimental set-up of this magnetic force tensiometer is described in Figure 2.4.

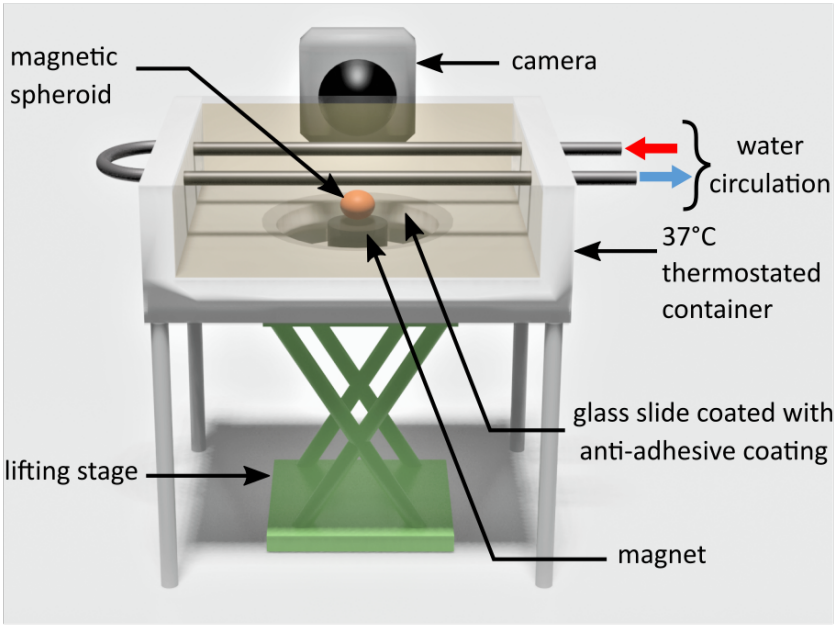


**Figure 2.4 Set-up of the magnetic force tensiometer.** A spheroid formed by magnetic molding is deposited in a temperature-regulated tank sealed with glass slides on its sides and on the bottom. A permanent magnet is approached under the spheroid generating a magnetic force that flattens the spheroid. The aggregate side profile is monitored with a camera.

The shape at equilibrium of the multicellular aggregate is therefore determined by the balance between magnetic forces and capillary forces. From the comparison between experimental and theoretical profiles, surface tension of the aggregate can be measured. The theoretical profiles were determined by analogy with a sessile drop and by solving

numerically the associated differential equations. The detailed equations are presented in Appendix B.

Thanks to this procedure, the capillary constant of the system $c = f_v/\gamma = \kappa^2$ can be determined for each multicellular aggregate (with $f_v$ and $\gamma$ the force per unit of volume and the spheroid surface tension respectively). By measuring the magnetic moment of the aggregate with Vibrating-Sample Magnetometry (VSM), the magnetic force per unit volume (fixed by the permanent magnet used as $f_v = M_v \times grad(B)$) can be calculated and the value of surface tension can be deduced. The typical shape of the obtained profiles is presented in Figure 2.5. From these theoretical profiles obtained for a 500 µm radius spheroid under a 100 g force (Figure 2.5a), we notice that the lower surface tension is, the more sensitive the magnetic tensiometer is. A sufficient deformation of the spheroid is therefore required to measure accurately its surface tension. This limitation is circumvented by increasing the size or the magnetic moment of the spheroid to obtain larger deformations (Figure 2.5b).

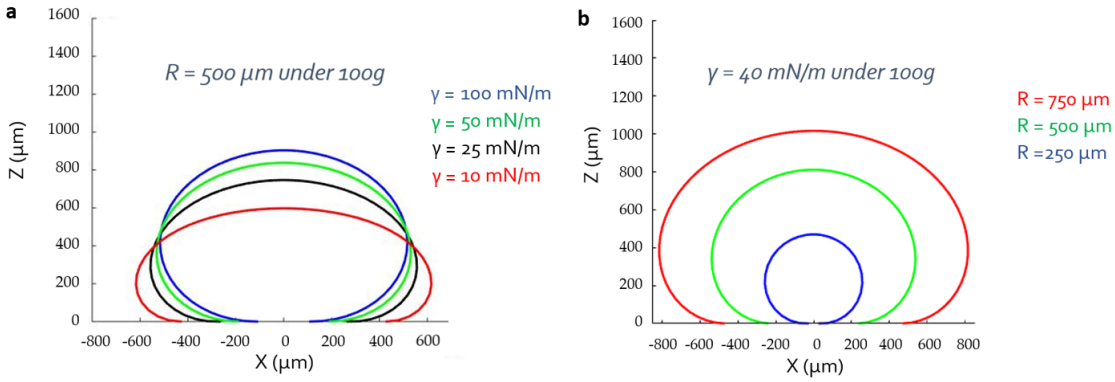


**Figure 2.5 Laplace profiles obtained by numerical integration for a multicellular aggregate under magnetic flattening (with $f_v$ equivalent to 100 g) for different surface tension values (a) or different radii (b).** In both cases, the profiles were plotted in non-wetting conditions.

From this experimental procedure, the surface tension of spheroids made of different cell types or formed in various conditions is obtained (Figure 2.6 a and c). Moreover, from the short-time scale deformation, the Young's modulus E of the tissue model is measured [29]. Indeed, by measuring the contact length 2L and using Hertz theory, E can be derived as $E = \frac{(1-\sigma^2)\pi M_v \ grad(B) R^4}{L^3}$ (Figure 2.6 a-b and d). In the following measurements, we assumed that the contact length at $t_0^+$ is equal to the contact length at $t_f$ since all our measurements were done such that $R \sim R_c$ with $R_c$ the critical radius for the elastocapillary transition. In that case, as described in Mazuel et al. [29], we have $L_{elastic} \sim L_{capillary}$ with $L_{elastic}$ the contact length obtained by elastic deformation and

$L_{capillary}$ the contact length reached thanks to capillary forces.

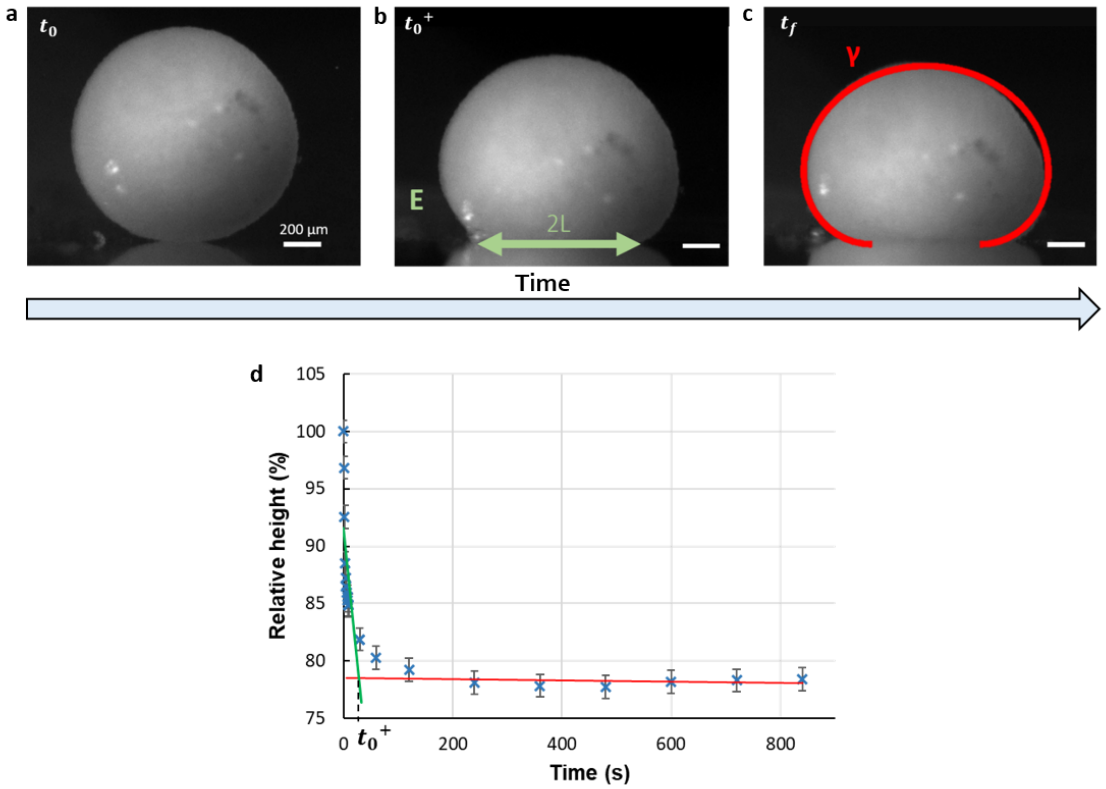


**Figure 2.6 Example of a spheroid flattened in the magnetic force tensiometer. a-c)** Representative images of a muscle precursor cell spheroid before magnetic flattening at $t_0$ **(a)**, 30 s after the magnet approach at $t_0^+$ **(b)** and after 20 min of flattening when the equilibrium shape is reached **(c)**. The contact length 2L in green at $t_0^+$ is measured to determine the Young's modulus while the spheroid surface tension is measured by fitting the aggregate profile at equilibrium at $t_f$ (fitted profile shown in red). The measured surface tension and Young's modulus for the presented spheroid are respectively 23 mN/m and 140 Pa. **d)** Representative relative height variation upon magnetic flattening as a function of time. Here, a fast elastic deformation is followed by a more viscous-like behavior to reach the capillary driven shape.

Combined with magnetic molding that enables to tune the cellular content and to add drugs during spheroid formation, the magnetic force tensiometer provides a great tool to easily probe the interplay between cell scale and global mechanical properties. Thanks to this tool, we investigated the role of the cell cytoskeleton on the global mechanics muscle precursor cell spheroids. The corresponding work is presented in the following paper preceded by a brief summary.

## 2.2 The interplay between microscopic properties and macroscopic mechanical properties of multicellular aggregates

### 2.2.1 The importance of intermediate filaments in the shape maintenance of myoblast model tissues

**Summary**

Viscoelastic properties of biological tissues drive their mechanical response to their surrounding environment. However the parameters influencing the 3D mechanics of these tissues, arising from the interplay with microscopic properties at the single cell level, are not fully understood yet.

In this study, we used mouse myoblast multicellular spheroids as simple tissue models. They were formed by a magnetic molding technique, that enables the control of the cellular content and the addition of drugs during spheroid formation to perturb individual cellular properties. The mechanical macroscopic properties of the resulting spheroids were measured by flattening the spheroids with magnetic forces. From their deformation, we were able to measure both the Young's modulus and the surface tension of these multicellular aggregates. First, we showed that perturbing intercellular adhesions, by decreasing cadherins efficiency with EGTA and disorganizing the actin cytoskeleton with Latrunculin A decreases both surface tension and the Young's modulus. We then highlighted the role of actomyosin contractility, showing that an inhibition of myosin II molecular motors decreases the surface tension and rigidity of spheroids in a dose response manner. Interestingly, the characteristic concentration of inhibition measured is of the same order of magnitude as for a single myosin II motor, pointing out the interplay between microscopic and mechanical macroscopic properties.

If the role of intercellular adhesions and of the actin cytoskeleton, both in terms of contractility and organization, had already been investigated [70] [71] [72], the role of intermediate filaments on the 3D mechanics of tissues has still not been deciphered. To give first insights to that question, we looked at the influence of the desmin network that are the main intermediate filaments of muscle cells, in collaboration with Sabrina Batonnet-Pichon and Florence Delort from BFA (Unit of Functional and Adaptive Biology). They constructed a cellular model of mouse muscle precursor cells that overexpresses a human mutated desmin D399Y. This model, developed to mimic the phenotypic changes ob-

served in patients suffering from desminopathies [83], presents a very specific phenotype with large cytoplasmic desmin aggregates [84]. By forming spheroids with cells overexpressing either a wild-type desmin or a mutated desmin, we showed that the presence of desmin cytoplasmic aggregates increases the surface tension and Young's modulus of the multicellular spheroids. We therefore revealed the fundamental role of this intermediate filament network architecture even at an early differentiation stage in this 3D undifferentiated and unorganized muscle tissue model.

# The importance of intermediate filaments in the shape maintenance of myoblast model tissues.

November 20, 2022

Irène Nagle[1], Florence Delort[2], Sylvie Hénon[1], Claire Wilhelm[1,3], Sabrina Batonnet-Pichon[2], Myriam Reffay[1]

**1** Laboratoire Matière et Systèmes Complexes, UMR 7057, Université de Paris and CNRS, 75205 Paris cedex 13, France
**2** Laboratoire Biologie Fonctionnelle et Adaptative, UMR 8251, Université de Paris and CNRS, 75013 Paris, France
**3** Present address : Laboratoire Physico-Chimie Curie, UMR 168, CNRS, Institut Curie, Université PSL, Sorbonne Université, 75005 Paris, France

Corresponding author : Myriam Reffay (myriam.reffay@u-paris.fr)

## Abstract

**Liquid and elastic behaviors of tissues drives their morphology and their response to the environment. They appear as the first insight into tissue mechanics. We explore the role of individual cell properties on spheroids of mouse muscle precursor cells and investigate the role of intermediate filaments on surface tension and Young's modulus. By flattening multicellular myoblast aggregates under magnetic constraint, we measure their rigidity and surface tension and show that they act as highly sensitive macroscopic reporters closely related to microscopic local tension and effective adhesion. Shedding light on the major contributions of acto-myosin contractility, actin organization and intercellular adhesions, we reveal the role of a major component of intermediate filaments in the muscle, desmin and its organization, on the macroscopic mechanics of these tissue models. Implicated in the mechanical and shape integrity of cells, intermediate filaments are found to be crucial to the mechanics of unorganized muscle tissue models even at an early stage of differentiation both in terms of elasticity and surface tension.**

## Introduction

Tissue-forming cells interact with each others and with their environment [1, 2, 3] giving rise to interesting visco-elastic fluid behaviors [4] that are determinant both in epithelia [5] and in 3D tissue-forming systems [6]. Physical properties such as surface tension [7, 8] and viscosity [9] can be introduced to predict tissue organization and shape [10]. Global mechanical characteristics of tissues emerge from individual cell components and their interplay [11, 12, 13] but whether they could be good reporters of individual cell behavior and global organization is still unknown.
Multicellular aggregates [14, 9] prove to be powerful tools to apprehend fundamental biological

processes as morphogenesis [15], development [16] and tumorigenesis [17, 18]. They are able to mimic various biological phenomena [19] and as model systems, are easier to use and to monitor than *in vivo* tissues [20]. Combining simplicity, reproducibility and biological significance, they are a system of choice both for biophysics and computation [21, 22, 23].
Myoblasts are widely studied cells to understand myogenesis because of their interest in myopathy modelling [24] and drug testing [25]. Muscle cell mutations implicated in numerous diseases have been extensively studied starting from symptoms to molecular origins identification [26, 27]. Among these mutations, the ones concerning intermediate filaments are of tremendous importance [28]. Intermediate filaments network is essential in muscle development, it provides mechanical integrity to the cell [29] and has a major role on the dynamical response to mechanical stimulation [30]. Desmin as a major component of intermediate filaments specifically expressed in smooth, skeletal and cardiac muscles present some mutations associated to muscle defects and myopathies. However the early effects of these mutations in tissues are unclear due to a lack of *in vitro* biomimetic muscle systems [31]. To address these limitations, we focus on mouse myoblast cells (C2C12) to test the sensitivity of 3D unorganized early stage muscle tissue models to individual cell modifications. C2C12 are adhesive and highly contractile cells (unsurprisingly regarding their function). Their high assumed surface tension makes them challenging to characterize. We designed an integrated sensitive magnetic tensiometer [32] to form stimulable myoblasts-derived tissues and to measure their surface tension and their elasticity.
In this study, we explore the interplay between macroscopic properties of model muscle tissues and the molecular or cellular processes. We investigate how surface tension and Young's modulus represent appealing tools to determine from the tissue scale, the microscopic properties. While actin and cadherins are implicated in surface tension of multicellular aggregates or embryo [33], the role of intermediate filaments in tissue shape maintenance has never been identified. Mutations in intermediate filaments severely hinder individual cell nanomechanical properties [34] and their network supports the shape of individual cells [35] and withstand applied constraints. Looking at the interplay between their organization and tissue shape maintenance or the tissue elasticity is thus primordial especially in the context of muscle. We look at cells expressing mutated desmin and exhibiting organization defects of the desmin cellular network to shed light on the crucial role of intermediate filaments on muscle tissue model global mechanics at an early stage of differentiation.

# Results

### Magnetic tensiometer for multicellular aggregates

C2C12 cells are labelled with superparamagnetic nanoparticles without altering their biological capacities [36, 37] nor inducing hypoxia or apoptosis (Figure 1 supplements 1 and 2). It is then possible to organize and stimulate them at will using external magnets. Magnets first drive cells in agarose molds to create spheroids of controlled size [32] and content, as inhibitors or reagents can be added at this stage (Figure 1a). Cohesive spheroids are obtained within 12 hours (Figure 1b) and their side profile is imaged (Figure 1c). Multicellular spheroids are fulfilled with cohesive cells that organize to form a tissue model with rounded cells at the core of the aggregate having cortical actin and more elongated cells at the periphery having contractile actin network. Their profile is recorded while a magnet is approached (Figure 1 supplements 3 and 4). Assuming that a multicellular cohesive aggregate can be modelled as a continuous elastic medium (as supported by confocal imaging, Figure 1b), surface tension and magnetic forces in volume compete to determine the equilibrium shape [14] while Young's modulus is at stake for the contact area [32] (Figure 1c and Figure 1 supplement 3). The height, width of the aggregate and the ending points of the contact zone are pointed in the TensioX application (Figure 1 supplement 3), a dedicated MatLab interface we developed to fit the obtained profile. The elasticity and the capillary parameter $c = \frac{M_v \ grad(B)}{\gamma}$ ($M_v$, $\gamma$ and $B$ stand for the magnetic moment

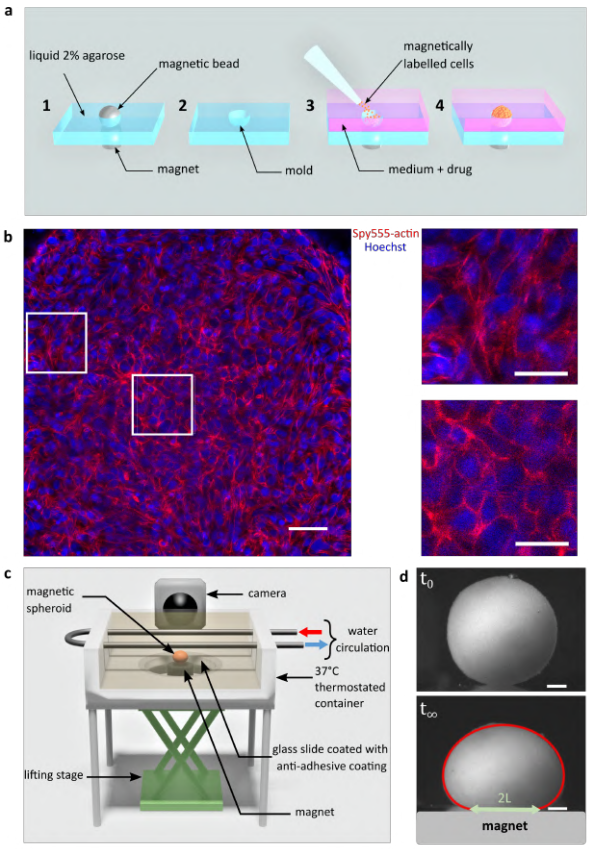


Figure 1: **Magnetic tensiometer integrated measurement set-up a)** Schematic of the magnetic molding process. A network of calibrated size steel beads deposited over cylindrical magnets is embedded in heated 2% liquid agarose **(1)**. After agarose gelling, beads are removed creating a semi-spherical mold **(2)**. Magnetically labelled cells are seeded in these non-adhesive treated molds. Magnets placed below each mold drive the cells inside the molds **(3)**. Due to high local cell density, cell-cell contacts develop to form cohesive multicellular aggregates within 12 hours **(4)**. **b)** Left panel: confocal image of a multicellular aggregates at 150 $\mu$m from the top of the aggregate. Actin (red) and nuclei (blue) are labelled. Scale bar = 50$\mu$m. Right panels: 75 $\mu$m long zooms for cells at the interface (up) or in the centre of the multicellular aggregate (down). The organisation of actin depends on the location of the cell within the aggregate. While it is mainly cortical for cells in the centre, actin is contractile at the periphery of the aggregate to maintain its shape. Scale bar = 25$\mu$m **c)** Schematic of the magnetic force tensiometer set-up. A temperature-regulated tank (37 °C) is sealed with a non-adhesive glass slide to ensure non-wetting conditions for the multicellular spheroid formed by magnetic molding (Methods and Figure 1a). A cylindrical neodymium permanent magnet (6 mm diameter and height, 530 mT, grad($B$) = 170 T.m$^{-1}$) is positioned underneath and approached thanks to a lifting stage. The tank is filled with transparent culture medium and the aggregate side profile is monitored with a camera. **d)** Representative pictures of C2C12 spheroid profiles. Top and bottom pictures show respectively a C2C12 spheroid before the magnet approach ($t_0$) and under magnetic flattening when the equilibrium shape is reached ($t_\infty$). The dynamics is shown in Figure 1 supplement 4. The spheroid surface tension is measured by fitting the aggregate shape with Laplace profile (red line) while the elastic modulus is extracted from the radius of the contact zone $L$ (green arrow) using Hertz theory as described in [32] (Figure 1 supplement 3). On this picture $\gamma = 21$ mN/m and $E = 100$ Pa. Scales bars = 200$\mu$m.

per unit of volume, the spheroid surface tension and the magnetic field respectively) [14] are extracted. Knowing the magnetic volume moment, the surface tension is easily deduced from $c$. The error measurement on the deformations is around $2-5\,\mu$m leading to a precision in the range of $5-20\%$ for surface tension and $5-10\%$ for the elasticity of C2C12 multicellular spheroids. In this regard, it should be noted that the surface tension of C2C12 spheroids is two orders of magnitude greater than that of classically studied cells such as F9 cells, for example. The error increases with surface tension because the spheroids are less deformed, which makes C2C12 cells a challenge to characterise. This error is smaller than the inherent distribution measured over different aggregates (Figure 2a-b).

**Relation between macroscopic properties and molecular or cellular characteristics: a multi-contribution pattern.**

The identified molecular origins of spheroid surface tension are numerous. While differential adhesion hypothesis has been first evidenced by Steinberg [38] and related with the level of cadherins [33], the role of actin cortex was pointed out in individual cells [39], in spheroids [9] or embryogenesis [40] evidencing a differential interfacial tension hypothesis combining the influence of adhesion and cell surface tension [41]. By comparing energy of cells in the core of the aggregate to the one at the interface, the surface tension is given by:

$$\gamma = T_{CM} - \frac{1}{2}(2T_{CC} - J_{CC}) \tag{1}$$

where $T_{CM}$, $T_{CC}$ and $J_{CC}$ stand for the cortical tension at the cell-medium (CM) or at the cell-cell (CC) interface and the intercellular surface adhesion energy ($J_{CC} > 0$) respectively [9]. We explore this multi-parameter influence by looking at cell-cell contacts inhibition and at changes in actin structure or acto-myosin contractility (Figure 2). Intercellular adhesion is mediated by multiple cell-cell adhesion proteins among which cadherins play a key role. EGTA as a calcium chelator, reduces the efficiency of this homophilic adhesion and modulates cell-cell adhesion strength. In multicellular aggregates EGTA has an impact on the acto-myosin network (Figure 3f and Figure 2 supplement 1). By reducing cell-cell contacts, it impairs the formation of the contractile network of acto-myosin at the periphery of the aggregate. At the single cell level, F-actin becomes mainly cortical whatever the cell location inside the aggregate. It may be related to a lack of strong enough cell-cell adhesions to maintain actin network and to a co-regulation of actin and cadherin tension. EGTA addition leads to a more than 5-fold decrease of both Young's modulus and surface tension (Figure 2a and b). The relationship between adhesion bond energy and the surface tension [33] is thus tested. An apparent proportionality between surface tension and Young's modulus is obtained (Figure 2 supplement 2), reminiscent of the one observed between surface tension and elasticity of the whole aggregate (itself related to cortical tension) through co-regulation mechanisms [42].
Latrunculin A disrupts the actin filaments by binding to actin monomers thus precluding its polymerization [43], its addition gives some non-connected patches of actin filaments with a lack of long-range organization (Figure 3f and Figure 2 supplement 1). Young's modulus as well as surface tension are dramatically decreased by its presence (Figure 2a and b). Besides, its action on macroscopic properties are dose-dependent as seen by the comparison between $0.15\,\mu$M (2-fold decrease) and $0.25\,\mu$M ($5-7$-fold decrease) concentrations. Our results are consistent with the dependence previously noticed between surface tension and viscosity for latrunculin-treated cells [11] and extend this dependance to stiffness.
To further test the sensitivity of the magnetic tensiometer, we selected reagents with a wider accessible range still allowing cohesive spheroid formation (Figure 2 supplement 3). $(-)$-Blebbistatin inhibits contractility by blocking myosins. $(\pm)$-Blebbistatin is a cell-permeable mixed compound containing around $50-60\%$ of the active negative enantiomer that acts as a selective, potent, and reversible inhibitor of non-muscle myosin II without affecting actin filaments assembly. In

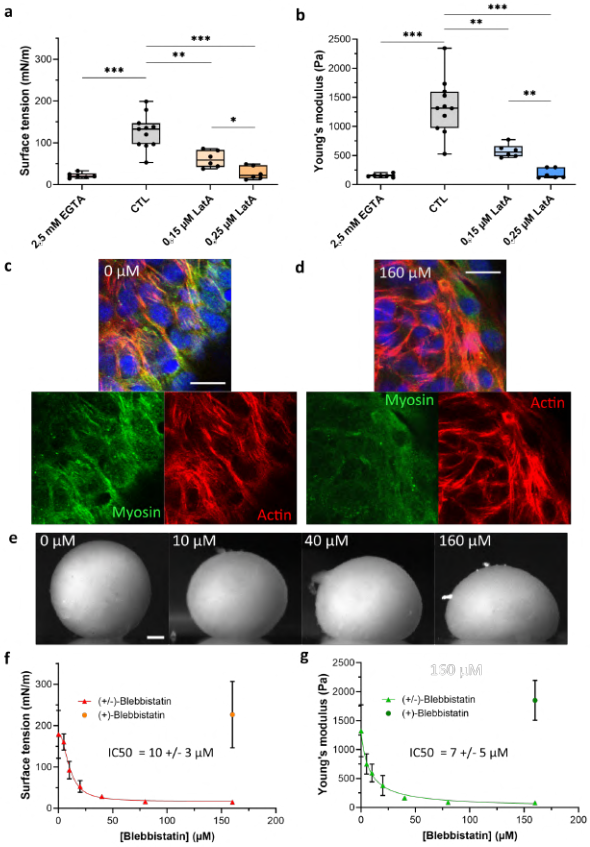


Figure 2: **Co-action of cortical tension and intercellular adhesion in multicellular spheroid surface tension and Young's modulus a-b)** Variation of surface tension (a) and Young's modulus (b) of C2C12 spheroids for 2.5 mM EGTA (calcium chelator), 0.15 $\mu$M and 0.25 $\mu$M latrunculin A (actin disruptor). Floating bars represent min to max variations and the midline indicates the median. **c)** Representative confocal images of acto-myosin organisation for cells at the periphery of an untreated multicellular aggregate. Nuclei (blue), F-Actin (red) and phospho-myosin (green) are labelled. Actin and myosin networks mostly colocalize and form a contractile radial organization. Scale bar = 20 $\mu$m. **d)** Representative confocal image of acto-myosin organisation for cells at the periphery of a multicellular aggregate treated with 160 $\mu$M blebbistatin. Nuclei (blue), F-Actin (red) and phospho-myosin (green) are labelled. Myosin network is almost disrupted compare to actin network. Scale bar = 20 $\mu$m. **e)** Representative pictures of C2C12 spheroids under magnetic flattening at equilibrium for (±)-blebbistatin concentration ranging from 0 to 160 $\mu$M are given for comparison. Scale bar = 200 $\mu$m. Variations of both surface tension (**f**) and Young's modulus (**g**) with (±)-blebbistatin concentrations are reported. Inhibition curves are fitted for the surface tension (red curve) and the Young's modulus (green curve) with a dose-response providing an $IC_{50}$ value for the (±)-blebbistatin of $10 \pm 3\,\mu$M and $7 \pm 5\,\mu$M respectively corresponding to an $IC_{50}$ for the (−) active enantiomer of blebbistatin around $6 \pm 2\,\mu$M and $4 \pm 3\,\mu$M respectively as the ratio of the active negative form is around 50-60%.

the multicellular aggregates environment, it impairs the activity of myosins reducing contractility (Figure 2c and d). Its inhibition potency is quantified *in vitro* by an $IC_{50}$ values ranging from 2 to 7 $\mu$M depending on myosin type [44]. In our experiments, (±)-blebbistatin is used on a wide range of concentrations ($0 - 160\,\mu$M) and leads to an increase in the aggregate deformation with increasing concentration (Figure 2e) while the inactive (+)-blebbistatin does not affect

mechanical properties. Surface tension and Young's modulus dramatically decrease with (−)-blebbistatin concentration (Figure 2f and g) with a decay by up to 10 fold. The extracted $IC_{50}$ is around $6 \pm 2\,\mu$M for surface tension and $4 \pm 3\,\mu$M for elasticity reproducing the one obtained at the molecular level (as the ratio of the active negative enantiomer is around $50 - 60\%$).

**Correlation with geometrical analysis: tensions at the interfaces**

By analogy with fluids, surface tension in multicellular aggregates arises from the energy difference between cells at the interface with the medium, and cells surrounded by others. The shape of cells at the surface of multicellular aggregates can thus be used to relate tissue surface tension to cell tensions. Looking at cell surface morphology on multicellular aggregates cryosections (Figure 3a) upon the use of the different drugs, we are able to test the relation between surface cell shape and arrangement on one hand, and macroscopic surface tension on the other. Latrunculin A and EGTA treated aggregates show rounded cells at the interface while control cells flatten on the surface without extending over multiple cells. (±)-Blebbistatin treated aggregates have an intermediate behavior. To quantify these observations, we extracted both the roughness of the profile and the mean contact angle $\alpha$ between cells at the interface (Figure 3b-d). They show similar variations. For control aggregates and (+)-blebbistatin aggregates, cells at the surface spread out, having a flat angle at the cell-cell contacts and a small roughness length. Drug drastic effects can be noticed on EGTA and latrunculin A treated aggregates: roughness increases (by 3 for the latrunculin A cells and by 2 for EGTA cells) while contact angles deviate from flat angle to get close to 100°. Overall, the surface tension variations are correlated with a change of morphology of the cells at the interface. As already noticed [41], high surface tension usually appears as the hallmark of flattened cells and low roughness. However, the case of (±)-blebbistatin inhibitor shows that multiple parameters have to be considered as the low surface tension obtained with the myosin inhibitor does not lead to rounded cells at the interface. Surface tension arises from a balance between cortical tension at the cell-medium and adhesion and cortical tension at the cell-cell interface (Equation 1) [41, 9]. Surface tension quantifies this interplay and not only the tension at the cell-medium interface while being predominant.

None of the considered aggregates shows up elongated surface cells extending over multiple inner cells, meaning that the effective cell-cell interfacial energy $2T_{CC} - J_{CC}$ is smaller than the double of the cortical tension at the cell medium interface. In this configuration, differential interfacial tension hypothesis and more sophisticated models provide similar results [41] and the local mechanical equilibrium at the three phases cell/cell/medium contact line gives the relation [9]:

$$2T_{CM}\cos(\frac{\alpha}{2}) = 2T_{CC} - J_{CC} \tag{2}$$

Both effective cell-cell tension $2T_{CC} - J_{CC}$ and cortical tension at the cell medium interface $T_{CM}$ can then be deduced from surface tension and contact angle measurements:

$$T_{CM} = \frac{\gamma}{1-\cos\frac{\alpha}{2}} \quad ; \quad 2T_{CC} - J_{CC} = 2\gamma\frac{\cos\frac{\alpha}{2}}{1-\cos\frac{\alpha}{2}}$$

First we checked that the tension at the cell-medium interface is predominant in the value of surface tension. As noticed on the cryosections, EGTA and latrunculin A impact predominantly the tension at the cell-medium interface with a reduction by a factor around 3. EGTA by reducing cell-cell adhesion impairs the formation of contractile actin network at the frontier of the aggregate, actin is mostly cortical (Figure 3f). Latrunculin A by depolymerizing actin reduces global cortical tension as well as the cell-cell adhesion by weakening cadherin anchorage through actin. Feedbacks between adhesion molecules and the cytoskeleton are indeed abundant and explain the lower variations of effective cell-cell tension upon latrunculin A and EGTA addition due to a possible compensation of the tension decrease by a decrease of adhesion ($J_{CC}$).

Besides blebbistatin has a significant effect on both effective adhesion and tension at the cell

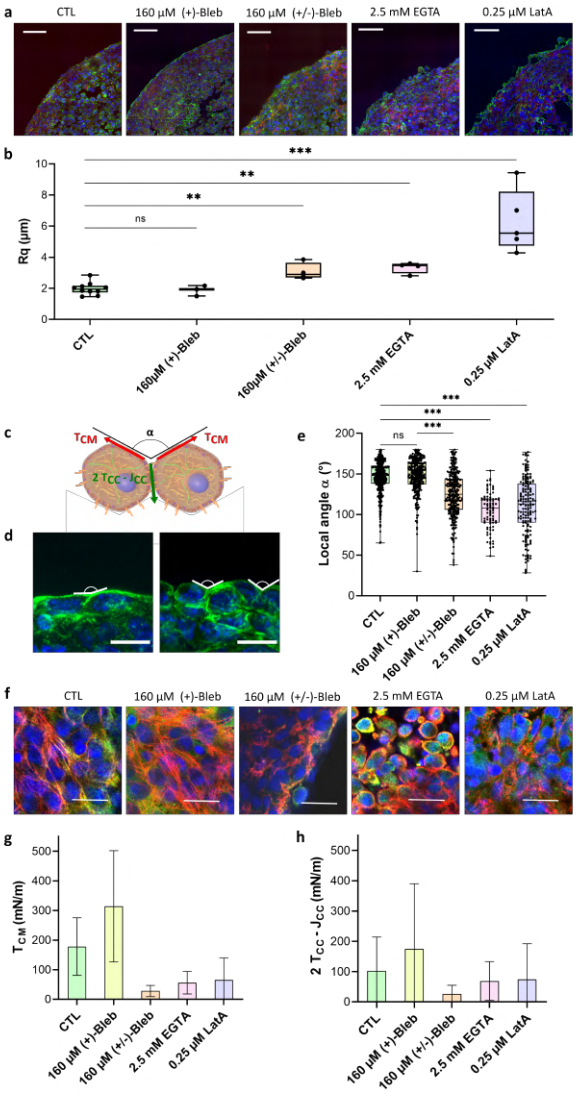


Figure 3: **Geometrical analysis of cells at the aggregate surface a)** Immunofluorescence images of cryosections of multicellular aggregates obtained by magnetic molding with different conditions. Control cells are compared to aggregates produced with 160 $\mu$M (+)-blebbistatin (inactive enantiomer), 160 $\mu$M (±)-blebbistatin (active enantiomer), 2.5 mM EGTA or 0.25 $\mu$M latrunculin A. DAPI is shown in blue, pan-cadherin in green, and F-actin in red. Scale bar = 50 $\mu$m. **b)** Profile surface roughness parameter $R_q$ (root-mean-squared) in each condition for at least $N = 3$ spheroids. **c)** Schematic of two neighbouring cells with a local contact angle $\alpha$ and the respective tension at the cell-medium interface $T_{CM}$ and effective tension at the cell-cell contact $2T_{CC} - J_{CC}$. **d)** Examples of immunofluorescence images of spheroids from which the local angles were measured. Nuclei are shown in blue and pan-cadherin is shown in green. Scale bar = 10 $\mu$m. **e)** Contact angle between cell surfaces measured in each condition for at least $N = 3$ spheroids either on cryosections or 3D aggregates (Figure 3 supplement 1). **f)** Examples of immunofluorescence images of the upper cells on spheroids obtained with different conditions. Nuclei are shown in blue, actin is shown in red, phospho-myosin in green. Colocalisation of phospho-myosin and actin appears yellow. Scale bar = 25 $\mu$m. **g-h)** Deduced values of the cell tension at the cell-medium interface (**g**) and of the effective adhesive tension at the cell-cell contact (**h**) in each condition.

medium as it impacts neither intercellular adhesions nor the cytoskeleton structure but the ability of the cell cortex to contract. This inhibitor by decreasing tension at the cortex reduces both

$T_{CM}$ and $T_{CC}$ thus affecting tension and effective cell-cell adhesion in a more drastic way than latrunculin or EGTA.
Hence the magnetic tensiometer appears as a highly sensitive tool to look at tissue model mechanics and its relation with modifications at the cellular level.

**Role of intermediate filaments in macroscopic mechanical properties of muscular tissue models.**

Desmin is an intermediate filament specific to muscle cells where it plays an essential role in maintaining mechanical integrity and elasticity [46] at the single cell level. It stands as a marker for muscular cell differentiation but its role on tissue surface tension maintenance and elasticity has not been explored. Desmin mutations are involved in human diseases such as certain skeletal and cardiac myopathies [47], characterised histologically by intracellular protein aggregates containing desmin. We focus on C2C12 myoblasts expressing desmin with the missense mutation D399Y [45]. We use 3 cell lines: A21V cells which are stably transfected with an empty vector and are control cells, desWT-Cl29 cells which stably express exogenous desmin WT with a ratio around 1:1 compared to endogenous desmin, and desD399Y-Cl26 cells which stably express exogenous mutated desmin with a ratio around 1:1 compared to endogenous desmin [48]. Desmin overexpression and modification do not affect desmin organization of adherent cells in the absence of induced protein aggregation (Figure 4 supplement 1). Surface tension and Young's modulus are not or hardly impacted by the overexpression of desmin (wild-type or mutated) (Figure 4f). Comparing A21V cells to desWT-Cl29, one can notice a slight decrease in elasticity (Figure 4f) but which is not measured for desD399Y-Cl26 cells. Besides, as the local contact angle and roughness are similar in all three cell types (Figure 5a-b), the deduced cell-medium and effective cell-cell tensions also have values which are not significantly different (Figure 5e-f). The three actin networks and the phospho-myosin networks (Figure 5 supplement 1) are also similar.
In this cellular model, desmin aggregation is induced by heat shock in 2D culture (Figure 4a-d and Figure 4 supplement 1) but also in multicellular spheroids (Figure 4e and Figure 4 supplement 2). *In vivo*, heat shock is not a common stress, but in skeletal muscle, it models the increase in heat experienced during exercise and the fever in case of infection. In desmin mutated cells (desD399Y-Cl26), heat shock duration monitors the percentage of cells presenting desmin-aggregates with up to 30% of cells for 2 hours stress compared to a 2% ratio in the case of wild-type desmin expression (desWT-Cl29) (Figure 4c-d). As desmin aggregation is induced by heat shock in this model, the effect of protein aggregation and physical inducer have to be carefully deciphered. Measurements on A21V control cells allow the effect of a heat shock on surface tension and Young's modulus to be verified. Heat shock decreases both Young's modulus and surface tension of A21V control aggregates (Figure 4g and Figure 4 supplement 3). Conversely, heat shock does not impact roughness and local contact angles between cells at the periphery of the A21V multicellular aggregates (Figure 5a-b). The decrease of surface tension therefore translates at the cell tension level and both cell-medium and cell-cell tensions decrease (Figure 5e-f). This result is corroborated by the observation of actin network at the periphery of the multicellular aggregates: heat shock does not drastically modified actin distribution but slightly decreases the number of stress fibers (Figure 5c). The effect of heat shock on the properties of aggregates of cells overexpressing WT desmin (desWT-Cl29) is similar to that observed for A21V control cells (Figure 4g and Figure 4 supplement 3), but different for aggregates of cells overexpressing mutated desmin (desD399Y-Cl26) (Figure 4g and Figure 4 supplement 3).
Focusing on desmin organization, we compare cells expressing mutated desmin (desD399Y-Cl26) to cells expressing wild-type desmin (desWT-Cl29). an increase in surface tension and elasticity dependent on the heat shock duration is observed in cells overexpressing mutated desmin (Figure 4f-g): the surface tension of spheroids of desD399Y-Cl26 cells is 1.8-fold higher than the one of desWT-Cl29 cells and their elasticity is 2-fold higher for 30 min heat shock. The

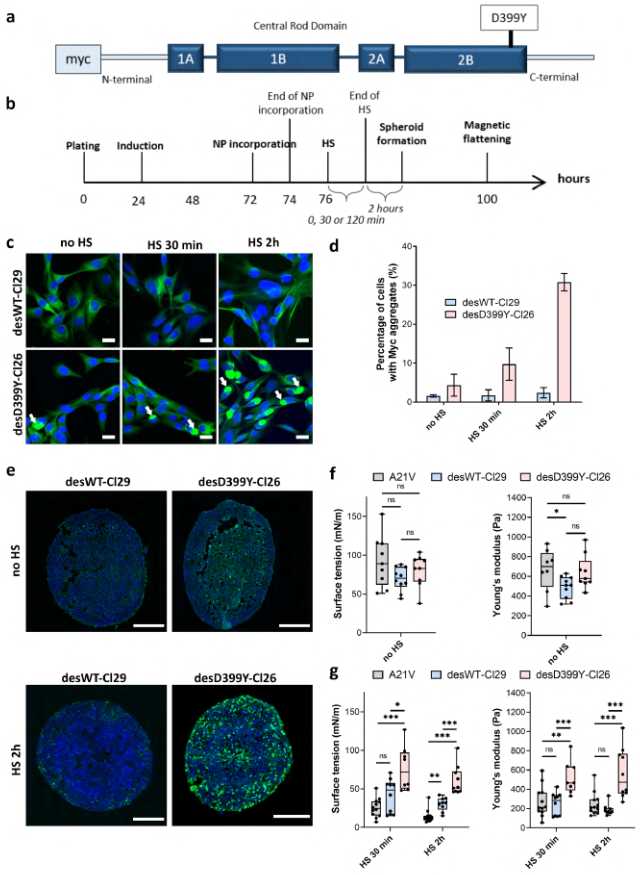


Figure 4: **Effect of heat shock and protein aggregation of desmin on surface tension and Young's modulus of C2C12 spheroids a)** Representation of desmin with the missense mutation D399Y located in Rod Domain. The expressed exogenous mutated desmin is Myc-tagged at the N-terminus (adapted from Figure 1 from [45]). **b)** Experimental procedure. Desmin expression was induced 24 h after cell plating with doxycyclin for 48 h. Magnetically labelled cells (see Methods) experienced a heat shock (HS) for 0, 30 or 120 min before spheroids were molded. Spheroid surface tension and Young's modulus were measured 3 days after expression induction. **c)** Immunofluorescence images of desWT-Cl29 (cells stably expressing exogenous desmin WT) and desD399Y-Cl26 cells (cells stably expressing exogenous mutated desmin) in 2D after 0, 30 or 120 min HS. DAPI is shown in blue and the tag Myc in green. Scale bar = 20 $\mu$m. **d)** Percentage of cells with desmin protein aggregates for each condition. Desmin protein aggregation increases for desD399Y-Cl26 cells with the duration of the HS while it remains stable around 2% for desWT-Cl29 cells. Mean values represented with respective standard deviations and at least 3 independent experiments for each condition. **e)** Immunofluorescence images of multicellular aggregate cryosections of desWT-Cl29 or desD399Y-Cl26 cells with or without HS. DAPI is visible in blue, Myc-tag in green. The results are reminiscent of the ones in 2D. DesD399Y-Cl26 spheroids exhibit sparse aggregation without HS, enhanced by 2 h HS. Scale bar = 200 $\mu$m. See Figure 4 supplement 2 for zoomed images. **f)** Surface tension and Young's modulus of A21V cells (control cells stably transfected with empty vector) spheroids compared with desWT-Cl29 and desD399Y-Cl26 cells to test for the influence of desmin overexpression. **g)** Surface tension and Young's modulus of A21V cells, desWT-Cl29 and desD399Y-Cl26 spheroids with a HS of 0 (no HS), 30 or 120 min. (f-g) At least 3 independent experiments for each condition and $N = 8$ spheroids. Floating bars represent min to max variations and the midline indicates the median.

effect is even greater for a 2 h heat shock with a 2 times higher surface tension of multicellular aggregates and a 3 times higher Young's modulus for cells expressing mutated desmin compared to cells expressing the wild-type. The effects on mechanical properties are therefore correlated with the percentage of cells containing desmin aggregates. Local cell disorganization modifies surface tension probably through individual cell tension modifications.

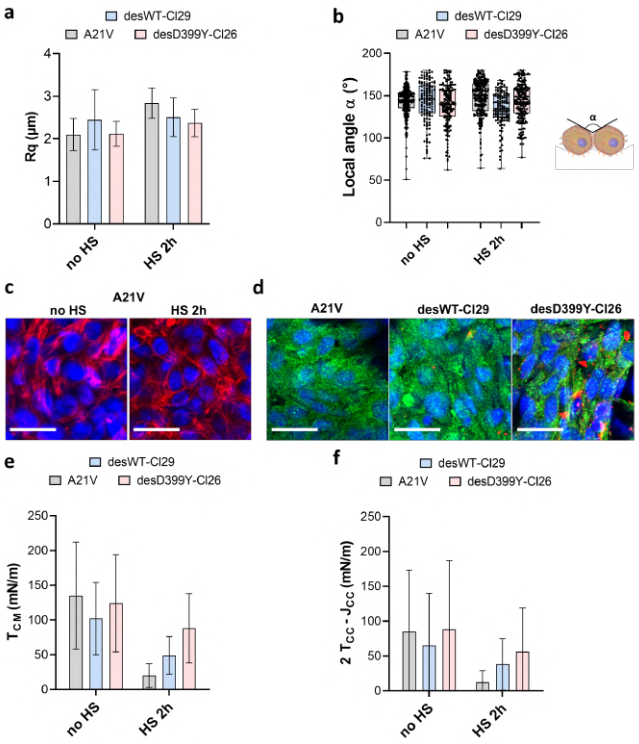


Figure 5: **Geometrical analysis of cells at the aggregate surface for C2C12 A21V, desWT-Cl29 and desD399Y-Cl26 spheroids. a)** Profile surface roughness parameter Rq (root-mean-squared) in each condition for at least $N = 3$ spheroids **b)** Local contact angle between cells at the surface measured in each condition for at least $N = 3$ spheroids. **c)** Representative confocal images of actin network for the A21V cells at the surface of the multicellular aggregate with or without HS. Nuclei are labelled in blue and F-actin in red. Scale bar = 25 $\mu$m. **d)** Representative confocal images of phospho-myosin and desmin aggregates distribution for cells at the surface of multicellular aggregates. A21V cells are compared to cells overexpressing desmin (desWT-Cl29 and desD399Y-Cl26) after 2 h heat shock. Nuclei are labelled in blue, phospho-myosin in green and desmin aggregates in red. Scale bar = 25 $\mu$m. **e-f)** Deduced values of the cell tension at the cell-medium interface (**f**) or of the effective tension at the cell-cell contact (**g**) in each condition.

Looking at the local geometry at the surface of multicellular aggregates, cells overexpressing desmin also show a predominance of tension at the cell medium interface (Figure 5). When desmin overexpression is induced, cortical tension at the cell-medium interface slightly increases (by a factor of 2) comparing desWT-Cl29 and desD399Y-Cl26 spheroids while effective adhesion is less impacted. Overexpression of wild-type and mutated desmin does not change phospho-myosin distribution on the overall aggregate (Figure 5 supplement 1) and desmin aggregates are not colocalized with contractile points (Figure 5 and Figure 5 supplement 1). However mutated desmin aggregation strengthens long range phospho-myosin filaments at the periphery of the spheroid (Figure 5d) which increases acto-myosin network contractility.

## Discussion


Figure 6: **Evolution of $\gamma$, E, $T_{CM}$ and 2 $T_{CC}-J_{CC}$ depending on intercellular adhesions, the actin network, acto-myosin contractility and intermediate filaments.**

Magnetic tensiometry gives a high sensitivity and precision even on a cellular system that does not easily deform as muscle cells. It thus pushes back the limits of macroscopic mechanics sensitivity to molecular modifications. In our study, the values obtained for cellular tensions either at the cell-medium interface or at the intercellular one confirm this specificity as tensions are two to three orders of magnitude higher than the ones measured in 3D F9 aggregates [9] or in embryo [6, 49]. This result is not surprising as spheroids of C2C12 cells organized in a highly contractile structure with a high density of stress fibers at the periphery. This tensile network makes them challenging to characterize thus requiering sensitive tools. Magnetic tensiometer sensitivity even for these high surface tension model tissues is in the range of the one obtained with compression plates tensiometer experiments for lower surface tension cell aggregates [50] and proved to be more accurate for more deformable spheroids [32]. The accessible range of measurable surface tension with the magnetic tensiometer is therefore larger.
In addition, the magnetic tensiometer measurements allow to provide dose-response curves thus representing an accurate tool to quantitatively determine inhibitors action on mechanical properties. Its robustness is related to the spheroid formation technique that allows to provide well-controlled aggregates of unprecedented size with radius and content perfectly monitored in less than 24 hours [32]. It offers a unique opportunity to explore mechanical properties even in a dose-dependant manner and to quantitatively extract the effects of mutations.

Measuring surface tension and elasticity proves to be a powerful tool to explore tissue mechanical properties. Both are key elements on tissue shape maintenance [51, 52]. Looking at 3D unorganized model tissues, we recapitulate the major cellular factors that influence tissue shape and response to perturbations. Unsurprisingly, intercellular adhesions and actin cortex structure or contractility are fundamental as was already demonstrated *in vivo* [53, 54]. Their decrease reduces both surface tension and elasticity (Figure 6). In our study, the major contribution of cell contractility in tissue shape maintenance is pointed out regarding the resulting decay obtained for surface tension and stiffness at high concentration of blebbistatin. Inhibition at the microscopic level correlates with surface tension and elasticity evolution, confirming them as relevant indicators of molecular state and cellular contractility checked by looking at acto-myosin network. The crucial role of acto-myosin contractility is also corroborated by microscopic observations. Long-range actin network at the periphery of the multicellular aggregates is fundamental to macroscopic shape maintenance while the slightest modification of this network drastically changes this property.
Altogether, our results suggest that measuring mechanical properties at tissue-scale provides insights into the molecular level [55] and that conversely, molecular modifications can induce mechanical changes at tissue-scale. Complemented by local measurements of the contact angle

of cells at the surface of our multicellular aggregates, our approach is able to determine the relative influence of cytoskeleton structure, adhesion molecules and cortical tension on the surface tension and may distinguish tension from adhesion modifications.
Desmin is the most representative intermediate filament for muscle cells. It has a pivotal role in myofibril architecture in mature muscle but also exerts important function on the adaptation of muscle cells to passive stretch and contractility [56]. Desmin organization defects severely impact muscle formation and maintenance, they cause myopathies or cardomyopathies [26]. In desminopathies, desmin aggregates are characteristic of the pathology, however these aggregates remain heterogeneously distributed within the cardiac or skeletal muscle tissues. Furthermore, the adult onset of the disease and the wide spectrum of phenotypes point a sensitivity to the environmental factors. Heat shock taken as an exogenous stress in our cell model, manages to mimic heterogenous desmin aggregation in model tissues. However at the same time, it is documented that the heat stress chosen as a transducer of desmin aggregation in desD399Y cells, can affect the biomechanical properties of skeletal muscle cells or myofibres [57]. In our experiments, we reproduce these results as heat shock decreases both surface tension and Young's modulus for cells without desmin aggregation by impacting actin contractility. This mechanism observed *in vivo* may be seen as a protective effect to avoid muscle damage. Desmin aggregation seems to impair this mechanism and is potentially the signature of a lack of cell adaptation.
Furthermore, in single cells, desmin aggregation has been associated to sarcomere misalignment but also impacts biomechanical properties [58]. We measure its action on surface tension and elasticity: desmin aggregation leads to an increase on both elasticity and surface tension. Desmin acts on muscle functioning and integrity [59, 60], its disorganization may hinder individual cell contractility [61] and homeostasis [62]. Our results highlight its major role at the tissue level where it impacts on cell tension mainly at the cell-media interface by increasing cell contractility. In zebrafish, it was shown that invalidation of the *snaib* factor induced extrusion of cardiomyocytes with increased contractility and an alteration of the *desmb* gene (ortholog of the *des* gene in humans) [63]. Overexpression of desmin recapitulates this process and highlights its role in maintaining the myocardial wall. In our model, desmin does not increased but is mutated and this mutation induces desmin aggregation. However, the same increase in contractility which may lead over time to myofibril fragility which could have an impact on sarcomere alignment and force transmission in cardiac or skeletal muscle in myopathies. Intermediate filaments organization therefore appears as essential in muscle tissue shape maintenance and mechanical properties even at an early stage of differentiation. At the individual scale, mutated desmin cells show modified reorientation dynamics [64] and are slightly (but not significantly) stiffer [46], a behavior reminiscent of the elasticity increase noticed on mutated desmin filaments D399Y [65]. However 2D studies fail to reproduce the severity of the effects on tissue mechanics. Conversely, stiffening is translated at the multicellular scale on the Young's modulus (Figure 4g) but the effect is enhanced. While a 1.4-fold increase was noticed in single cell elasticity, macroscopic Young's modulus of multicellular aggregates significantly increased by 3-fold when comparing mutated to wild type desmin. Moreover while desmin overexpression does not affect surface tension (Figure 4f), desmin protein aggregation rises its value (Figure 4g). Protein aggregates by giving a more rigid network nodes actually strenghten cell cortex [46] and may reinforce effective cortex tension thus increasing tissue surface tension. Compared to wild-type desmin, they enhance macroscopic long range contractile network efficiency.
We demonstrate that desmin aggregation impacts both elasticity and surface tension of myoblast spheroids pointing out the importance of desmin organization on macroscopic tissue mechanics even at early stage of differentiation. Surface tension and elasticity are thus sensitive reporters of the individual cellular state but also of the multicellular organization. Two reasons may be involved. First spheroids are made of about 150 000 cells; measuring macroscopic properties allows the properties of individual cells to be averaged over a large population. Secondly collective effects appear as as the change in cell organisation modulates both cell-medium and cell-cell

tensions, both of which are involved in surface tension [9]. Desmin maintains shape of multicellular aggregate, its role on individual cell is translated and its action is enhanced at the tissue level.

## Conclusion

Macroscopic properties of multicellular spheroids such as surface tension and elasticity appear as highly sensitive markers for cell cortex and cell-cell adhesion modifications. Measuring them by an approach based on magnetic cell labelling and multicellular aggregates tensiometry allows to explore dose-response evolution correlated with microscopic inhibition potency. The precision provided by the magnetic tensiometer opens a new field of investigation to test the impact of potential drugs or genetic modifications on the mechanics of early-stage tissue models that can be extended to little deformable cell types. We first identified the usual suspects of cellular mechanics (actin network, acto-myosin contractility and cell-cell adhesion) as being fundamental in tissue surface tension and elasticity but our approach was also used on a cellular model of desmin-related myopathies. It demonstrated the crucial role of intermediate filaments in tissue shape maintenance and Young's modulus. Desmin disorganization induces macroscopic changes in early-stage tissue models, undetected from now at the individual cellular scale. Like actin or cadherins, desmin acts as an important integrator of tissue shape maintenance. The fully integrated system of magnetic molding and magnetic tensiometry can be envisioned as a powerful tool for the study of fundamental biological processes and for the detection of mechanical effects leading to a better understanding of skeletal muscle dystrophies.

## Methods

### C2C12 cell culture

C2C12 WT (CRL-1772 - RRID:CVCL_0188) were obtained from ATCC and cultured in Dulbecco's modified Eagle's medium (DMEM, Gibco), supplemented with 1% Penicillin-Streptomycin (P/S, Gibco) and 10% Fetal Bovine Serum (FBS, Gibco). Their identity has been authenticated by COI assay. C2C12 A21V (stably transfected with empty vector), desWT-Cl29 (stably expressing exogenous human WT desmin) and desD399Y-Cl26 (stably expressing exogenous human D399Y desmin) were cultured in 1% P/S, 20% FBS, 1 mg/mL Geneticin (10131027, Gibco) and 2 $\mu$g/mL Puromycin (P7255, Sigma-Aldrich) as described in Segard et al. [45]. All cell lines were tested negative for mycoplasma contamination.

### Magnetic labelling

Iron oxide superparamagnetic nanoparticles (8 nm diameter) (provided by PHENIX laboratory, UMR 8234, Paris), were obtained by alkaline coprecipitation followed by an oxidation into maghemite according to Massart procedure [66]. Finally, the aqueous solution was stabilized electrostatically by the adsorption of citrate anions on the nanoparticles surface.
Cells were magnetically labelled thanks to an incubation of 2h with a solution of iron oxide nanoparticles at $[Fe] = 4$ mM and supplemented with 5 mM citrate in RPMI medium (Gibco). The viability and the proliferation of cells after magnetic labelling were assessed by Alamar Blue showing no impact of the magnetic labelling right after the labelling or after one day (Figure 1 supplement 1).

### Magnetic molding

Labelled C2C12 cells were incubated for at least 2h in complete medium. Agarose molds were previously prepared by heating a solution of 2% agarose (A0576, Sigma-Aldrich) in phosphate buffer saline (PBS) up to boiling. The resulting solution was then poured into a 60 mm culture Petri dish containing 1.6 mm steal beads (BI 00151, CIMAP) held in place by magnets below the

Petri dish. Once the agarose solidified, the beads were removed carefully and the agarose wells were coated with a non-adhesive coating solution (07010, Stemcell Technologies) for 30 min at room temperature (RT). Cells were then detached with 0,05% Trypsin-EDTA and seeded in the wells thanks to magnet attraction (about $1.5\,10^5$ cells per well). Spheroids were then incubated overnight at 37°C, 5% $CO_2$ in complete medium in normal conditions. At this point, the culture medium may be modified to add inhibitors (Figure 1). Spheroids were then extracted from the wells by gently pipetting the surrounding liquid. Spheroids of $530 \pm 60\,\mu$m radius (N = 167) were obtained.
By measuring the magnetic moment of the aggregate with Vibrating-Sample Magnetometer (VSM) measurements (PPMS - Quantum Design) the magnetic moment per unit volume of the aggregate $M_v$ can be determined and the value of surface tension deduced. $M_v$ measurements ranged from 150 to 500 $A.m^{-1}$ and were determined for each experiment. The force per unit of volume exerted on the spheroids ranged from $2.5\,10^4$ to $8.5\,10^4\,\mathrm{N.m^{-3}}$.

**Magnetic force tensiometer**

The magnetic force tensiometer is composed of a temperature-regulated tank at 37°C sealed at the bottom and the sides by glass slides, a 6x6 mm cylindrical neodymium permanent magnet (S-06-06-N, Supermagnete, $B = 530\,\mathrm{mT}$, $grad(B) = 170\,\mathrm{T/m}$, averaged value between $100\,\mu$m and 1.5 mm from the surface of the magnet), a lifting stage to approach the magnet and a camera (QICAM FAST1394, QImaging) equipped with a 1.5x zoom lens (MVL6X12Z, Thorlabs). The temperature regulated tank is filled with transparent culture medium (DMEM, high glucose, HEPES, no phenol red, Gibco). The bottom slide is treated with a non-adhesive solution (07010, Stemcell Technologies) to guarantee non-wetting conditions for the multicellular spheroids. Horizontality of the bottom slide has to be carefully checked. The aggregate side profile is registered with the camera. The magnet is approached at $150\,\mu$m from the bottom of the aggregate. The macroscopic mechanical properties of the spheroid are obtained by the spheroid profile at equilibrium (10 min under magnetic flattening to ensure that equilibrium is reached). Surface tension is measured by fitting the spheroid profile at equilibrium with Laplace profile while Young's modulus is determined thanks to the radius of the contact zone $L$ and using Hertz theory as described in [32]. The Young's modulus $E$ equals $E = \frac{(1-\sigma^2)\pi M_v\ grad(B) R^4}{L^3}$ where $\sigma$ stands for the Poisson ratio ($\sigma = 1/2$), $M_V$ represents the magnetic moment per unit volume, $R$ and $L$ are the initial radius and the radius of the contact zone respectively. Briefly for the surface tension measurements, theoretical profiles were obtained by integrating numerically the Laplace law for capillarity and minimizing the quadratic error on the height $h$, the width $w$ and the volume $V$ of the spheroid (Figure 1 supplement 3) to extract the capillary constant $c = \frac{M_v\ grad(B)}{\gamma}$ [14].
Depending on conditions, flattening occurs either with a two times regime or exhibit a single time decay. Spheroids have two ways of deformations to reach their capillary-driven equilibrium shape : first a rapid elastic deformation then a more viscous fluid behavior. This competition is driven by the size of the aggregate meaning that above a critical radius $R_C$ [32], elastic deformation is complete and may be followed by viscouslike behavior to reach capillary-driven limit. Here all the measurements were done with a spheroid radius in the range of this critical radius so that Young's modulus can be extracted. This modulus is extracted from the first step deformation while the surface tension is deduced from equilibrium shape. Tensio𝕏 is a dedicated MATLAB generated application freely available to extract both surface tension and Young's modulus from initial and flattened profiles. Images of the initial and final state are first downloaded. User has to define the initial radius, the height and the width by pointing left/right and top/bottom frontiers of the spheroid on the two images. The radius of the contact zone is also extracted. The scale factor, the magnetic force per unit volume and an estimated surface tension value are entered. The obtained fit is then superimposed on the flattened spheroid image to check for its relevance and the deduced Young's Modulus and surface tension are registered in a separated

data file.

### Measurements of mechanical properties of C2C12 spheroids

#### In drug conditions

For inhibitor conditions, the drug was added in the medium when the cells were seeded in the wells. C2C12 spheroids were then incubated overnight at 37°C, 5% $CO_2$ in DMEM 10% FBS, 1% P/S supplemented with the chosen concentration of EGTA (03777, Sigma-Aldrich), Latrunculin A (L5163, Sigma-Aldrich), (+)-Blebbistatin (203392, Sigma-Aldrich) or (+/-)-Blebbistatin (203390, Sigma-Aldrich). For (+/-)-Blebbistatin, inhibition curves were fitted with the function $Y(X) = Bottom + \frac{(Top-Bottom)}{1+\frac{IC_{50}}{X}^{HillSlope}}$ and with no constraints applied on the 4 variable parameters.

#### C2C12 expressing mutated desmin

At day 0, cells were plated at 3000 cells/cm$^2$ ($2.25\,10^5$ cells seeded in a T-75 flask). After 24h of incubation at 37°C, 5% $CO_2$, expression of exogen desmin was induced by supplementing the culture medium with 10 $\mu$g/mL doxycylin (D9891, Sigma-Aldrich) for 2 days. The medium was replaced with fresh medium every 24h. Iron oxide nanoparticles were incorporated into the cells at day 3. After 2 hours of recovery, a heat shock (HS) with a water bath at 42°C for 0, 30 or 120 min was applied to the cells. 2 hours later, cells were detached and used to form spheroids by magnetic molding or seeded in 24-well plates for desmin aggregation evaluation. After an overnight incubation at 37°C, 5% $CO_2$, spheroids were magnetically flattened to measure their mechanical macroscopic properties, then fixed for 1 h at room temperature in 4% paraformaldehyde (PFA, J61899, Alfa Aesar). The corresponding cells grown in 2D in the 24-well plates were fixed for $15 - 20$ min at RT in 4% PFA, to assess the percentage of cells with Myc aggregation for each condition.

### Cryosections and immunofluorescence

Spheroids were fixed in 4% PFA for 1 h at RT and stored in PBS at 4°C. For cryosections, spheroids were embedded in OCT (Optimal Cutting Compound, 361603E, VWR) for 1h at room temperature, they were then frozen in iso-pentane (24872.260, VWR), cooled down in liquid nitrogen, and then stored at −20°C. 6-10 $\mu$m cryosections were obtained (Leica CM1520). For immunofluorescence labelling, cryosections or fixed cells were permeabilized $15 - 20$ min in 0,1% Triton X-100 at RT while whole aggregates where permeabilized 1 day in 1% Triton X-100 at 4°C. Non-specific interactions were prevented by an incubation with 5% BSA (#05479, Sigma-Aldrich) for 1 h at RT (increased to 2 days at 4°C for whole aggregates). Pan-cadherin (rabbit anti-pan cadherin (dilution 1:100 in PBS 0.5% BSA, C3678, Sigma) for 2h at RT), phospho-myosin (rabbit phospho-myosin light chain 2 (Thr18/Ser19) antibody (dilution 1:50 in PBS 0.5% BSA, #3674, Cell Signaling) for 2 h at RT) and desmin (dilution 1:100, in PBS 0.5% BSA, D8281 or SAB4200707, Sigma) were labelled. Three first primary antibodies were coupled with an Alexa Fluor 488 goat anti-rabbit secondary antibody (dilution 1:500 in PBS 0.5% BSA, #4412, Cell Signaling Technology) for 2h at RT while the last one was coupled to an Alexa Fluor 555 anti-mouse secondary antibody. Myc was labelled using mouse c-Myc (9E10) Alexa Fluor 647 (dilution 1:100 in PBS 0.5% BSA, sc-40AF647, Santa Cruz Biotechnologies) for 2 h at RT. F-actin was labelled using SiR-actin or SPY555-actin (dilution 1:1000 in PBS, Spirochrome) for 1h30 at RT, while nuclei were labelled with DAPI (dilution 1:1000 in PBS, D9564, Sigma-Aldrich) or Hoechst 33342 (dilution 1:1000 in PBS, H3570, Invitrogen) for 15-20 min at RT. All the samples were mounted with Fluoromont (F4680, Sigma-Aldrich) and stored at 4°C after gelation of the mounting medium at RT. Labelling of the whole aggregates were done in the same conditions but the incubation times were extending to 2 days at 4°C. Cryosections were imaged either on a Nikon microscope A1r25HD with a 100x oil objective or on an Axio observer Zeiss microscope equipped with a CSU-X1 Spinning disk with a 63x oil objective.

Whole aggregates were imaged on a Zeiss 780 confocal microscope equipped with a 20x water immersion objective.

**Roughness measurements**

The contour profile of the spheroids was extracted manually with Fiji (ImageJ) thanks to immunofluorescence images of spheroid cryosections (pan-cadherin, F-actin or phospho-myosin). The extracted experimental profile was then fitted by a circular arc and the roughness parameter $R_q$ was measured by computing for each experimental point the distance $z$ to the circular arc and then calculating $R_q = \frac{1}{N}\sqrt{\sum_i z_i^2}$ with $N$ the number of points of the experimental contour. The smaller $R_q$ is, the less rough the surface of the spheroid is, and the closer it is to a circular arc.

**Local contact angle measurements**

Local contact angles were measured thanks to pan-cadherin immunofluorescence images of spheroid cryosections or spheroids imaged in 3D. Contact angles between cells at the spheroid surface were measured on Fiji (ImageJ). Pan-cadherin labelling was used to confirm the adhesion between two neighbouring cells for each measurement. Measurements were performed on at least 3 spheroids for each condition and angles were measured all over the surface of the spheroid. No significant differences were noticed regarding the imaging source (cryosections or spheroids) as evidenced in Figure S1

**Statistical analysis**

All statistical tests were performed with a two-sided Mann-Whitney U test (Wilcoxon test) with MATLAB. p-value is used to indicate the statistical significance of the results (*, ** and *** correspond to $p < 0.05$, $p < 0.01$ and $p < 0.001$ respectively).

## Acknowledgements

The authors thank Alexandre Fromain for his help on VSM measurements and Ali Abou Hassan for providing us magnetic nanoparticles. This work was supported by the Program Emergence(s) de la Ville de Paris (Grant MAGIC Project). The study was partially supported by the Labex Who Am I?, Labex ANR-11-LABX-0071, the Université de Paris, Idex ANR-18-IDEX-0001 funded by the French Government through its Investments for the Future program, by the AFM (french association for myopathies) AFM-22956, and by the French Defense Procurement Agency (DGA-AID) France. We acknowledge the ImagoSeine core facility of the Institute Jacques Monod (member of the France BioImaging, ANR-10-INBS-04) and France Lam at the Cellular Imaging facility of IBPS for her advices on deep penetration tissue imaging. We thank the staff of the MPBT (physical properties - low temperature) platform of Sorbonne Université for their support.

## Data availability

Data supporting the findings of this study are available within the article and its Supplementary information files. Computing resources should be found on Github (https://github.com/mreffay/INagle-MReffay).

## Author contribution

I.N., F.D., S.H., S.B.P. and M.R. conceived the idea; I.N., F.D., S.B.P. and M.R. did the immunofluorescence experiments; I.N. and M.R. performed the tensiometry experiments; I.N. and M.R. created the TensioX MatLab application; C.W, S.B.P. and M.R. supervised the study;

I.N. and M.R. wrote the manuscript. F.D., S.H. and S.B.P. proofread the manuscript.

## References


[1] Vanessa Barone and Carl-Philip Heisenberg. Cell adhesion in embryo morphogenesis. *Current Opinion in Cell Biology*, 24(1):148–153, feb 2012.

[2] D. Humphrey, E.R. Dufresne, and M.A. Schwartz. Mechanotransduction and extracellular matrix homeostasis. *Nature Rev. Mol. Cell Biol.*, 15(8):802–812, october 2014.

[3] Dhiraj Indana and Ovijit Chaudhuri. Tumor biology: Cells under pressure. *Elife*, 10:e68643, april 2021.

[4] Thomas Lecuit and Pierre-Francois Lenne. Cell surface mechanics and the control of cell shape, tissue patterns and morphogenesis. *Nature Reviews Molecular Cell Biology*, 8:633–644, 2007.

[5] Alessandro Mongera, Payam Rowghanian, Hannah J. Gustafson, Elijjah Shelton, David A. Kealhofer, Emmet K. Carn, Friedhelm Serwane, Adam A. Lucio, James Giammona, and Otger Campas. A fluid-to-solid jamming transition underlies vertebrate body axis elongation. *Nature*, 561:401–405, September 2018.

[6] Jean-Leon Maitre, Hélène Berthoumieux, Simon Frederik Gabriel Krens, Guillaume Salbreux, Franck Julicher, Ewa Paluch, and Carl-Philipp Heisenberg. Adhesion functions in cell sorting by mechanically coupling the cortices of adhering cells. *Science*, 338(6104):253–256, October 2012.

[7] S. Ehrig, B. Schamberger, M. Bidan, A. West, C. Jacobi, K. Lam, P. Kollmannsberger, A. Petersen, P. Tomancak, K. Kommareddy, F. D. Fischer, P. Fratzl, and John W. C. Dunlop. Surface tension determines tissue shape and growth kinetics. *Science advances*, 5(9), 2019.

[8] Nicolas Harmand, Anqi Huang, and Sylvie Hénon. 3d shape of epithelial cells on curved substrates. *Phys. Rev. X*, 11(3), August 2021.

[9] Tomita Vasilica Stirbat, Abbas Mgharbel, Selena Bodennec, Karine Ferri, Hichem C Mertani, Jean-Paul Rieu, and Hélène Delanoë-Ayari. Fine tuning of tissues viscosity and surface tension through contractility suggests a new role for $\alpha$-catenin. *PLoS One*, 8(2):e52554, 2013.

[10] Raphael Etournay, Marko Popovic, Matthias Merkel, Amitabha Nandi, Corinna Blasse, Benoit Aigouy, Holger Brandl, Gene Myers, and Guillaume Salbreux. Interplay of cell dynamics and epithelial tension during morphogenesis of the drosophila pupal wing. *eLife*, June 2015.

[11] Karoly Jakab, Brook Damon, Francoise Marga, Octavian Doaga, Vladimir Mironov, Ioan Kosztin, Roger Markwald, and Gabor Forgacs. Relating cell and tissue mechanics: Implications and applications. *Developmental dynamics*, 237:2438–2449, 2008.

[12] Monika E. Dolega, Sylvain Monnier, Benjamin Brunel, Jean-Francois Joanny, Pierre Recho, and Giovanni Cappello. Extracellular matrix in multicellular aggregates acts as a pressure sensor controlling cell proliferation and motility. *eLife*, may 2021.

[13] Steffen Grosser, Jurgen Lippoldt, Linda Oswald, Matthias Merkel, Daniel M. Sussman, Frédéric Renner, Pablo Gottheil, Erik W. Morawetz, Thomas Fuhs, Xiofan Xie, Steve Pawlizak, Anatol W. Fritsch, Benjamin Wolf, Lars-Christian Horn, Susanne Briest, Bahriye Aktas, M. Lisa Manning, and Joseph A. Kas. Cell and nucleus shape as an indicator of tissue fluidity in carcinoma. *Phys. Rev. X*, 11(1), February 2021.

[14] Ali Kalantarian, Hiromasa Ninomiya, Sameh M I Saad, Robert David, Rudolf Winklbauer, and A. Wilhelm Neumann. Axisymmetric drop shape analysis for estimating the surface tension of cell aggregates by centrifugation. *Biophys J*, 96(4):1606–1616, Feb 2009.

[15] Elisabete C. Costa, André F. Moreira Duarte de Melo-Diogo, Vítor M. Gaspar, Marco P.Carvalho, and Ilídio J.Correia. 3d tumor spheroids: an overview on the tools and techniques used for their analysis. *Biotechnol Adv.*, 34(8):1427–1441, december 2016.

[16] F. Birey, J. Andersen, C.D. Makinson, S. Islam, W. Wei, N. Huber, H. C. Fan, K.R. Cordes Metzler, G. Panagiotakos, N. Thom, N.A. O'Rourke, L.M. Steinmetz, J.A. Bernstein, J. Hallmayer, J.R. Huguenard, and S.P. Paşca. Assembly of functionally integrated human forebrain spheroids. *Nature*, 545:54–59, 2017.

[17] Montel. F., Delarue M., Elgeti J., Malaquin L., Basan M., Risler T., Cabane B., Vignjevic D., Prost J., Cappello G., and Joanny J-F. Stress clamp experiments on multicellular tumor spheroids. *Phys. Rev. Lett.*, 107(18):188102, 2011.

[18] S. Gunti, Hoke A.T.K., K.P. Vu, and N.R. London. Organoid and spheroid tumor models: Techniques and applications. *Cancers*, 13(4):874, 2021.

[19] M. Nikolaev, O. Mitrofanova, N. Broguiere, S. Geraldo, D. Dutta, Y. Tabata, B. Elci, N. Brandenberg, I. Kolotuev, N. Gjorevski, H. Clevers, and M.P. Lutolf. Homeostatic mini-intestines through scaffold-guided organoid morphogenesis. *Nature*, 585:574–578, september 2020.

[20] Giada Bassi, Maria Aurora Grimaudo, Silvia Panseri, and Monica Montesi. Advanced multi-dimensional cellular models as emerging reality to reproduce in vitro the human body complexity. *Int. J. Mol. Sci.*, 22(3):1195, 2021.

[21] David Gonzalez-Rodriguez, Karine Guevorkian, Stéphane Douezan, and Françoise Brochard-Wyart. Soft matter models of developing tissues and tumors. *Science*, 338(6109):910–917, Nov 2012.

[22] Matthieu Martin and Thomas Risler. Viscocapillary instability in cellular spheroids. *New journal of physics*, 23:033032, march 2021.

[23] Joseph Ackermann, Martine Ben Amar, and Jean-Francois Joanny. Multi-cellular aggregates, a model for living matter. *Physics Reports*, 927:1–29, may 2021.

[24] Mollie M. Smoak, Hannah A. Pearce, and Antonios G. Mikos. Microfluidic devices for disease modeling in muscle tissue. *Biomaterials*, 198:250–258, 2019.

[25] Pei Zhuang, Jia An, Chee Kai Chua, and Lay Poh Tan. Bioprinting of 3d in vitro skeletal muscle models: A review. *Materials and designs*, 193:108794, 2020.

[26] Sabrina Batonnet-Pichon, Anthony Behin, Eva Cabet, Florence Delort, Patrick Vicart, and Alain Lilienbaum. Myofibrillar myopathies: New perspectives from animal models to potential therapeutic approaches. *Journal of Neuromuscular Diseases*, 4(1):1–15, 2017.

[27] Heinz Jungbluth, Susan Treves, Francesco Zorzato, Anna Sarkozy, Julien Ochala, Caroline Sewry, Rahul Phadke, Mathias Gautel, and Francesco Muntoni. Congenital myopathies: disorders of excitation-contraction coupling and muscle contraction. *Nat. Rev.Neurol.*, 14(3):151–167, 2018.

[28] Dutour-Provenzano G. and Etienne-Manneville S. Intermediate filaments. *Current Biology*, 31(10):R522–R529, 2021.

[29] Chang L. and Goldman R.D. Intermediate filaments mediate cytoskeletal crosstalk. *Nat. Rev. Mol. Cell Biol.*, 5:601–613, 2004.

[30] E.E.Charrier, A. Asnacios, R. Milloud, R. De Mets, M.Balland, F. Delort, O. Cardoso, P. Vicart, S. Batonnet-Pichon, and S. Hénon. Desmin mutation in the c-terminal domain impairs traction force generation in myoblasts. *Biophys. J.*, 110(2):470–480, 2016.

[31] Arne D. Hofemeier, Tamara Limon, Till M. Muenker, Bernhard Wallmeyer, Alejandro Jurado, Mohammad E. Afshar, Majid Ebrahimi, Roman Tsukanov, Nazar Oleksiievets, Jorg Enderlein, Penney M. Gilbert, and Timo Betz. Global and local tension measurements in biomimetic skeletal muscle tissue reveals early mechanical homeostasis. *eLife*, January 2021.

[32] Francois Mazuel, Myriam Reffay, Vicard Du, Jean-Claude Bacri, Jean-Paul Rieu, and Claire Wilhelm. Magnetic flattening of stem-cell spheroids indicates a size-dependent elastocapillary transition. *Physical Review Letters*, 114(9), Mar 2015.

[33] Ramsey Foty and Malcolm Steinberg. The differential adhesion hypothesis: a direct evaluation. *Developmental biology*, 278:255–63, 2005.

[34] H. Herrmann, H. Bär, L. Kreplak, S.V. Strelkov, and U. Aebi. Intermediate filaments: from cell architecture to nanomechanics. *Nature Review Molecular Cell Biology*, 8:562–573, 2007.

[35] R.D. Goldman, S. Khuon, Y.H. Chou, P. Opal, and P.M. Steinert. The function of intermediate filaments in cell shape and cytoskeletal integrity. *J. Cell Biol.*, 134:971–983, 1996.

[36] Aurore Van de Walle, Jose E Perez, Ali Abou-Hassan, M Hemadi, Nathalie Luciani, and Claire Wilhelm. Magnetic nanoparticles in regenerative medicine: what of their fate and impact in stem cells? *Materials Today Nano*, 53:100084, 2020.

[37] Aurore Van de Walle, Jelena Kolosnjaj-Tabi, Yoann Lalatonne, and Claire Wilhelm. Ever-evolving identity of magnetic nanoparticles within human cells: The interplay of endosomal confinement, degradation, storage, and neocrystallization. *Accounts of chemical research*, 53:2212–2224, 2020.

[38] Malcolm Steinberg. Reconstruction of tissues by dissociated cells. some morphogenetic tissue movements and the sorting out of embryonic cells may have a common explanation. *Science*, 141:401–408, 1963.

[39] Priyamvada Chugh, Andrew G. Clark, Matthew B. Smith, Davide A. D. Cassani, Kai Dierkes, Anan Ragab, Philippe P. Roux, Guillaume Charras, Guillaume Salbreux G, and Ewa K. Paluch. Actin cortex architecture regulates cell surface tension. *Nature Cell Biology*, 19:689–697, 2017.

[40] Natalie Heer and Adam Martin. Tension, contraction and tissue morphogenesis. *Development*, 144(23):4249–4260, 2017.

[41] M. Lisa Manning, Ramsey A. Foty, Malcolm S. Steinberg, and Eva-Maria Schoetz. Coaction of intercellular adhesion and cortical tension specifies tissue surface tension. *Proceeding of the National Academy of Sciences USA*, 107(28):12517–12522, 2010.

[42] Miao Yu, Aria Mahtabfar, Paul Beelen, Yasir Demiryurek, David I. Shreiber, Jeffrey D. Zahn, Ramsey Foty, Liping Liu, and Hao Lin. Coherent timescales and mechanical structure of multi-cellular aggregates. *Biophysical Journal*, 114(3):652a, 2018.

[43] M. Coué, S.L. Brenner, I. Spector, and E.D. Korn. Inhibition of actin polymerization by latrunculin a. *FEBS Letters*, 213:316–318, 1987.

[44] Hai-Man Zhang, Huan-Hong Ji, Tong Ni, Rong-Na Ma, Aibing Wang, and Xiang dong Li. Characterization of blebbistatin inhibition of smooth muscle myosin and nonmuscle myosin-2. *Biochemistry*, 56(32):4235–4243, 2017.

[45] Bertrand-David Segard, Florence Delort, Virginie Bailleux, Stéphanie Simon, Emilie Leccia, Blandine Gausseres, Fatma Briki, Patrick Vicart, and Sabrina Batonnet-Pichon. N-acetyl-l-cysteine prevents stress-induced desmin aggregation in cellular models of desminopathy. *PLoS One*, 8(10):e76361, 2013.

[46] Catherine Even, Gilles Abramovici, Florence Delort, Anna F. Rigato, Virginie Bailleux, Abel de Sousa Moreira, Patrick Vicart, Felix Rico, Sabrina Batonnet-Pichon, and Fatma Briki. Mutation in the core structure of desmin intermediate filaments affects myoblast elasticity. *Biophysical Journal*, 113:627–636, 2017.

[47] L.G. Goldfarb, P. Vicart, H.H. Goebel, and M.C. Dalakas. Desmin myopathy. *Brain*, 127:723–734, 2004.

[48] F. Delort, B-D. Segard, C. Hakibilen, F. Bourgois-Rocha, E. Cabet, P. Vicart, M-E. Huang, G. Clary, A. Lilienbaum, O. Agbulut, and S. Batonnet-Pichon. Alterations of redox dynamics and desmin post-translational modifications in skeletal muscle models of desminopathies. *Experimental Cell Research*, 383:111539, 07 2019.

[49] J-L. Maître, R. Niwayama, H. Turlier, F. Nédélec, and T. Hiiragi. Pulsatile cell-autonomous contractility drives compaction in the mouse embryo. *Nat. Cell Biology*, 17:849–855, 2015.

[50] Abbas Mgharbel, Hélène Delanoë-Ayari, and Jean-Paul Rieu. Measuring accurately liquid and tissue surface tension with a compression plate tensiometer. *HFSP*, 3(3):213–221, 2009.

[51] Christian Dahmann, Andrew C Oates, and Michael Brand. Boundary formation and maintenance in tissue development. *Nat Rev Genet.*, 12(1):43–55, january 2011.

[52] Sangwoo Kim, Marie Pochitaloff, Georgina A Stooke-Vaughan, and Otger Campàs. Embryonic tissues as active foams. *Nat. Phys.*, 17:859–866, july 2021.

[53] Jos Käfer, Takashi Hayashi, Athanasius F. M. Marée, Richard W. Carthew, and François Graner. Cell adhesion and cortex contractility determine cell patterning in the drosophila retina. *Proc. Natl Acad. Sci.*, 104(47):18549–18554, 2007.

[54] Norihiro Iijima, Katsuhiko Sato, Erina Kuranaga, and Daiki Umetsu. Differential cell adhesion implemented by drosophila toll corrects local distortions of the anterior-posterior compartment boundary. *Nat. Comm.*, 11:6320, 2020.

[55] Daniel Gradeci, Anna Bove, Giulia Vallardi, Alan R Lowe, Shiladitya Banerjee, and Guillaume Charras. Cell-scale biophysical determinants of cell competition in epithelia. *ELife*, 10:e61011, 2021.

[56] S. Diermeier and K. et al. Iberl, J.and Vetter. Early signs of architectural and biomechanical failure in isolated myofibers and immortalized myoblasts from desmin-mutant knock-in mice. *Scientific Reports*, 7, 2017.

[57] M. Locke and C. Celotti. The effect of heat stress on skeletal muscle contraction. *Cell Stress Chaperones*, 19(4):519–527, nov 2013.

[58] C.S. Clemen, H. Herrmann, S.V. Strelkov, and R. Schroder. Desminopathies: pathology and mechanisms. *Acta Neuropathologica*, 125:47–75, nov 2013.

[59] Elisabeth E Charrier, Lorraine Montel, Atef Asnacios, Florence Delort, Patrick Vicart, François Gallet, Sabrina Batonnet-Pichon, and Sylvie Hénon. The desmin network is a determinant of the cytoplasmic stiffness of myoblasts. *Biol. Cell*, 110(4):77–90, February 2018.

[60] Emma J. van Bodegraven and Sandrine Etienne-Manneville. Intermediate filaments from tissue integrity to single molecule mechanics. *Cells*, 10(8):1905, July 2021.

[61] Agathe Franck, Jeanne Lainé, Gilles Moulay, Eline Lemerle, Michaël Trichet, Christel Gentil, Sofia Benkhelifa-Ziyyat, Emmanuelle Lacène, Mai Thao Bui, Guy Brochier, Pascale Guicheney, Norma Romero, Marc Bitoun, and Stéphane Vassilopoulos. Clathrin plaques and associated actin anchor intermediate filaments in skeletal muscle. *Molecular Cell Biology*, 30(5):579–590, January 2019.

[62] G. Agnetti, H. Herrmann, and S. Cohen. New roles for desmin in the maintenance of muscle homeostasis. *The FEBS journal*, 289:2755–2770, 2021.

[63] A. Gentile, A. Bensimon-Brito, R. Priya, H-M. Maischein, J. Piesker, S. Guenther, F. Gunawan, and D. YR Stainier. The emt transcription factor snai1 maintains myocardial wall integrity by repressing intermediate filament gene expression. *Elife*, 10:e66143, June 2021.

[64] E. Leccia, S. Batonnet-Pichon, A. Tarze, V. Bailleux, J. Doucet, M. Pelloux, F. Delort, V. Pizon, P. Vicart, and F. Briki. Cyclic stretch reveals a mechanical role for intermediate filaments in a desminopathic cell model. *Physical Biology*, 10(1), 2013.

[65] L. Kreplak and H. Bär. Severe myopathy mutations modify the nanomechanics of desmin intermediate filaments. *Journal of Molecular Biology*, 385:1043–1051, 2009.

[66] R. Massart. Preparation of aqueous magnetic liquids in alkaline and acidic media. *IEEE Trans. Magn.*, 17:1247–1248, 1981.

**Data Files**

**Figure 1- Figure 1 supplement 1 - source data 1: Source data of the Alamar-Blue test values for the different magnetic labelling conditions reported in Figure 1 supplement 1.** Measurement of the fluorescence ($\lambda_{exc} = 570\,\text{nm}$ and $\lambda_{em} = 585\,\text{nm}$) after 1h30 incubation with the Alamar blue solution.

**Figure 1 - Figure 1 supplement 4 - source data 1: Source data of the evolution of the height of multicellular aggregates presented on Figure 1 supplement 4.** The dynamic of flattening process is reported for 5 different aggregates. **Figure 2 - source data 1: Source data of surface tension and Young's modulus measurements for control cell aggregates, EGTA or latrunculin A-treated cell aggregates reported on Figure 2a,b.** Both surface tension and Young modulus were extracted from aggregate profiles using TensioX application. Means, medians and standard deviations were extracted

**Figure 2 - source data 2: Source data of the surface tension and Young's modulus measurements for control cell aggregates,blebbistatin-treated cell aggregates reported in Figure 2f,g.** ±-blebbistatin was used at different concentrations. Both surface tension and Young's modulus were extracted from the aggregates profiles. using TensioX application. Means, medians and standard deviations were extracted for each condition and compared.

**Figure 3 - source data 1 : Source data of the roughness of imaged multicellular aggregates in various conditions presented in Figure 3a.** Roughness of the different multicellular aggregates were reported and compared. Aggregates contours were first extracted then the roughness of the contour was calculated. Means, medians and standard deviations were reported for each condition.

**Figure 3 - source data 2 : Source data of the local contact angles and the tension at the cell-medium and the cell-cell interfaces measured on multicellular aggregates in various conditions reported on Figures 3e,g,h.** Local contact angles of cells within an aggregate are manually measured and the distribution of the local contact angle is given. From the mean surface tension, both the tension at the cell-medium and at the cell-cell medium are deduced.

**Figure 4 - source data 1: Source data for the surface tension and the Young's modulus measurements of aggregates shown in Figure 4d,f,g** Both surface tension and Young's modulus were extracted from the profile of aggregates made of either control A21V, desWT-Cl29 or desD399Y-Cl26 cells. using TensioX application. Means, medians and standard deviations were extracted for each cell type and compared.

**Figure 5 - source data 1 : Source data of the roughness of multicellular aggregates for control A21V, desWT-Cl29 and desD399Y-Cl26 cells presented in Figure 5a.** Roughness of the different multicellular aggregates were reported and compared. Aggregates contours were first extracted then the roughness of the contour was calculated. Means, medians and standard deviations were reported for each condition. **Figure 5 - source data 2 : Source data of the local contact angles measured for control A21V, desWT-Cl29 and desD399Y-Cl26 cells and presented in Figures 5b,e,f.** Local contact angles of cells within an aggregate are manually measured and the distribution of the measured local contact angles is given. From the mean surface tension, both the tension at the cell-medium and at the cell-cell medium are deduced for each cell type.

**Supplementary Figures**

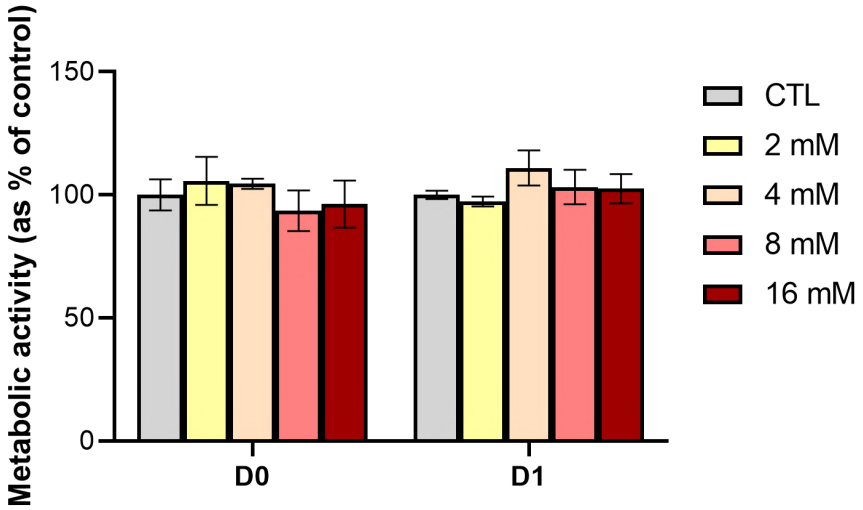


Figure 1 supplement 1: **Metabolic activity for unlabelled (CTL) and labelled cells ([Fe] = 2 to 16 mM and 2 hours incubation time), 2 hours (D0) and one day (D1) after nanoparticle incorporation.** To assess metabolic activity, the metabolic test Alamar Blue was used. Fluorescence was measured at $\lambda_{exc} = 570\,\text{nm}$ and $\lambda_{em} = 585\,\text{nm}$. Values are interpreted relative to control values (unlabelled cells in complete medium, CTL) obtained under similar conditions. No influence of nanoparticle incorporation was observed on the metabolic activity and on the cell viability at D0 or D1 and for concentrations up to 16 mM.

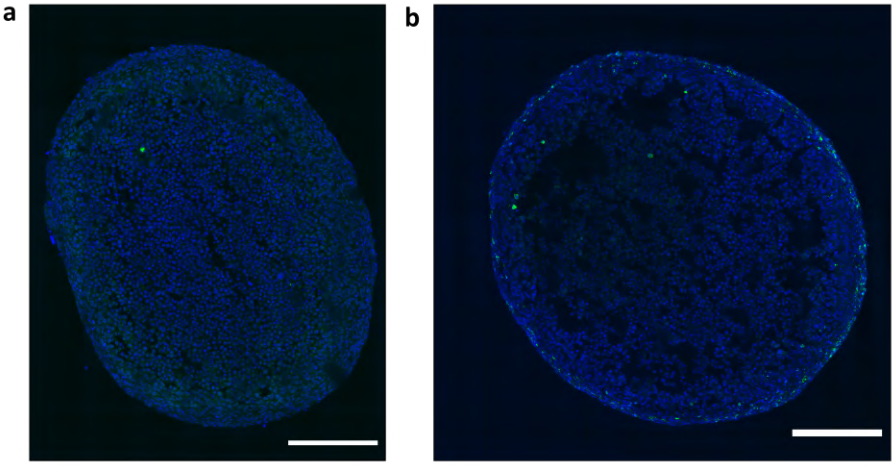


Figure 1 supplement 2: **Immunofluorescence images of C2C12 spheroid cryosections to confirm non-hypoxic and non-apoptotic conditions in spheroids. a)** DAPI is shown in blue and HIF$\alpha$ in green. HIF$\alpha$ is almost absent from the images. **b)** DAPI is shown in blue and cleaved caspase-3 in green. Only 2% of cells show a positive signal to cleaved caspase-3. Scale bars = $200\,\mu$m.

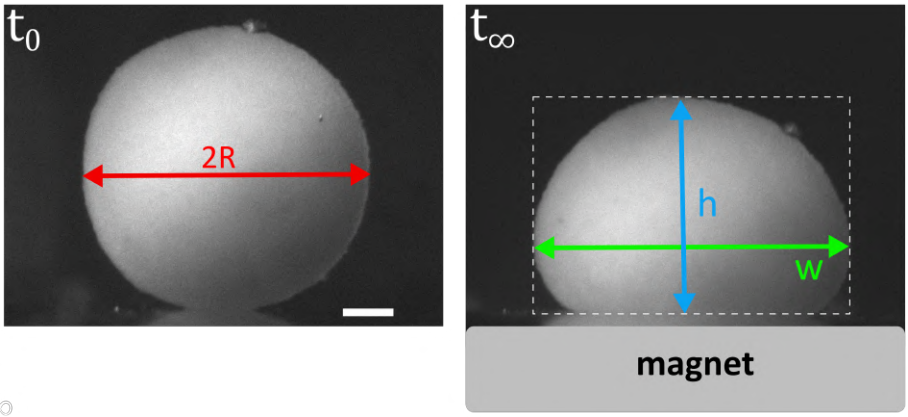


Figure 1 supplement 3: **Extraction of experimental volume, width and height of the spheroid.** The experimental volume V is calculated from the radius R of the spheroid at $t_0$ . The experimental width w (in green) and height h (in blue) are measured from the spheroid equilibrium profile. All these measurements are used in the minimisation program of the TensioX application.

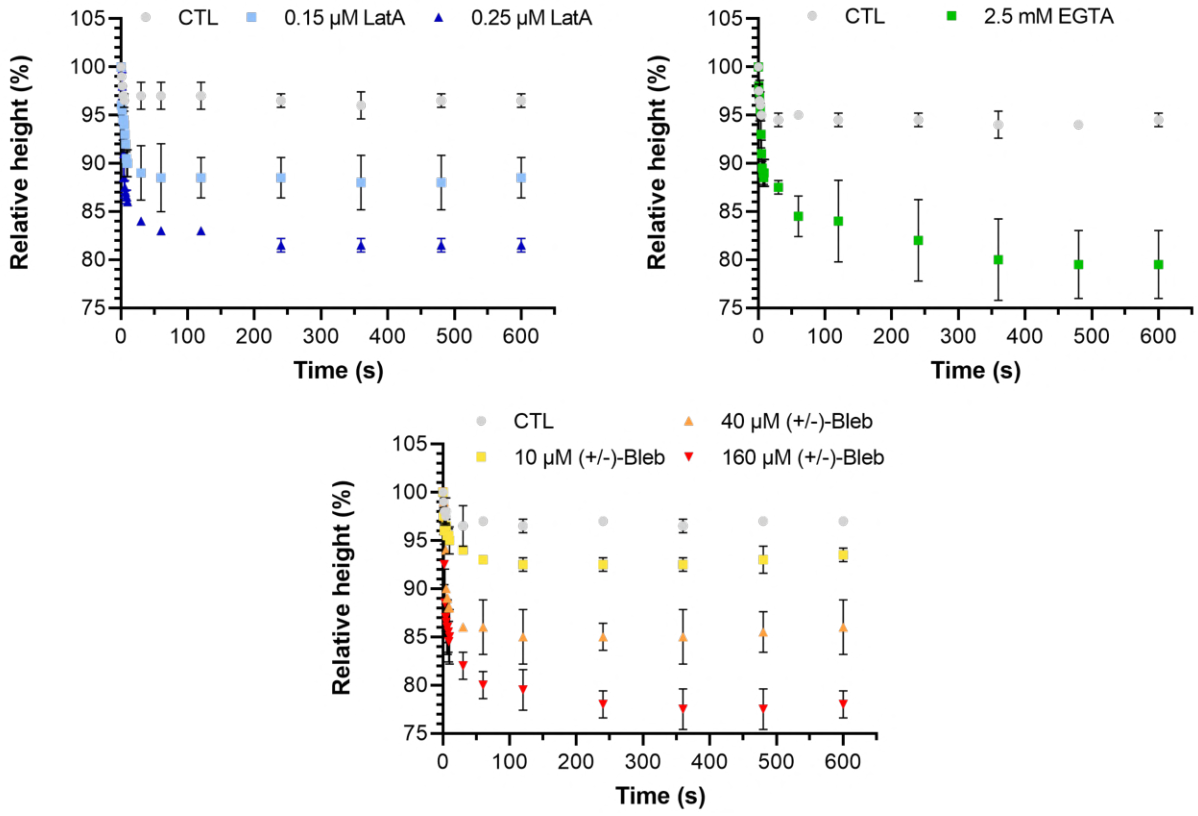


Figure 1 supplement 4: **Relative height of the aggregate as a function of time for control, Latrunculin A (LatA), EGTA and (±)-Bleb (±)-Bleb) conditions.** At $t = 0$ s, the magnet is approached and the height of the spheroid is monitored over time. After 10 min of flattening, the equilibrium shape is reached and the height of the spheroid remains stable for each condition. Each curve corresponds to at least $N = 2$ spheroids. Mean values are represented with respective standard deviations.

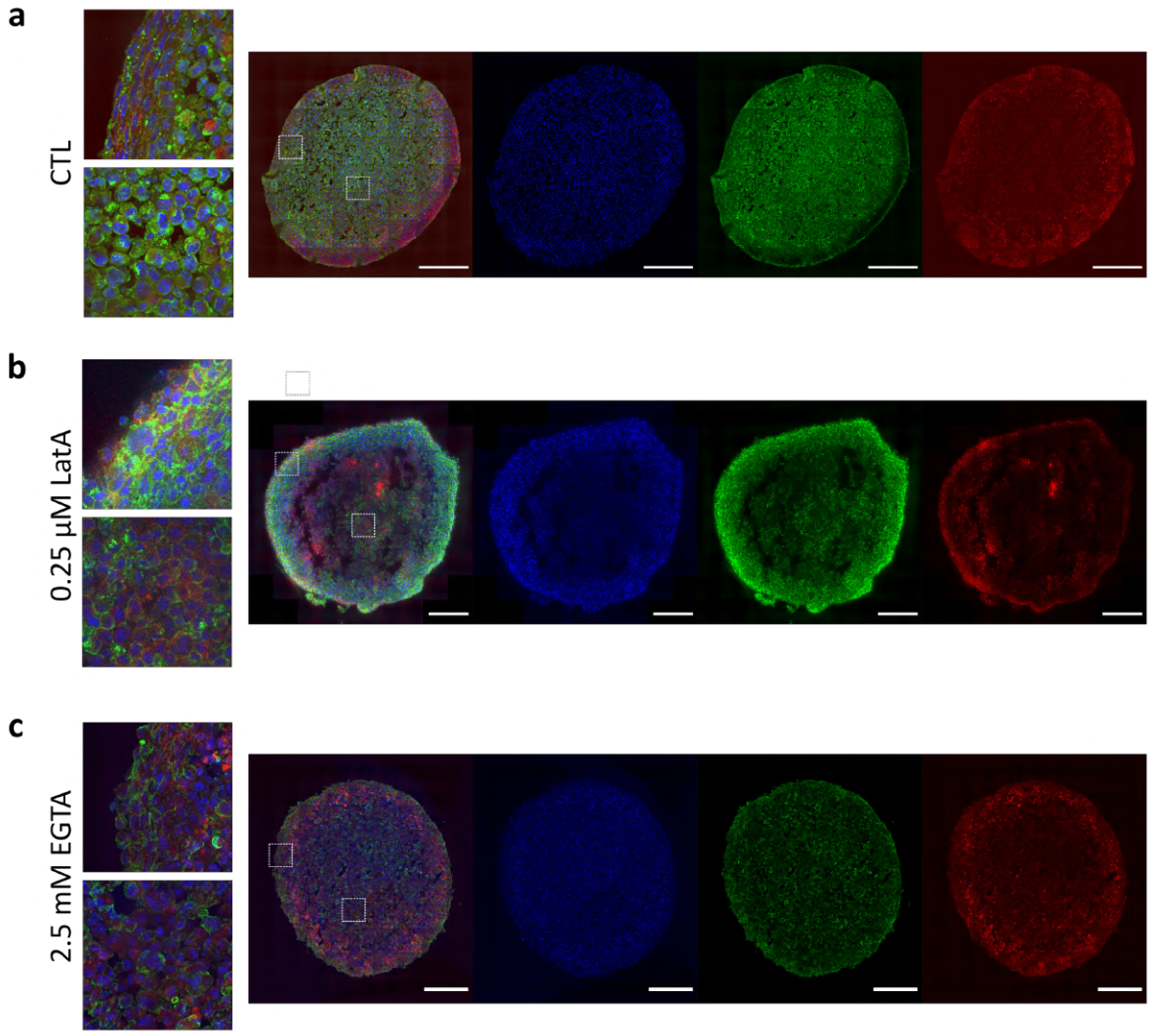


Figure 2 supplement 1: **Immunofluorescence images of C2C12 spheroid cryosections for control conditions (a),** 0.25 $\mu$**M Latrunculin A (b) and** 2.5 **mM EGTA (c).** DAPI is shown in blue, pan-cadherins are in green and F-actin is shown in red. Scale bar = 200 $\mu$m and scale bar = 40 $\mu$m for zoomed images.

tension as a function of Young Modulus.png

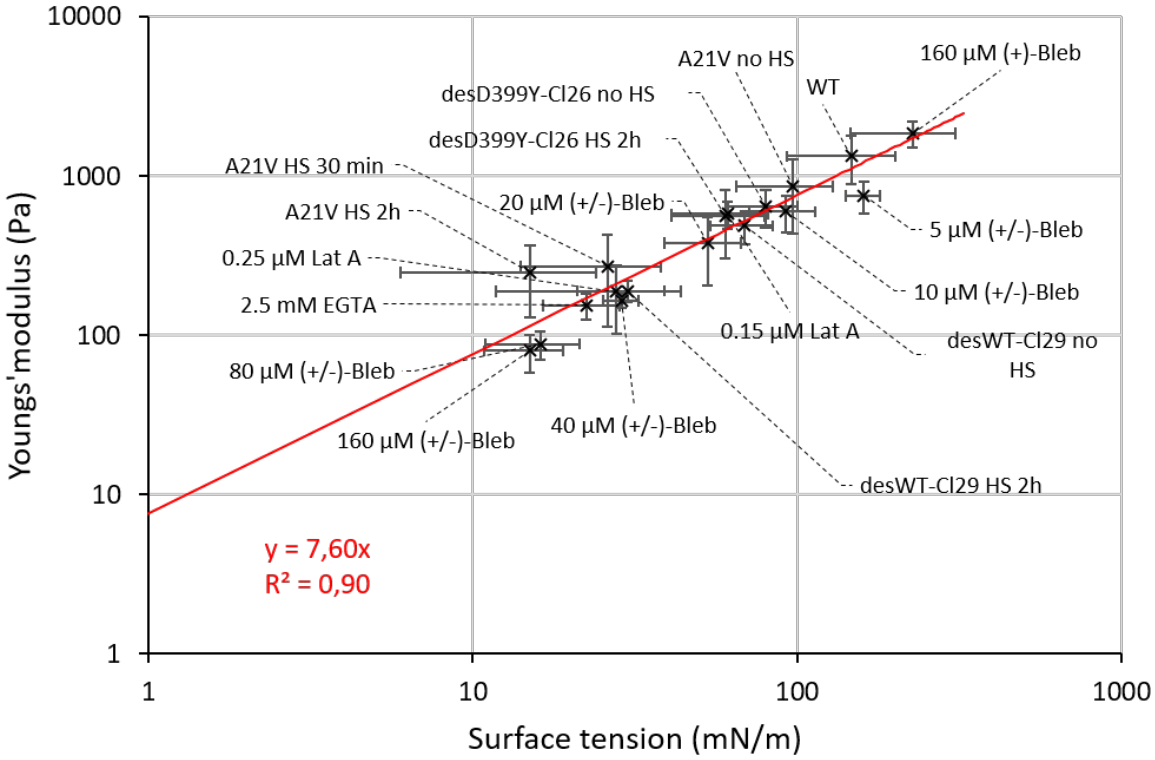


Figure 2 supplement 2: **Young's modulus of C2C12 spheroids as a function of their surface tension.** Young's modulus and surface tension are proportional across all the conditions tested for C2C12 spheroids. Values are represented in logarithmic scale.

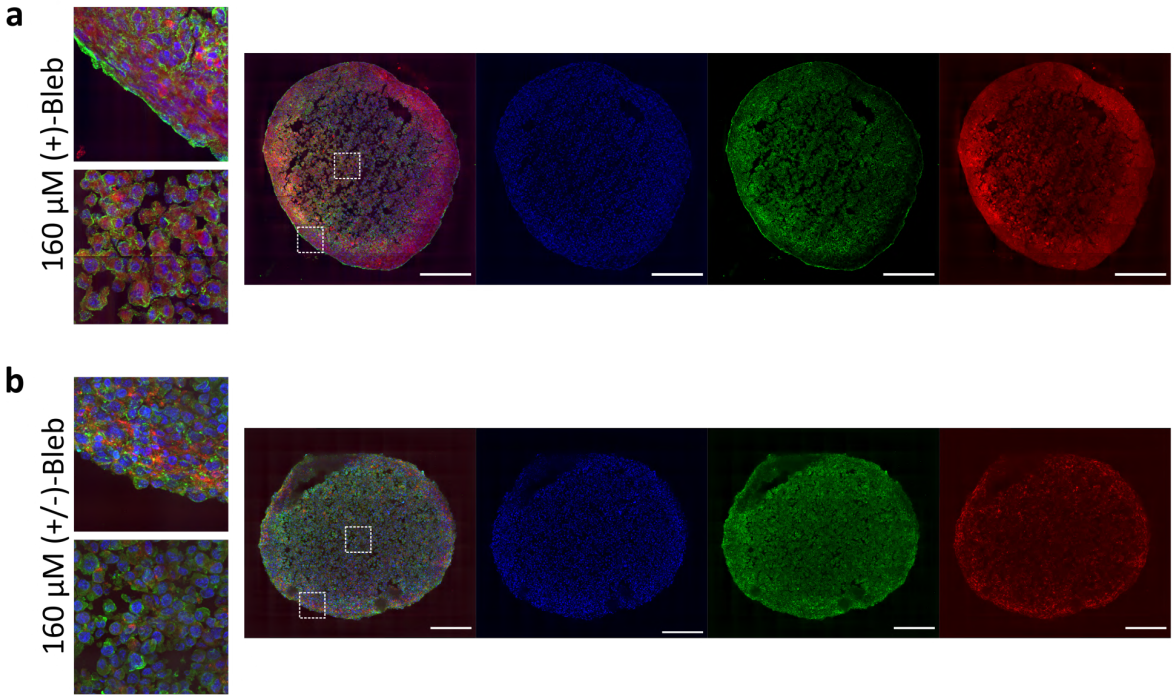


Figure 2 supplement 3: **Immunofluorescence images of C2C12 spheroid cryosections for 160 $\mu$M (+)-Blebbistatin (a) and 160 $\mu$M ($\pm$)-Blebbistatin (b).** DAPI is shown in blue, pan-cadherins are in green and F-actin is shown in red. Scale bar = 200 $\mu$m and scale bar= 40 $\mu$m for zoomed images.

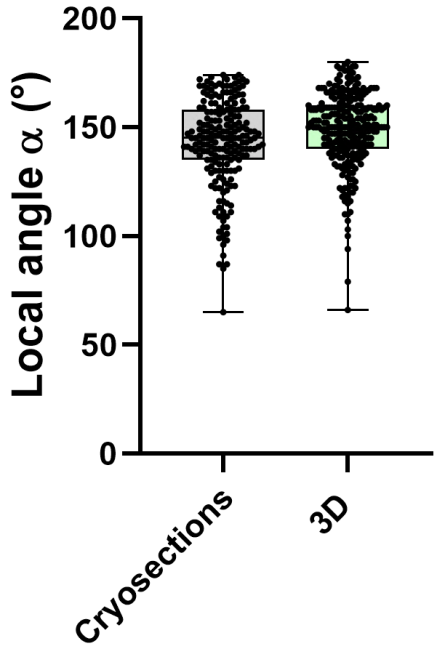


Figure 3 supplement 1: **Comparison between local angles measured on spheroid cryosections or 3D images for C2C12 WT spheroids.** Local angles were measured on the surface of the spheroids for $N = 3$ spheroids for each type of measurement. Measured angles on cryosections have a median of 145° and measured angles on 3D images have a median of 150°. This 5 degree difference is below the measurement error on the local angles.

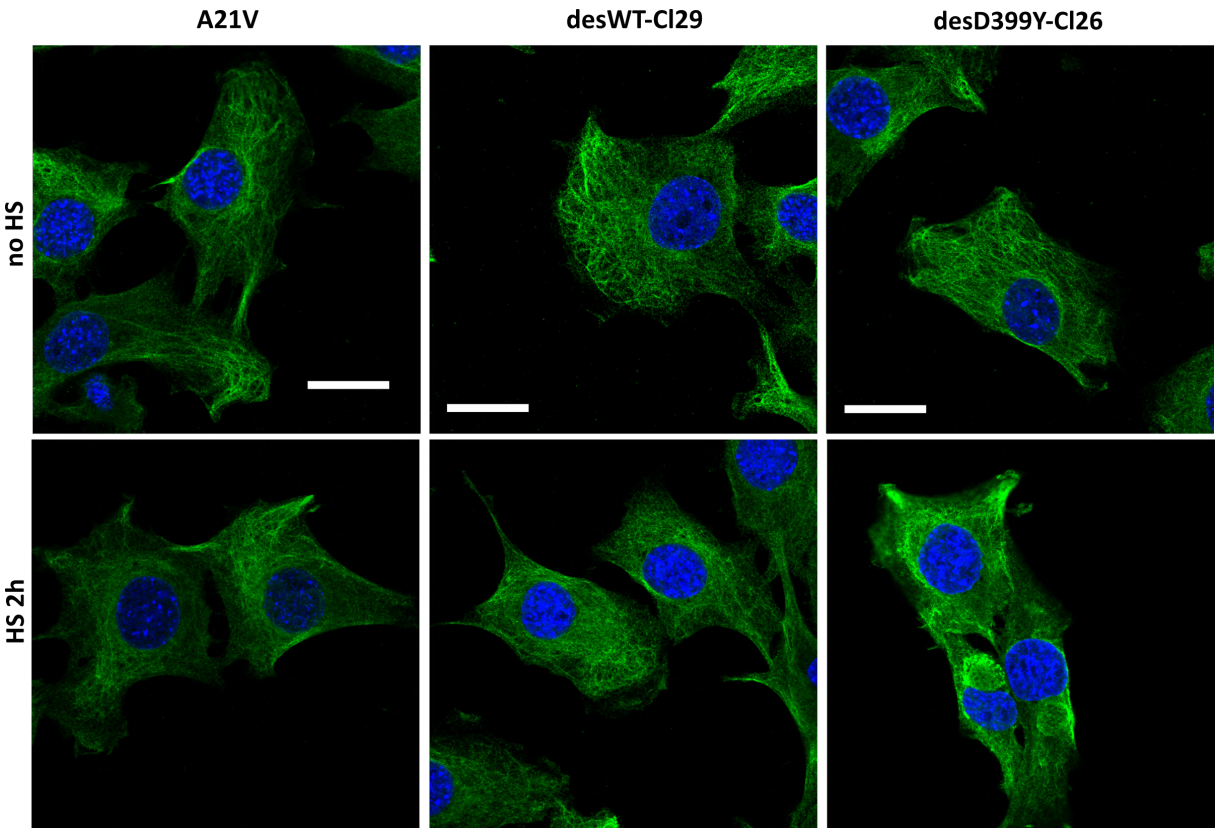


Figure 4 supplement 1: **Desmin organization** Immunofluorescence images of desmin on adherent cells of control A21V, desWT-Cl29 and desD399Y-Cl26 cell lines for no HS or 2 hours HS. Hoechst signal (nuclei) is shown in blue, desmin is shown in green. Scale bar = 20 $\mu$m.

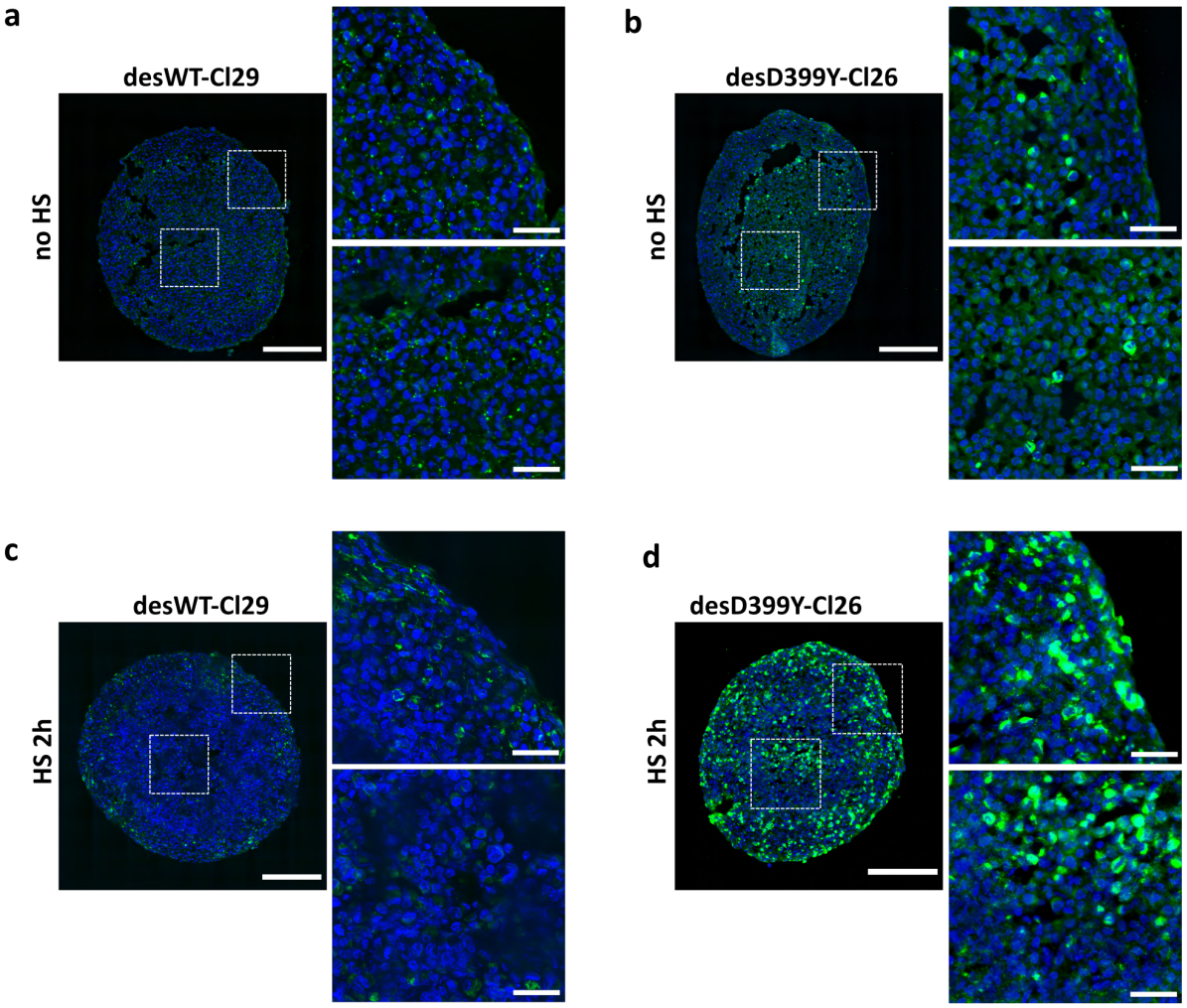


Figure 4 supplement 2: **Immunofluorescence images of C2C12 spheroid cryosections of desWT-Cl29 (a,c) and desD399Y-Cl26 cells (b,d) for no HS (a,b) or 2 hours HS (c,d).** DAPI is shown in blue and Myc is shown in green. Scale bar = 200 $\mu$m and scale bar = 40 $\mu$m for zoomed images.

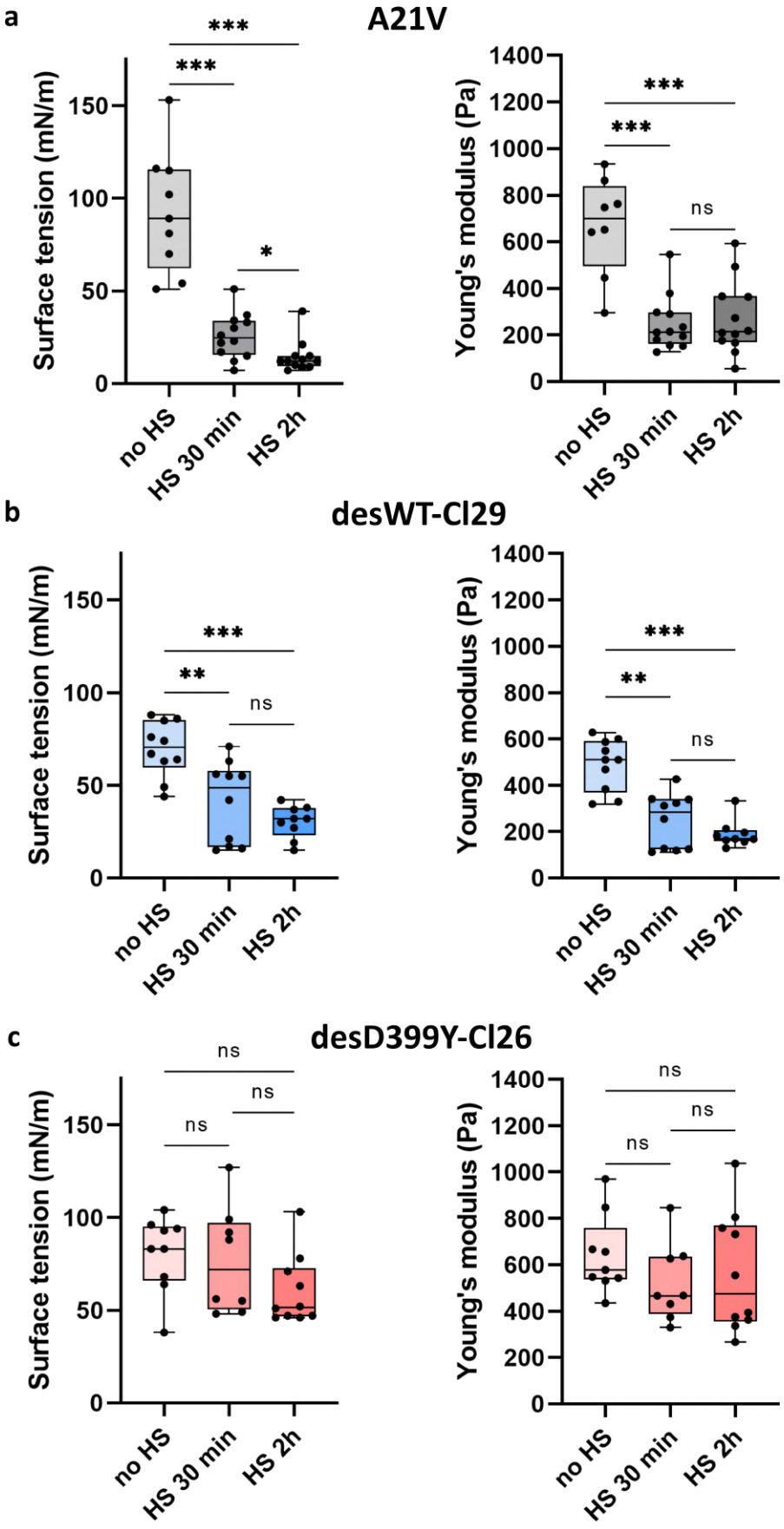


Figure 4 supplement 3: **Surface tension and Young's modulus of A21V spheroids (a), of desWTCl29 spheroids (b) and desD399Y-Cl26 (c) with no HS, HS 30 min or HS 2h.**

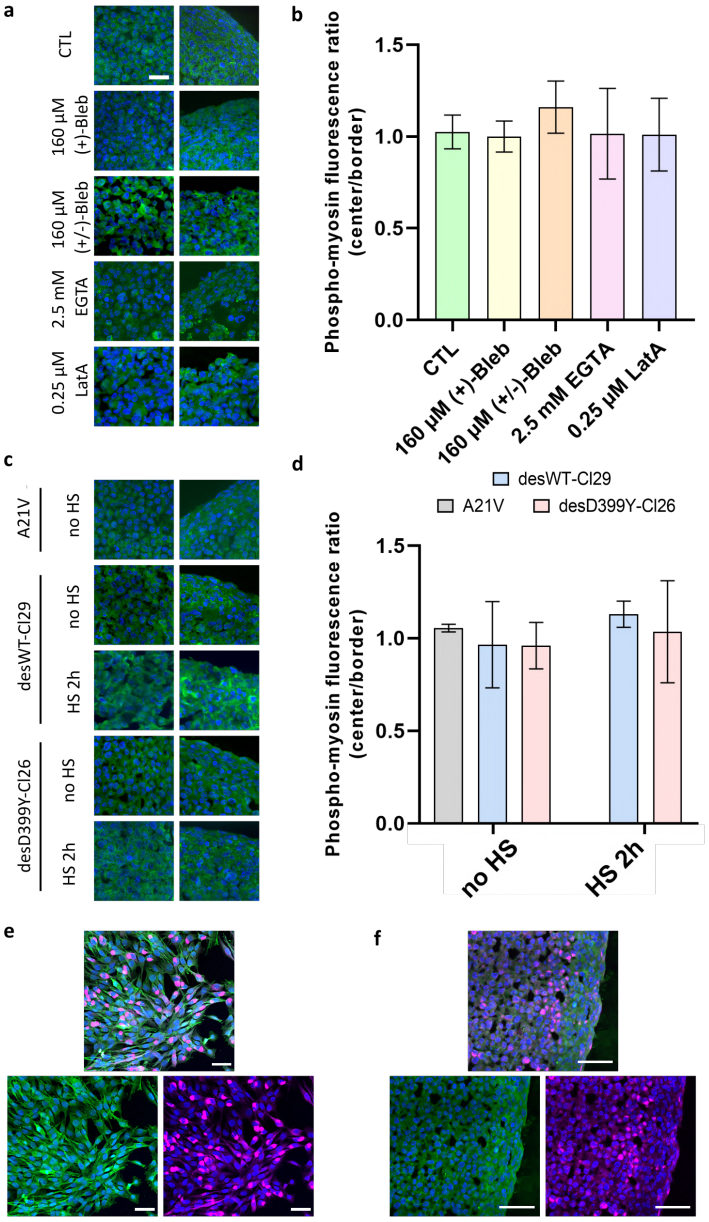


Figure 5 supplement 1: **Quantification of phospho-myosin distribution in the spheroids. a-c)** Immunofluorescence images of C2C12 WT (a) or A21V, desWT-Cl29 and desD399Y-Cl26 (c) spheroid cryosections in the different experimental conditions. Nuclei are shown in blue and phospho-myosin is shown in green. Scale bar = 25 $\mu$m. **b-d)** Quantification of phospho-myosin distribution between the center and the border of the spheroids. Ratio between the phospho-myosin fluorescence normalized by the number of nuclei at the center and at the border of the spheroid for C2C12 WT (b) or A21V, desWT-Cl29 and desD399Y-Cl26 (d). For all experimental conditions, the ratio is around 1 evidencing a uniform distribution of phospho-myosin across the spheroid. **e-f)** Immunofluorescence images of desCl26-D399Y after 2/,h HS in 2D (e) or in 3D (spheroid cryosection) (f). Nuclei, phospho-myosin and exogenous desmin (Myc) are labelled in blue, green and magenta respectively. No increase in phospho-myosin fluorescence intensity is observed in 2D or 3D at the location of the desmin aggregates. Scale bars = 50 $\mu$m.

### 2.2.2 Discussion and perspectives

#### Desmin mutations

In this paper, the influence of a desmin point mutation altering the intermediate filament architecture of cells on the 3D mechanics of a simple undifferentiated and unorganized muscle tissue was investigated.

This point mutation D399Y (aspartic acid replaced by tyrosine) is present on chromosome 2q35 of patients giving rise to a partial aggregation of the extrasarcomeric desmin causing a structural myofibrillar disorganization [83] [85]. These protein aggregates are the main pathological symptoms of desminopathies and more generally myofibrillar myopathies that are very often characterized by a progressive muscular weakness. Desminopathies were first described in 1998 [86] and more than 60 related mutations in the human desmin gene have been reported ever since [87]. In France, this is the most frequent myofibrillar myopathy and more than 20 families affected have been fully characterized [83].

The impact of these desmin mutations has first been studied at the filament level, showing altered nanomechanical properties [85] that were hypothesized to change the biomechanical characteristics of the corresponding cells and tissues. In the last 10 years, evidence has been gathered showing that the mechanical response of diseased myoblasts at the single cell level can indeed be impaired which could contribute to this muscle pathology.

First, primary human myoblasts derived from patients expressing a mutated desmin R350P were shown to be about two times stiffer than control cells thanks to magnetic tweezers probing the whole cell [88]. In the case of mouse myoblasts expressing the mutant E413K, no influence was measured on the cortex stiffness by optical tweezers. However, the cytoplasm was softer when the intermediate filament network was partially depleted by the formation of desmin aggregates as measured thanks to magnetic tweezers. Similarly, the global stiffness measured at the cellular level with a single cell rheometer was lower for the mutants E413K. Finally, this mutation impaired the traction force generated by the myoblasts as measured with traction force microscopy or with a single cell rheometer [87]. Conversely, for mouse myoblasts expressing the mutated desmin D399Y presented in the previous article, the individual Young's modulus of cells measured by AFM increased slightly but not significantly in comparison to control cells and the rigidity was higher at the position of desmin aggregates [89]. These cells had been also shown to have an altered orientational dynamics and reduced cell deformation upon stretching [90] coherent with

an increased cell stiffness.

Various effects are therefore obtained on the cell mechanical characteristics for several different point mutations. The mechanical changes seem to be mutant specific (as observed for individual filaments [85]) but in all the studied cases we observe an alteration of the myoblast passive and/or active mechanical response. Moreover their impact were investigated on 2D while 3D tissues appear as the best relevant models. At this scale, micro-tissues formed from satellite cells from R349P knock-in mice also presented altered active properties with an increase of contractile forces in comparison to wild-type cells [91].

In the previous article, we focused on the point mutation D399Y. At the level of the mutated single filament, local variations of the tensile properties were measured [85] and as already mentioned, this mutation increases non significantly cell rigidity (result on individual cells on 2D substrate) [89]. At the tissue model level, we revealed that this difference on the rigidity is enhanced, probably originating from collective effects. With this study on simple muscle tissue models, we reinforced the hypothesis that D399Y mutations and more generally desminopathies are at least partly due to impaired single cell mechanical properties that are translated at the tissue scale. Indeed, we evidenced for the first time altered mechanical properties of desmin mutated myoblasts that are propagating at the 3D level but also on a more biophysical point of view, the role of intermediate filaments on the mechanical response of a 3D tissue model.

It would be very interesting to test the influence of other desmin missense mutations on the 3D mechanics of myoblast spheroids such as E314K for example that is having an opposite effect on single cells that appear softer and also less contractile [87] [92].

### The role of the extracellular matrix

In the previous study, we looked at the role of individual microscopic properties such as the actomyosin network, both in terms of contractility and organization, the intercellular adhesions and the intermediate filaments on the 3D mechanics of myoblast spheroids. However, the influence of the extracellular environment or matrix has not been investigated yet.

In order to explore the role of the extracellular matrix (ECM) with a simple model, we adapted the protocol of spheroid formation to include ECM proteins and formed C2C12 spheroids by adding Matrigel during the spheroid formation. Matrigel matrix is a solubilized membrane matrix secreted by mouse Engelbreth-Holm-Swarm sarcoma cells, whose main components are laminin ($\sim$ 60%) and collagen IV ($\sim$ 30%). Matrigel

is therefore mainly composed of laminin that is the main component of basal lamina in the native muscle [93]. Cells were resuspended in a solution of ice-cold 2 mg/mL Matrigel (356234, Corning) instead of complete medium before seeding them in the agarose molds. After an overnight incubation at 37°C, 5% $CO_2$, spheroids were retrieved from the molds and their mechanical properties were measured.

First, we checked that the resulting spheroids formed with Matrigel contained indeed ECM proteins. Laminin being the main component of Matrigel, we performed immunofluorescence images of spheroid cryosections to check its presence in the Matrigel spheroids (Figure 2.7 a). By quantifying approximately laminin quantity in Matrigel spheroids by Dot Blot, we obtained about 60 times more laminin in comparison to control spheroids (Figure 2.7 b) which confirms the presence of Matrigel extracellular proteins in the 3D spheroids. Interestingly, there is a basal expression of laminin in C2C12 spheroids in which cells seem to express laminin extracellular proteins in 3D in less than 24 hours. This expression of laminin corresponds to approximately 0.01 µg for 1000 cells. This value should be confirmed by reproducing and improving this Dot Blot experiment with a more adapted calibration curve and by obtaining homogeneous blots of same sizes.

To measure the mechanical properties of these Matrigel spheroids, a first round of experiments was carried out with spheroids formed with 1.6 mm diameter molds (average radius of 550 µm), and a non significant increase of surface tension was noticed (data not shown). The spheroids presenting very high surface tension and Young's modulus, the observed deformations were really small reducing the measurement precision. Therefore, we formed spheroids of higher radii (R = 720 ± 100 µm) with 2.4 mm diameter agarose molds in order to obtain higher deformations and to push the detection limits of the set-up. A significant increase of surface tension was measured between the control spheroids ($\gamma = 157 \pm 42$ mN/m) and the Matrigel spheroids ($\gamma = 216 \pm 43$ mN/m), while there was no difference on the Young's modulus between control ($E = 1300 \pm 300$ Pa) and Matrigel spheroids ($E = 1100 \pm 400$ Pa) except a non significant decrease. In contrast with what was measured for drug conditions or with mutated desmin cells in the results presented in the previous paper section 2.2.1, the surface tension and the Young's modulus do not change proportionally : here surface tension increases while the Young's modulus stay constant or even decreases. If we define the characteristic elastocapillary length of the multicelullar aggregate by $l = \frac{\gamma}{E}$, it means that the addition of extracellular matrix increases this characteristic length.

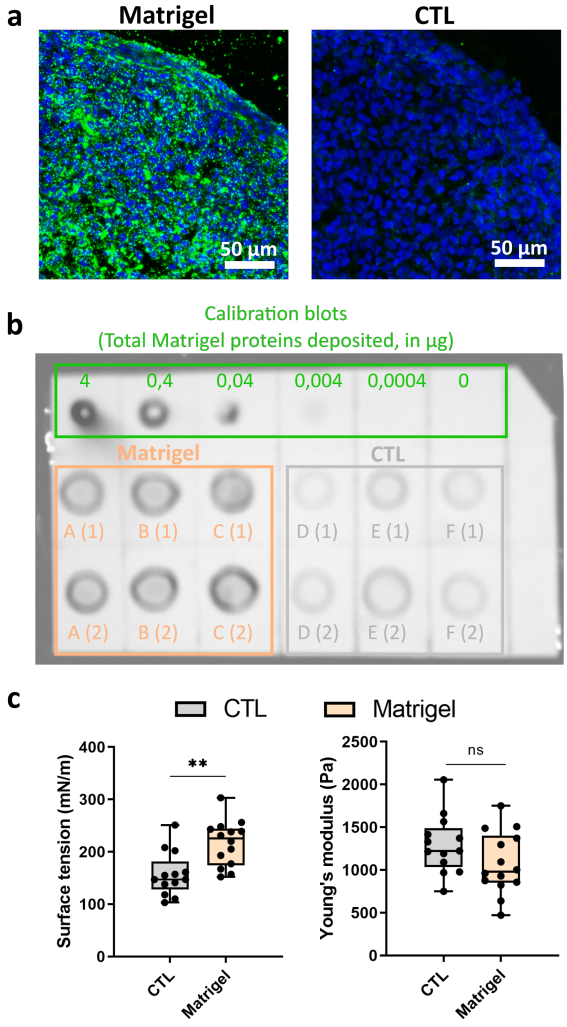


**Figure 2.7 The addition of Matrigel during C2C12 spheroid formation increases its surface tension.** **a)** Immunofluorescence images of spheroid cryosections for Matrigel or control (CTL) spheroids. Nuclei are labelled in blue with DAPI while laminin is labelled in green (with a rabbit anti-laminin primary antibody, L9393, Sigma). Laminin is clearly present and homogeneous in the Matrigel spheroids while it is not visible in control spheroids. **b)** Dot Blot of protein extracts of Matrigel (A, B and C) vs control (D, E and F) spheroids. Calibration blots are emphasized in green and 2 µL was deposited for each blot. For sample blots, 4 µL of proteins extracts were deposited corresponding to about 2 µg proteins. **c)** Surface tension (left) and Young's modulus (right) measured with the magnetic tensiometer for control and Matrigel spheroids. At least N= 13 spheroids and 3 independant experiments.

These preliminary results show that we are able to form spheroids containing ECM proteins and give first insights on their effect on 3D tissue mechanics. As already mentioned, laminin, the main component of Matrigel, is the main element of basal lamina in the native muscle [93]. This is why it is so commonly used in muscle micro-tissues [94]. However, as it is produced from sarcoma cells, it contains a variety of other proteins and growth factors that are not of high relevance for myoblasts. It could be more interesting

to use Matrigel or other extracellular proteins such as collagen I in the context of tumor cells. Indeed, collagen I is the main component of the extracellular matrix and its expression is frequently increased during tumorigenesis [95].

To test the influence of collagen I on the 3D mechanics of multicellular aggregates, we used the previous protocol to form spheroids of mouse colon carcinoma cells (CT26) including ECM proteins. During magnetic molding, instead of resuspending the cells in Matrigel before the seeding in the agarose molds, CT26 cells were resuspended in 0.1 mg/mL collagen I (354236, Corning). After an overnight incubation at 37°C, 5% $CO_2$, the surface tension and the Young's modulus of the spheroids were measured with the magnetic force tensiometer (Figure 2.8). A significant increase between control and collagen I spheroids was measured on the surface tension while no significant difference was observed on the Young's modulus. Here again, it seems that we loose the proportionality observed in the article section 2.2.1 between surface tension and the Young's modulus when we add ECM proteins, pointing to a distinct effect of the extracellular matrix.

In conclusion, by adapting the protocol of spheroid formation, we were able to form spheroids containing ECM proteins and to measure their macroscopic mechanical properties. These multicellular aggregates containing matrix proteins are a simplified model to study the role of the ECM on the 3D mechanics of tissues. Some other models could be imagined such as multicellular aggregates of cells secreting ECM, fibroblasts for example, and their mechanical properties could be monitored over time and as a function of the amount of ECM proteins secreted.

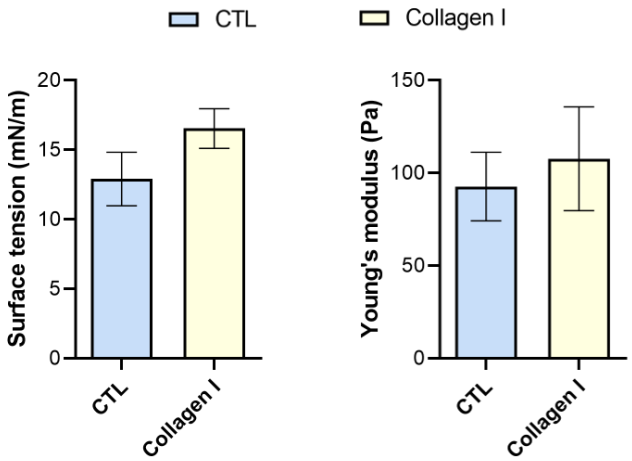


**Figure 2.8 The addition of collagen I during CT26 spheroid formation increases their surface tension.** Surface tension (left) and Young's modulus (right) measured with the magnetic tensiometer for control and collagen I spheroids. N = 3 spheroids for each condition.

### Conclusion and outlook

In conclusion, by combining the magnetic molding and the magnetic tensiometer, we have a great tool to decipher the interplay between cell scale and global mechanical properties of tissues. Here, we focused on the influence of the cell cytoskeleton or the extracellular matrix but many other aspects can be investigated such as the invasive or metastatic properties of tumor cells. In next section 2.3, we explored the link between individual tumor cell properties and the global mechanics of the resulting spheroids as tumor models, in the context of epithelial-mesenchymal transtion in human breast cancer.

# 2.3 Mechanical properties of human breast cancer cell tissue models and their relation with tumor related properties of individual cells

## 2.3.1 Introduction

### Breast cancer progression

Breast cancer is the most common malignancy for women worldwide. It is due to an abnormal proliferation of epithelial cells in the terminal ducts of the mammary gland, either in the lobules or in the ducts (Figure 2.9). One can distinguish tumors expressing oestrogen and progesteron receptors (ER and PR) and tumors that do not express ER, PR or human epidermal growth factor receptor 2 referenced as triple negative cancer that show poorer prognosis for the patients [96].

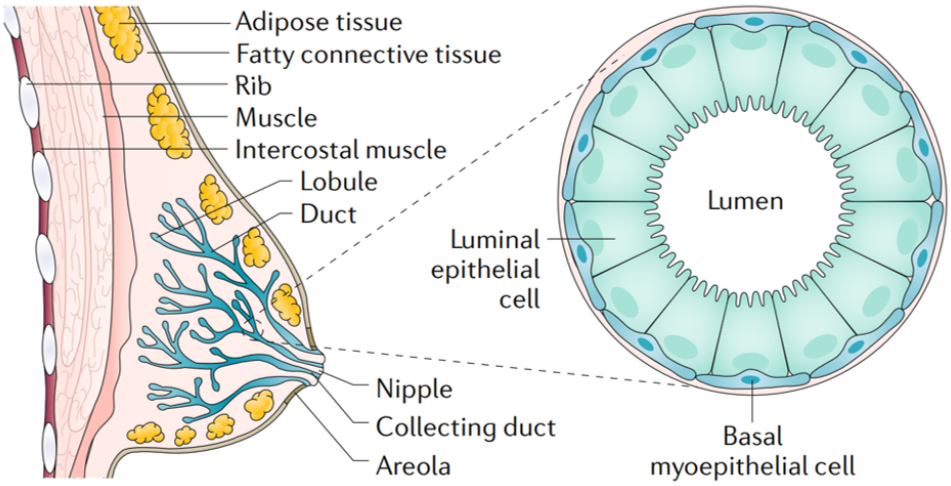


**Figure 2.9 The mammary gland.** Figure from Harbeck et al. [96].

After breast cancer initiation with abnormal proliferation of epithelial cells, further transformation by genetic changes or epigenetic alterations can lead to the formation of an *in situ* carcinoma. At this stage the basal membrane is still intact and the tumor is localized in the lobule or the duct. Upon additional transformation and epithelial-mesenchymal transition (EMT), the carcinoma can become invasive by breaking and fragmenting the basal lamina (rich in collagen IV and laminin) and invading the stroma (rich in fibrillar collagen I). Cells can then intravasate into blood or lymph vessels and are transported passively to distant organs where they can extravasate and form a new carcinoma at a secondary site by a mesenchymal-epithelial transition (MET) [97] (Figure

2.10).

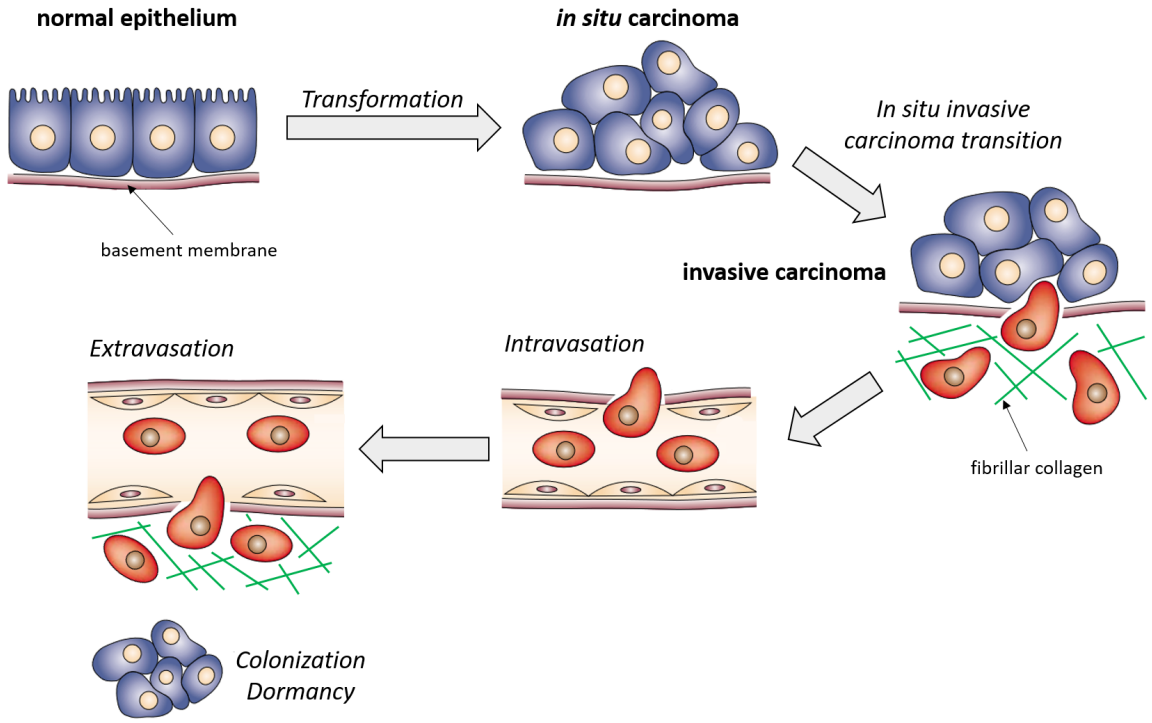


**Figure 2.10 Breast cancer progression, from abnormal proliferation of epithelial cells to metastasis formation.** Adapted from Thiery et al. [97].

In this chapter, we will focus on the transition between *in situ* carcinoma and invasive carcinoma for ductal carcinoma (Figure 2.10). This corresponds to the invasion step that is an early step of the metastatic cascade and involves the degradation of the matrix.

## A cellular model to investigate the invasive switch

To investigate this invasion step of the breast ductal carcinoma progression, Mathieu Boissan and his team at the Saint-Antoine hospital have developed a unique model to reproduce the transition from ductal carcinoma *in situ* (DCIS) to invasive carcinoma, by generating an EMT hybrid intermediate through NME1 ablation.

### The NME gene family

NDPK (nucleoside diphosphate kinase) are enzymes encoded by the NME/NM23 genes. This gene family is composed of 10 genes among which 4 are ubiquitous: NME1, NME2, NME3 and NME4. They are localized in the cytoplasm, the membrane and the nuclei except for NME4 that is localized in the mitochondria. These nucleoside diphosphate kinase phosphorylate the nucleoside diphosphate (NDP) into triphosphate (NTP),

synthesizing in particular GTP [98].

NME1 was described as the first metastasis suppressor gene in 1988 [99]. In their study, Steeg et al. used different murine melanoma cell lines with varying metastatic potentials and showed that NME1 expression is reduced in highly metastatic cell lines. Besides, inverse association has been shown between NME1 expression and the metastatic potential of several human solid tumors (mainly of epithelial origin, and melanoma) [98]. NME1 is not a tumor suppressor gene, it does not prevent the tumor formation however it inhibits the invasion through the basement membrane. NME2 has a much less metastasis suppressor effect.

**NME1 and NME2 KO in the MCF10DCIS.com cell line**

Mathieu Boissan and his team constructed genome edited MCF10DCIS.com cell lines by CRIPSR-Cas9 to generate knock-outs of NME1 and NME2 (Figure 2.11). The human MCF10DCIS.com cell line is derived from a xenograft originating from MCF10AT cells that were injected into immunodeficient mice. The MC10AT is itself a premalignant variant of the normal-like immortalized breast epithelial cell line MCF10A [100]. MCF10DCIS.com is a triple negative and epithelial-like (E-cadherin positive) cell line with low invasive properties.

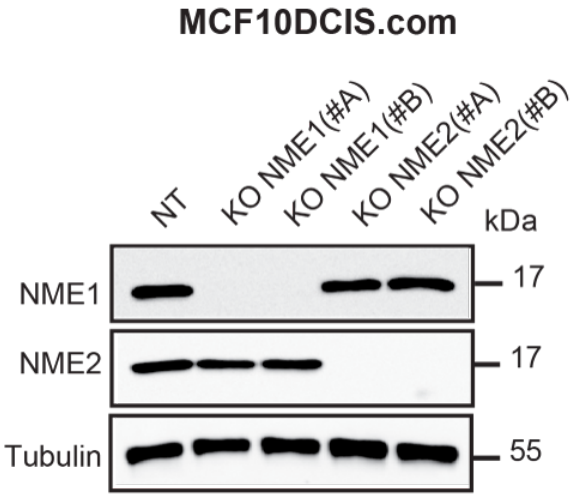


**Figure 2.11 The MCF10DCIS.com KO NME1 and KO NME2 cell lines.** Western blot of NT, KO NME1 and KO NME2 cells. NT cells correspond to the cells treated with a non targetting-vector during genome editing, they are the control condition. NME1 and NME2 were knocked-out with two different guide RNAs each (clone A and B). We observe that NME1 and NME2 were efficiently inactivated for each clone and that no cross-influence is observed upon inactivation. Western Blot obtained by Mathieu Boissan.

The MCF10DCIS.com is a great model to reproduce the *in situ* transition and invasion

observed in humans thanks to an intraductal xenograft model. Indeed, a few weeks after injecting the cells in the mammary duct of immunodeficient mice, a carcinoma in situ forms and evolves spontaneously into an invasive carcinoma after 10 to 12 weeks [101].

By knocking out NME1, Mathieu Boissan and his team were able to induce an hybrid intermediate EMT state. Indeed, 4 weeks post-intraductal injection, all tumors developed from MCF10DCIS.com NT cells (control non inactivated cell line treated with a non-targetting vector) formed carcinoma *in situ*. While for NME1 knock-out cells, 20 to 40 % of the tumors were invasive and had already crossed the basement membrane. Knocking-out NME1 therefore accelerates the transition from carcinoma *in situ* to invasive carcinoma [98]. MCF10DCIS.com KO NME1 are therefore an hybrid intermediate state of EMT, where epithelial markers such as E-cadherins are decreased and mesenchymal markers such as N-cadherins are increased (Figure 2.12). The transition is however not full since some epithelial markers remain such as beta-catenin or cytokeratin 18. In the case of NME2, only a few percent of tumors were invasive confirming that NME2 does not act as a metastatis supressor gene.

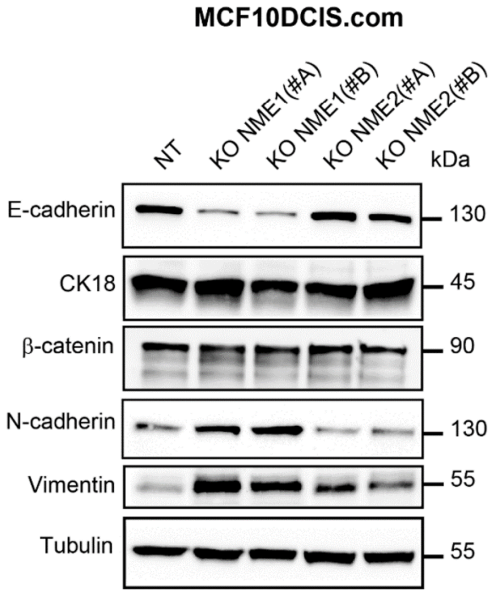


**Figure 2.12 Protein levels of epithelial and mesenchymal markers in MCF10DCIS.com NT, KO NME1 and KO NME2 cells.** Western blot of MCF10DCIS.com NT, KO NME1 and KO NME2 cells cultured in 2D. Decreased levels of E-cadherin proteins and unchanged levels of cytokeratin 18 (CK18) and $\beta$-catenin (epithelial markers) are observed for NME1-depleted cells. Whereas for the mesenchymal markers N-cadherin and vimentin, protein levels are increased upon NME1 inactivation. No changes are observed for KO NME2 cells in comparison to NT control cells. Tubulin is used as a loading control. Adapted from Huna et al. [102].

Ablation of NME1 was shown to accelerate the *in vivo* transition from *in situ* to invasive breast tumors by increasing the levels of MT1-MMP (membrane-anchored matrix metalloproteinase membrane-type 1) [98]. MT1-MMP plays a key role for the invasion of the basement membrane. Its expression levels increase during human breast cancer progression at the transition between *in situ* to invasive carcinoma. Moreover, MT1-MMP is required for the basement membrane invasion since MCF10DCIS.com MT1-MMP ablated cells formed mostly *in situ* tumors 10 weeks post injection while NT cells formed 100 % of invasive carcinoma at this stage [101]. The mechanism brought to light by Lodillinsky et al. [98] explaining this accelerated transition involves the control of MT1-MMP surface levels through endocytosis by NME1. NME1 will fuel locally dynamin with GTP for endocytosis [103] that will lead to the endocytosis of the surface MT1-MMP, reducing the MT1-MMP membrane expression levels. By inactivating NME1, the MT1-MMP surface levels are therefore increased, accelerating the switch from *in situ* to invasive carcinoma through basement membrane matrix remodeling and degradation. Eventhough NME1 and NME2 have the same kinase activity, NME2 does not seem to act as a metastasis suppressor gene but the detailed mechanism still remains to be elucidated.

### Probing mechanical properties across EMT

Mathieu Boissan and his team therefore developed a great model to generate an hybrid state of EMT by knocking out the NME1 gene. If the depletion of NME1 was studied on a biological point of view and was shown to favor invasion of tumors by increasing the MT1-MMP surface levels, the mechanical properties across this EMT have not been explored.

To address this question, we probed the mechanical properties of these different human breast cancer cell lines across EMT at the tissue level. Spheroids were formed thanks to the magnetic molding technique and their surface tension was then measured with the magnetic force tensiometer. The cell lines used are summed up Figure 2.13. The MCF10A corresponds to the normal-like epithelial cells, while the MCF10DCIS.com NT originates from a malignant transformation. MCF10DCIS.com KO NME2 cells behave in a similar manner as NT cells forming *in situ* carcinoma. Finally, by depleting NME1, an accelerated EMT is observed in MCF10DCIS.com KO NME1 cells favoring the switch from *in situ* to invasive carcinoma. While mechanical studies on human breast cancer cells are generally carried out on cell lines with different origins [104], here all cell lines have the same genetic background increasing the relevance of the study.

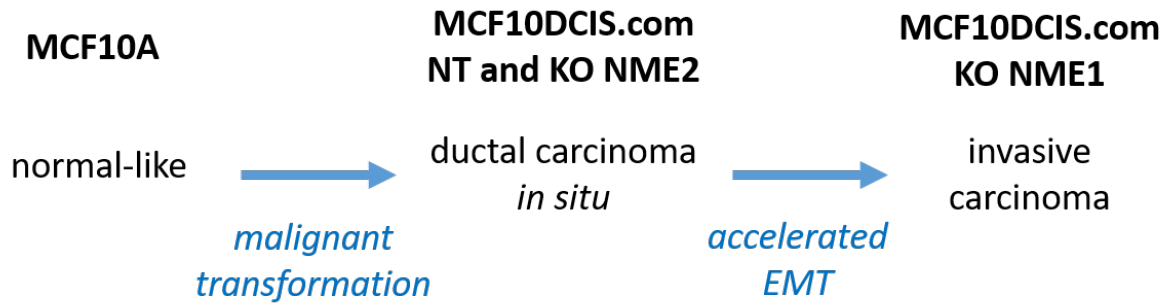


**Figure 2.13 Summary of the cellular models used to probe the mechanical properties of human breast epithelial cells across EMT**

In the following paper, we probed the tumour-related properties of cells at the individual scale and their mechanical properties in tumor models across this broad spectrum EMT.

### 2.3.2 Surface tension of model tissues during malignant transformation and epithelial–mesenchymal transition

**Summary**

The epithelial-mesenchymal transition is associated with an enhanced invasion and migration and an increased metastatic potential of cells. The influence on the global mechanics at the tissue scale of such transition is still unexplored, as is the relationship between adhesion, migration or invasion properties of cells with the 3D mechanics of tumors. In this paper, we focus on the influence of the NME1 metastasis suppressor in human breast cancer cells (MCF10DCIS.com) on the mechanics of tumor models and the correlation with individual cell properties. The inactivation of NME1 by CRISPR-Cas9 leads to the formation of an hybrid and more advanced state of EMT in comparison to control cells (NT), increasing the expression of mesenchymal markers such as N-cadherins and decreasing the expression of epithelial markers such as E-cadherins.

The tumor-related properties of the KO NME1 cell lines were first explored. Cell-cell adhesion force, characterized by AFM measurements, was 30% smaller than for NT control cells. Directional migration and invasion of basement membrane, respectively measured by wound healing assays and Boyden chamber assays, were significantly higher in comparison to NT control cells. To quantify the global mechanics of NME1 inactivated cells, we formed spheroids by magnetic molding and then measured their apparent surface tension thanks to the magnetic tensiometer, evidencing a 2- to 3-fold decrease in comparison to NT control cell spheroids. Interestingly, the inactivation of the close NME1 isoform, NME2, did not lead to any change in invasion, migration, adhesion or surface tension properties. Finally, spheroids of normal-like epithelial cells have a surface tension two times higher than the corresponding breast cancer cells obtained through malignant transformation.

To conclude, we evidenced here the correlation between the invading and metastatic properties of individual cells and a macroscopic mechanical property of the resulting 3D tumor models. We showed that surface tension of spheroids not only decreases upon EMT but also upon malignant transformation from normal epithelial cells to tumoral cells. Thus, surface tension could be used as a read-out for tumor aggressiveness, paving the way for studies on the metastatic potential of tumors in 3D.

frontiers | Frontiers in Cell and Developmental Biology

TYPE Original Research
PUBLISHED 30 August 2022
DOI 10.3389/fcell.2022.926322



OPEN ACCESS

EDITED BY
Claudia Tanja Mierke,
Leipzig University, Germany

REVIEWED BY
Mohit Kumar Jolly,
Indian Institute of Science (IISc), India
Ian Y Wong,
Brown University, United States
Laura Kaufman,
Columbia University, United States

*CORRESPONDENCE
Mathieu Boissan,
mathieu.boissan@inserm.fr
Myriam Reffay,
myriam.reffay@u-paris.fr

†These authors have contributed equally to this work

SPECIALTY SECTION
This article was submitted to Cell Adhesion and Migration, a section of the journal Frontiers in Cell and Developmental Biology

RECEIVED 22 April 2022
ACCEPTED 07 July 2022
PUBLISHED 30 August 2022

CITATION
Nagle I, Richert A, Quinteros M, Janel S, Buysschaert E, Luciani N, Debost H, Thevenet V, Wilhelm C, Prunier C, Lafont F, Padilla-Benavides T, Boissan M and Reffay M (2022), Surface tension of model tissues during malignant transformation and epithelial–mesenchymal transition. *Front. Cell Dev. Biol.* 10:926322. doi: 10.3389/fcell.2022.926322



# Surface tension of model tissues during malignant transformation and epithelial–mesenchymal transition

Irène Nagle[1], Alain Richert[1], Michael Quinteros[2], Sébastien Janel[3], Edgar Buysschaert[1], Nathalie Luciani[1], Henry Debost[4], Véronique Thevenet[1], Claire Wilhelm[5], Céline Prunier[4], Frank Lafont[3], Teresita Padilla-Benavides[2], Mathieu Boissan[4*†] and Myriam Reffay[1*†]

[1]Laboratoire Matière et Systèmes Complexes, UMR 7057, Université Paris Cité and CNRS, Paris, France, [2]Molecular Biology and Biochemistry Department, Wesleyan University, Middletown, CT, United States, [3]Univ. Lille, CNRS, Inserm, CHU Lille, Institut Pasteur Lille, U1019—UMR 9017—CIIL—Center for Infection and Immunity of Lille, Lille, France, [4]Sorbonne Université, Centre de recherche Saint-Antoine, CRSA, Paris, France, [5]Physico-Chimie Curie, Institut Curie, CNRS UMR 168, Paris, France

Epithelial–mesenchymal transition is associated with migration, invasion, and metastasis. The translation at the tissue scale of these changes has not yet been enlightened while being essential in the understanding of tumor progression. Thus, biophysical tools dedicated to measurements on model tumor systems are needed to reveal the impact of epithelial–mesenchymal transition at the collective cell scale. Herein, using an original biophysical approach based on magnetic nanoparticle insertion inside cells, we formed and flattened multicellular aggregates to explore the consequences of the loss of the metastasis suppressor NME1 on the mechanical properties at the tissue scale. Multicellular spheroids behave as viscoelastic fluids, and their equilibrium shape is driven by surface tension as measured by their deformation upon magnetic field application. In a model of breast tumor cells genetically modified for NME1, we correlated tumor invasion, migration, and adhesion modifications with shape maintenance properties by measuring surface tension and exploring both invasive and migratory potential as well as adhesion characteristics.

KEYWORDS

**mechanobiology, migration, invasion, adhesion, multicellular aggregates, breast tumor, magnetic nanoparticles**

## Introduction

In his seminal work, *On growth and form* (Thompson, 1992), D'Arcy Thompson first described the notion that the shapes of biological tissues are determined by physical principles. How shapes emerge from cellular interactions and their physical properties has been a central question in biology for decades. The fact that cells in suspension are observed to be round and that experimental data have shown that mixing cell populations drives cell sorting suggests the existence of a tissue surface tension (Steinberg, 1963). In fluids, both the Young–Laplace law and the Young–Dupré equation describe the shape of droplets and their wetting properties by simple force balance introducing surface tension. By analogy, in tissues, surface tension is essential to determining tissue shape (Ehrig et al., 2019; Hashmi et al., 2022). Considering cells in tissues as molecules in fluids, surface tension at the tissue scale is related to the energy difference between cells in the bulk and cells at the surface of the tissue. This fluid analogy about tissue behavior is still valid under force application: when compressed, a multicellular aggregate flattens due to modification of the cell position with cells pushed to the surface (Hayashi and Carthew, 2004). This increases the actual surface area, dissipating the applied force and minimizing the overall energy (Merkel and Manning, 2017; Hannezo and Heisenberg, 2019). To be predictable, these macroscopic physical properties have to be correlated with more microscopic biological insights. Surface tension formally depends both on the adhesion energy between cells and on the interaction area (Amack and Manning, 2012). Cell–cell adhesion was first identified as a key component of tissue surface tension (Foty and Steinberg, 2005) giving rise to the differential adhesion hypothesis (DAH) postulated by Steinberg. Investigations of the DAH explored *in vitro* actually revealed the predominant role of actin contractility in surface tension (Maître et al., 2012) and shed light on the multitude of factors that contribute to surface tension (Brodland, 2002; Krieg et al., 2008; Heer and Martin, 2017; Nagle et al., 2021). The DAH was, therefore, extended to effective adhesion to take into account both cell–cell adhesion and cell mechanical properties implied in the surface contact area (Manning et al., 2010; Gonzalez-Rodriguez et al., 2012). Thus, surface tension has been hypothesized as being highly sensitive to any modification in cytoskeletal organization and intercellular adhesion.

Cells in living organisms experience physical forces, such as compression, tension, hydrostatic pressure, and shear stress (Northcott et al., 2018). They respond to these forces by modifying their shape and by generating forces. In this regard, tumor cells behave abnormally because they have lost cell–cell adhesion and have growth defects (Pham et al., 2010; Zhang et al., 2020) that give rise to abnormal shapes. Moreover, by remodeling the extracellular matrix, tumor cells can invade adjacent tissue (Mierke, 2020). Tumor progression seems to require abnormal adhesion and mechanical properties at the individual cell scale. How these cell properties translate at the collective tridimensional scale is still unknown. Tridimensional multicellular spheroids appear to be the simplest models to mimic a tissue (Hirschhaeuser et al., 2010), especially in the context of tumors. They provide a potential tool to decipher metastatic potential as long as two criteria are met: 1/obtaining a reproducible perfectly controlled model tissue, and 2/identifying easily measurable macroscopic properties that can serve as a hallmark of metastatic potential. Surface tension as an index of shape generation and maintenance is an appealing candidate indicator of change in mechanical properties and, thus, the invasive potential of tumors. To measure surface tension from model tissues, one has to be able to deform them. Most techniques used to mechanically stimulate spheroids involve confining them either by encapsulation (Alessandri et al., 2013), application of osmotic pressure (Montel et al., 2011), or compression between rigid plates. Magnetic compression, by contrast, utilizes magnetic nanoparticles (Mazuel et al., 2015) to exert volume forces on the cells, mimicking the stress experienced by tumors due to extracellular matrix stiffening and abnormal tissue growth (Mary et al., 2022).

Epithelial–mesenchymal transition (EMT) is often associated with metastasis. The transition from an epithelial to a mesenchymal phenotype is not a simple switch; it comprises a large spectrum of phenotypes resulting in decreased cell–cell adhesion and enhanced migration and invasion (Pastushenko and Blanpain, 2019). However, most studies on the biomechanics of tumor cells focus on malignant transformation and do not consider EMT. NME1, first identified as a metastasis suppressor (Steeg et al., 1988; Boissan et al., 2005), is an inhibitor of EMT (Huna et al., 2021). Its loss induces a hybrid state of EMT intermediate between fully epithelial and fully mesenchymal states, that represents an unprecedented way to look at biophysical tool sensitivity (Huna et al., 2021). While there are now around 30 identified metastasis suppressor genes (Khan and Steeg, 2018), NME1 was first discovered and the most extensively characterized at the mechanistic and clinical levels. Its expression in melanomas and in epithelial tumors such as breast, liver, colon, and cervical carcinomas shows an inverse correlation with metastatic potential. This inverse relationship between NME1 expression and metastatic potential is most strongly observed in breast tumors. NME2 is a closely related isoform of NME1. While the two proteins are 88% identical in sequence and share many common properties, the role of NME2 is far from being elucidated.

In this study, we investigate how EMT affects surface tension by inducing the loss of NME1 and one of its close isoforms, NME2, in a purely cellular tridimensional model tissue. We also explore the relationship between surface tension and adhesion in accordance with the differential adhesion hypothesis upon NME1 or NME2 inactivation. Moreover, we explore the role of both NME1 and NME2 in such metastasis-associated biological processes as EMT, migration, and invasion by using

a breast tumor cell line model. We also shed light on the relationship between surface tension and more dynamic parameters such as migration and invasion, which are major hallmarks of EMT upon NME1 or NME2 inactivation. We show that surface tension decreases not only during the transition from a normal to a malignant cellular state but also during tumor progression across EMT. Thus, reduction of surface tension can be used as a readout of malignant transformation and tumor aggressiveness.

# Materials and methods

## CRISPR/Cas9 gene editing

### CRISPR guides

Lentiviral plasmid guides targeting human NME1 and NME2 were generated in the pLenti U6gRNA Cas9-GFP-Puro vector. These vectors and the non-target guide (pLenti CRISPR-NT CONTROL) were purchased from Merck-Sigma-Aldrich. Two different guides were designed for both NME1 and NME2: NME1(#A) (#HS0000009943, target sequence GACGGGCCG AGTCATGCTCGGG), NME1(#B) (#HS0000009940, target sequence GAACACTACGTTGACCTGAAGG), NME2(#A) (#HS0000056847, target sequence TCATCGCCATCAAGC CGGACGG), and NME2(#B) (#NME2-0-76, target sequence AAGACCGACCATTCTTCCCTGG).

### Lentiviral vectors productions and MCF10DCIS.com cells transduction

These steps were performed with the help of the GIGA Viral vectors platform (University of Liège, Belgium). In brief, Lenti-X 293T cells (Clontech) were co-transfected with pcgpV (Cell Biolabs), pRSV-Rev (Cell Biolabs), and VSV-G (Cell Biolabs) encoding vectors together with pLenti U6gRNA NME1-Cas9-GFP-Puro or pLenti U6gRNA NME2-Cas9-GFP-Puro or pLenti CRISPR-NT CONTROL. Lentiviral supernatants were collected 48–96 h post-transfection, filtrated, and concentrated 100x by ultracentrifugation. Lentivirus stocks were titrated with qPCR Lentivirus Titration (Titer) Kit (abm) and used to transduce cells. After 72 h, cells were selected with 2 µg/ml puromycin (Cayla/Invivogen). Then, cells expressing GFP were isolated and cloned by FACS on a FACSaria III 4L sorter (BD Biosciences). Each clone was tested by Western blotting. Clones that were negative for NME1 or NME2 expression were selected for further experiments.

### Sequencing

Selected clones were analyzed by miSeq in order to confirm mutations in NME1 or NME2-coding sequences, as previously described (Huna et al., 2021).

## Cell lines and culture

MCF10A cells were obtained from ATCC (CRL-10317) and cultured in DMEM/F12 medium (Gibco) supplemented with 5% horse serum, 20 ng/ml EGF (Sigma-Aldrich), 0.5 µg/ml hydrocortisone (Sigma-Aldrich), 10 µg/ml insulin (Sigma-Aldrich), 50 µg/ml Bovine Pituitary Extract (Gibco). MCF10DCIS.com cell line was purchased from Asterand. MCF10DCIS.com cells invalidated for NME1 or NME2 were obtained by CRISPR-Cas9 gene editing, as described in the previous section. The MCF10DCIS.com cells and their derivatives were cultured in an advanced DMEM/F12 medium supplemented with 5% horse serum and 2 mM glutamine. All cells were maintained at 37°C in a 5% $CO_2$ atmosphere.

## Proteins extraction and Western blotting

Proteins from cell extracts were electrophoretically separated on 10% sodium dodecyl sulfate (SDS) polyacrylamide gels, transferred onto nitrocellulose membranes, and probed with highly specific NME1 and NME2 rabbit polyclonal antibodies (Boissan et al., 2005). Immunoblots were revealed with peroxidase-coupled secondary antibodies and enhanced chemiluminescence (ECL) Plus substrate (GE Healthcare). α-tubulin antibodies (Thermo Fisher Scientific) were immunoprobed as indexes of the cellular protein level.

After a rinse with PBS, multicellular spheroids were homogenized and solubilized in ice-cold 30 mM Tris-EDTA, pH 7.2, containing 1 mM DTT, 1% (v/v) Triton X-100, 10% (w/v) anti-phosphatase cocktail and 14% (w/v) anti-protease cocktail (Roche), for 30 min on ice, followed by centrifugation at 12000 g for 20 min at 4°C. The proteins in the supernatants were then quantified using a Bradford assay and used for Western blot analysis. Proteins from multicellular spheroids extracts were separated on 7.5% SDS–polyacrylamide gels and electroblotted onto PVDF membranes. After being rinsed in TBS-Tween 20 buffer (TBST), the blots were blocked for 1 h in TBST with 5% (w/v) non-fat dry milk, then probed overnight at 4°C with either E-cadherin (1:1,000, Cell Signaling #14472) or N-cadherin (1:1,000, Sigma-Aldrich, #SAB5700641) specific antibodies. After three washes with TBST, the blots were incubated with horseradish peroxidase-linked anti-rabbit Ig from sheep. Peroxidase activity was revealed with a chemiluminescent detection kit (ECL Plus substrate, GE Healthcare), Beta-actin antibodies (Thermo Fisher Scientific) were immunoprobed as indexes of the cellular protein level and analysis was processed by ImageJ software.

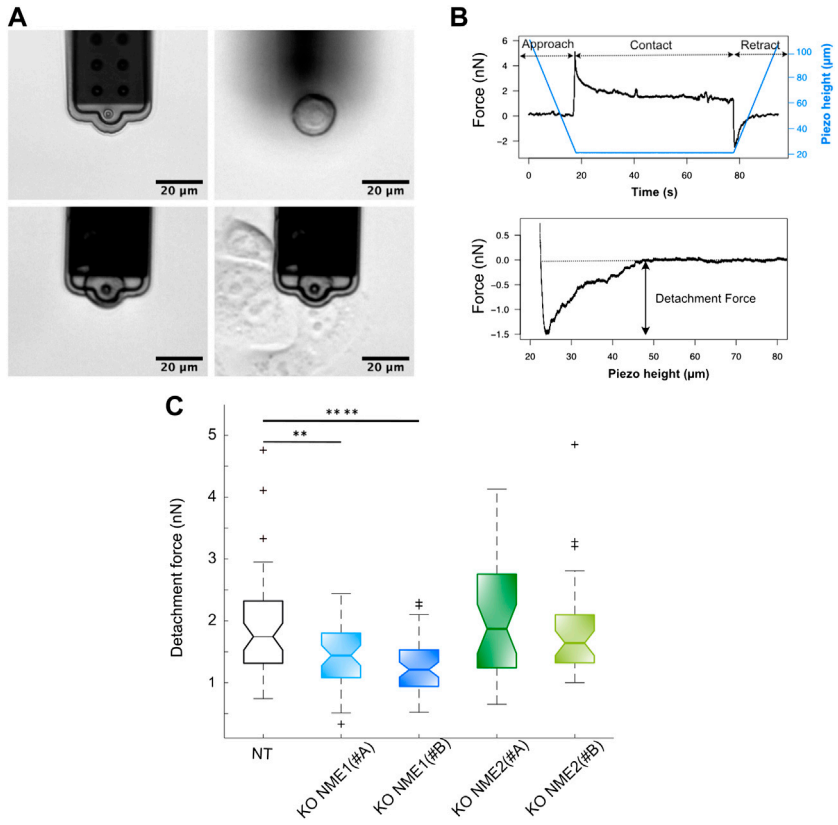


FIGURE 1
Inactivation of NME1 reduces cell–cell adhesion force. **(A)** Top left: FluidFM® micropipette. Top right: suspension cell sedimented on the dish. Bottom left: cell picked up by negative pressure in the micropipette channel. Bottom right: cell vs. cell contact. **(B)** Top: piezo height vs. time (blue) and force vs. time (black) plots of a cell vs. cell interaction. Force increases up to 5 nN for contact, and then height is kept constant for 60 s as cells relax. Finally, cantilever is retracted at a constant speed, and a negative detachment force is observed. Bottom: force vs. piezo height plot example where detachment force is measured. **(C)** Boxplots of detachment forces from MCF10DCIS.com cells in which NME1 or NME2 was inactivated (on average, $n$ = 45 cells were tested per condition). Notch plots show means ± SEM and first to third quartiles of three independent biological replicates measured. ****$p < 0.0001$; **$p < 0.01$ relative to NT control cells.

## Atomic force microscopy

Atomic force microscopy (AFM) experiments were performed on a JPK NanoWizard® III system (Bruker, Berlin, Germany) coupled to a Zeiss Axio Observer. Z1 optical microscope with a ×40 air objective mounted on a PIFOC (Physik Instrumente, Karlsruhe, Germany). The AFM was equipped with an additional Z piezo scanner of 100 µm (JPK CellHesion) and the FluidFM® technology add-on (Cytosurge, Glattbrugg, Switzerland). FluidFM® micropipettes of 4 µm aperture and 0.3 N/m nominal spring constant were used. Micropipettes were first cleaned in plasma oxygen for 2 min at 20W. They were then covered with 0.1 mg/ml PLL (20)-g [3.5]-PEG (2) (SuSoS, Dübendorf, Switzerland) both inside and outside the cantilever for 1 h in order to ease cell release. Micropipettes were then rinsed in ultrapure water and mounted on the dedicated holder. The real spring constant was determined using the off-contact Sader method after 5 min thermalization.

Cells were cultured on several 40 mm Petri dishes (TPP, Trasadingen, Switzerland) in a complete medium. Suspension cells were obtained by incubation in 0.05% trypsin-EDTA for 5 min at 37°C to detach the cells, followed by trypsin inactivation in a complete medium for 30 min at 37°C in a $CO_2$ incubator. Another dish of cells was cultured in an advanced DMEM/F12 medium complemented with 10 mM HEPES buffer (imaging medium) before placement on the AFM stage with 37°C temperature control. A few microliters of suspended cells were added to the dish, and the cells were allowed to settle on the bottom of the dish for 1–2 min before being picked up by the micropipette using a soft contact (1 nN) and pressure of −100 mbar. Once picked up, the pressure was decreased to − 10 mbar and the cell was allowed to rest away from the surface for 5 min. This cell was then brought into contact with a spread cell with an initial 5 nN contact force (Figure 1A). The AFM height was kept constant for 60 s, and then the micropipette was retracted at constant velocity (5 µm/s). This same cell was allowed to rest for a few minutes and then brought into contact with three different cells before being

released by applying a pressure of 500 mbar. An average number of 45 cell–cell detachment curves with at least three different cell cultures per condition were recorded. The detachment force was analyzed using JPK DP software (6.3.50) as the lowest point in the retraction curve after a baseline correction (Figure 1B).

## Wound healing assay

Cells were grown to confluency on 24-well plates and starved for 24 h in a serum-free medium. They were treated for 2 h with 10 µM Cytosine$\beta$-D-Arabinofuranoside (AraC) to inhibit cell proliferation. After starvation, cells were scratch-wounded using a sterile 200 µL pipette tip, and suspended cells were removed by washing with PBS twice. Cell migration into the wound was monitored every 24 h until wound closure using the ×10 objective of an Echo Rebel microscope. The bottom of the plate was marked for reference, and the same field of the monolayers was photographed immediately after performing the wound ($t$ = 0 h) and at different time points after the scratch. A total of 30 scratches were analyzed for each condition from three independent experiments.

## Matrigel invasion assay

Matrigel invasion assay was performed following the Transwell chamber method as described (Olea-Flores et al., 2019). In brief, BioCoat Matrigel invasion chambers with 8.0 µm PET membranes placed in 6-well plates were used to seed cells that were previously treated for 2 h with 10 µM Cytosine $\beta$-D-Arabinofuranoside (AraC) to inhibit cell proliferation. The cells were plated at a density of 1.25 × $10^5$ cells/mL in 2 ml of a serum-free medium on the top chamber, as recommended by the manufacturer. The lower chamber of the Transwell contained 2.5 ml of culture medium supplemented with serum. Cells were incubated for 24 h at 37°C in a 5% $CO_2$ atmosphere. Following incubation, cells and Matrigel on the upper surface of the Transwell membrane were gently removed with cotton swabs. Invading cells on the lower surface of the membrane were washed and fixed with methanol for 5 min and stained with 0.1% crystal violet diluted in PBS. Images from 5 fields of three independent biological replicates were taken and used for cell quantification using FIJI software, version 1.44p (NIH, Bethesda, MD, USA) (Schindelin et al., 2012).

## Magnetic cell labeling

Iron oxide superparamagnetic nanoparticles (8 nm diameter) were obtained by alkaline coprecipitation, followed by oxidation into maghemite according to the Massart procedure (Boitard et al., 2021). The aqueous solution was stabilized electrostatically by adsorbing citrate anions to the surface of the nanoparticles.

MCF10A cells were incubated for 23 min with a solution of iron oxide nanoparticles with [$Fe$] = 1 mM supplemented with 5 mM citrate in RPMI medium (Gibco), while the other cell types were incubated for 45 min in a solution of iron oxide nanoparticles at [$Fe$] = 4 mM and supplemented with 5 mM citrate in RPMI medium. The labeling medium was then discarded and replaced by a complete medium for at least 2 h before cells were trypsinized and detached. Cell proliferation after magnetic labeling was assessed using Alamar Blue (Sigma-Aldrich) assay.

## Magnetic molding

Labeled cells were seeded in semi-spherical 2% agarose molds due to magnet attraction. Agarose molds were obtained from agarose gelification around 1.2 mm steel beads (BI 00151, CIMAP) as previously described (Mazuel et al., 2015). Spheroids were incubated overnight at 37°C, 5 %$CO_2$ in a complete medium and extracted from the wells by gently pipetting the surrounding liquid. The resulting spheroids had a radius of 450 ± 70 µm.

## Magnetic force tensiometer

Magnetic forces were exerted by a 6 × 6 mm cylindrical neodymium permanent magnet (S-06-06-N, Supermagnete). The generated magnetic field is almost constant over the aggregate height at around 530 mT, and the magnetic gradient [grad(B)] was 170 T/m. One multicellular aggregate was deposited at 37°C in a temperature-regulated tank, whose bottom interface is made of a non-adhesive treated glass slide (30 min incubation with anti-adherence rinsing solution from Stemcell Technologies). Images of the aggregate profile were taken using a FLIRFly camera (Teledyne FLIR) equipped with a 1.5× zoom lens and an additive 5 × lens (Thorlabs) through sealed glass slides. The magnet is approached at 150 µm from the bottom of the multicellular spheroid. The equilibrium shape of the multicellular aggregate is reached after 10 min. The surface tension $\gamma$ is deduced from the flattened profile of the aggregate by using the TensioX dedicated MatLab application (Nagle et al., 2021). In brief, it integrates Laplace laws for capillarity and minimizes the quadratic error on the height ($h$), width ($w$) and volume ($V$) of the spheroid (Kalantarian et al., 2015) to extract the capillary constant $c = \frac{M_V \mathrm{grad}(B)}{\gamma}$, where $M_V$ represents the magnetic moment per unit volume. Indeed, the profile can be described by the following equation derived from Laplace laws (Kalantarian et al., 2015): $\frac{d\phi}{ds} = 2b + cz - \frac{\sin(\phi)}{x}$, where $\phi$ is the angle of inclination of the profile, $s$ stands for the arc length along the profile, and $b$ is the curvature at the apex. By assessing $M_V$

with vibrating sample magnetometry (VSM) measurements, the surface tension $\gamma$ can be deduced.

## Indirect immunofluorescence analysis

Cells in 2D monolayers grown on glass coverslips were fixed with 4% paraformaldehyde for 15 min, permeabilized with 0.1% Triton X-100 for 5 min, and then incubated with either anti-E-cadherin rabbit monoclonal antibody (1:200; Cell Signaling Technology Inc.) or anti-Pan-cadherin rabbit polyclonal antibodies (1:100; Sigma-Aldrich). The secondary antibody used was AlexaFluor 488-conjugated goat anti-rabbit IgG (ThermoFisher Scientific). Nuclei were stained with DAPI (ThermoFisher Scientific). Images were obtained by confocal microscopy (Leica equipped with a ×40 water immersion objective).

Multicellular spheroids were fixed with 4% paraformaldehyde for 60 min permeabilized with 1% Triton X-100 for 2 days. They were incubated for 24 h with E-cadherin rabbit polyclonal antibodies (1:200; Cell Signaling Technology Inc.) at 4°C. The secondary antibody used was AlexaFluor 488-conjugated goat anti-rabbit IgG (ThermoFisher Scientific). Nuclei were stained with Hoechst 3342 (Invitrogen). Images were obtained by confocal microscopy (Zeiss LSM780 with a ×20 water immersion objective).

## Alamar blue metabolic assay

The metabolic activity of the cells was quantified using the Alamar Blue assay. For nanoparticles condition, the assay was performed 2 h and 1 day after the magnetic cell labeling while control cells were not labeled. The Alamar Blue reagent (Sigma-Aldrich) was incubated (10% in DMEM) with each cell type for 1 h according to supplier protocol, and the signal was detected using a fluorescence plate reader (Enspire, Perkin Elmer) at 570 nm excitation wavelength and 585 nm emission wavelength in 96-well plates.

## Statistics

Graphs and statistics were processed using MatLab. Notched boxplots were used to represent the median, the first and third quartiles and the confidence interval for comparison. All statistical tests were performed with a two-sided Mann–Whitney U test (Wilcoxon test) using MatLab. $p$-value is used to indicate the statistical significance of the results: *, **, ***, ****, ***** correspond to $p < 0.05$, $p < 0.01$, $p < 0.001$, $p < 0.0001$, and $p < 0.00001$, respectively.

# Results

## Characterization of EMT-associated biological processes driven by inactivation of NME1

Cells undergoing EMT lose epithelial characteristics and integrity, acquire mesenchymal features, and become further motile and invasive (Brabletz et al., 2021). Thus, decreased cell–cell adhesion and enhanced migration and invasion are considered hallmarks of EMT.

To obtain cell lines in which the NME1 or NME2 genes were completely and stably inactivated, we performed CRISPR–Cas9 gene editing in the human breast tumor cell line MCF10DCIS.com using two independent guide RNAs specific to the NME1 gene, NME1 (#A) and NME1 (#B), and two for the NME2 gene, NME2 (#A) and NME2 (#B). To provide a control cell line for experiments with the NME1-and NME2-ablated cells, we subjected MCF10DCIS.com cells to the CRISPR–Cas9 procedure but omitted a guide RNA [No-targeting (NT) cells] (Huna et al., 2021). The ablation of the two proteins, NME1 and NME2, was validated by immunoblot analysis in the different clones (Supplementary Figure S1). NME1-ablated cells, unlike NME2-ablated cells, are the only cell line that lose epithelial features and acquire mesenchymal characters (Huna et al., 2021).

### Specific loss of NME1 reduces cell–cell adhesion force

AFM measurements were performed to explore modifications in cell–cell adhesion force by measuring cell–cell detachment after a short-term adhesion of 60 s. The inactivation of NME1, but not of its closely related isoform NME2, moderately but significantly decreases detachment force. The measured mean adhesion force for NME1-ablated cells is 1.4 ± 0.5 (mean ± std) using the NME1 (#A) guide and 1.2 ± 0.4 nN using the NME1 (#B) guide. The measured mean adhesion force for NME2-ablated cells is 2.0 ± 1 nN using the NME2 (#A) guide and 1.9 ± 0.8 nN using the NME2 (#B). The measured mean adhesion force for NT control cells is 1.8 ± 0.8 nN (Figure 1). Thus, inactivation of NME1 but not of NME2 reduces cell–cell adhesion force.

### Specific inactivation of NME1 increases directional migration

In order to assess the migration of NME1-and NME2-ablated cells, we performed a wound-healing assay, in which a confluent cell monolayer was breached and the degree of migration to close the wound in a given time period was determined. When comparing the wounds immediately after the scratch (0 h) and 24 h later, NME1-ablated cells treated with either guide covered over 75% of the scratched area, whereas the NT control and NME2-ablated cells only covered 55% of the area (Figure 2).

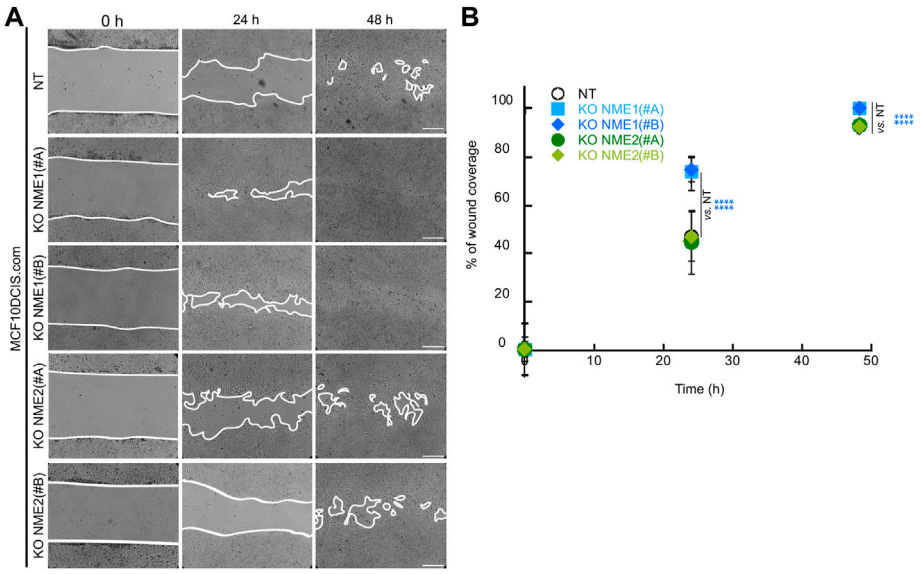


FIGURE 2
Inactivation of NME1 promotes directional migration. **(A)** Representative light microscopy images of the wound healing assay of MCF10DCIS.com cells in which NME1 or NME2 was inactivated. Time 0 represents confluent monolayer wounds at 0 h, and wounds were monitored until NME1-ablated cell monolayers became fully closed 48 h after scratching the monolayer. Images are representative of three independent biological replicates. Scale bar: 100 μm. **(B)** Quantification of the area of migration over time shown in **(A)**. Data show means ± SD of three independent biological replicates imaged. ****$p < 0.0001$ relative to NT control cells.

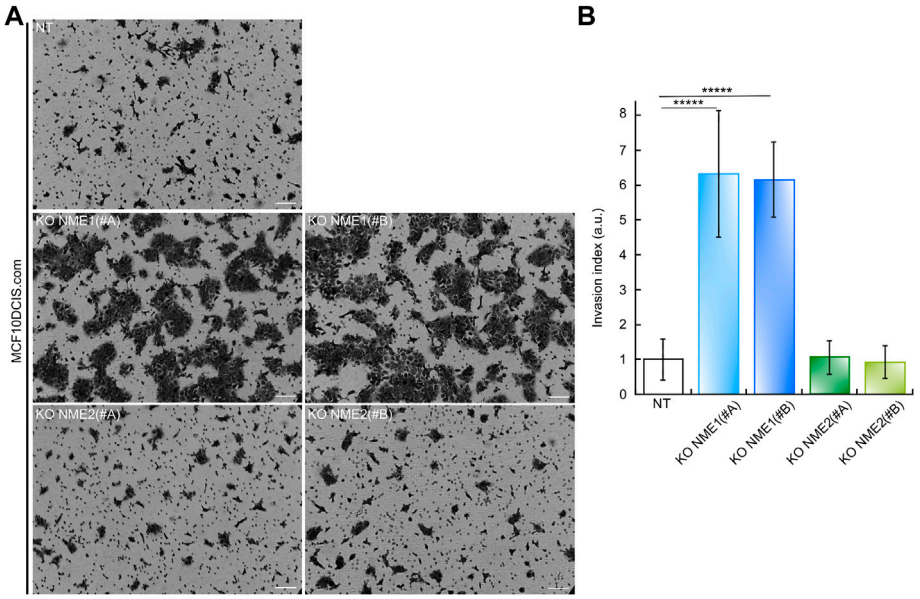


FIGURE 3
Inactivation of NME1 promotes invasion through Matrigel. **(A)** Representative light microscopy images of Matrigel invasion assay of MCF10DCIS.com cells in which NME1 or NME2 was inactivated after 24 h. (Scale bar: 100 μm) **(B)** Quantitative analysis of the invasion assay presented in **(A)**. The data show the means ± SEM of three independent biological replicates imaged and are expressed as an invasion index defined as the ratio of the number of invading NME1-ablated cells or invading NME2-ablated cells on the number of invading NT control cells. By definition, the invasion index of NT control cells is 1. *****$p < 0.00001$ relative to NT control cells.

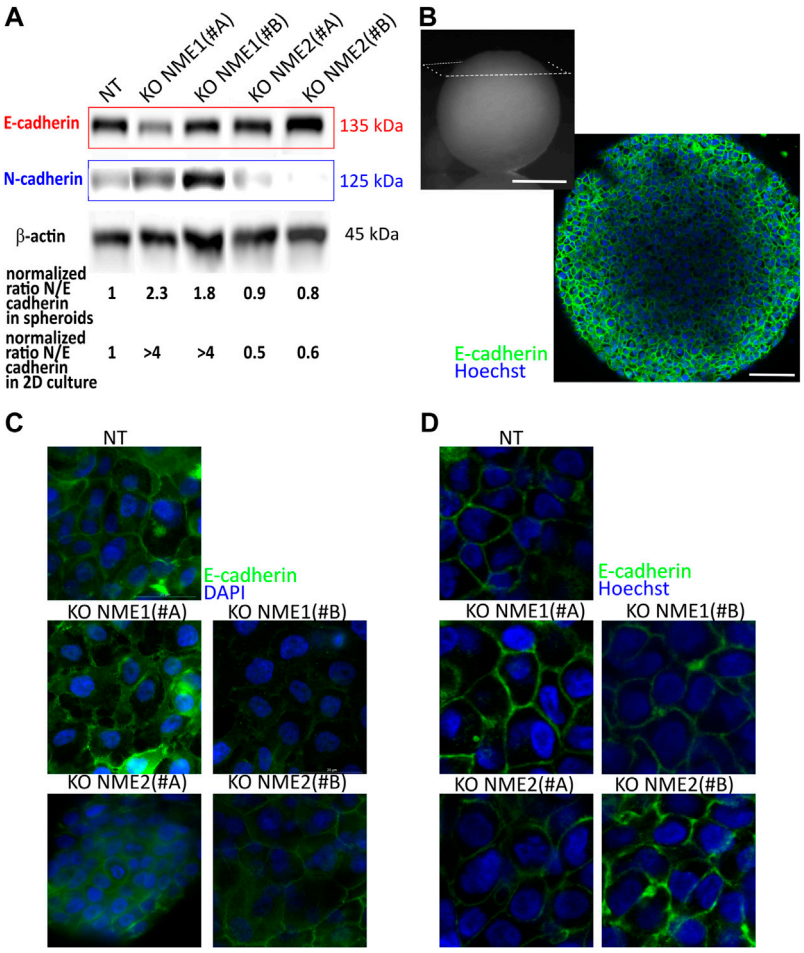


FIGURE 4
E-cadherin and N-cadherin expression are modified in spheroids of NME1-ablated cells. **(A)** Western blot analysis of E-cadherin and N-cadherin expression in NT-control cells compared to cells where NME1 or NME2 were inactivated. β-actin was used as a loading control. The ratio of N- to E-cadherin is calculated and renormalized to the ratio obtained for NT control cells. This ratio is explored in 3D spheroids and in 2D culture (data analyzed from Huna et al. (2021)). **(B)** Top left: image of a spheroid of 1 mm diameter of NT control cells. The observation plane is indicated in white (Scale bar: 500 μm). Bottom right: image obtained at 70 μm depth penetration of E-cadherin localization. Nuclei are stained by Hoechst (Scale bar: 50 μm). **(C)** Immunofluorescence confocal images of 2D culture cells from MCF10DCIS.com cells in which NME1 or NME2 was inactivated. E-cadherin antibody labeling is used. Nuclei are labeled with DAPI. The field of view is a square of 50 μm-long. **(D)** Immunofluorescence confocal images of multicellular spheroids from MCF10DCIS.com cells in which NME1 or NME2 was inactivated taken at a distance from the top of the aggregate between 50 and 80 μm. The field of view is a square of 50 μm-long. E-cadherin antibody labeling is used. Images of nuclei labeled with Hoechst are superimposed.

After 48 h, NME1-ablated cells had fully covered the wound, whereas NT control and NME2-ablated cells still had open wounded areas that accounted for approximately 10% of the original scratched area (Figure 2). Thus, directional migration induced by wound closure is increased when NME1 is inactivated but not when NME2 is inactivated.

## Specific inactivation of NME1 increases invasion into the basement membrane

To investigate the functional consequences of inactivating NME1 and NME2 in MCF10DCIS.com cells, we also studied their invasion of Matrigel, a basement membrane extract. Cells were plated on top of a polycarbonate membrane covered with Matrigel, through which invasive cells could cross and invade the opposite side of the membrane (Figure 3). After 24 h of culture, the number of NME1-ablated cells crossing the Matrigel was, on average, much higher than the number of invading NT control cells. This was true whatever the NME1 (#A) or NME1 (#B) guide (Figure 3). Inactivation of NME1 induces a 6.5-fold increase in the invasion index as defined as the ratio of the number of invading cells to the number of invading NT control cells. By contrast, the number of NME2-ablated cells crossing the Matrigel is similar to the number of invading NT control cells for both cells treated with the NME2 (#A) or the NME2 (#B) guide.

These data indicate that invasion through Matrigel is increased when NME1 is inactivated but not when NME2 is inactivated.

## Multicellular stimulable spheroids: From two-dimensional to three-dimensional environment

Model tissues of defined cell type, shape and size were obtained by magnetic molding techniques to assess their 3D organization. Using superparamagnetic nanoparticles incorporated into cells through the endocytosis pathway, the cells were given magnetic properties that allowed them to behave like induced magnets that can be either driven or stimulated at will using external magnets. Viability and lack of cytotoxicity of the magnetic labeling were confirmed using the Alamar Blue assay by measuring the unchanged metabolic activity of the cells after labeling (Supplementary Figure S2). Moreover, the incorporation of magnetic nanoparticles was shown to have no impact on cell–cell adhesion, migration, or invasion (Supplementary Figure S3). These magnetic forces can concentrate seeded cells in a well of determined size within 1 min. After 20 h of maturation, a cohesive, perfectly reproducible multicellular spheroid about 1 mm diameter is formed due to cell–cell adhesions.

We first looked at the organization of the spheroids to see how the modification of cell–cell adhesion is transduced at the tridimensional level. In adherent cells, epithelial integrity is disrupted upon inactivation of NME1 (Figure 4C). By contrast, in tridimensional multicellular spheroids, NME1 and NME2 inactivation do not impact E-cadherin localization (Figures 4B,D). Looking at protein expression, E-cadherin levels are slightly decreased by NME1 inactivation, while N-cadherin expression is increased. These results correspond to the ones observed in 2D culture (Huna et al., 2021), though the impact of NME1 inactivation is reduced in the multicellular spheroid model compared to that in 2D culture (Figure 4A). E-cadherin expression is reduced by approximately 20% compared to the NT-controls, while it was reduced by 40% in 2D culture (Figure 4A). Looking at the N/E cadherin ratio, which is one hallmark of EMT, multicellular spheroids reproduce the tendency observed in 2D cultures meaning that the NME1 inactivation induced an increase of this ratio compared to NT-controls but while the increase is in the 2-fold range in 3D multicellular aggregates, it was noticed in the 4-fold range for 2D culture. As expected, the overall level of total cadherin is also decreased by NME1 inactivation (Supplementary Figure S4). Thus, a tridimensional environment modifies the cadherin expression compared to two-dimensional models.

## Surface tension variations across EMT

### Specific inactivation of NME1 strongly decreases surface tension

The surface tension of model tissues can be determined by flattening magnetic spheroids *via* a permanent magnet approach (Figure 5A). For a given initial size, the flatter the spheroid looks at equilibrium, the smaller its surface tension is (Mazuel et al., 2015). Surface tension is deduced from the fit of the aggregate profile (David et al., 2009; Kalantarian et al., 2015) (Figure 5B).

Starting from the same spheroid radius, aggregates of NME1-ablated cells, whether treated with the NME1 (#A) or NME1 (#B) guide, look flatter than both the aggregates of NT control and NME2-ablated cells, whether treated with the NME2 (#A) or NME2 (#B) guide (Figure 5B). The surface tension values of spheroids of NME1-ablated cells are 4 ± 3 mN/m (mean ± sd) for cells treated with the NME1 (#A) guide and 7 ± 2 mN/m for those treated with the NME1 (#B) guide. The NT control cell aggregate surface tension value is 16 ± 9 mN/m. By contrast, aggregates of NME2-ablated cells have a surface tension value of 16 ± 5 mN/m and 13 ± 5 mN/m for cells treated with the NME2 (#A) guide and the NME2 (#B) guide, respectively, which is close to the value obtained for the NT control cell aggregates (Figure 5C).

Surface tension is thus strongly modified upon NME1 inactivation, while the inactivation of NME2 does not significantly impact it.

## Surface tension decreases during malignant transformation

MCF10A cells are considered a common normal-like breast cell model. These cells are derived from the benign proliferative breast tissue and are not tumorigenic (Soule et al., 1990). From them, genetic alterations have been created to study breast tumor progression. Here we studied one of its derivatives, the *in situ* carcinoma cells, MCF10DCIS.com, in which NME1 or NME2 were ablated. To find the potential of surface tension measurements in malignant transformation, we compared migration, invasion, and surface tension of normal-like MCF10A cells to carcinoma MCF10DCIS.com cells. Directional migration is enhanced in MCF10A cells compared to MCF10DCIS.com cells (Figure 6B). The migration mode in the 2 cell types differs as MCF10A cells are epithelial and migrate collectively, while MCF10DCIS.com cells migrate randomly with a more individual mode (Figure 6A). The invasion of the basement membrane is not modified by the malignancy state of the cells and is the same as the one measured for the NT MCF10DCIS.com control cells (Figures 6C,D). In sharp contrast, the surface tension of the multicellular aggregates from MCF10A cells is significantly higher than that of the multicellular aggregates from MCF10DCIS.com, 45 ± 18 mN/m vs. 21 ± 9 mN/m, respectively (Figures 6E,F). At the same time,

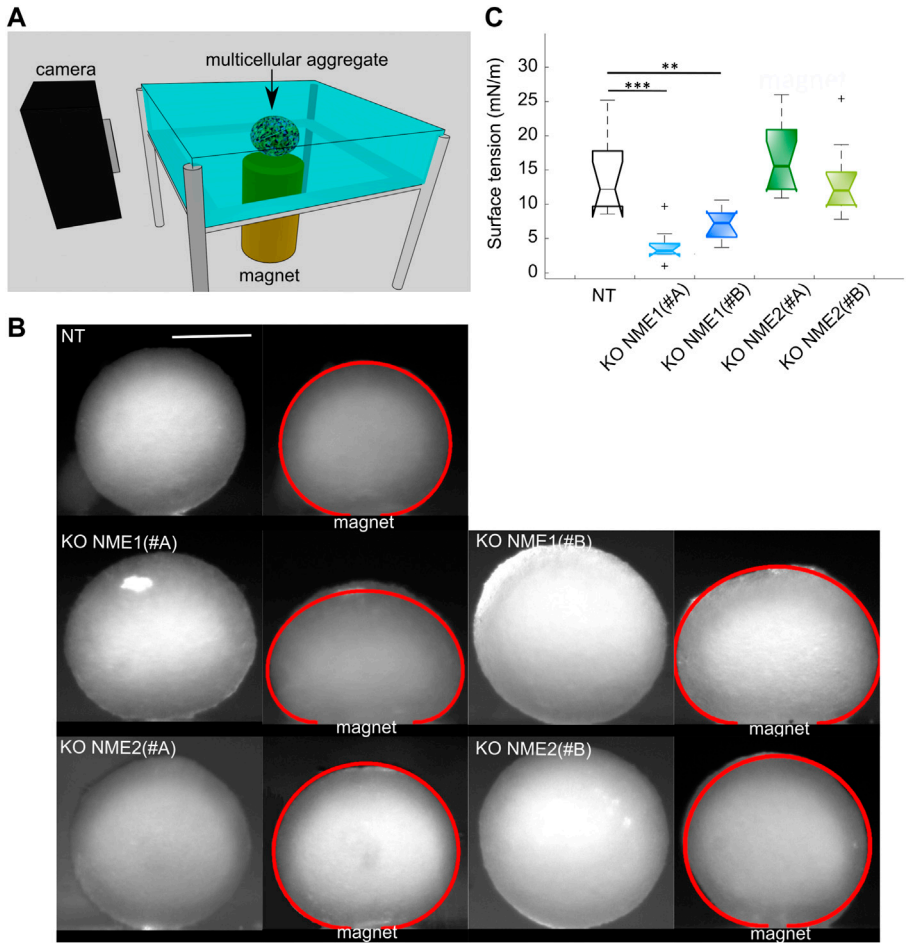


FIGURE 5
Surface tension is reduced after NME1 inactivation. **(A)** Magnetic tensiometer. A multicellular aggregate is seeded in a glass-side temperature-regulated homemade tank. A camera records its profile from the moment a permanent magnet is put in contact with the bottom slide of the tank. **(B)** Representative side profile images before and after the magnet approach for multicellular aggregates made from MCF10DCIS.com cells in which NME1 or NME2 was inactivated (scale bar: 500 μm). Initial aggregates radii are of a comparable range. The obtained fits of the flattened profiles are superimposed in red. Aggregates of NME1-ablated cells are more flattened than aggregates of either NT or NME2-ablated cells. **(C)** Surface tension obtained from the different cell types presented in **(B)**. Median, standard deviation, and 95% interval of confidence are indicated. Each cell type's measurements have been repeated over $N = 3$ independent experiments and over 9–15 multicellular aggregates. Only significant tests are indicated (**$p < 0.01$, ***$p < 0.001$). Results are compared to NT control cells.

the detachment force of the MCF10A cells has been reported to be in the 2.5 nN range (Pawlizak et al., 2015), while MCF10DCIS.com cells have a detachment force in the 2 nN range according to our data. Thus, surface tension also decreases during the transition from a normal state to a malignant cellular state.

## Discussion

We focus on a model of epithelial–mesenchymal transition induced by the loss of the metastasis suppressor NME1 in breast tumor cells. In this model, we first investigated the associated hallmarks of EMT by measuring cell–cell adhesion force, cell migration, and invasion. For this, we compared three different cell lines: ductal breast carcinoma *in situ* that are considered control tumor cells and two derivative cell lines obtained by inactivation of either NME1 or its closely related isoform NME2. AFM measurements show that loss of NME1 decreases cell–cell adhesion force, which corresponds well to the observed reduction of cell surface levels of E-cadherin upon NME1 inactivation (Huna et al., 2021). Previous functional aggregation and dispersion assays in the same cell line (Huna et al., 2021) already raised the possibility of modification of cell-cell adhesion but AFM measurements extend it to premature and early cell–cell links with a 60 s contact and fully quantify cell–cell

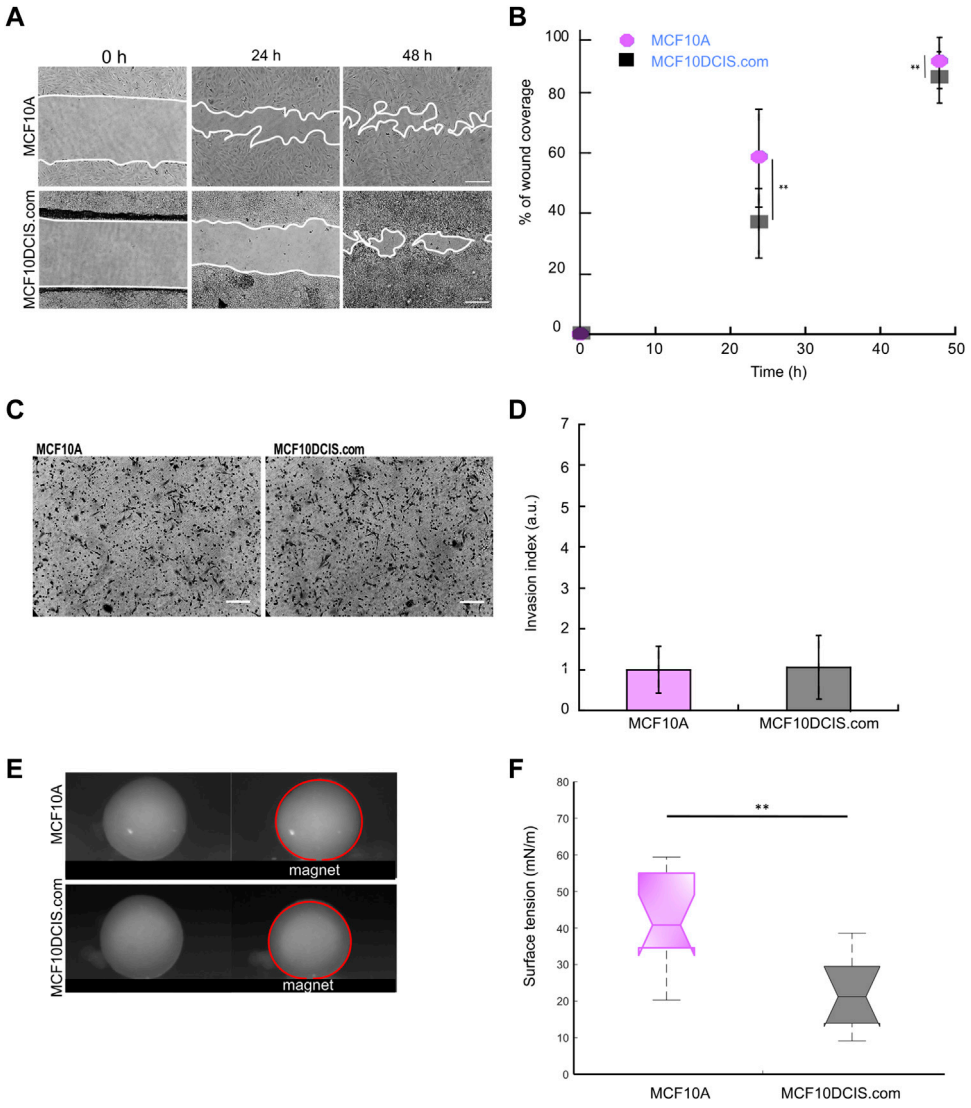


FIGURE 6
Behavior of the normal-like MCF10A cells compared to *in situ* carcinoma MCF10DCIS.com cells Three parameters are studied: **(A** and **B)** the migration over a scratch wound within 48 h, as shown in Figure 2, **(C** and **D)** the invasion through Matrigel using a Boyden chamber assay, as shown in Figure 3, and **(E** and **F)** the surface tension of multicellular aggregates using a magnetic tensiometer, as shown in Figure 5 (**$p < 0.01$).

adhesion force. The decrease of cell–cell adhesion force although moderate compared to the strong effects observed both in E-cadherin cell surface level and aggregate size after dispersion, suggests that quickly forming intercellular adhesions as well as the number of links is modified by NME1 inactivation.

Migration by mimicking potential diffusion properties of malignant cells and invasion constitute important read-outs for EMT (Friedl and Wolf, 2003). The loss of NME1 leads to increased 2D directional migration in a wound healing assay and 2D invasion through Matrigel, which mimics the basement membrane, in a Boyden chamber assay. By contrast, the absence of NME2, which is highly homologous to NME1, has no effect on cell–cell adhesion, cell migration, or invasion in the same tumor cells, indicating a highly specific function of NME1 in these EMT-associated biological processes. NME1 has been identified as the first metastasis suppressor, showing reduced expression in high melanoma metastatic cells and as a suppressor of breast, liver, and colon carcinoma metastasis through mechanisms that are not yet well-understood (Steeg et al., 1988; Boissan et al., 2005).

Several studies have demonstrated a fundamental role for NME1 in the promotion of endocytosis through interaction with

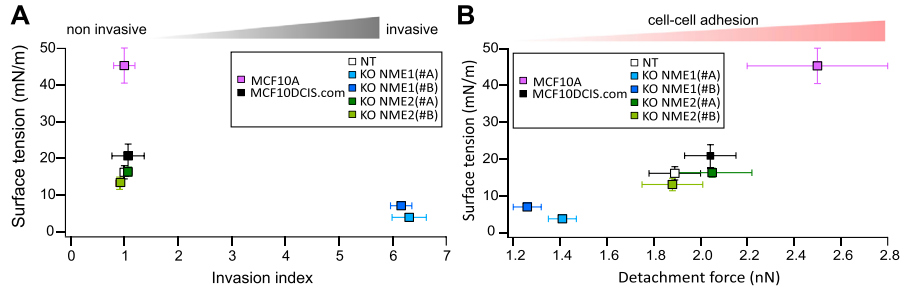


FIGURE 7
Surface tension comparison with invasion and adhesion. **(A)** The results obtained for the surface tension of aggregates from normal-like cells (MCF10A) and tumoral cells (MCF10DCIS.com and derivatives) are reported as a function of their invasion index. Means are indicated, and error bars show the SEM. **(B)** The results obtained for the surface tension of aggregates from normal-like cells and tumoral cells are reported in relation to their adhesion force measured by AFM after a 60 s contact. MCF10A adhesion force is extracted from Pawlizak et al. (2015). Means are indicated, and error bars show the SEM.

dynamin. This endocytic function of NME1 could contribute to its activity towards the regulation of cell–cell adhesion, cell migration, and invasion during tumor progression. NME1 can promote the turnover of adherents junction components, including E-cadherin, through its endocytic controlling function, which is crucial for epithelial integrity (Palacios et al., 2002; Woolworth et al., 2009). In cooperation with dynamin, NME1 also contributes to the suppression of cell migration by promoting endocytosis of chemotactic receptors at the cell surface of migrating cells (Hsu et al., 2006). Indeed, NME1 facilitates the downregulation of activated chemotactic receptors *via* dynamin-mediated endocytosis, whereas the absence of NME1 increases the levels of cell surface receptors which results in oversensitized cells to chemotactic signals and elevated cell migration. Finally, NME1 promoted dynamin-mediated endocytosis of the transmembrane metalloproteinase MT1-MMP, known as a key player in tumor invasion, resulting in a strong reduction of surface MT1-MMP levels and a concomitant reduction of extracellular matrix degradation and invasion (Lodillinsky et al., 2021). Thus, promoting endocytosis is a major function of NME1 that limits EMT-related processes.

The physical and biological mechanisms regulating EMT and tumor progression have been determined in 2D *in vitro* assays, but the dimensionality of the environment is a key factor to understand tumorigenesis (Friedl et al., 2012). Two-dimensional cultures fail to recapitulate the three-dimensional structure of a tumor. Therefore, the translation of these properties from 2D to 3D is critical and has to be explored. In a purely cellular 3D environment, cell–cell adhesions are required for the cohesion of the cell assembly. Multicellular aggregates appear to be the most appropriate three-dimensional models to study mechanical properties (Gonzalez-Rodriguez et al., 2012; Giverso et al., 2019) and they represent an excellent model of the macroscopic behavior of tissues (Costa et al., 2016; Nikolaev et al., 2020; Ackermann et al., 2021). Being an intermediate stage between cell monolayers and biological tissues (Lin et al., 2008), 3D models recapitulate numerous biological processes while being more easily monitored and reproducible. We used magnetic techniques to rapidly form 1 mm spheroids for observation of the macroscopic properties of tissues (Mazuel et al., 2015). While NME1 inactivation impairs epithelial integrity in 2D culture, this effect is not conserved in 3D as the localization of E-cadherin is not impacted in spheroids. This decrease in impact of NME1 inactivation in 3D spheroids is also reflected in E-cadherin expression, as the lack of E-cadherin is less important in spheroids compared to NT-control cells. The 3D environment is based on cell–cell adhesion formation, thus increasing the expression of E-cadherin. Cell–cell interaction enhancement has already been observed in 3D culture environments in the context of tumor cell spheroids (Bissell et al., 2002; DesRochers et al., 2012; Kim et al., 2019). E-cadherin expression is controlled both by epigenetic and environmental factors during cancer progression, while the loss of E-cadherin has been proven to be reversible in breast cancer. E-cadherin expression has been restored in tumor spheroids *via* the demethylation of the E-cadherin promoter in a model of breast cancer (Graff et al., 2000). In contrast to E-cadherin, the level of N-cadherin is enhanced in these model tissues upon NME1 inactivation. Finally, the 3D environment recapitulates the overall effects of NME1 inactivation observed in 2D cultures and confirms the intermediate EMT state of NME1 ablated cells while reducing the difference with the NT-control cells.

Material properties derived from soft matter concepts reveal as powerful tools to describe and predict the behavior of living tissues (Gonzalez-Rodriguez et al., 2012). Among them, surface tension depends mainly on adhesion and tension and is related to shape determination and maintenance. Our data show that

surface tension is strongly decreased upon NME1 inactivation but not by NME2 inactivation. Surprisingly, this decrease is more important than the one measured by cell–cell adhesion determination, and it appears to be a translating difference observed in migration and invasion assays as highlighted in Figure 7. Surface tension is a complex macroscopic property related to effective adhesion, which considers intercellular adhesion as well as cell tension. This means that there may be some reinforcement due to the multiple impacts of NME1 both on adhesion and on cell stiffness. Importantly, epithelial cells have been shown to spontaneously convert to a mesenchymal migratory and invasive phenotype when plasma membrane tension was reduced, and that increasing plasma membrane tension was sufficient to suppress tumor migration, invasion, and metastasis (Tsujita et al., 2021). Remarkably, surface tension is measured in a 3D environment, and the effect of NME1 may actually be reinforced by the dimension change as cell–cell adhesion is at the heart of tissue modelling and shape maintenance. The mechanical properties of cells are regulated by their environment. While the influence of the extracellular matrix has been extensively studied (Levental et al., 2009; Stowers et al., 2019), the impact of cell organization and dimension is emerging as essential (Long Han et al., 2019).

Surface tension also decreases when comparing normal to tumoral state. MCF10A cells are a model of normal-like breast cells, whereas MCF10DCIS.com are *in situ* breast carcinoma cells. Adhesion is significantly reduced during this transformation (Pawlizak et al., 2015), and surface tension actually reflects these changes (Figure 7). Surface tension recapitulates the evolution of cell–cell adhesion upon malignant transformation and EMT thus extending the DAH upon these processes (Figure 7B). Differences in surface tension are larger. Indeed, while a 30% increase is measured on detachment force, surface tension is actually doubled. There are two main reasons for this strengthening. First, the 3D structure strongly implicates cell–cell adhesions and may enhance adhesion changes. Second, while surface tension predominantly depends upon cell–cell adhesion, it is also affected by other biomechanical properties. The greater sensitivity of surface tension may actually reveal this multi contribution.

In addition, invasion measurements appear to be highly sensitive to EMT modifications but fail to distinguish between cells during malignant transformation (Figure 7A). Surface tension thus appears to be a full range indicator of biophysical modifications both in malignant transformation and EMT.

While individual cell stiffness has been identified as a potential biomarker of metastatic potential (Guck et al., 2005; Xu et al., 2012), surface tension arises as an indicator of malignant transformation and tumor aggressiveness that can be measured on tissue-like structures closer to the actual tumor environment than cells grown in 2D culture. This property appears to be highly sensitive to any changes in adhesion, while also being easier to measure. Abnormal cell–cell adhesion, as well as enhanced migration and invasion, stand as three major hallmarks of tumor aggressiveness. They clearly indicate tumor progression upon hybrid states encountered in EMT. Decreased surface tension appears to be an appealing fourth one. Indeed, it is highly correlated with the three major hallmarks of tumor progression in our breast tumor model. Moreover, surface tension acts as a read-out of malignant transformation (from normal to tumoral state) and as a read-out of tumor aggressiveness (from tumoral non-invasive to tumoral invasive state) in breast tumor models.

## Conclusion

These results demonstrate that surface tension through its multiparameter dependence reflects cell organization, mechanics, and adhesion and can serve as a sensitive indicator of the state of the cells undergoing EMT as well as through the transformation from a normal state to a malignant state. Important changes in surface tension are detectable in response to subtle phenotype changes. Surface tension proved to be highly sensitive to any changes in adhesion properties at the single-cell level while being measured at the more biomimetic scale of model tissue. We investigated the sensitivity of the magnetic tensiometer across the EMT using a model of EMT induced by the loss of NME1. NME1, by acting on cell–cell interactions through E-cadherin turnover, participates in the maintenance of tissue integrity and shape. Thus, surface tension can be considered a signature of tumor aggressiveness during the EMT. This new biophysical tool appears crucial in the investigation of metastatic potential in tridimensional environments.

## Data availability statement

The raw data supporting the conclusion of this article will be made available by the authors, without undue reservation.

## Author contributions

IN, AR, EB, and MR performed the surface tension experiments. MR did the immunofluorescence imaging. MQ and TP-B performed the migration and the invasion assays. MB and HD did the immunoblot analysis for NME1/NME2 expression. EB and NL did the immunoblot analysis for E-cadherin and N-cadherin expression. VT synthetized the

superparamagnetic nanoparticles. SJ performed the AFM experiments. FL, TP-B, MB, and MR designed the experiments. MB and MR supervised the study and wrote the original draft. IN, SJ, TP-B, NL, CW, and CP reviewed and edited the manuscript.

## Funding

This work was supported by the Research Program Emergence(s) de la ville de Paris (Grant MAGIC Project), the French Defense Procurement Agency (DGA-AID), France, and Wesleyan University institutional funds.

## Acknowledgments

The authors thank Mathieu Receveur and Oune-Saysavanh Souramasing for their help with designing and building the observation tank for surface tension measurements. The authors acknowledge the staff of the MPBT (physical properties—low temperature) platform of Sorbonne Université for their support. The authors thank S. J Weiss (Division of Medical Genetics, Department of Internal Medicine, Life Sciences Institute, University of Michigan, Ann Arbor MI, USA) for helpful discussions on invasion assays. The authors thank Cat McCann for insightful discussions and help with editing the manuscript.

## Conflict of interest

The authors declare that the research was conducted in the absence of any commercial or financial relationships that could be construed as a potential conflict of interest.

## Publisher's note



## Supplementary material

The Supplementary Material for this article can be found online at: https://www.frontiersin.org/articles/10.3389/fcell.2022.926322/full#supplementary-material

**SUPPLEMENTARY FIGURE S1**
Ablation of NME1 or NME2 expression assessed by Western blot analysis. MCF10DCIS.com human breast carcinoma cells were treated with two independent guide RNAs specific for the NME1 gene, NME1 (#A) and NME1 (#B), and two for the NME2 gene, NME2 (#A) and NME2 (#B). Cells without guides are NT control cells.

**SUPPLEMENTARY FIGURE S2**
Metabolic activity for unlabeled (CTL) and labeled cells (with NP) 2 h (D0) and 1 day (D1) after nanoparticle incorporation. To assess metabolic activity, the metabolic test Alamar Blue was used. Fluorescence was measured at $\lambda_{exc}$ = 570 nm and $\lambda_{em}$ = 585 nm. Values are interpreted relative to control values (unlabeled cells in complete medium, CTL) obtained under similar conditions. No influence of nanoparticle incorporation was observed on the metabolic activity at D0 or D1.

**SUPPLEMENTARY FIGURE S3**
Lack of impact of nanoparticles on cell–cell interaction, cell migration, and invasion. **(A)** Boxplots of detachment forces from NT control cells either labeled or not by nanoparticles (in average $n$ = 45 cells were tested per condition). **(B)** Top: Representative light microscopy images of the wound healing assay of MCF10DCIS.com NT control cells either labeled (bottom) or not (top) with nanoparticles. Time 0 represents confluent monolayer wounds at 0 h and wounds were monitored until 48 h after scratching the monolayer. Images are representative of three independent biological replicates. Scale bar: 100 µm. Bottom: Quantification of the area of migration over time shown in the top part. Data show means ± SD of three independent biological replicates imaged. **(C)** Left: Representative light microscopy images of Matrigel invasion assay of MCF10DCIS.com NT control cells either treated or not with nanoparticles after 24 h. (Scale bar: 100 µm) Right: Quantitative analysis of the invasion assay presented at the left. The data show the means ± SEM of three independent biological replicates imaged and are expressed as an invasion index defined as the ratio of the number of invading magnetically labeled cells to the number of invading unlabeled cells. By definition, the invasion index of unlabeled cells is 1.

**SUPPLEMENTARY FIGURE S4**
Cell surface cadherin expression is reduced in spheroids of NME1-ablated cells. **(A)** Top left: image of a spheroid of 1 mm diameter of NT control cells. The observation plane is indicated in white. Top right: image obtained at 50 µm depth penetration. The position of the zoom is indicated by the white square. **(B)** Immunofluorescence confocal images of multicellular spheroids from MCF10DCIS.com cells in which NME1 or NME2 was inactivated taken at 50 µm from the top of the aggregate. Pan-cadherin antibody labeling both N-cadherin and E-cadherin is used (green). The same conditions in terms of illumination and recording are applied. Images of nuclei labeled (blue) are added. (Scale bars: 20 µm) **(C)** Quantitative analysis of the mean intensity of the pan-cadherin labeling renormalized to the NT control cells. Means and standard deviations are represented. $N$ = 4 aggregates were imaged for each condition. * $p < 0.05$, ** $p < 0.01$.

## References

Ackermann, J., Ben Amar, M., and Joanny, J-F. (2021). Multi-cellular aggregates, a model for living matter. *Phys. Rep.* 927, 1–29. doi:10.1016/j.physrep.2021.05.001

Alessandri, K., Sarangi, B. R., Gurchenkov, V. V., Nassoy, P., KieBling, T. R., Fetler, L., et al. (2013). Cellular capsules as a tool for multicellular spheroid production and for investigating the mechanics of tumor progression *in vitro*. *Proc. Natl. Acad. Sci. U. S. A.* 110, 14843–14848. doi:10.1073/pnas.1309482110

Amack, J. D., and Manning, M. L. (2012). Knowing the boundaries: extending the differential adhesion hypothesis in embryonic cell sorting. *Science* 338, 212–215. doi:10.1126/science.1223953

Bissell, M. J., Radisky, D. C., Rizki, A., Weaver, V. M., and Petersen, O. W. (2002). The organizing principle: microenvironmental influences in the normal and malignant breast. *Differentiation* 70, 537–546. doi:10.1046/j.1432-0436.2002.700907.x

Boissan, M., Wendum, D., Arnaud-Dabernat, S., Munier, A., Debray, M., Lascu, I., et al. (2005). Increased lung metastasis in transgenic nm23-null/sv40 mice with hepatocellular carcinoma. *J. Natl. Cancer Inst.* 97 (11), 836–845. doi:10.1093/jnci/dji143

Boitard, C., Michel, A., Ménager, C., and Griffete, N. (2021). Protein denaturation through the use of magnetic molecularly imprinted polymer nanoparticles. *Molecules* 26 (13), 3980. doi:10.3390/molecules26133980

Brabletz, S., Schuhwerk, H., Brabletz, T., and Stemmler, M. P. (2021). Dynamic emt: a multi-tool for tumor progression. *EMBO J.* 40 (18), e108647. doi:10.15252/embj.2021108647

Brodland, G. W. (2002). The differential interfacial tension hypothesis (dith): a comprehensive theory for the self-rearrangement of embryonic cells and tissues. *J. Biomech. Eng.* 124, 188–197. doi:10.1115/1.1449491

Costa, E. C., Moreira Duarte de Melo-Diogo, A. F., Gaspar, V. M., Carvalho, M. P., and Correia, I. J. (2016). 3d tumor spheroids: an overview on the tools and techniques used for their analysis. *Biotechnol. Adv.* 34 (8), 1427–1441. doi:10.1016/j.biotechadv.2016.11.002

David, R., Ninomiya, H., Winklbauer, R., and Neumann, A. W. (2009). Tissue surface tension measurement by rigorous axisymmetric drop shape analysis. *Colloids Surf. B Biointerfaces* 72 (2), 236–240. doi:10.1016/j.colsurfb.2009.04.009

DesRochers, T. M., Shamis, Y., Alt-Holland, A., Kudo, Y., Takata, T., Wang, G., et al. (2012). The 3d tissue microenvironment modulates dna methylation and e-cadherin expression in squamous cell carcinoma. *Epigenetics* 7 (1), 34–46. doi:10.4161/epi.7.1.18546

Ehrig, S., Schamberger, B., Bidan, C. M., West, A., Jacobi, C., Lam, K., et al. (2019). Surface tension determines tissue shape and growth kinetics. *Sci. Adv.* 5, eaav9394. doi:10.1126/sciadv.aav9394

Foty, R. A., and Steinberg, M. S. (2005). The differential adhesion hypothesis: a direct evaluation. *Dev. Biol.* 278 (1), 255–263. doi:10.1016/j.ydbio.2004.11.012

Friedl, P., Sahai, E., Weiss, S., and Yamada, K. M. (2012). New dimensions in cell migration. *Nat. Rev. Mol. Cell Biol.* 13, 743–747. doi:10.1038/nrm3459

Friedl, P., and Wolf, K. (2003). Tumour-cell invasion and migration: diversity and escape mechanisms. *Nat. Rev. Cancer* 3 (5), 362–374. doi:10.1038/nrc1075

Giverso, C., Di Stefano, S., Grilloa, A., and Preziosi, L. (2019). A three dimensional model of multicellular aggregate compression. *Soft Matter* 15, 10005–10019. doi:10.1039/c9sm01628g

Gonzalez-Rodriguez, D., Guevorkian, K., Douezan, S., and Brochard-Wyart, F. (2012). Surface tension determines tissue shape and growth kineticssoft matter models of developing tissues and tumors. *Science* 338, 910–917. doi:10.1126/science.1226418

Graff, J. R., Gabrielson, E., Fujii, H., Baylin, S. B., and Herman, J. G. (2000). Methylation patterns of the e-cadherin 5' cpg island are unstable and reflect the dynamic, heterogeneous loss of e-cadherin expression during metastatic progression. *J. Biol. Chem.* 275 (4), 2727–2732. doi:10.1074/jbc.275.4.2727

Guck, J., Schinkinger, S., Lincoln, B., Wottawah, F., Ebert, S., Romeyke, M., et al. (2005). Optical deformability as an inherent cell marker for testing malignant transformation and metastatic competence. *Biophys. J.* 88, 3689–3698. doi:10.1529/biophysj.104.045476

Hannezo, E., and Heisenberg, C-P. (2019). Mechanochemical feedback loops in development and disease. *Cell* 178, 12–25. doi:10.1016/j.cell.2019.05.052

Hashmi, A., Tlili, S., Perrin, P., Martinez-Arias, A., and Lenne, P-F. (2022). Cell-state transitions and collective cell movement generate an endodern-like region in gastruloids. *Elife* 11, e59371. doi:10.7554/eLife.59371

Hayashi, T., and Carthew, R. W. (2004). Surface mechanics mediate pattern formation in the developing retina. *Nature* 431, 647–652. doi:10.1038/nature02952

Heer, N. C., and Martin, A. C. (2017). Tension, contraction and tissue morphogenesis. *Development* 144 (23), 4249–4260. doi:10.1242/dev.151282

Hirschhaeuser, F., Menne, H. H., Dittfeld, C., West, J., Mueller-Klieser, W., Kunz-Schughart, L. A., et al. (2010). Multicellular tumor spheroids: an underestimated tool is catching up again. *J. Biotechnol.* 148 (3–15), 3–15. doi:10.1016/j.jbiotec.2010.01.012

Hsu, T., Adereth, Y., Kose, N., and Dammai, V. (2006). Endocytic function of von hippel-lindau tumor suppressor protein regulates surface localization of fibroblast growth factor receptor 1 and cell motility. *J. Biol. Chem.* 281 (17), 12069–12080. doi:10.1074/jbc.M511621200

Huna, A., Nawrocki-Raby, B., Padilla-Benavides, T., Gavard, J., Coscoy, S., Bernard, D., et al. (2021). Loss of the metastasis suppressor nme1, but not of its highly related isoform nme2, induces a hybrid epithelial-mesenchymal state in cancer cells. *Int. J. Mol. Sci.* 22 (7), 3718. doi:10.3390/ijms22073718

Kalantarian, A., Ninomiya, H., Saad, S. M. I., Savid, R., Winklbauer, R., Wilhelm Neumann, A., et al. (2015). Axisymmetric drop shape analysis for estimating the surface tension of cell aggregates by centrifugation. *Biophys. J.* 96 (4), 1606–1616. doi:10.1016/j.bpj.2008.10.064

Khan, I., and Steeg, P. S. (2018). Metastasis suppressors: functional pathways. *Lab. Invest.* 98 (2), 198–210. doi:10.1038/labinvest.2017.104

Kim, M. J., Chi, B. H., Yoo, J. J., Ju, Y. M., Whang, Y. M., Chang, I. H., et al. (2019). Structure establishment of three-dimensional (3d) cell culture printing model for bladder cancer. *Plos One* 14 (10), 0223689. doi:10.1371/journal.pone.0223689

Krieg, M., Arboleda-Estudillo, Y., Puech, P.-H., Käfer, J., Graner, F., Müller, D. J., et al. (2008). Tensile forces govern germ-layer organization in zebrafish. *Nat. Cell Biol.* 10, 429–436. doi:10.1038/ncb1705

Levental, K. R., Yu, H., Kass, L., Lakins, J. N., Egeblad, M., Erler, J. T., et al. (2009). Matrix crosslinking forces tumor progression by enhancing integrin signaling. *Cell* 139 (5), 891–906. doi:10.1016/j.cell.2009.10.027

Lin, R-Z., Chang, H.-Y., and Chang, H. Y. (2008). Recent advances in three-dimensional multicellular spheroid culture for biomedical research. *Biotechnol. J.* 3, 1172–1184. doi:10.1002/biot.200700228

Lodillinsky, C., Fuhrmann, L., Irondelle, M., Pylypenko, O., Li, X-Y., Bonsang-Kitzis, H., et al. (2021). Metastasis-suppressor nme1 controls the invasive switch of breast cancer by regulating mt1-mmp surface clearance. *Oncogene* 40, 4019–4032. doi:10.1038/s41388-021-01826-1

Long Han, Y., Pegoraro, A. F., Li, H., Li, K., Yuan, Y., Xu, G., et al. (2019). Cell swelling, softening and invasion in a three-dimensional breast cancer model. *Nat. Phys.* 16, 101–108. doi:10.1038/s41567-019-0680-8

Maître, J-L., Berthoumieux, H., Krens, S. F. G., Salbreux, G., Jülicher, F., Paluch, E., et al. (2012). Adhesion functions in cell sorting by mechanically coupling the cortices of adhering cells. *Science* 338, 253–256. doi:10.1126/science.1225399

Manning, M. L., Foty, R. A., Steinberg, M. S., and Schoetz, E-M. (2010). Coaction of intercellular adhesion and cortical tension specifies tissue surface tension. *Proc. Natl. Acad. Sci. U. S. A.* 107 (28), 12517–12522. doi:10.1073/pnas.1003743107

Mary, G., Malgras, B., Perez, J. E., Nagle, I., Luciani, N., Pimpie, C., et al. (2022). Magnetic compression of tumor spheroids increases cell proliferation *in vitro* and cancer progression *in vivo*. *Cancers (Basel)* 14 (2), 366. doi:10.3390/cancers14020366

Mazuel, F., Reffay, M., Du, V., Bacri, J-C., Rieu, J-P., Wilhelm, C., et al. (2015). Magnetic flattening of stem-cell spheroids indicates a size-dependent elastocapillary transition. *Phys. Rev. Lett.* 14 (9), 098105. doi:10.1103/PhysRevLett.114.098105

Merkel, M., and Manning, L. (2017). Using cell deformation and motion to predict forces and collective behavior in morphogenesis. *Semin. Cell Dev. Biol.* 67, 161–169. doi:10.1016/j.semcdb.2016.07.029

Mierke, C. T. (2020). Mechanical cues affect migration and invasion of cells from three different directions. *Front. Cell Dev. Biol.* 28, 583226. doi:10.3389/fcell.2020.583226

Montel, F., Delarue, M., Elgeti, J., Malaquin, L., Basan, M., Risler, T., et al. (2011). Stress clamp experiments on multicellular tumor spheroids. *Phys. Rev. Lett.* 107, 188102. doi:10.1103/PhysRevLett.107.188102

Nagle, I., Delort, F., Hénon, S., Wilhelm, C., Batonnet-Pichon, S., and Reffay, M. (2021). Multiparameters dependance of tissue shape maintenance in myoblasts multicellular aggregates: the role of intermediate filaments. *BioXriv*. doi:10.1101/2021.12.18.473332

Nikolaev, M., Mitrofanova, O., Broguiere, N., Geraldo, S., Dutta, D., Tabata, Y., et al. (2020). Homeostatic mini-intestines through scaffold-guided organoid morphogenesis. *Nature* 585, 574–578. doi:10.1038/s41586-020-2724-8

Northcott, J. M., Dean, I. S., Mouw, J. K., and Weaver, V. M. (2018). Feeling stress: the mechanics of cancer progression and aggression. *Front. Cell Dev. Biol.* 28, 17. doi:10.3389/fcell.2018.00017

Olea-Flores, M., Zuniga-Eulogio, M., Tacuba-Saavedra, A., Bueno-Salgado, M., Sanchez-Carvajal, A., Vargas-Santiago, Y., et al. (2019). Leptin promotes expression of emt-related transcription factors and invasion in a src and fak-dependent pathway in mcf10a mammary epithelial cells. *Cells* 8 (10), 1133. doi:10.3390/cells8101133

Palacios, F., Schweitzer, J. K., Boshans, R. L., and D'Souza-Schorey, C. (2002). Arf6-gtp recruits nm23-h1 to facilitate dynamin-mediated endocytosis during adherens junctions disassembly. *Nat. Cell Biol.* 4 (12), 929–936. doi:10.1038/ncb881

Pastushenko, I., and Blanpain, C. (2019). Emt transition states during tumor progression and metastasis. *Trends Cell Biol.* 29 (3), 212–226. doi:10.1016/j.tcb.2018.12.001

Pawlizak, S., Fritsch, A. W., Grosser, S., Ahrens, D., Thalheim, T., Riedel, S., et al. (2015). Testing the differential adhesion hypothesis across the epithelial-mesenchymal transition. *New J. Phys.* 17, 083049. doi:10.1088/1367-2630/17/8/083049

Pham, K., Frieboes, B. H., Cristini, V., and Lowengrub, J. (2010). Predictions of tumour morphological stability and evaluation against experimental observations. *J. R. Soc. Interface* 8 (54), 16–29. doi:10.1098/rsif.2010.0194

Schindelin, J., Arganda-Carreras, I., Frise, E., Kaynig, V., Longair, M., Pietzsch, T., et al. (2012). Fiji: an open-source platform for biological-image analysis. *Nat. Methods* 9, 676–682. doi:10.1038/nmeth.2019

Soule, H. D., Maloney, T. M., Wolman, S. R., Peterson, W. D., Jr, Brenz, R., M McGrath, C., et al. (1990). Isolation and characterization of a spontaneously immortalized human breast epithelial cell line, mcf10. *Cancer Res.* 50 (18), 6075–6086.

Steeg, P. S., Belavicqua, G., Kopper, L., Thorgeirsson, U. P., Talgmadge, J. E., Liotta, L. A., et al. (1988). Evidence for a novel gene associated with low tumor metastatic potential. *J. Natl. Cancer Inst.* 80, 200–204. doi:10.1093/jnci/80.3.200

Steinberg, M. S. (1963). Reconstruction of tissues by dissociated cells. Some morphogenetic tissue movements and the sorting out of embryonic cells may have a common explanation. *Science* 141, 401–408. doi:10.1126/science.141.3579.401

Stowers, R. S., Shcherbina, A., Israeli, J., Gruber, J. J., Chang, J., Nam, S., et al. (2019). Matrix stiffness induces a tumorigenic phenotype in mammary epithelium through changes in chromatin accessibility. *Nat. Biomed. Eng.* 3, 1009–1019. doi:10.1038/s41551-019-0420-5

Thompson, D. W. (1992). *On growth and form*. Dover Publications Inc.

Tsujita, K., Satow, R., Asada, S., Nakamura, Y., Arnes, L., Sako, K., et al. (2021). Homeostatic membrane tension constrains cancer cell dissemination by counteracting bar protein assembly. *Nat. Commun.* 12 (1), 5930. doi:10.1038/s41467-021-26156-4

Woolworth, J. A., Nallamothu, G., and Hsu, T. (2009). The drosophila metastasis suppressor gene nm23 homolog, awd, regulates epithelial integrity during oogenesis. *Mol. Cell. Biol.* 29 (17), 4679–4690. doi:10.1128/MCB.00297-09

Xu, W., Mezencev, R., Kim, B., Wang, L., McDonald, J., Sulchek, T., et al. (2012). Cell stiffness is a biomarker of the metastatic potential of ovarian cancer cells. *PLos one* 7 (10), e46609. doi:10.1371/journal.pone.0046609

Zhang, H., Li, B., Shao, Y., and Feng, X-Q. (2020). Morphomechanics of tumors. *Curr. Opin. Biomed. Eng.* 15, 51–58. doi:10.1016/j.cobme.2020.01.004

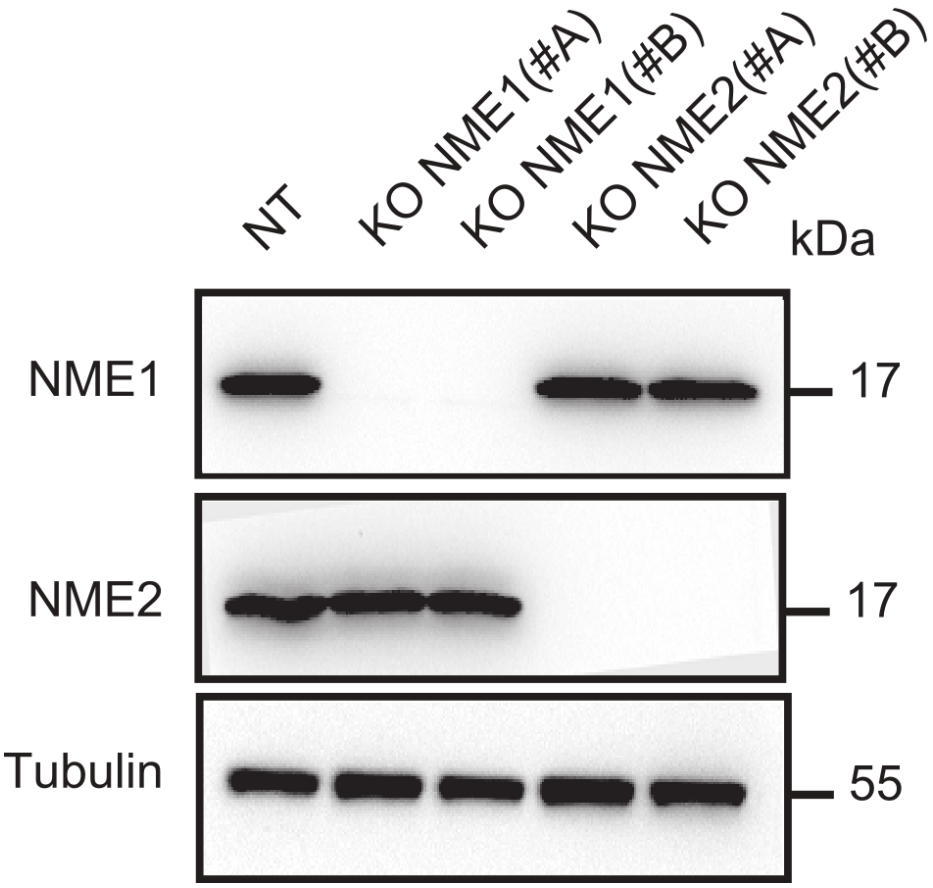


*SUPPLEMENTARY FIGURE S1*

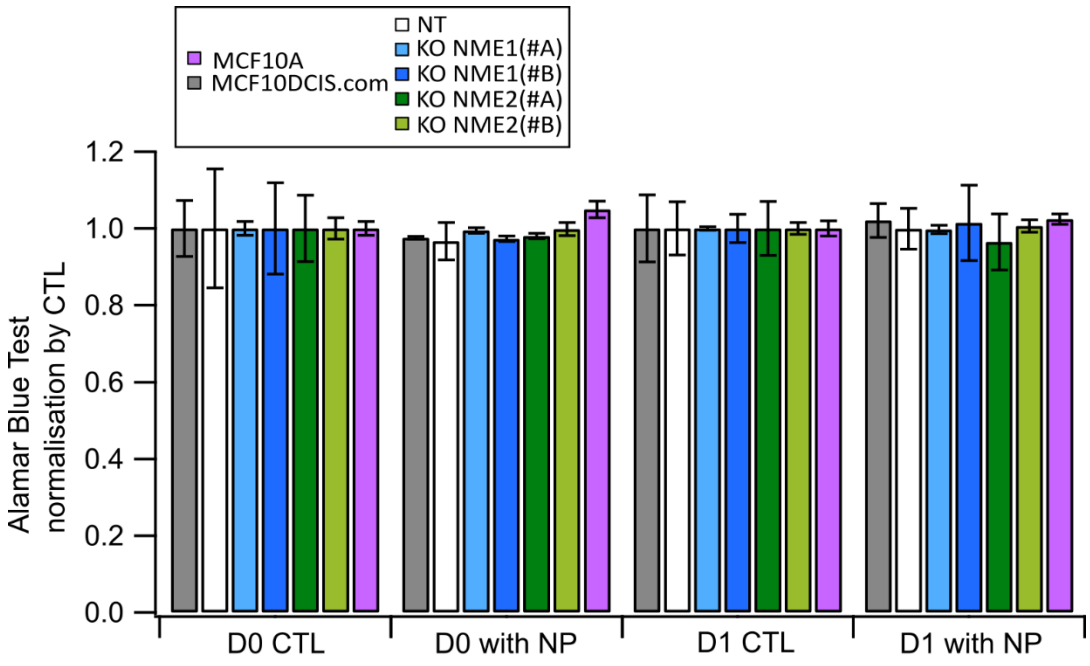


*SUPPLEMENTARY FIGURE S2*

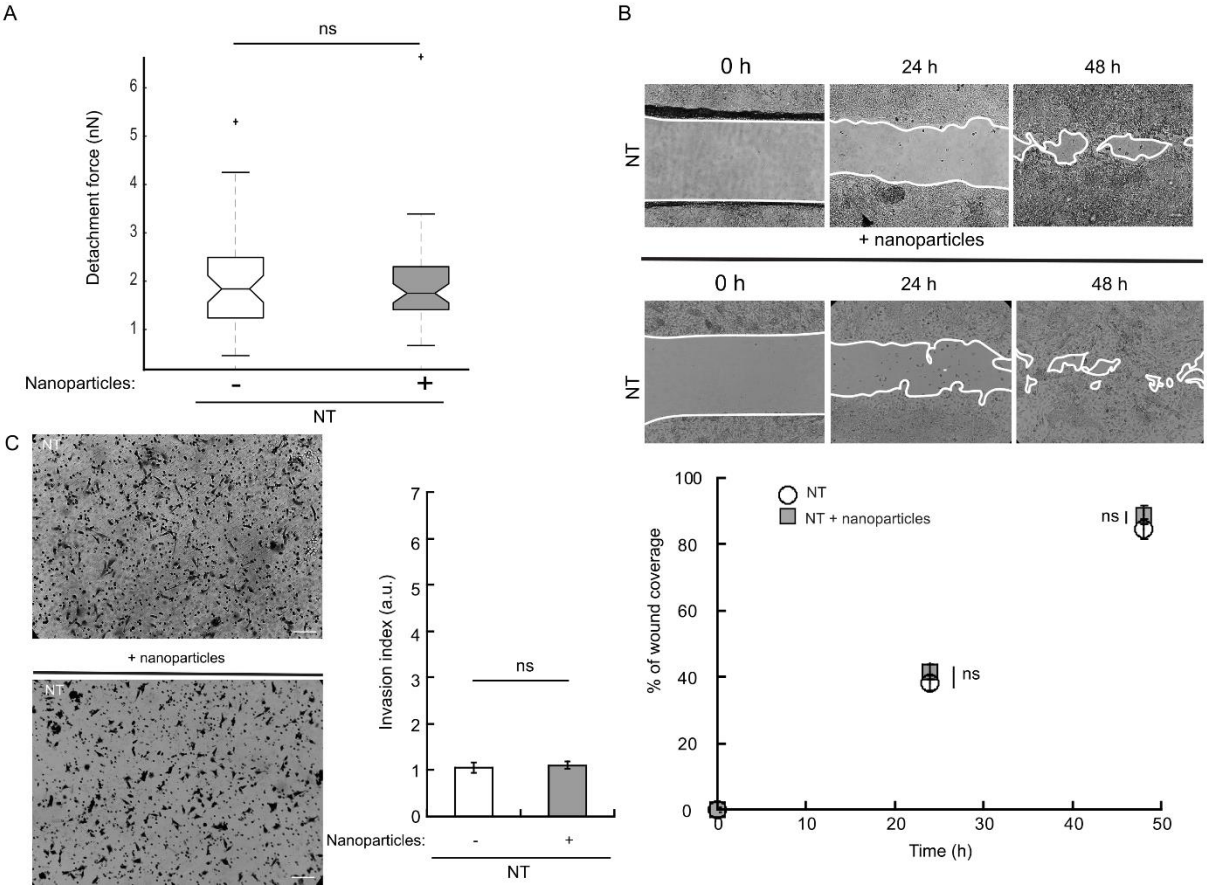


*SUPPLEMENTARY FIGURE S3*

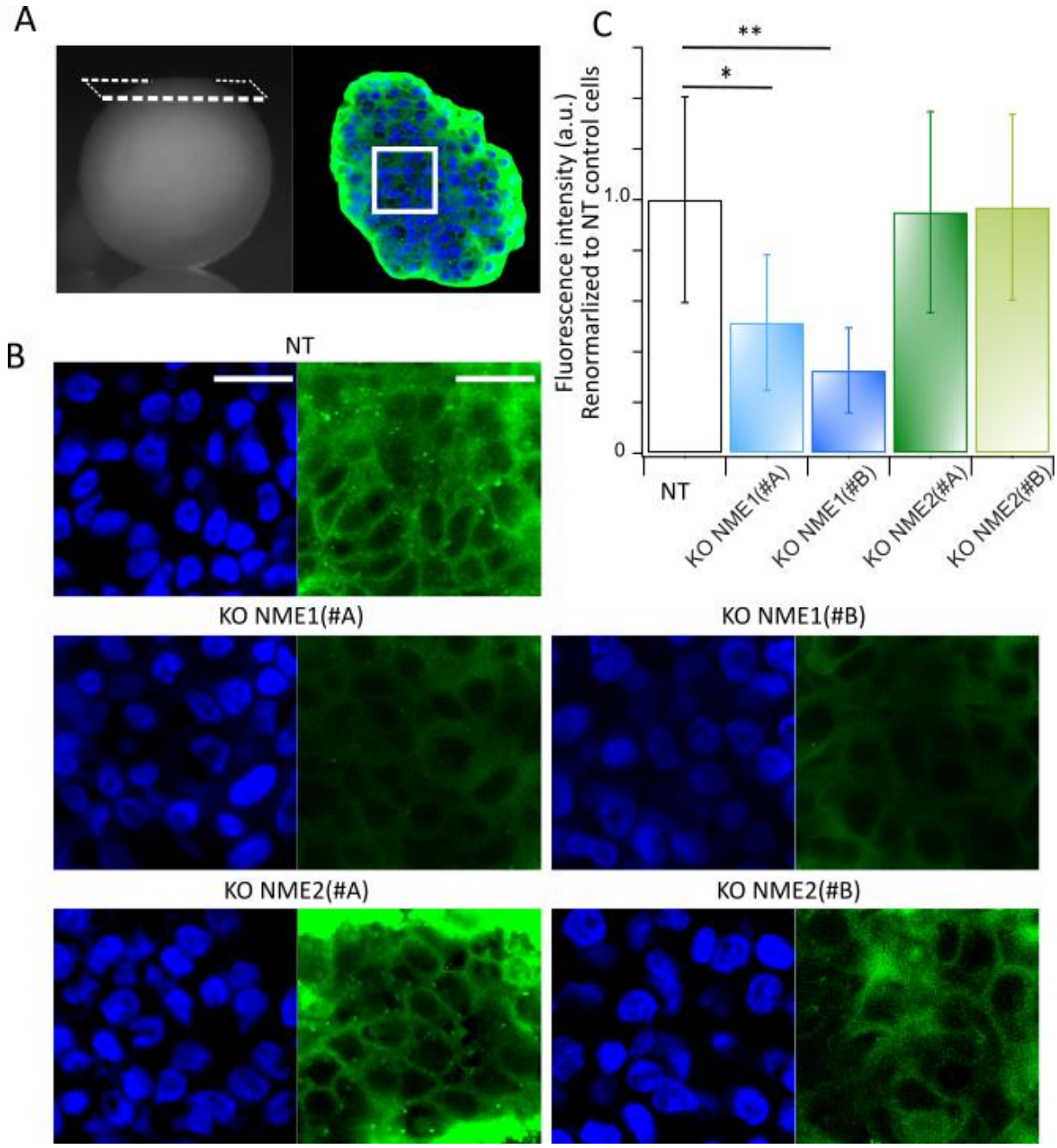


*SUPPLEMENTARY FIGURE S4*

### 2.3.3 Discussion and perspectives

In the previous work, we showed in a model of human breast cancer cells, that surface tension of tumor models can be seen as a signature of tumor aggressiveness upon malignant transformation and EMT. Regarding cell-cell adhesions, we observe a decrease of the adhesion force upon NME1 inactivation of about 30%, while the surface tension decrease is 2- to 3-fold. This larger decrease, evidences the likely contribution of other parameters than cell-cell adhesions into the macroscopic surface tension of these tumor spheroids.

This cellular model, comprising MCF10A, MCF10DCIS.com and MCF10DCIS.com KO NME1 and NME2 (see Figure 2.13), initially developed to study the biological aspects involved in the transition from carcinoma *in situ* to invasive carcinoma, is also relevant for biophysical studies, to investigate the mechanics of tumor cells across EMT and malignant transformation. One of the main advantages of this model is that all the cells have the same genetic background enabling for accurate comparisons between the cell lines.

In conclusion, the combination of magnetic molding providing controlled spheroid shape and cellular content and the magnetic force tensiometer provides a promising tool to study a variety of parameters, from microscopic properties such as adhesion properties to ECM, that are influencing the global mechanical properties of multicellular aggregates.

To try and understand better the role of each individual parameter on the 3D mechanics of spheroids, we are now working with Hervé Turlier and Nicolas Ecker (CIRB, Collège de France). They adapted their 3D numerical model of spheroids [105] to add a volumic force reproducing the configuration of the magnetic tensiometer. The simulated spheroids consist of only 50 cells in comparison to about 100k cells for a 1 mm spheroid of muscle precursor cells. By optimizing the simulations, Nicolas Ecker was able to achieve the simulation of spheroid flattening composed of 500 cells. If this cell number is still lower than the one in our experimental conditions, it provides several number of cells from the surface to the center of the *in silico* spheroid. By fitting the profile at equilibrium of the spheroid, surface tension could be extracted and correlated with changes in tension between cells. For instance, we considered up to now that spheroids are homogeneous objects. However, we often observe a few cell layers at the surface that have a more elongated shape. By tuning the effective tensions of surface cells, these 3D numerical simulations would offer a model to test the influence of the first cell layer tension on the macroscopic apparent surface tension measured.

With the magnetic force tensiometer, mechanical measurements are obtained through the application of a constant force and at the global tissue scale. Developing an integrated approach to measure the dynamical mechanical properties of biological tissues at diffe-

rent scales from microscopic to macroscopic would help to decipher the cross-talk between theses different levels. In this last section, the mechanical properties across breast cancer progression were probed at the tissue level. To investigate further these mechanical properties across the invasive switch in human breast cancer cells, we could imagine a multiscale approach to characterize the cell mechanics from the subcellular scale to the tissue scale. Measuring for instance the rheological properties from the cytoplasm or the single cell level to the tissue level would offer a complete overview of tumor cell mechanics, helping to decipher the influence of malignant transformation and EMT. For instance, two previous PhD students of the team, François Mazuel and Gaëtan Mary, have developed a rheological tool for multicellular aggregates using magnetic forces that enables rheological measurements at tissue scale. This approach, that will be presented in chapter 3, could be applied to study the rheology of human breast cancer tumor models across EMT and malignant transformation.

# Chapter 3

# Rheology of multicellular aggregates

## Contents



## 3.1 Introduction : from single cell to tissue scale rheology

In the previous chapter, tissue mechanical measurements were performed through the application of a static force and the observation of the resulting deformation. However, cell and tissue properties are much richer and depend on the timescale as well as the amplitude of force application. Methods to probe tissues through dynamical stimulations are therefore required to explore their time-dependent mechanical properties. The first results on tissue rheology show many similarities with the single cell response that we will briefly introduce.

### 3.1.1 Rheology of single cells

#### Experimental methods to probe cell rheology

Many different experimental techniques have been developed to perform rheological measurements on living cells at different time and length scales (see Figure 3.1). While particle tracking microrheology (Figure 3.1 e) is a passive method recording the random motion of beads in cells to extract local rheological properties [106], all the other presented techniques are based on the application of a force and the monitoring of the resulting deformation. Atomic force microscopy (AFM) [89], magnetic twisting cytometry [107], magnetic tweezers [92] and optical tweezers [108] (Figure 3.1 a-d) probe the local submicrometer scale cell rheology, whereas the parallel-plate rheometer [109], the optical stretcher [110] and acoustic methods [111] (Figure 3.1 f-g) are probing the rheological properties at the single cell scale. Each method presents its advantages and limitations and is probing different mechanical contributions to the global response [112] [113] [114].

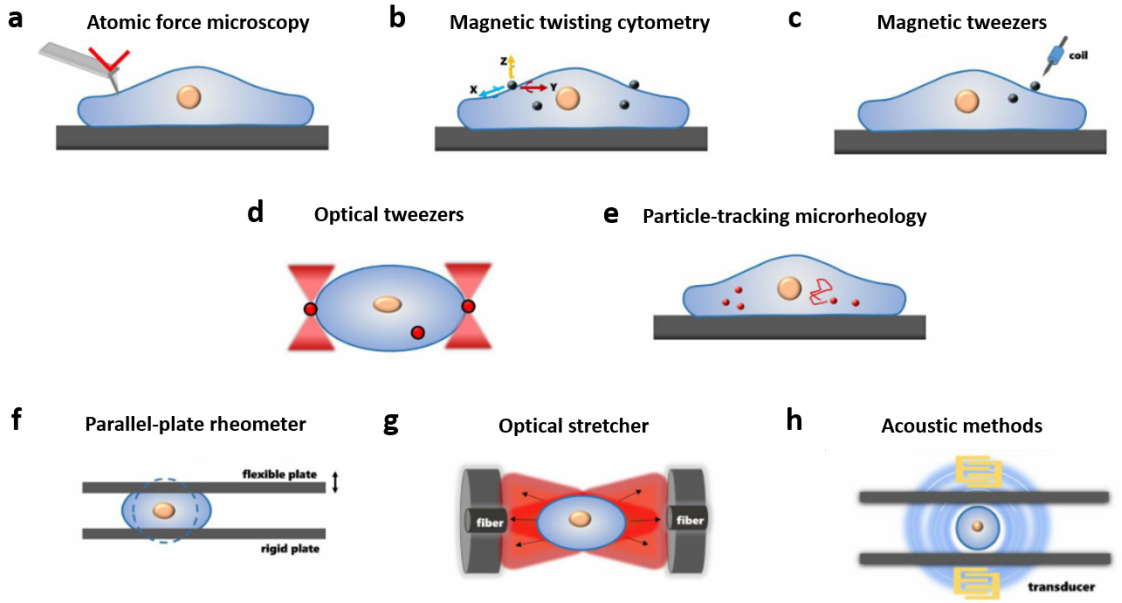


**Figure 3.1 Experimental methods to probe the cell rheological properties.** While atomic force microscopy, magnetic twisting cytometry, magnetic and optical tweezers and particle-tracking microrheology probe the cell mechanical properties at the local scale (a-e), the parallel-plate rheometer, the optical stretcher and acoustic methods (f-h) probe the cell mechanics at the global cell-scale. Adapted from Hao et al. [114].

#### Power-law response

From experiments performed with different experimental techniques, cell lines and

time scales, a common power-law response has been described for single cell rheology. For instance, if we consider a creep experiment where a cell is submitted to a constant stress $\sigma_0$ at t = 0, the resulting deformation $\epsilon(t)$ depends on a power-law of time. By defining the creep function $J(t)$, we can write :

$$J(t) = \frac{\epsilon(t)}{\sigma_0} = J_0(\frac{t}{\tau})^\alpha$$

Time is renormalised by $\tau = 1\,s$ by convention and the prefactor $J_0$ is inversely proportional to an elastic modulus. The exponent $\alpha$ is comprised between 0 and 1. If $\alpha = 0$, we recover Hooke's law corresponding to a purely elastic solid ($\epsilon(t) = \sigma_0 J_0$), while for $\alpha = 1$, we recover the law of newtonian fluids corresponding to a viscous liquid ($\dot{\epsilon} = \frac{\sigma_0 J_0}{\tau}$). For cells, an intermediate exponent is observed with $\alpha$ between 0.1 and 0.5. Figure 3.2 presents a typical curve for a creep experiment for F9 cells measured with a magnetic bead rheometer with $\alpha = 0.3$, as well as the two boundary responses for $\alpha = 0$ and $\alpha = 1$. This intermediate value of $\alpha$ for cells evidences their viscoelastic behavior.

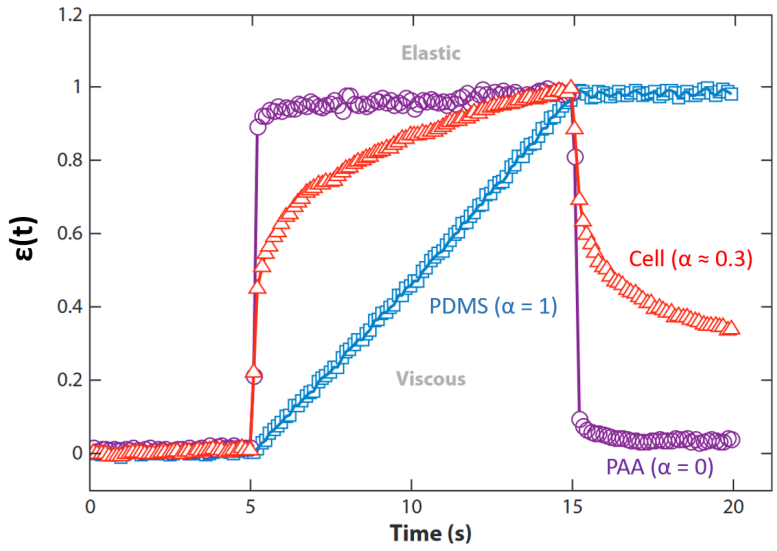


**Figure 3.2 Creep responses for a viscous or elastic material in comparison to cells.** Experimental creep response for an illustrative elastic material (polyacrylamide-bis-acrylamide (PAA) hydrogel) in purple, for a viscous material (polydimethylsiloxane (PDMS) silicone oil) and for a cell (F9 embryonic carcinoma cells) in red. In all these cases, the creep response follows a power-law, from $\alpha = 0$ for an elastic material to $\alpha = 1$ for a viscous material and $\alpha = 0.3$ for F9 cells. Adapted from Kollmannsberger et al. [112].

If springs and dashpots coupled in series or parallel can be introduced to empirically model cell response in some specific cases, this power-law response reveals that cells can not be described by a finite number of elastic and viscous elements with specific relaxation times. Indeed, the viscoelastic spectrum of living cells does not have any distinct timescales that could be identified to specific processes or elements and that

would have a physical meaning. By putting in series an infinite number of elementary units (such as spring-dashpot elements) with various relaxation times, we recover the power-law over many order of magnitudes of time or frequency. Interestingly, we recover the same power-law response for suspended epithelial monolayers [115] suggesting that this could be a general behavior of cells and tissues.

### 3.1.2 Rheological properties of multicellular aggregates

To investigate the rheological properties of 3D tissues, experimental tools still need to be developed. Some studies focused on the local rearrangements of cells during stress application, thanks to biomimetic prototissues or spheroids passing through microfluidic constrictions for instance [63] [116], trying to link the microscopic properties and rearrangements and tissue behavior. However, very few experimental methods exist to look at the global resulting deformation of 3D tissues upon force application. Stirbat et al. have adapted a commercial shear rheometer to multicellular aggregates: a shear stress is applied to hundreds of aggregates placed between to parallel plates [24] (see Figure 3.3). The aim is to capture both the intercellular rheology due to cell rearrangements and the single intracellular cell rheology. With this tool, stress-deformation curves are obtained. However no absolute measurements are possible due to the difficult control of multicellular aggregate number and therefore of the contact area.

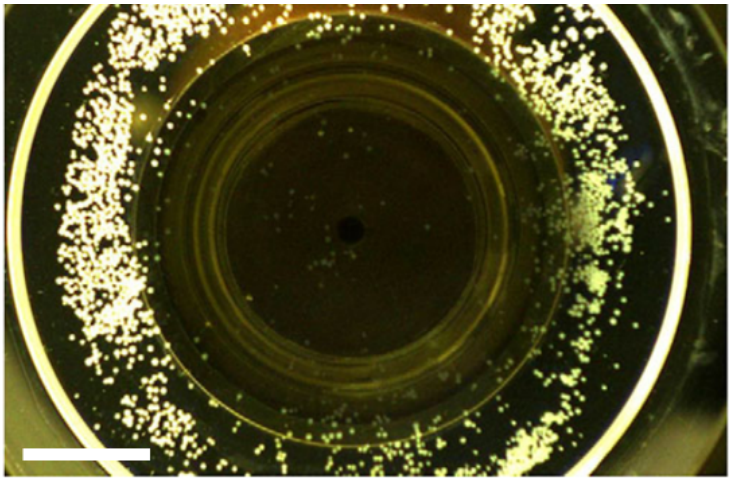

**Figure 3.3 A shear rheometer set-up adapted to multicellular aggregates.** Hundreds of F9 aggregates are placed between two transparent parallel plates. Scale bar = 1 cm. Adapted from Stirbat et al. [24].

## 3.2 Material and methods : The magnetic rheometer

In the team, an alternative method to determine the rheology of multicellular aggregates was developed by two previous PhD students (François Mazuel and Gaëtan Mary). The principle is here to apply a magnetic force per unit of volume that can be varied across time by using an electromagnet instead of permanent magnets (Figure 3.4 a). In comparison to other techniques, we can here obtain the stress-strain curves for a single multicellular aggregates while applying a versatile and controlled stimulation.

Measurements were carried out on F9 mouse embryonic carcinoma cells that have been extensively characterized and studied both at the single cell [112] [117] and tissue level [24] [118] [72]. F9 cylindrical multicellular aggregates were formed thanks to the magnetic molding technique (Figure 3.4 b). This cylindrical shape was chosen instead of spheres in order to guarantee a quasi constant area of contact during the deformation of the aggregate. The electromagnet was put under the F9 multicellular aggregate whose side profile was monitored with a camera upon force application (Figure 3.4 a) to measure the height variation $\delta h(t)$. Thanks to an amplified signal generator providing current to the electromagnet, various stimuli can be applied, from step (Figure 3.4 d) to sinusoidal forces superimposed on a step force (Figure 3.4 e-f) or even broad spectrum signals [43]. This magnetic rheometer is a highly versatile tool to screen multicellular aggregates rheology and to evidence non-linearities at high stresses (as described in Mary, Mazuel et al. [43]).

In the magnetic rheometer, the applied stress is always compressive and its local value at any altitude z above the glass slide on which the aggregate is deposited is equal to the sum of all magnetic forces that are exerted on the cells located above in the aggregate :

$$\sigma_{loc}(z) = \int_{z}^{h(t)} f_v(z')dz' \tag{3.1}$$

In our case, $f_v$ is constant for the aggregate so the stress $\sigma_{loc}$ increases linearly with the distance from the top of the aggregate. $M_v$ is measured by Vibrating Sample Magnetometry (VSM) allowing to deduce $f_v$. We define an average stress $\sigma$ applied to the aggregate such that $\sigma = \frac{1}{2}\, h(t)\, f_v \simeq \frac{1}{2}\, h_0\, f_v$. Indeed, the height variation of the aggregate is below 5% : for the maximal applied force $f_v$ that corresponds to about 1 Pa in stress, the maximal deformation $\delta h$ is 50 µm for an initial height of the aggregate $h_0 = 1\, mm$.

To study the rheological behavior of the aggregates and assuming a linear local rheology, the aim is to relate the measured macroscopic strain $\epsilon(t) =< \epsilon_{loc}(z,t) >_z$ (with $\epsilon_{loc}(z,t)$ the local deformation in the aggregate) to the earlier and present values of the

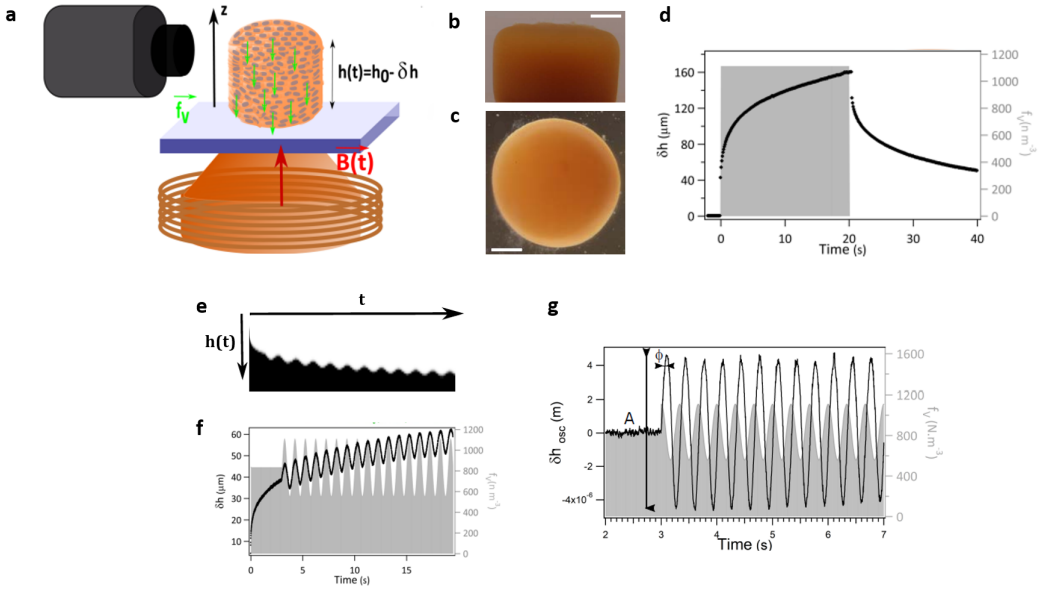


**Figure 3.4 The magnetic rheometer.** **a)** Schematics of the set-up. The magnetic aggregate is deposited in a tank filled with culture medium and thermostated at 37 °C. The sides of the tank are sealed with glass slides and the side profile of the aggregate is monitored with a camera. To generate a magnetic field, an electromagnet is placed under the aggregate. It is composed of a central soft iron polar piece (with a 5 mm diameter polar piece at the top) surrounded by a coil. An amplified signal generator supplies the coil with current. **b-c)** Side and top views of cylindrical F9 aggregates formed by magnetic molding (incubation conditions with nanoparticles at [Fe] = 2 mM in RPMI and 5 mM citrate for 2 hours). Scale bars = 500 µm. **d-f)** The magnetic forces per unit of volume applied to the aggregate are shown with the gray area while the measured deformations of the top of the aggregate are shown with black markers. Thanks to the signal generator, we are able to apply various signals such as a step force (d) or a combination of a sinusoid at 1 Hz superimposed on a step (f). **e)** Kymograph example of the upper interface of the aggregate when a sinusoid superimposed to a step force is applied. **g)** Extracted oscillatory contribution of the aggregate upper interface deformation (in black) and sinusoidal part of the applied force (in gray). The amplitude A and the phase shift $\phi$ are measured at different frequencies. Adapted from Mary, Mazuel et al. [43].

macroscopic strain $\sigma(t)$.

The variation of the upper interface of the aggregate is monitored upon force application and the deformation $\epsilon$ is defined as the ratio between the height variation of the upper interface $\delta h(t)$ and the initial height of the aggregate $h_0$:

$$\epsilon(t) = \frac{\delta h(t)}{h_0} \tag{3.2}$$

For a constant stress application $\sigma(t) = \sigma_0$, we define the classical creep function $J(t)$ as $\epsilon(t) = \sigma_0 J(t)$. From the experiments, G. Mary and F. Mazuel showed that it coincides with a power law $J(t) = J_0(\frac{t}{\tau})^{\alpha}$ on four order of magnitudes, from 0.01 s to 100 s

(with $\tau = 1\ s$ by convention). They measured $\alpha = 0.21 \pm 0.03$ (mean $\pm$ SD) and $J_0 = (4.8 + 2.3, -0.9) \times 10^{-2} Pa^{-1}$ (mean $\pm$ SD) for F9 multicellular aggregates [43].

In the linear regime and for an arbitrary applied stress, the deformation $\epsilon(t)$ can be written as a function of the creep function $J(t)$ and the imposed stress history $\sigma(t)$. Indeed, the applied stress can be seen a series of infinitesimal stress steps :

$$d\sigma(t') = \frac{d\sigma}{dt}(t')dt' \quad with\ t' \leq t \tag{3.3}$$

so that the strain $\epsilon(t)$ can be written as the following sum :

$$\epsilon(t) = \int_0^t J(t - t')\frac{d\sigma}{dt}(t')dt' \tag{3.4}$$

In the case of a sinusoidal varying stress of pulsation $\omega$ instead of a constant stress and in the linear regime, we can define a complex viscoelastic modulus:

$$E^*(\omega) =\mid E^*(\omega) \mid e^{i\phi(\omega)} = \frac{\sigma^*(\omega)}{\epsilon^*(\omega)} \tag{3.5}$$

From equation 3.4 and for an oscillatory stress with amplitude $\sigma_{osc}$ at an angular frequency $\omega$ superimposed on a steplike stress signal (Figure 3.4 e-f), we therefore obtain a sinusoidal strain response with complex amplitude :

$$\epsilon^*_{osc}(\omega) = J^*(\omega)\sigma_{osc} \tag{3.6}$$

with

$$E^*(\omega) = \frac{1}{J^*(\omega)} = \frac{(i\omega\tau)^\alpha}{J_0\Gamma(1+\alpha)} \tag{3.7}$$

where $\Gamma$ is the Euler function. By defining $E_0$ as $E_0 =\mid E^*(f = 1Hz) \mid$ and $\phi$ the phase of the complex Young's modulus, we have $E_0 J_0 = \frac{(2\pi)^\alpha}{\Gamma(1+\alpha)}$ and $\phi = \frac{\alpha\pi}{2}$.

By applying sinusoidal stress signals at different frequencies and measuring the amplitude and the phase of the resulting deformation (Figure 3.4 g), one can therefore extract $E_0$, $\alpha$ and $J_0$, the latter showing similar results to the measurements obtained with the step-like stresses.

This experimental set-up was used to probe the rheology of tissue models (creep and oscillatory experiments or broad spectrum stimulation combined with inference analysis) evidencing a power-law response (see Figure 3.4) and non-linearities at high stresses with a stress-stiffening. Besides, the link between microscopic and macroscopic properties was

investigated and especially the influence of intercellular (cell-cell adhesions) and intracellular (actin) components in this tissue model rheology. All these results are published in Mary, Mazuel et al. [43].

My contribution to this work consisted in cross-validating the method by comparing measurements obtained with the magnetic rheometer to a microplate rheometer developed by Atef Asnacios adapted from single cells to multicellular aggregates (to measure the rheology of multicellular aggregates from the parallel plates, one has to adapt their shape from cylinders to cuboids). Finally, I adapted the technique to CT26 cells (mouse colon carcinoma cells), to show the potential extension of this rheology technique to other cell types.

## 3.3 Results

### 3.3.1 Cross-validation of the technique with microplate rheometry

In order to validate the magnetic rheometer measurement method, we compared the obtained results to measurements done by a microplate rheometer adapted for multicellular aggregates. This device is composed of two parallel plates in between the multicellular aggregate is compressed. One of the plates is rigid while the other one is flexible. The force F applied to the aggregate is determined by the deflexion $\delta$ of the flexible plate $F = k\delta$ knowing the calibrated stiffness $k$. Two main technical challenges had to be overcome. First of all, the multicellular aggregate being larger and softer than the individual cells, the flexible plate had to be adapted. To this mean, Atef Asnacios developed spatula-like plates with a thin neck (about 100 µm width and 5 mm long) and wide tips (about 1 mm width) to obtain a plate with a low stiffness (28 nN/µm) while being able to hold the multicellular aggregate between the plates. Moreover, we had to produce multicellular aggregates that could be adapted to both set-ups. Indeed, the aggregate could only be held on its lateral sides with the microplates (Figure 3.5 c-d). This is why we had to change the geometry of aggregates from cylinders to cuboids (Figure 3.5 a-b) to obtain flat lateral sides of the aggregate for the contact area not to vary upon stress application.

Briefly, the applied stress $\sigma$ was defined by $\sigma = \frac{F}{S} = \frac{k\delta}{S}$ with S the contact area corresponding to $S = Lh$ and L and h being respectively the width and the height of the F9 aggregates (cf Figure 3.5 d). The uniaxial strain is defined by $\epsilon = \frac{L-L_0}{L_0}$ where $L$ and $L_0$ are respectively the distances after and before compression. The apparent measured

modulus reads $E = \frac{\sigma}{\epsilon}$. Sinusoidal stresses were applied at different frequencies and the complex elastic modulus $\mid E^*(\omega) \mid$ and phase were extracted to be compared to the one obtained with the magnetic rheometer.

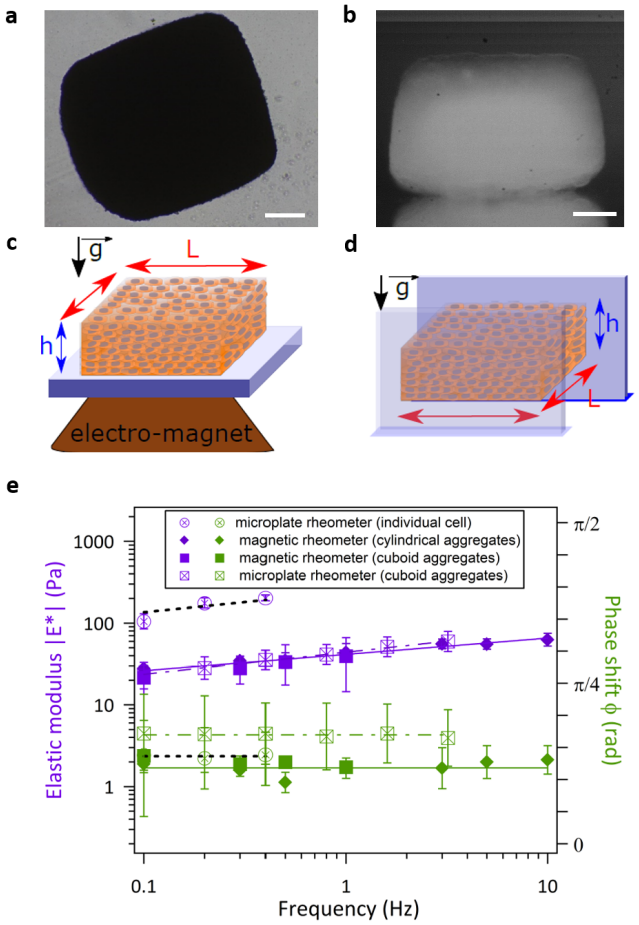


**Figure 3.5 Cross-validation of the magnetic rheometer and the microplate rheometer.** **a-b)** Top and side views of cuboid aggregates of 1 mm side and about 600 µm height. **c-d)** Schematic pictures of the magnetic rheometer (c) and the parallel-plate rheometer (d). **e)** Modulus (purple) and phase (green) of the complex viscoelastic modulus $E^*$ of cylindrical (diamonds) or cuboid (squares) F9 aggregates plotted in logarithmic scale. N = 45 aggregates for cylindrical aggregates and N = 7 for cuboid aggregates. The experimental points are fitted by a power law for the modulus (purple lines) and by a constant for the phase (green lines) corresponding to $E_0 = 45 \pm 12$ Pa and $\alpha = 0.27 \pm 0.04$. Results for F9 single cells loaded with nanoparticles measured by the microplate rheometer are added for comparison (empty circles). c,d,e are extracted from Mary, Mazuel et al. [43].

First of all, we had to check that the new cuboidal geometry was not affecting the measured rheological properties of the multicellular aggregates. Both cuboid and cylindrical F9 aggregates were formed by magnetic molding. Cuboids were formed thanks to 1 x 1 mm molds and resulting aggregates were 1 mm side and 600 µm height. The

rheological behavior of cuboid and cylindrical aggregates was measured with the magnetic rheometer by applying step signals superimposed with sinusoidal stresses (as described section 3.2) with frequencies ranging from 0.1 to 10 Hz (Figure 3.5 e). No difference was observed on $\mid E^*(\omega) \mid$ or $\phi$ between cylindrical (filled diamonds) and cuboidal aggregates (filled squares), evidencing that the multicellular aggregate shape does not influence its rheological properties.

To compare the magnetic and the microplate rheometer, we formed F9 cuboidal aggregates and measured their complex modulus $E^*(\omega)$ with both techniques. Measurements were done successively on the same aggregate with each technique. With the microplate rheometer, the same power-law is observed with $\alpha = 0.27 \pm 0.04$ and an elastic modulus $E_0 = 45 \pm 12\ Pa$, confirming the power-law rheology of multicellular aggregates. Results obtained with the magnetic rheometer (filled squares) or with the microplate rheometer (empty squares) are presented in Figure 3.5 e (N = 7 aggregates). Interestingly, no significant difference between the two techniques is observed for the elastic modulus $\mid E^*(\omega) \mid$ and the phase shift $\phi$, cross-validating the magnetic and the microplate rheometer as valuable tools for the rheology of multicellular aggregates. This result also highlights that there is no anistropy due to the aggregate formation method since measurements are carried out in two different configurations (as shown Figure 3.5 c-d).

### 3.3.2 Adaptation to another cell line

To highlight the versatility of the magnetic rheometer, we decided to test the method with another cell line. Indeed, the magnetic labeling working with all cell types tested up to now, the magnetic rheometer could be applied to any cell line provided that cells are able to form cohesive aggregates. We formed by magnetic molding cylindrical aggregates of mouse colon carcinoma cells (CT26) with iron oxide nanoparticle labeling conditions of [Fe] = 1 mM in RPMI and no citrate for 2 hours (Figure 3.6 a). We observed the same power-law rheology $J(t) = J_0(\frac{t}{\tau})^\alpha$ as observed for the F9 mutlicellular aggregates, on several order of magnitudes (creep function presented Figure 3.6 b). We measured $\alpha = 0.23 \pm 0.02$ and $J_0 = 0.03 \pm 0.01\, Pa^{-1}$. By applying sinusoidal stress signals at different frequencies superimposed on a step stress (Figure 3.6 c), we were able to extract the modulus $E_0$ at around 80 Pa, two times higher than for the F9 aggregates. This value is the same as the one measured for the Young's modulus of CT26 multicellular spheroids in section 2.2.2, Figure 2.8.

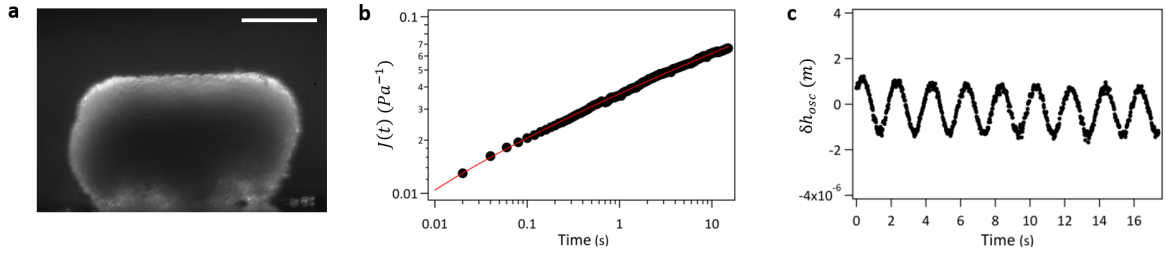


**Figure 3.6 Rheology of cylinders of CT26 cells.** **a)** Side view of a cylindrical CT26 multicellular aggregate. Scale bar = 500 µm. **b)** Creep function of a CT26 cylindrical multicellular aggregate plotted in logarithmic scale. The applied step force per unit of volume is $1.1\,kN.m^{-3}$. The experimental points (in black) are fitted with $J(t) = J_0(\frac{t}{\tau})^{\alpha}$ and $\alpha = 0.23 \pm 0.02$ and $J_0 = 0.03 \pm 0.01\,Pa^{-1}$. **c)** Extracted oscillatory contribution of the aggregate upper interface deformation when submitted to a force step of $830\,N.m^{-3}$ superimposed with a sinusoidal signal around the step force at a frequency of 0.5 Hz and an amplitude of $280\,N.m^{-3}$. The extracted Young's modulus is about 80 Pa.

## 3.4 Conclusion and perspectives

This magnetic rheometer represents a promising tool to probe the rheology of multicellular aggregates for a wide range of cell types or conditions. The measurements obtained by magnetic rheometry were cross-validated thanks to a parallel-plate rheometer developed by Atef Asnacios adapted for multicellular aggregates that also constitutes a new technique to perform rheology experiments on 3D tissue models.

Thanks to the magnetic rheometer, non-linearities could be explored in F9 cell aggregates, evidencing a stress-stiffening at higher stresses [43]. However, the deformations were always below 5%. Increasing the applied stress and therefore the resulting deformation would enable to screen for other non-linearity regimes. We are now adapting the electromagnet and the set-up to generate higher magnetic field gradients and therefore higher magnetic forces. The emergence of non-linearities for 3D biological tissues at large deformations is indeed an open research subject with few contributions in the literature.

As mentioned in chapter 2 section 2.3, this tool could be combined with rheology at the single cell or intracellular scale to obtain a multiscale picture of the tissue rheology from the cell cytoplasm to the 3D tissue scale. The MCF10DCIS.com model would be a good candidate to explore the rheology at different scales across EMT or malignant transformation.

Finally, by adding extracellular proteins during formation or using cells secreting ECM, the role of ECM could be explored as its contribution on tissue rheology and mechanics is much less clear than intercellular adhesions for instance. However, studying ECM secre-

ting cells would imply to culture the multicellular aggregates for several days or weeks. Such long culture times require nanoparticles that degrade more slowly, since a decrease of the magnetic moment leads to a decrease of the resulting deformation upon magnetic force application and therefore a decrease in the measurement sensitivity. Changing the nanoparticles coating could be a possible solution [119].

# Part II

# Tissue engineering of the skeletal muscle

# Chapter 4

# A magnetic stretcher to drive organization and differentiation into muscular cells

## Contents

## 4.1 Introduction

The skeletal muscle is one of the most abundant tissue types in the human body with about 30 to 40 % of the body mass [120]. Its function can however be impaired because of genetic, metabolic or neuromuscular diseases such as dystrophia [121], diabetes [122], ageing or Huntington disease [123].

The skeletal muscle has an anisotropic and aligned multiscale structure : individual muscular cells are aligned with each other forming entangled bundle of muscle fibers that compose the muscle (see chapter 1 section 1.4). Creating *in vitro* models of the skeletal muscle would offer a polyvalent platform for fundamental studies in tissue biology but also for the development of new drugs or gene therapies to treat muscular diseases or traumatisms. However reproducing the skeletal muscle organization and function *in vitro* is still a real challenge. Strategies to create an artifical muscle need to meet a set of requirements : (i) reproduce the muscle architecture without a support scaffold, (ii) use mechanical stimulations to enhance differentiation. The proposed approach in this part is to take advantage of magnetic fields and forces to control remotely the cell organization and to stimulate the resulting 3D tissue model.

### 4.1.1 Myogenesis

In the embryo, embryonic progenitors give rise to myoblasts that are muscle precursor cells then able to differentiate into mature muscular fibers. From these embryonic progenitors, some remain as satellite cells in the mature adult muscle. These satellite cells are implicated in the tissue homeostasis as they can differentiate into new fibers upon activation after a muscle damage. Once activated, satellite cells proliferate and become myoblasts. These muscle precursor cells first align with each other and differentiate into myocytes that are able to fuse with each other generating long polynucleated cells called myotubes. After a maturation process, myotubes become functional muscular fibers, the myofibers, that are able to contract. After the fusion into myotubes, nuclei go through several positioning processes. Nuclei are initially centered in the myotubes. They first spread to be equally distributed in the polynucleated cells and then they move towards

the periphery of myofibers where they are finally located and anchored [124] (Figure 4.1 a).

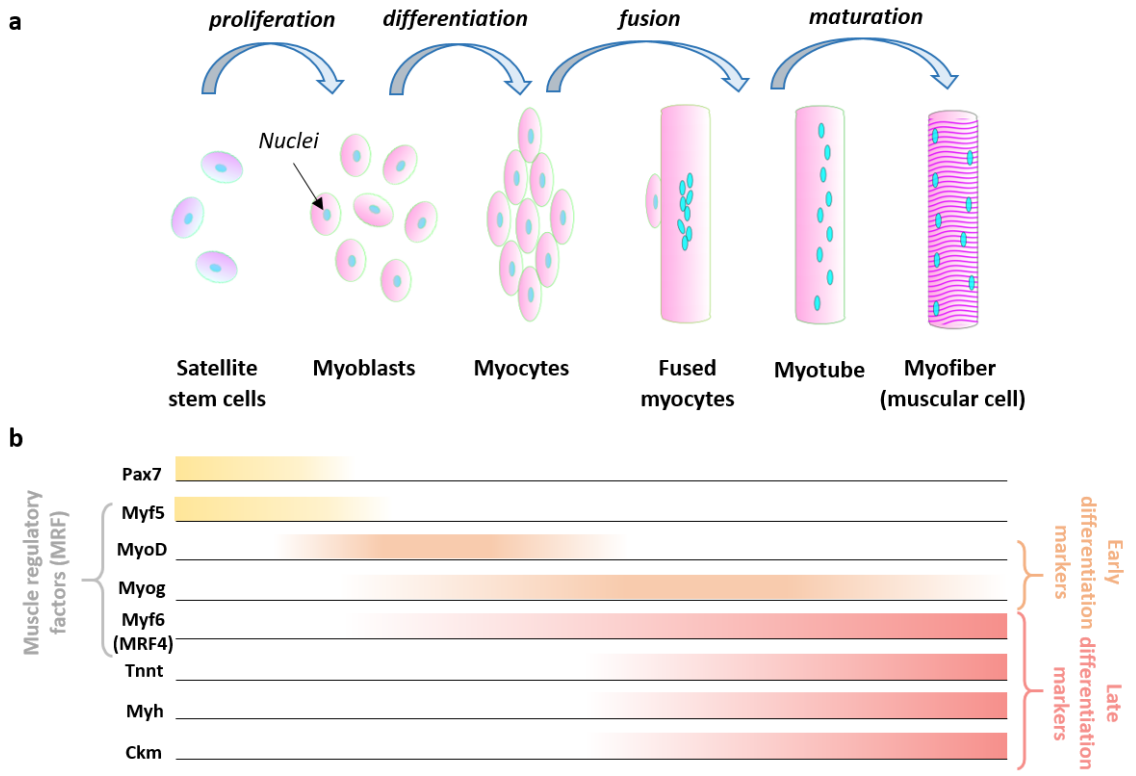


**Figure 4.1 Skeletal muscle differentiation process.** **a.** Differentiation process from satellite stem cells to functional muscular cells. Myoblasts differentiate into myocytes that align and fuse with each other to form long polynucleated cells called myotubes and finally mature muscular cells or myofibers. **b.** Expression of muscle transcription factors and protein differentiation markers during myogenesis. Figure adapted from [125] [126] [127] [128].

During this differentiation process, the expression of the muscle regulatory factors (MRF) Myf5, MyoD, Myogenin (Myog) and Myf6 (also referenced as MRF4) play a key role. While Myf5 and MyoD commit the cells to the myogenic program in the early differentiation, myogenin and Myf6 are required for the formation of myotubes from the fusion of myocytes. Pax7 is also a key transcription factor of early lineage specification [125]. At a later stage in differentiation and once myocytes start to fuse, proteins involved in the formation of sarcomeres (see chapter 1 section 1.4) are expressed such as troponin (Tnnt) or myosin heavy chain (Myh). Troponin is located on the actin thin filaments while myosin heavy chain is part of the myosin thick filaments. Finally, enzymes such as creatine kinase muscle (Ckm), which catalyzes the production of phosphocreatinine acting as an energy reservoir of ATP *in situ*, is overexpressed during myotube formation

and maturation (cf Figure 4.1 b).

### 4.1.2 Tissue engineering of the skeletal muscle

One can distinguish three main approaches that can be applied for tissue engineering and more specifically skeletal muscle tissue engineering : *in vitro*, *in vivo* and *in situ* tissue engineering. While *in vitro* tissue engineering is based on the development of a functional muscle tissue, *in vivo* tissue engineering involves the transplantation of cells and various growth factors or scaffolds in the patients. Finally, *in situ* skeletal muscle tissue engineering relies on the use of biomaterials to trigger endogenous regeneration [129]. Here we confine our scope to *in vitro* skeletal muscle tissue engineering. This approach is interesting not only for *in vivo* regeneration aspects but also for disease modelling and drug testing applications [130].

To generate and to improve tissue engineered skeletal muscle constructs, current strategies modulate both the constituents (cells, ECM) and their environment (biochemical, biophysical or topological cues). We will present briefly each aspect individually.

#### Progenitor cells for skeletal muscle tissue engineering

Various cell populations can be used for skeletal muscle tissue engineering. These cells need to be able to proliferate *in vitro* and to differentiate into mature muscular fibers. The ideal source of cells is autologous because of their non-immunogenicity in case of clinical applications.

The **C2C12 cell line** is the most widely used for skeletal muscle tissue engineering. It is an immortalised murine myoblast isolated by Yaffe et al. in 1977 [131] from thigh muscle of 2-month old C3H normal mice 70h after a crush injury and followed by selective serial passages of myoblasts. It is now a common cell line commercially available and its rapid proliferation and efficient differentiation make it a model of choice for tissue-engineered skeletal muscle constructs. As this cell line is frequently used for muscle engineered studies, objective comparative analysis with already published works are made possible circumventing the variability between different isolated primary myoblast populations. However, the fact that C2C12 cells are xenogenic does not make them appropriate for clinical translation. Moreover, some differences have been reported in the behavior of cells in comparison with human myoblasts [132].

**Satellite cells**, also called muscle stem cells, that are stem-like cells present in the

adult muscle, are able to migrate towards the injury and to differentiate into mature muscle fibers. These cells are also widely used for skeletal muscle tissue engineering because of their efficient differentiation. However, they can not be expanded for a long time in culture because of senescence, reducing the myogenic potential of cells. Besides, the collection method is invasive and the yield of isolation is low.

**Mesenchymal stem cells** (MSCs) are extracted from bone marrow (invasive procedure) or the umbilical cord (non-invasive procedure). They can differentiate into muscle cells however their myogenic differentiation potential is lower than for satellite cells. Moreover the collection from bone marrow is painful and invasive while autogenic MSCs from umbilical cord are rarely available.

**Induced pluripotent stem cells** (iPSCs) are cells derived from a donor tissue (from skin to blood cells) that have been reprogrammed back to an embryonic-like multipotent state. They have the ability of unlimited self-renewal and can be used to derive muscle progenitor cells. In theory, autologous iPSCs are the best candidates for clinical applications. However, the processes of cellular reprogramming and for terminal differentiation are very complex. Further research is also needed to achieve safe myogenesis for example reducing the risk of tumor formation [132].

From these different cell types many strategies have been developed to try and reproduce skeletal muscle organization and functionality in 2D or 3D.

### Methods to engineer skeletal muscle constructs

#### 2D culture models

One of the first strategies developed to reproduce the skeletal muscle alignment and organization is the use of 2D geometrical confinement or patterned substrates above the micron scale to provide suitable topographical cues to promote cell orientation and differentiation (Figure 4.2 a-b). More recently, this micropatterning has been improved by the addition of topological guidance cues at the nanometer scale reproducing in a more biomimetic way the extracellular matrix (Figure 4.2 c-d). Interestingly, through micropatterning approaches, these systems composed of anisotropic cells have been shown to have certain characteristics of active nematic behavior [133] [134]. Although these topological and patterning strategies enhance myoblast elongation, alignment and differentiation and have helped to identify key parameters influencing myogenesis, these 2D constructs can not be easily recovered and lack the 3D environment of physiological conditions. Because of their low thickness and the difficulty to achieve contractile functional tissues, they are

also an unadapted option for clinical translation.

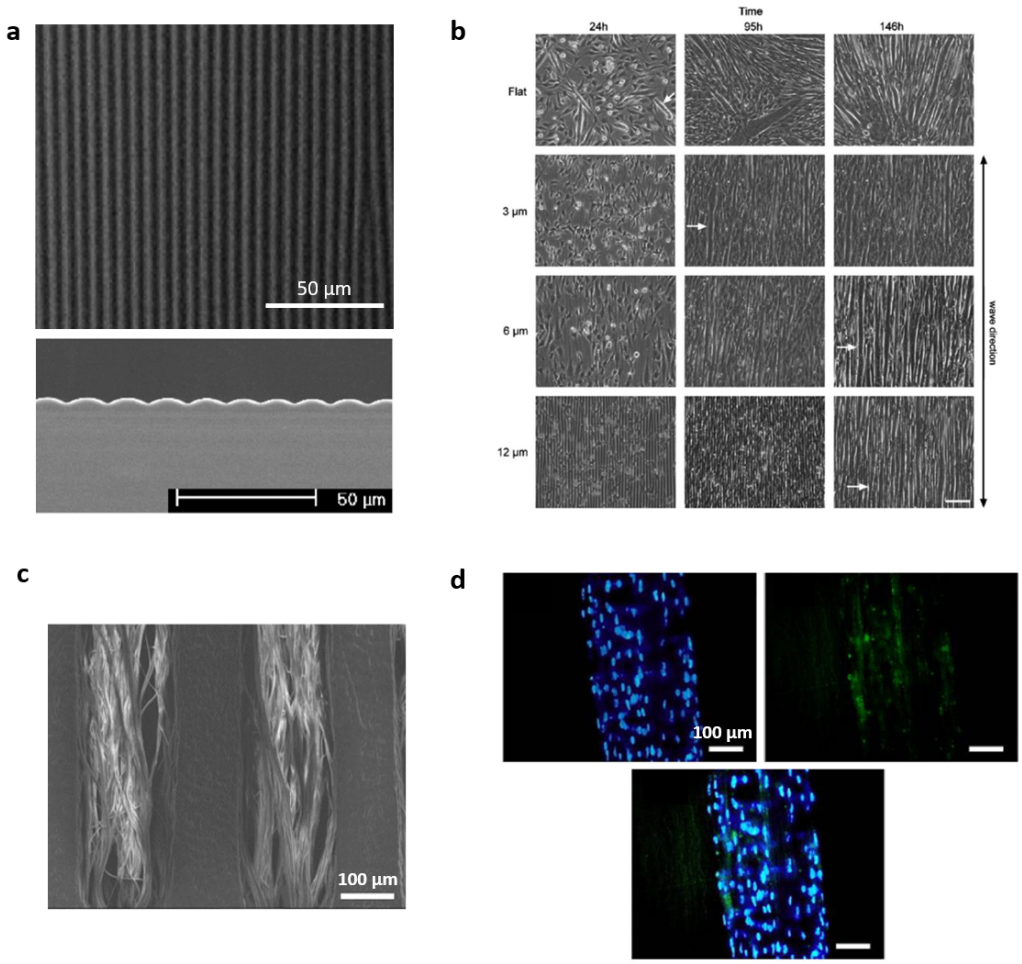


**Figure 4.2 Examples of 2D micropatterning for myoblast alignment and differentiation.** **a)** Scanning electron microscopy images of PDMS substrate with 12 µm waves, top view (top), cross-sectional view (bottom). **b)** Representative images of C2C12 cells during differentiation on flat substrates or different wave size substrates presented in (a). Patterns promote myoblast alignment and fusion into myotubes. Scale bar = 100 $\mu$m. Figures (a) and (b) adapted from Lam et al. [135]. **c)** Scanning electron microscopy images of aligned PEG (poly(ethylene glycol)) hydrogel micropatterns of 200 µm width and PCL (polycaprolactone) electrospun nanofibers. **d)** Immunofluorescence images of nuclei (blue) and MHC (green) on the micropatterns presented in (c), showing an alignment of cells parallel to the patterns and enhancement of differentiation. Figures (c) and (d) adapted from Cha et al. [136].

To overcome the limitations of classical 2D cell culture, many 3D skeletal muscle culture models have emerged over the past 30 years. For all of them, the aim is to create a biomimetic microenvironnement for the cells comprising the appropriate ECM and the mechanical and biological signals to stimulate muscle formation and maturation [137].

### 3D Scaffolds

Many scaffold-based approaches have been developed to mimic the native anisotropic structure of the ECM, presenting the cells to micro- or nano-scale topological cues. We will here introduce briefly some of the main strategies employed.

**Aligned nanofibers** have been used to guide the formation of aligned myotubes. They can be manufactured by various techniques among which electrospinning that has been widely used for muscle skeletal engineering. Electrospinning takes advantage of electric forces and electrostatic repulsion to generate micro or nanofibers from melted polymers. The polymers used can be conductive providing the possibility for electric stimulation of the constructs (Figure 4.3 a-b).

**Porous hydrogels** providing geometrical confinement with unidirectionnal channels or anisotropic microstructures can also promote successfully differentiation into aligned myotubes. Hydrogels have been widely employed in tissue engineering and regenerative medicine thanks to their high content in water and their tunable chemical and mechanical properties. They can be derived from various synthetic or natural origins and numerous materials have been used such as collagen, fibrin, hyaluronic acid, PEG or even decellularized ECM. Scaffolds can be obtained from decellularized skeletal muscle tissues that conserve biomechanical properties and ECM structure close to the native tissue [141]. An example of porous hydrogels for skeletal muscle constructs is the use of collagen hydrogels obtained by freeze-drying. This generates anisotropic structures and microchannels that enhance C2C12 differentiation (Figure 4.3 c-f). They can also be used in combination with nanofibers to provide a controlled anisotropic structure at the nanoscale.

**3D bioprinting** relies on 3D printing to combine and arrange cells, biomaterials and functional molecules. Much progress has been achieved with this technique especially thanks to the ability to control spatially and to incorporate different specific cell types trying to mimic the neuromuscular junction or vascularization [142]. Various biocompatible bio-inks can be used and Figure 4.3 g-h presents an example of 3D bioprinted skeletal muscle constructs based on the alignment and fibrillation of collagen upon printing of the cell-laden bio-ink.

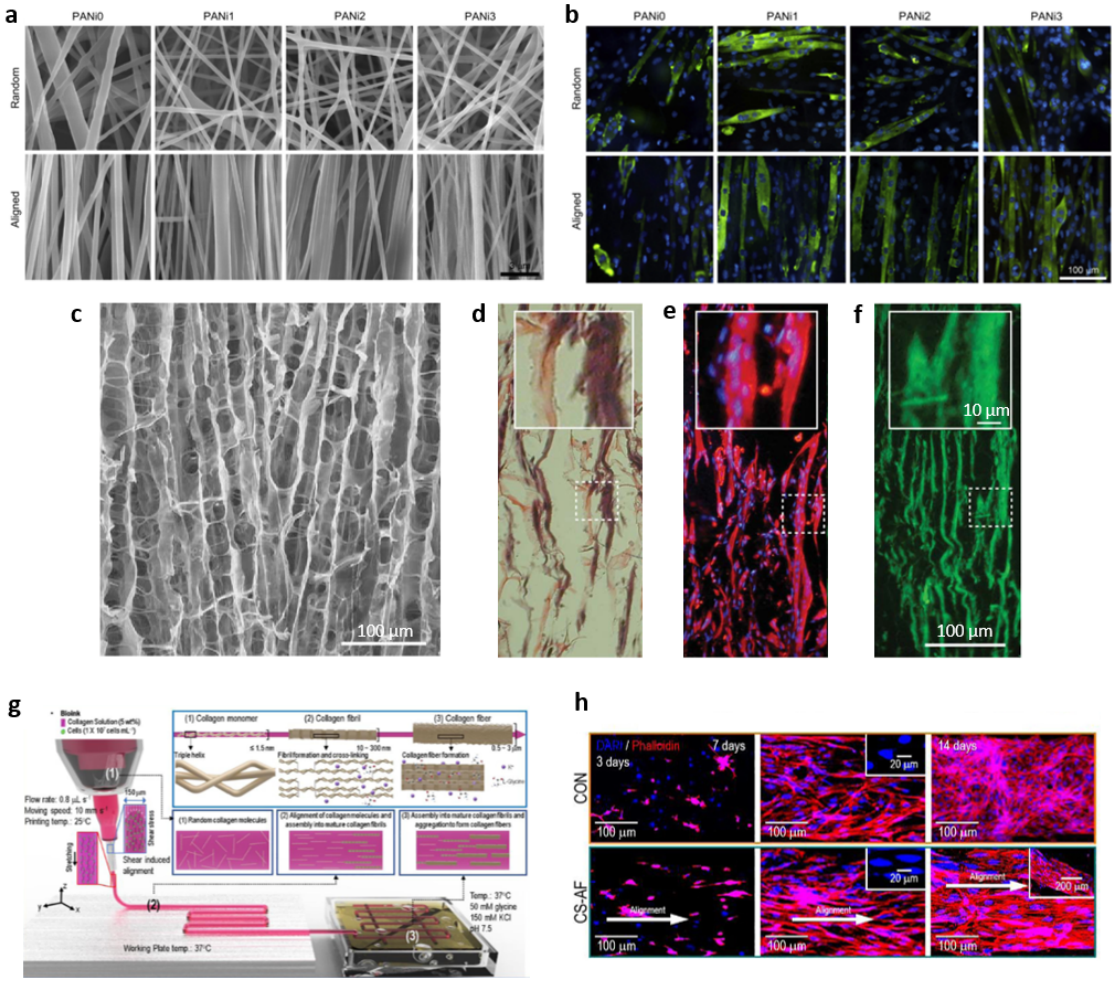


**Figure 4.3 Illustrative examples of frequently used 3D scaffolds techniques for skeletal muscle constructs, electrospun nanofibers (a-b), hydrogels (c-f) and 3D bioprinting (g-h).** **a)** Scanning electron microscopy images of electrospun PCL/PANi (polycaprolactone/polyaniline) nanofibers. **b)** Immunofluorescence images of C2C12 cells on the corresponding substrate after 7 days of differentiation with myosin heavy chain (MHC) stained in green. a-b adapted from Ku et al. [138]. **c)** Scanning electron micrograph of a collagen sponge obtained by unidirectional freezing. We observe both a longitudinal structure with large pores and a sponge structure at a smaller scale with holes and bridges. **d)** Haematoxylin-eosin staining of C2C12-derived myotubes obtained in the collagen sponge. Collagen matrix appears in pink while myotubes are in purple. **e)** Immunofluorescence images of the region shown in (d) with MHC in red and nuclei in blue. **f)** Immunofluorescence images of the region shown in (d) with laminin in green to evidence the basal lamina of myotubes. c-f adapted from Kroehne et al. [139]. **g)** Schematics of the 3D cell printing process of collagen fibers. A glycine/KCl buffer solution is used to formulate a bioink to obtain oriented fibrillated collagen after 3D printing. **h)** Immunofluorescence images of C2C12 cells after 3, 7 or 14 days in the control condition (CON) vs in the collagen sponge (CS-AF). Nuclei and actin are labelled with DAPI (blue) and phalloidin (red) respectively. g-h adapted from Kim et al. [140].

### Scaffold-free approaches

The scaffold-free strategy is an alternative approach to the use of scaffolds and hydrogels and it relies on the cells own secretion of ECM and self-assembly in 3D tissues. No exogenous component is added which enables to get rid of the lot variability of commercial ECM protein solutions [137]. Scaffold approaches require the design of complex matrixes that need to be biocompatible but also biodegradable and non-immunogenic in the case of clinical translation. Although scaffold-free approaches circumvent these challenging requirements, only a few teams have focused on this type of technique.

First, cells cultured in 2D micropatterned surfaces can delaminate forming cell sheets that can be stacked [143] or can comprise sheets of different cell types such as neuronal or vascular sheets [144]. Another team used magnetic C2C12 cells to generate cell sheets, strings or circular tissue constructs with no external matrix [145]. However, these techniques requiring longer times of tissue formation (about a month) and being not easily automated and scaled up, scaffold methods have often been preferred [137]. Moreover, in these examples, no mechanical or electrical stimulations can be applied to the constructs while there are necessary for differentiation into myofibers.

### Biophysical cues

Environment has to be fully controlled for muscle tissue engineering. Biochemical and geometrical cues have been extensively studied and have been proven to be key elements. However, physical environment is not limited to geometry, thus mechanical and electrical stimuli also represent promising tools. For instance, neuronal electrical stimulation plays a key role for skeletal maturation and contraction [137].

Concerning biophysical cues, a number of studies have demonstrated the essential role of mechanical stimuli enhancing both cell alignment and muscle differentiation with various types of strains ranging from static to cyclic strains [146]. However, the optimal stimulation parameters remain largely unknown (frequency, duration, amplitude...). Stimulation parameters have been mostly studied in the 2D configuration and the conclusions are not necessarily translatable to 3D [147]. Moreover, if mechanical stimuli probably impact integrin and calcium ion channels [51], the exact underlying mechanotransduction mechanism is not completely understood yet.

Herein we propose a magnetic scaffold-free 3D approach with mechanical stimulation as an alternative strategy to the aforementioned methods.

## 4.2 Material and methods

### 4.2.1 The magnetic stretcher device

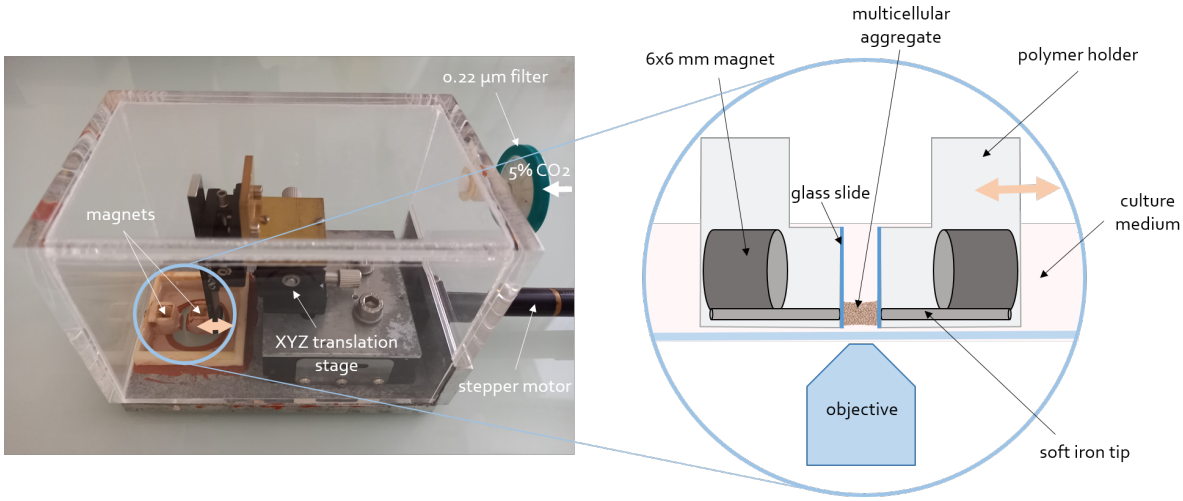


**Figure 4.4 The magnetic stretcher device.** Illustrative image and schematics of the magnetic stretcher set-up.

In order to stimulate mechanically 3D multicellular aggregates, the magnetic stretcher device was developed by Vicard Du, a PhD student in the group from 2011 to 2015 to drive the differentiation of embryonic stem cells (ESC) towards the mesodermal cardiac pathway thanks to a cyclic stimulation [32], but resulting with no specific structural organization. The idea behind my thesis was to modify this set-up to adapt it to muscle differentiation from myoblasts not only to induce their fusion and differentiation but also to drive their 3D long-range organization and alignment. For this project, we selected the murine myoblast C2C12 cell line (CRL-1772, ATCC) as the most widely used model for muscle differentiation studies.

The magnetic stretcher device shown in Figure 4.4 for live bright field imaging is composed of two 3D printed polymer holders (PA2200, polyamide). Each of them contains a 6 x 6 mm permanent neodymium magnet (530 mT at the surface and 170 T/m magnetic field gradient, S-06-06-N, Supermagnete) in contact with a cylindrical soft iron tip (iron content higher than 95%). The microtips, covered with a pasted glass slide, attract the magnetic cells which enables the formation of a cohesive multicellular aggregate held between the two pieces. Magnetic forces being proportional to the magnetic field gradient, forces are high close to the microtips ($f_v = M_v \times grad(B)$). They therefore act as magnetic clamps holding the multicellular aggregate as described in Du et al. [32]. One piece of the magnetic stretcher is fixed while the other can be moved by a stepper motor (Z812B,

Thorlabs) actuated by a controller (KDC101 or TDC001, Thorlabs). Once the cohesive aggregate is formed, it can be stimulated mechanically by displacing the mobile piece with the desired stimulation pattern. Temperature in the device is regulated at 37°C (incubation chamber, Digital Pixel). $CO_2$ is regulated by adding 10 mM HEPES to the medium or by flowing humidified air at 5% $CO_2$ (8920, Messer).

To perform in-depth imaging and observe the cell organization in the core of the aggregate, we had to adapt our set-up on the 2-photon upright microscopes we used (Leica SP5 and SP8). In close collaboration with the laboratory's mechanic workshop (Laurent Réa and Mathieu Receveur) and Thierry Savy, we designed and constructed a magnetic stretcher device that could fit under the 2-photon microscopes while enabling the temperature and the atmosphere regulation at 37°C, 5% $CO_2$. In comparison to the device for bright field microscopy, the pieces are flipped up side down to allow observation with an immersion objective. The tank is made of anodized stainless steal and a heating and temperature probes are inserted to ensure temperature regulation (see appendix C). Finally, humidity and $CO_2$ are regulated by flowing humidified air at 5% $CO_2$ (8920, Messer).

In order to form a cohesive myoblast aggregate that could be mechanically stimulated, the experimental device and the experimental conditions had to be optimized. To avoid the detachment upon formation or the tearing of the aggregate, we optimized various parameters for instance the soft iron tip diameter and shape, the initial cell number and distance between pieces, the aggregate formation method and the stretching conditions.

### 4.2.2 Optimization of the experimental conditions to generate a stretchable cohesive myoblast aggregate

#### Simulation of the magnetic field

To characterize and optimize the magnetic stretcher set-up, the magnetic field was simulated thanks to the finite element COMSOL MultiPhysics software (trial license and additional module AC/DC). The aim was to identify the important parameters to obtain the most interesting magnetic field gradient distribution for our application. Indeed, having a high magnetic field gradient and therefore a high magnetic force at the tip of each part of the magnetic stretcher could prevent the detachment of the aggregate during the experiment. First, to improve the set-up, two main parameters were studied: the diameter of the needle and its shape. Then, the magnetic field gradient was simulated to characterize the magnetic stretcher set-up for the most relevant configuration selected.

One single part of the magnetic stretcher is modeled by a permanent 6 x 6 mm neodymium magnet (remanent flux density of 1.38 T) in contact with a 9 mm-long soft iron needle, and the whole is enclosed in a cylinder of water. A second cylinder of water is visible at the tip of the needle, the region of interest, where the mesh is finer for the finite element computations (Figure 4.5 a).

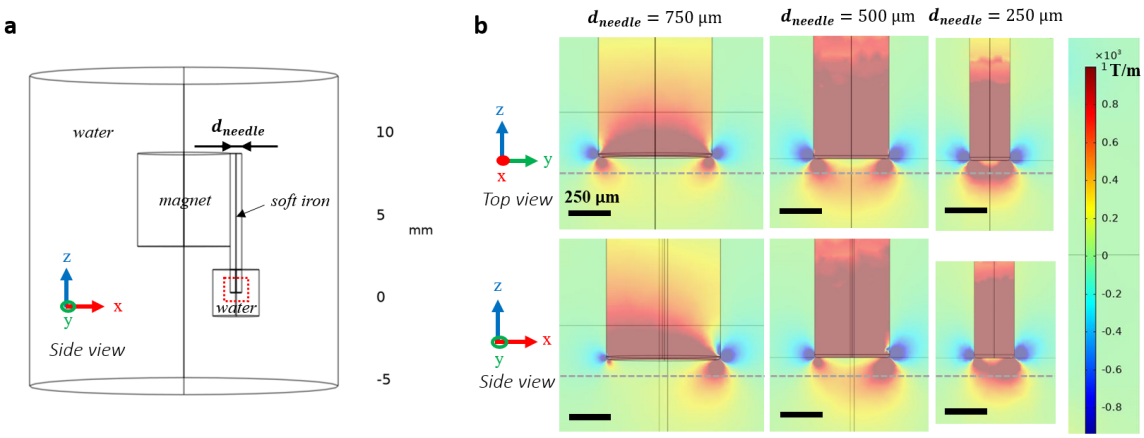


**Figure 4.5 Influence of the tip diameter on the magnetic field gradient generated.** **a)** Configuration used for the simulation of the magnetic field on one side of the magnetic stretcher. The needle in contact with the magnet is made of soft iron and the surrounding media is made of water. The external cylinder indicates the edges of the simulation where the boundary conditions are applied. A second black cylinder is visible around the tip corresponding to the location where the finite element mesh was refined. In red is the part presented in (b). **b)** 2D mapping of the simulated magnetic field gradient at the center of the tip for a tip diameter of 750, 500 or 250 µm, plane (yz) (top view) and plane (xz) (side view). The magnetic field gradient represented is $\frac{dB_z}{dz}$ which corresponds to the component involved in the magnetic force in the z direction. In gray is represented the position of a #0 glass slide of about 100 µm that would be glued on the tip before depositing the cells.

We first studied the influence of the needle diameter $d_{needle}$ on the magnetic field gradient for one single part of the magnetic stretcher with a soft iron tip diameter varying from 250 µm to 750 µm (diameter used in the previous set-up) (Figure 4.5 b). In all figures, the magnetic field gradient represented is $\frac{dB_z}{dz}$ which corresponds to the magnetic force component applied to the cells in the z direction. As expected, we observe that the magnetic field gradient is very high close to the tip but sharply decreases as the distance from the tip increases. Moreover the smaller the tip diameter is, the higher and the more homogeneous the magnetic field gradient is, pointing towards a diameter tip as small as possible for our application (Figure 4.5 b). 100 µm away from the middle of the tip, the magnetic field gradient generated by a 750 µm, 500 µm or 250 µm diameter tip is respectively about 200 T/m, 400 T/m and 1000 T/m (see appendix A Figure A.3 for the detailed quantification). From the side view images (Figure 4.5 b bottom), we also notice

that there is a stronger asymmetry of the magnetic field gradient with larger tips. A gray dashed line is added to materialize the position of a #0 glass slide (100 µm thickness) glued on the tip. The accessible part for the cells deposited is below this gray line for each image. The choice of the glass slide thickness is crucial to maximize the magnetic field gradient applied to the cells close to the tip and that is why we chose glass slides with the smallest thickness available.

We then evaluated the effect of changing the shape of the cylindrical soft iron tip to a sharper tip. Figure 4.6 presents the studied geometry corresponding to a needle of initial diameter 750 µm and a final tip diameter of 500 or 250 µm after a linear decrease on 2.5 mm. We then compared the resulting magnetic field gradients for a needle with a constant diameter to a needle with a truncated conical shape with the same final diameter. We observe that both on top and side views, the magnetic field gradient distributions are similar for needles having the same final tip diameter. Therefore, it seems that the shape does not significantly influence the magnetic field gradient. The most relevant parameter to optimize the gradient is thus the tip diameter. Since it is easier to obtain soft iron wires with a constant diameter than to design it with a precise shape, the configuration with a constant diameter was selected for the following work.

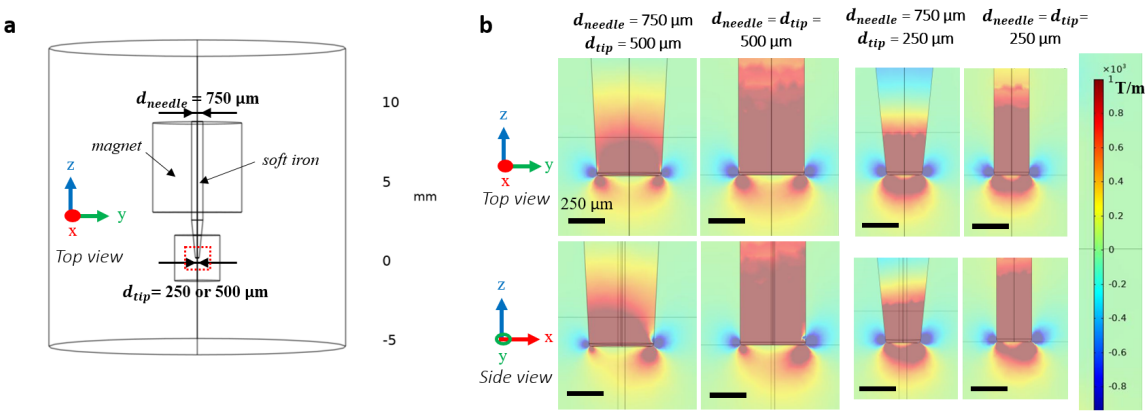


**Figure 4.6 Impact of the shape of the soft iron piece on the magnetic field gradient generated.** **a)** Configuration used for the simulation of the magnetic field for one part of the magnetic stretcher with a constant needle diameter of 750 µm decreasing linearly on 2.5 mm to a 500 or 250 µm tip diameter. The region of interest presented in (b) is shown in red. **b)** 2D mapping of the simulated magnetic field gradient at the center of the needle for a truncated cone with a final tip diameter of 500 µm and 250 µm compared to a needle with the same constant diameter. Top (yz) and side (xz) views.

We tested experimentally the two configurations with 250 or 500 µm diameter soft iron tips that offered the highest magnetic field gradients. While the 500 µm diameter configuration, allowed to obtain stable aggregates between the two pieces, aggregates formed

between the 250 µm diameter tips did not allow for the formation of a cohesive aggregate in a reproducible manner. A diameter of 500 µm for the soft iron tips was therefore chosen and we simulated the magnetic field gradient in the magnetic stretcher device in this configuration (Figure 4.7). While the magnetic field gradient and therefore the applied magnetic force is maximal close to the tips, it is close to zero in the central part between the two pieces where the majority of cells will be located (for a detailed quantification see appendix A Figure A.4 and A.5). Magnetic forces therefore act as clamps at the level of the tips holding the aggregate between the two pieces, as also evidenced from velocity field measurements representative of the strain field upon stretching in Du et al. [32].

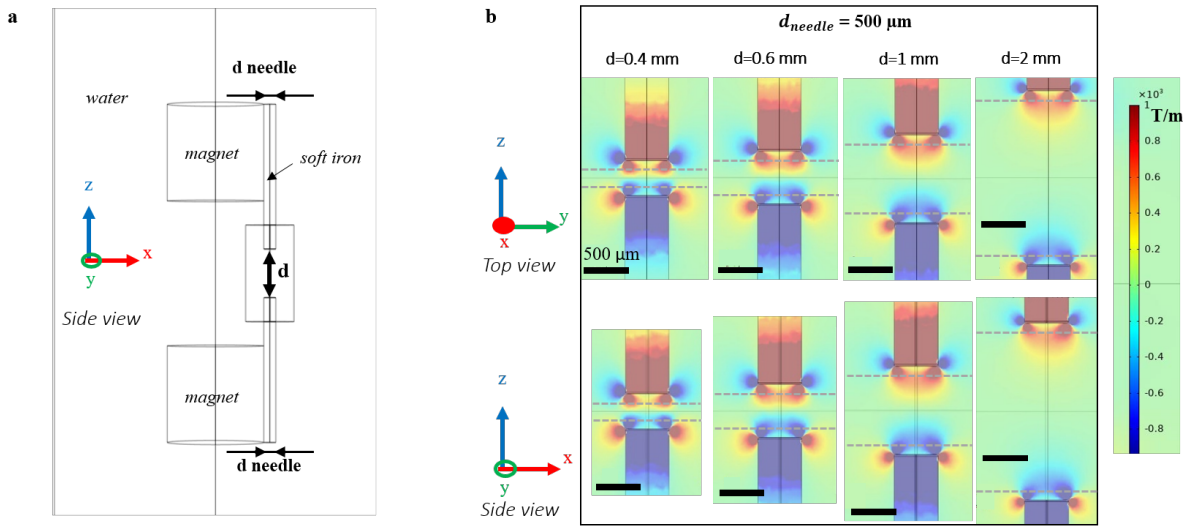


**Figure 4.7 Magnetic field gradient simulated in the configuration of the magnetic stretcher.** **a)** Schematics of the magnetic stretcher composed of two identical pieces at a distance d modeled by a permanent 6 x 6 neodymium magnet in contact with a 500 µm diameter soft iron tip. **b)** 2D mapping of the simulated magnetic field gradient at the center of the tips, for different distances d between the two parts of the magnetic stretcher. Top (yz) and side (xz) views.

### Cell number deposited and initial distance of the two pieces

Various numbers of cells can be deposited between the two pieces of the magnetic stretcher for the aggregate formation, offering a range of accessible conditions. However, for each amount of cells, the initial distance between the two pieces is comprised between two limit values. Indeed, if the distance is too large the aggregate will form and then retract from one of the two pieces as shown on the overnight formation Figure 4.8 a. If the distance is too small, the formed aggregate after one day in the magnetic stretcher will round up decreasing the area of contact with the glass slides and increasing the probability to detach upon stretching (Figure 4.8 b). Therefore, for each number of cells deposited, there is a need to finely tune the initial distance between pieces to achieve the formation of a stretchable cohesive aggregate.

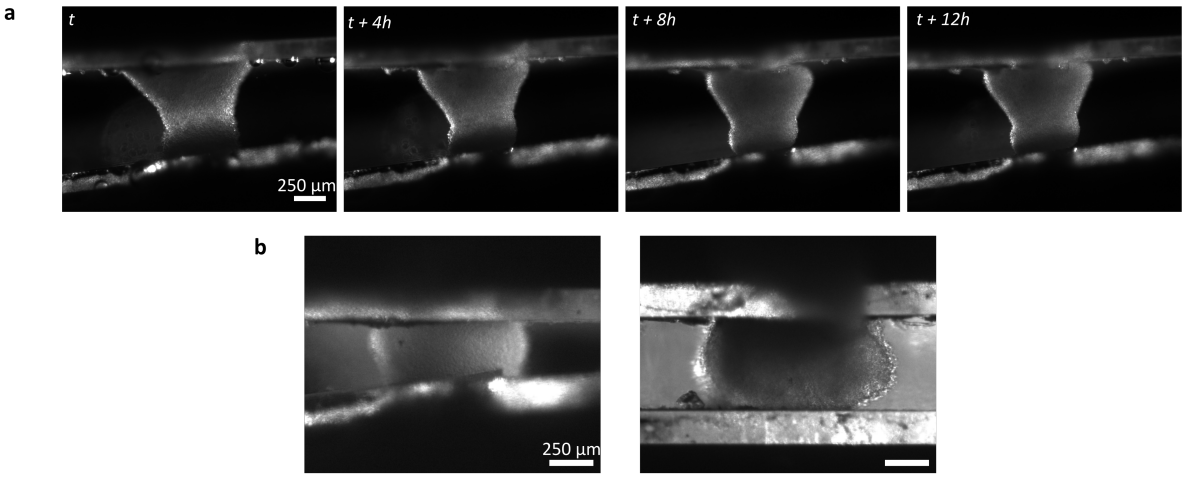


**Figure 4.8 Influence of the initial distance on the aggregate formation.** **a)** Bright field images of an experimental condition where pieces are too far away during the overnight formation of the aggregate. The multicellular aggregate retracts and starts to detach from the upper piece within a few hours. **b)** Two illustrative bright field image examples of aggregates at day 1 after the overnight formation where the pieces were too close initially. The resulting aggregate is convex increasing the probability of detachment under stretching.

### Aggregate formation methods

To obtain a reproducible stretchable aggregate after the overnight formation, we first tried to form the aggregate by depositing the magnetic cells on one single piece of the magnetic stretcher. Cells were first deposited on one piece forming a dome of non cohesive cells. They were then attracted by the second microtip by approaching the second piece as shown in Figure 4.9 a-b. Examples of resulting aggregates at day 1 for various cell

numbers deposited are shown in Figure 4.9 c. With this asymmetric way of depositing the cells, the aggregate shape at day 1 was not reproducible. Moreover it often led to asymmetric shapes that favor the retraction and the detachment of the aggregate.

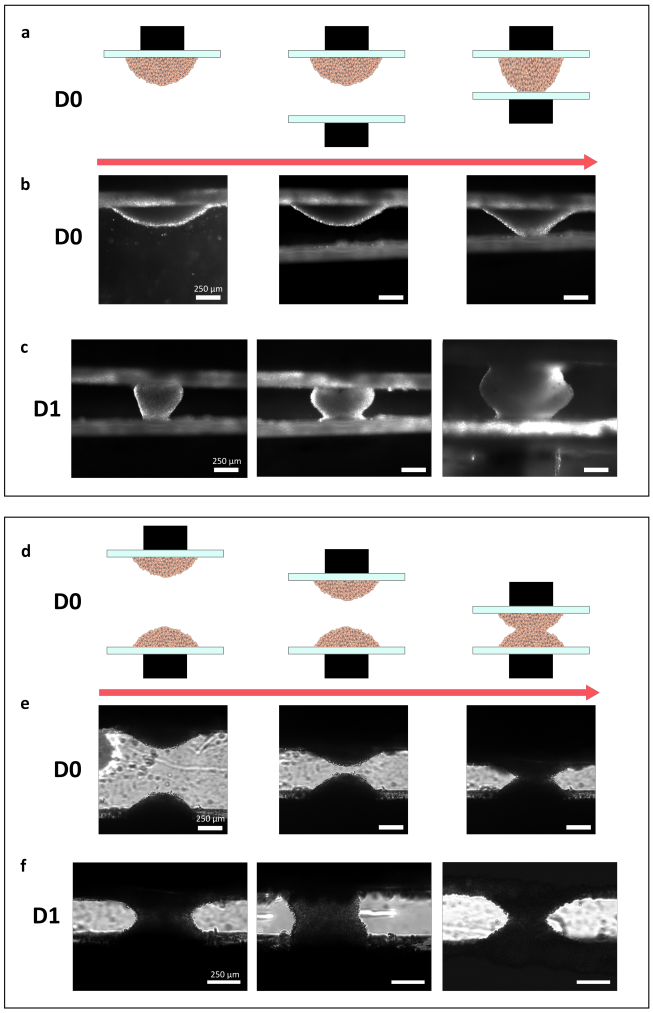


**Figure 4.9 Aggregate formation between the two magnetic pieces.** **a-b)** Schematics and representative bright field images of aggregate formation at day 0 by cell deposition on one magnetic piece. Magnetic cells are deposited on the top piece forming a non cohesive dome of cells. Cells are then attracted to the second piece upon its approach. **c)** Examples of resulting aggregates obtained at day 1 with an increasing initial number of cells (from left to right). The obtained aggregates have shapes varying from one experiment to the other and are often asymmetric. Credit for these illustrative pictures to Gaëtan Mary. **d-e)** Schematics and representative bright field images of aggregate formation at day 0 by cell deposition on two magnetic pieces. Magnetic cells are deposited on both pieces forming two non cohesive domes of cells that are approached and put into contact. **f)** Examples of resulting aggregates obtained at day 1 (about 10h after cell deposition) from an initial number of 100k cells. The obtained aggregates are symmetric and their shape is more reproducible between experiments.

An alternative way of cell deposition was set up by putting cells on both pieces in a symmetric manner. As in the first technique, the two magnetic pieces were approached

and the two domes of non cohesive cells were put in contact as shown Figure 4.9 d-e. This formation method leads to much more reproducible aggregates at day 1 than the formation by deposition on one single piece as shown Figure 4.9 f. We therefore selected this method of deposition to generate stretchable multicellular aggregates.

### Aggregate stretching

Once the cohesive multicellular aggregate is formed between the magnets, it can be linearly stretched by moving the mobile piece actuated by a step-by-step motor. We optimized the stretching parameters in order to stretch the aggregate without any detachment or tearing. Indeed, if the aggregate is stretched too early, for example only a few hours after cell deposition as shown Figure 4.10 a, it is very likely to detach from one of the two pieces. Besides, the stretching speed needs to be adjusted in order to be propagated to the whole aggregate and drive the cell alignment without inducing a tearing of the aggregate by stretching too fast as exemplified in Figure 4.10 b.

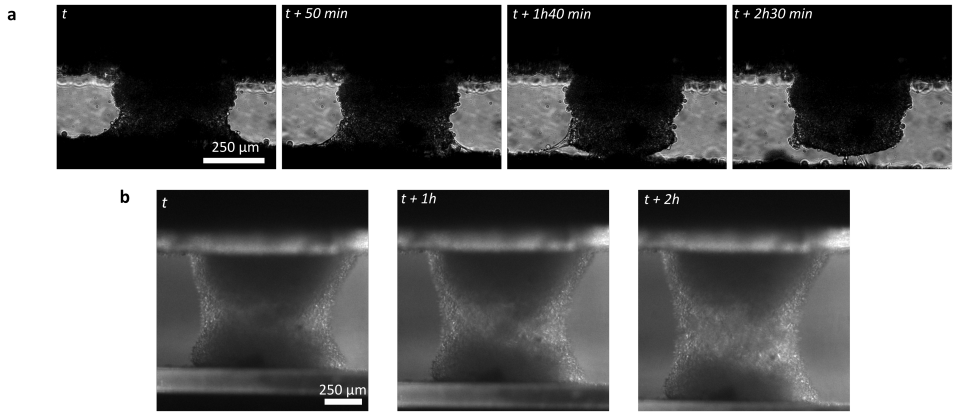


**Figure 4.10 Effect of the stretching timing and speed.** **a)** Illustrative bright field images of an experiment where the aggregate was stretched at 40 µm/h too early, only 7 hours after cell deposition. The aggregate detaches from the bottom magnetic piece within 2 hours. **b)** Bright field images of an extreme example where a cohesive aggregate is stretched at a very fast speed of 120 µm/h for 2 hours at day 1 leading to the tearing of the aggregate in its middle.

Even if the whole phase space of parameters was not explored, experimental conditions that enabled the formation of cohesive stretchable aggregates of about 100k cells were identified. For the continuation of the work, we fixed the following conditions (see Figure 4.9 d-f):

- Microtips of 500 µm diameter
- Initial symmetric deposition of cells on the two pieces (50k to 75k cells per microtip)

- Initial distance between the pieces of 350 to 400 µm (distance between the two glass slides)

In order to drive the alignment and the differentiation of myoblasts, we stretched the aggregate at day 1 at 20 µm/h for 6 hours.

### 4.2.3 Generation of fluorescent stable cell lines

To observe the cell 3D organization in live using 2-photon microscopy that allows in-depth imaging of tissues, we constructed stable C2C12 fluorescent cell lines.

To observe actin structures, we transfected cells with a puromycin Lifeact-GFP plasmid (pLVX-LifeAct-GFPtag2, gift from S. Coscoy) to generate a stable cell line. After antibiotic selection, sorting and amplification, fluorescence and differentiation ability were assessed. All Lifeact-GFP clones were fluorescent but only a few were still able to differentiate with the same phenotype as wild-type myoblasts. We selected one of these clones that we used in the following work and that will be referred to as the C2C12 Lifeact-GFP cell line.

In more details, the C2C12 Lifeact-GFP stable cell line was generated by transfecting the myoblasts with the puromycin Lifeact-GFP plasmid with Lipofectamine3000 reagents (L3000001, Invitrogen). Cells around 50 % confluency in 6-well plates were incubated with a 1:1 DNA to Lipofectamine 3000 Reagent ratio for 24 hours. Cells were then transferred in T-75 flasks, amplified and selected in complete medium supplemented with 2 µg/mL puromycin for 8 days. Cells were sorted by fluorescence-activated cell sorting (FACS Aria Fusion, BD Biosciences) and the 10% of cells with the highest fluorescence were dispensed at one cell per well in 96-well plates to obtain individual clone cell lines after amplification. 28 different colonies were obtained and after 2-3 weeks of amplification, 14 clones with a normal proliferation speed were obtained. All the 14 clones were expressing a similar level of Lifeact-GFP (Figure 4.11 a) but only a few were still able to differentiate. The selected clone shows a differentiation phenotype similar to that of C2C12 wild-type cells (Figure 4.11 b).

The C2C12 Lifeact-GFP multicellular aggregates in the magnetic stretcher were imaged in live thanks to an SP5 or SP8 Leica microscope coupled with a tunable wavelength laser (Mai Tai or Insight DeepSee, SpectraPhysics). All images were taken with a 20x water immersion objective (HCX APO L20X/1.00 W, Leica) at 900 or 980 nm. To do some high resolution imaging, stretched aggregates were fixed *in situ* then retrieved with a micropipette. 3D samples were then imaged by confocal microscopy thanks to an LSM

780 Zeiss microscope and with a 20x water immersion objective (W Plan-Apochromat 20x/1.0 DIC, Zeiss).

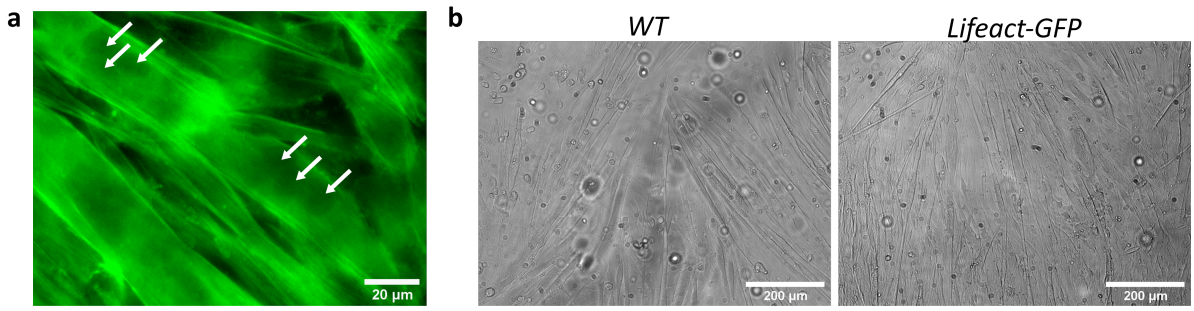


**Figure 4.11 The C2C12 Lifeact-GFP cell line.** **a)** Fluorescence image of C2C12 Lifeact-GFP after 3 days of differentiation in 2D. Actin is shown in green and nuclei are evidenced with white arrows. Polynucleated myotubes are visible. **b)** C2C12 WT vs C2C12 Lifeact-GFP cells after 3 days of differentiation in 2D. Both cell lines show a similar differentiation phenotype according to the myotubes length, width and density.

### 4.2.4 Comparison with 3D spheroids

To highlight the importance of mechanical stimulation in skeletal muscle differentiation and to avoid dimensionality issues, we compared the stretched multicellular aggregates to unstretched ones. For the control condition, we formed spheroids by magnetic molding with a size equivalent to the stretched aggregates (see appendix C for spheroid formation).

### 4.2.5 Myogenic differentiation read-outs

To study skeletal muscle differentiation, we looked at several read-outs at different levels to assess the differentiation and the organization of our microtissues. We focused on: (i) cell organization looking at cytoskeleton architecture, (ii) gene and protein expression.

#### Actin filament orientation extraction

Actin filament orientation of multicellular aggregates from the magnetic stretcher or control spheroids was extracted thanks to ImageJ and the plug-in OrientationJ (Biomedical Imaging Group, Ecole Polytechnique Federale de Lausanne, Switzerland) [148] from either live 2-photon microscopy images or confocal images on fixed samples. The "Analysis" and "Distribution" functions, used to obtain the orientation maps and the angle

distributions respectively, were applied with a local window of 2 pixels and with the gaussian gradient. Orientation of actin filaments was assessed on images located at 50 $\mu$m below the surface of the spheroid or of the aggregate from the magnetic stretcher. The quantification was done on the entire image for control spheroids and on the central part of the magnetic stretcher aggregate to get rid of artefacts due to the aggregate shape.

### Gene and protein expression

We performed both mRNA and protein level quantification to compare myogenic differentiation between control unstretched spheroids and stretched aggregates. RT-qPCR is a sensitive technique to precisely and quantitatively compare the mRNA level of selected genes. This technique is based on the amplification of an identified sequence in RNA from cell extracts. With the help of Nathalie Luciani, we designed the primer sequences of genes identified as essential in myogenesis: Myod1, Myog, Myf6, Tnnt1, Tnnt3, Myh1, Myh3, Myh4 and Ckm (sequences in appendix C Figure C.2). All these genes are known to be upregulated during skeletal muscle differentiation (cf Figure 4.1). The RPLP0 coding for the 60S acidic ribosomal protein P0 was chosen as a reference transcript. mRNA expression levels were measured for control spheroids and stretched aggregates from up to 8 independent experiments and 11 samples for each condition.

Protein quantification of the late differentiation markers Myf6 and MHC were performed by Western Blot to compare protein levels from control spheroids and stretched aggregates, to complement the mRNA measurements. This technique based on protein immunoblotting after electrophoresis is less sensitive than RT-qPCR but measures directly the level of protein expression. Detailed protocols for mRNA and protein quantification are described in appendix C.

## 4.3 Results and discussion: A magnetic stretcher for the 3D organization and differentiation of myoblasts

### 4.3.1 Iron oxide nanoparticle uptake does not impair the metabolic activity of myoblasts or their differentiation potential

First of all, we checked that the incorporation of iron oxide nanoparticles (NP) into the mouse muscle precursor cells does not impair their metabolic activity and ability to differentiate. C2C12 Lifeact-GFP cells were magnetically labelled leading to an uptake of about 3 pg of iron per cell (measured by magnetophoresis). The influence of the NP uptake on the metabolic activity of cells was first evaluated thanks to a resazurin-based assay, showing no difference in comparison with control cells after NP incorporation at day 0 and at day 1 (Figure 4.12 a). Besides, differentiation tests were performed after NP incorporation showing no phenotypic difference on the myotubes formation. Figure 4.12 b shows representative images of cells after 7 days of differentiation. Both in the control condition and with the incorporation of nanoparticles at day 0, long myotubes are obtained. These elongated polynucleated cells express myosin heavy chain, a marker of myogenic differentiation involved in the contraction of functional muscular cells, in both control and NP conditions after 3 days of differentiation (Figure 4.12 c).

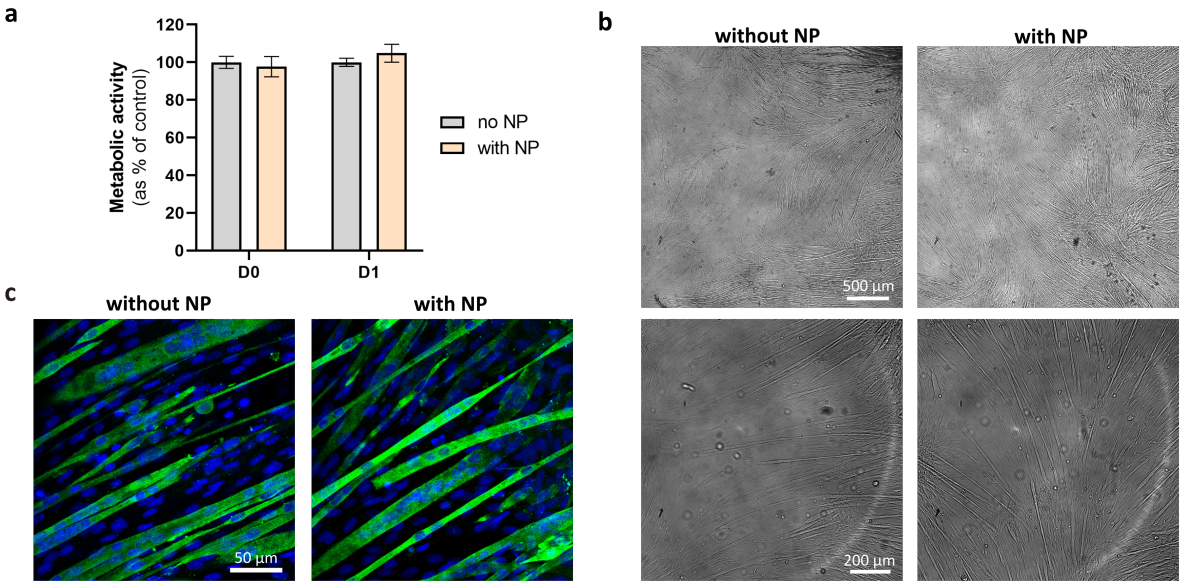


**Figure 4.12 Nanoparticle incorporation in myoblasts does not impair their metabolic activity or their ability to differentiate.** **a)** Metabolic activity of C2C12 Lifeact-GFP cells with or without nanoparticle (NP) 2 hours (D0) or one day (D1) after the incorporation ([Fe] = 2 mM for 30 min). Mean +/- SD (quadruplicates). **b)** Representative images of C2C12 Lifeact-GFP after 7 days of differentiation with or without NP incorporation at day 0. Long myotubes are visible in the entire field of view in both conditions. **c)** Immunofluorescence representative images of C2C12 Lifeact-GFP after 3 days of differentiation and incorporation of NP at day 0. MHC and nuclei are shown in green and blue respectively.

Finally, NP incorporation decreases slightly mRNA levels for all genes related to myogenic differentiation at day 1 after NP incorporation, probably due to the upregulation of genes involved in NP uptake and storage such as ferritin [42]. However, the same mRNA levels of the myogenic marker genes are recovered with or without NP incorporation for most genes at day 3 and for all genes at day 7 of differentiation (cf Figure 4.13). In conclusion, NP uptake does not alter significantly the cell metabolic activity or the ability of cell to differentiate at medium (3 days) and long term (7 days).

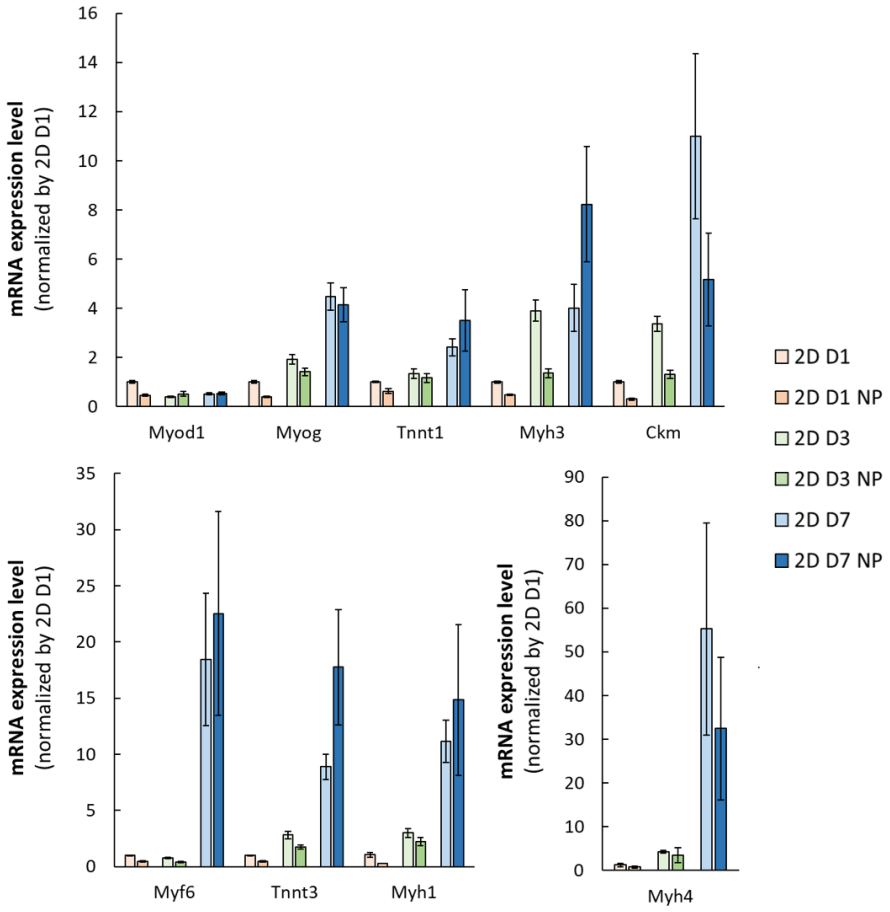


**Figure 4.13 mRNA expression levels measured by RT-PCR for 2D cultures with or without NP incorporation and after 1, 3 or 7 days of differentiation.** Expression levels are normalised by the mRNA levels at day 1 without NP incorporation (2D D1). RPLP0 was used as a housekeeping gene. Mean +/- SEM (quadruplicates).

### 4.3.2 Stretchable microtissues are formed thanks to the magnetic stretcher

As described section 4.2 and in order to generate cohesive and stretchable 3D multicellular aggregates, magnetically labelled cells were deposited in between two micromagnets (Figure 4.14 a). Magnetic forces enable the formation of the multicellular aggregate with no support matrix and act as clamps (magnetic forces about a few hundreds of pN close to the glass slides) holding the aggregate once it is cohesive (Figure 4.14 b-c).

Figure 4.14 d-e presents the procedure to form the cohesive aggregate between the two magnetic stretcher pieces. About 75k magnetically labelled cells are deposited on each piece forming a dome of non cohesive cells at day 0. The two pieces are then approached

(at a distance of 350 to 400 $\mu$m between the glass slides) and the two hemispheres are put in contact. After an overnight incubation, a cohesive aggregate is formed. The magnetic stretcher therefore allows the formation of stretchable microtissues with an aspect ratio controlled by the initial number of cells and the distance between tips. The overall shape obtained at short times is reminiscent of the one taken by a drop of fluid between two plates (catenoid and derivatives), implying that tissue surface tension plays an important role at that stage.

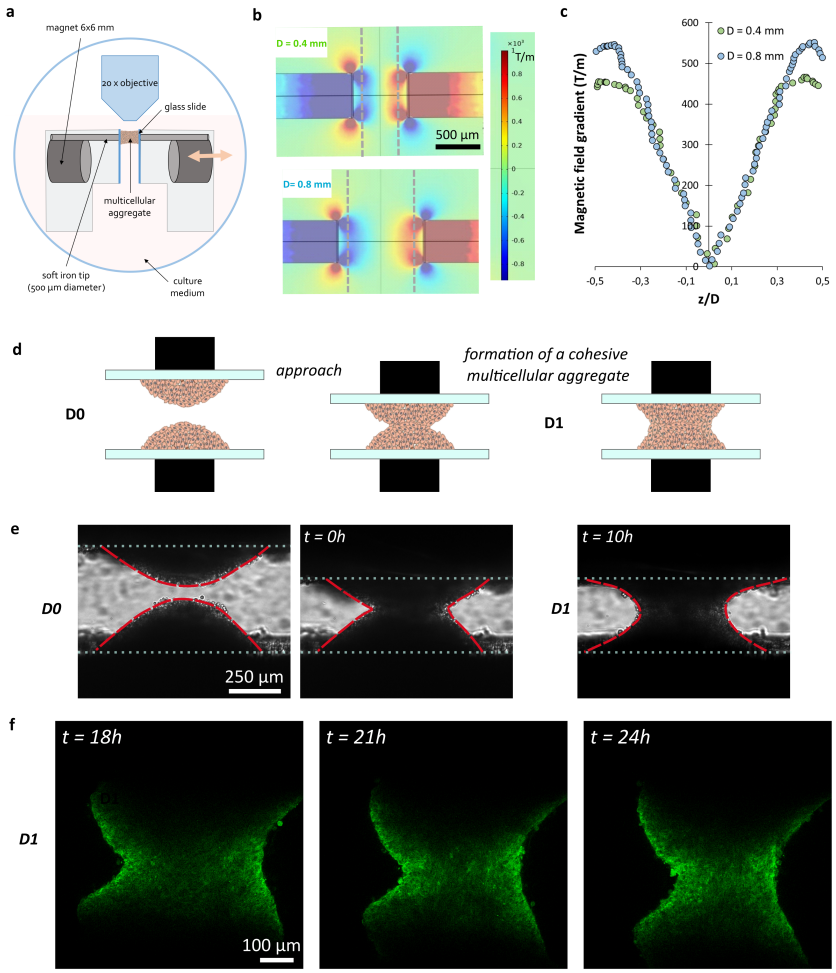


**Figure 4.14** **Microtissue formation and stretching in the magnetic stretcher device.** **a)** Schematics of the magnetic stretcher device. **b)** Simulation of the magnetic field gradient in the magnetic stretcher at the center of the tips and for a distance between glass slides of D = 0.4 mm or 0.8 mm. Glass slide positions are materialized with gray dashed lines. **c)** Magnetic field gradient simulated between the two pieces as a function of the position z and normalized by the distance D between the two glass slides for a distance of 0.4 mm or 0.8 mm. **d-e)** Schematics and representative images of the formation of a cohesive multicellular aggregate in the magnetic stretcher. First, magnetic cells in suspension are deposited on each micromagnet. Then, the two pieces are approached and a cohesive aggregate is formed overnight. **f)** Stretching of the multicellular aggregate at 20 µm/h for 6 hours after one day of aggregate formation in the magnetic stretcher.

While the aggregate formation is carried out in complete medium, the medium is changed to differentiation medium (2% Horse Serum) once the aggregate is cohesive at that day 1 time. A linear stretch of 20 µm/h for 6 hours is then started to mechanically stimulate and stretch the 3D structure as represented Figure 4.14 f in order to drive cell alignment and differentiation. The multicellular aggregate is then kept in the magnetic stretcher for 48 hours (day 2 and day 3).

### 4.3.3 The magnetic stretcher promotes actin alignment

To evaluate the 3D organization of multicellular aggregates, actin filament orientation was imaged, at day 1 and 2, in aggregates formed in the magnetic stretcher and compared to control 3D spheroids that were formed simultaneously. Figure 4.15 a shows actin representative images of control spheroids and aggregates in the magnetic stretcher at day 1 and 2 at 50 µm depth. By extracting the actin filament orientation through OrientationJ [148], we built orientation maps for each control spheroid and aggregate in the magnetic stretcher (Figure 4.15 a-b) and determined the angle distribution of actin filaments for each condition. The average angle distributions are represented in Figure 4.15c. While the actin filament orientation for control spheroids is uniform, we observe a peaked distribution in the case of the aggregates in the magnetic stretcher. Most filaments are oriented perpendicularly to the glass slides and in the direction of the stretch as it is clearly visible in the representative orientation maps shown (Figure 4.15 a-b). At day 2, the angle distribution is sharper than at day 1 for the aggregates in the magnetic stretcher. The magnetic stretcher therefore seems to drive alignment of actin filaments and cells in 3D in the direction of the stretching in the core of the aggregate. Interestingly, for the aggregates in the magnetic stretcher, the orientation of filaments at the surface of the aggregates (on a 20 $\mu$m thick enveloppe) are tilted at 70° from the orientation in the core of the aggregate, at 50 µm depth and below, as shown Figure 4.15 d-e. This suggests a spiral-like structure of cells surrounding the aggregate in the magnetic stretcher highly reminiscent of the spontaneous emergence of chiral actin structures observed by Ehrig et al. [149] who studied the growth of MC3T3 cells on curved PDMS 3D substrates. As for fibroblasts, myoblasts might preferentially choose a certain surface local curvature minimizing their bending explaining this tilting of cells on the surface of aggregates. Besides, some patches of actin filaments with similar orientations and about 50 µm wide were observed in control spheroids at day 2 as visible in Figure 4.15 a-b. In 2D, Mao et al. [150] observed that myofibers were forming bundles of same orientations of increasing size upon differentiation. In our case, the magnetic stretcher might take advantage of these bundles that seem to be also present in 3D and align them together in the direction

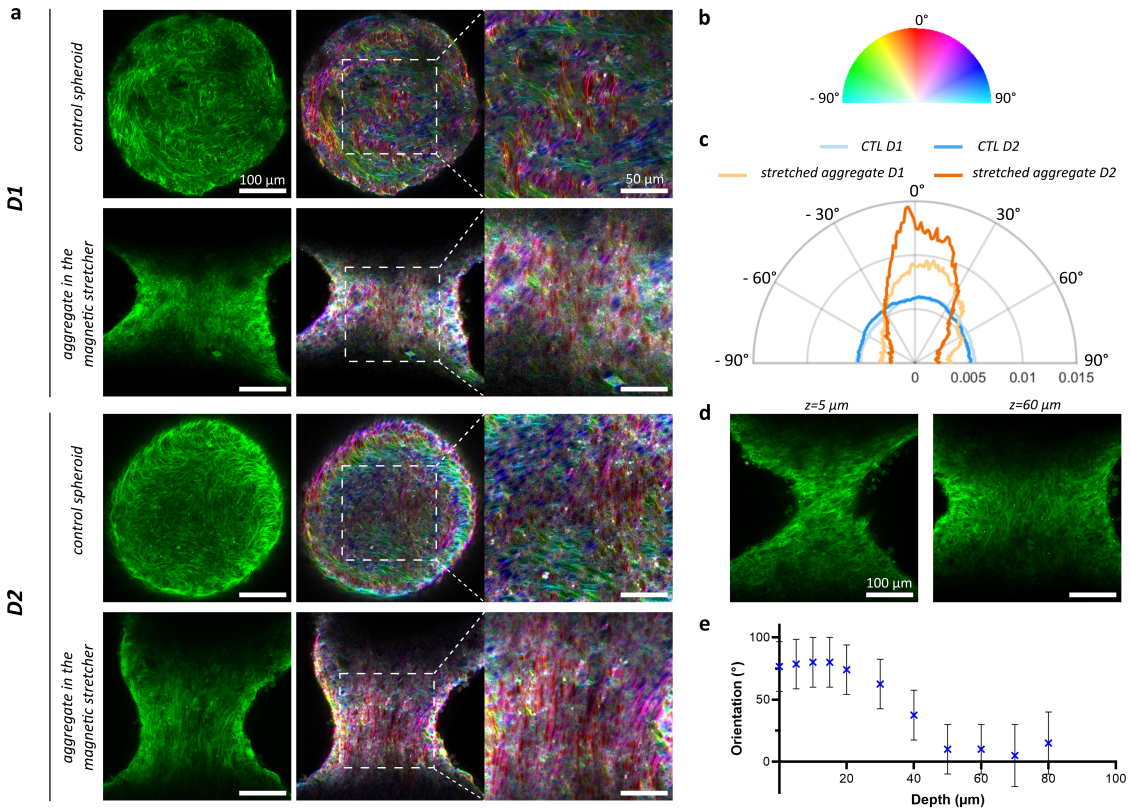


**Figure 4.15** **The magnetic stretcher drives the 3D alignement of actin filaments.** **a)** Left panel : representative images of C2C12 Lifeact-GFP control spheroids and stretched aggregates at day 1 (D1) and day 2 (D2) at about 50 µm depth. Actin is shown in green. Middle panel : corresponding images with filaments color coded according to their orientation. Right panel : zoom on the central area of the color coded orientation map. **b)** Color wheel of the orientation map. **c)** Angle distribution of actin filaments measured at 50 µm depth for control spheroids at day 1 (CTL D1) and day 2 (CTL D2) and for the aggregates in the magnetic stretcher at day 1 and day 2. A peaked distribution is observed for the stretched aggregate at day 2 in the direction of the stretching. N = 5 for control spheroids and N = 3 for aggregates in the magnetic stretcher. **d)** Representative images at 5 µm depth (left) and at 60 µm depth (right) of the aggregate in the magnetic stretcher at day 1 and before stretching. On the surface, actin filaments are oriented horizontally with a slight tilt, while in the core of the aggregate, they are oriented vertically. **e)** Orientation of the actin filaments as a function of depth for aggregate in the magnetic stretcher at day 1 and before stretching (N = 2).

of the stress and stretch, forming one unique bundle in the core of the aggregate. This size of a few tens of microns is close to the thickness of the enveloppe of C2C12 spheroids imaged after cryosection. It could represent a characteristic interaction length between cells. Stretching is thus able to orient cellular cytoskeleton to promote cell alignment but a peripheral region is influenced by interface issues. Tissue surface tension is also at stake to define the shape of stretched aggregates.

The 3D alignment of cell is probably due to two combined factors. First, the generation

of a tensed structure upon the aggregate formation in the magnetic stretcher, as shown Figure 4.14 e, seems to drive cell orientation since an anisotropic angle distribution is already visible at day 1 (cf Figure 4.15 a-c). This result is reminiscent of the analogous anisotropic boundary conditions obtained for microtissues formed between two cantilevers that drive actin alignment in the direction of stress [151]. Microtissues have also been formed with C2C12 cells evidencing an alignment in the stress direction and eventually a fusion of aligned myoblasts upon switching to differentiation medium [94]. While the microtissue technique requires the addition of an external matrix (collagen I and Matrigel) and provides thin constructs of only about 150 µm thick, we recover the same alignment effect in our matrix-free 3D system. Second, the stretching of the aggregate leads to a sharper angle distribution of actin filaments at day 2 in the core of the aggregate as visible Figure 4.15 a-c. This result is in line with uniaxial stimulations performed on 3D-scaffold skeletal constructs enhancing alignment of cells in the direction of the stretching [146]. Here again, we generated an alignment in a scaffold-free system where the stress is not applied to an exogenous substrate or matrix but directly to the cell themselves and potentially to their secreted ECM.

### 4.3.4 Myogenic differentiation is enhanced thanks to the magnetic stretcher

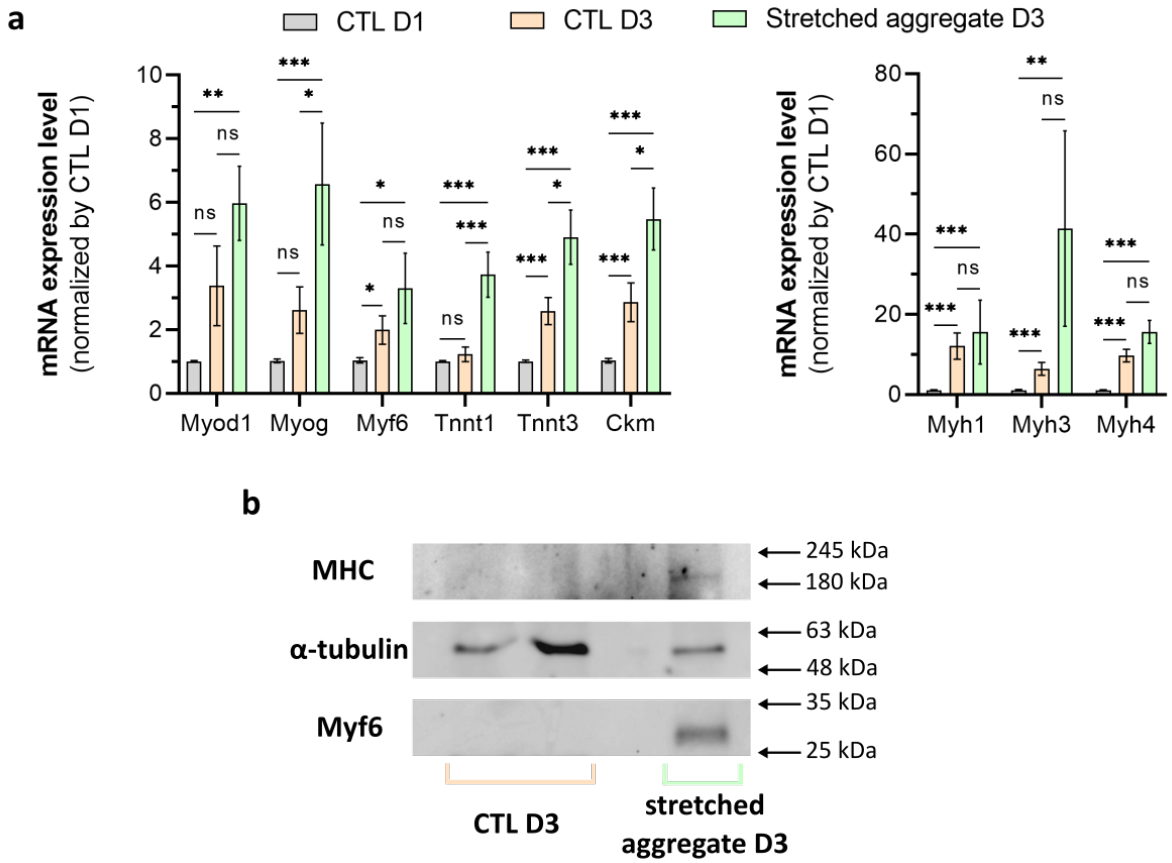


**Figure 4.16** **Differentiation towards the skeletal muscle is enhanced for stretched aggregates. a)** mRNA expression levels measured by RT-qPCR for control spheroids at day 1 and day 3, and for stretched aggregates at day 3. RPLP0 was used as a housekeeping gene. At least N = 11 for control spheroids, and 6 independent experiments and 4 to 8 independent experiments for stretched aggregates at day 3. Mean ± SEM. **b)** Western Blot of control spheroids and stretched aggregates at day 3 for MHC and Myf6. $\alpha$-tubulin is used as a loading control.

While individual C2C12 cells have a diameter of 18 ± 2 µm (mean ± SD), actin filaments in the core of the aggregate at day 2 were up to 150 µm long as visible Figure 4.15 a. This suggests that cells do not only align but also have started to differentiate and to fuse. Figure 4.16 a presents the RT-qPCR results measured for control spheroids at day 1 and 3 and stretched aggregates at day 3. The mRNA expression levels plotted are normalized by the mRNA levels of control spheroids at day 1. For the 9 genes studied, mRNA levels increased between day 1 and 3 for control spheroids evidencing the onset of differentiation towards the skeletal muscle thanks to the differentiation medium.

Interestingly, if we look at the Myh genes that are late differentiation markers, mRNA expression levels are higher for 3D control spheroids than cells in 2D at the same day of differentiation at day 3 (cf Figure 4.13), suggesting that the 3D environment favors myogenic differentiation. Now if we compare mRNA expression levels of control spheroids to stretched aggregates at day 3 we observe an upregulation for all genes demonstrating that the magnetic stretcher enhances differentiation towards the skeletal muscle.

These results were confirmed by comparing the protein levels from control spheroids and stretched aggregates at day 3 through Western Blot as shown Figure 4.16 b. We looked at the Myf6 and the MHC (myosin heavy chain) proteins that are known to be late differentiation markers [152]. While, MHC and Myf6 proteins are expressed in the case of the stretched aggregates, no signal was detected for control spheroids, evidencing that the magnetic stretcher enhances myogenic differentiation in comparison to control unstretched spheroids.

## 4.4 Conclusion and perspectives

With this study, we showed that stretching skeletal muscle precursor cells trapped between two magnets without a support matrix favors the 3D alignment of cells and the differentiation into muscular cells. This represents a first step to create skeletal muscle constructs reproducing its aligned structure with no need of an external matrix or substrate. Besides, the duration of the experiment should be highlighted since differentiation signals are obtained only after two days. Compared to conventional techniques, the speed of maturation is thus considerably accelerated. These results underline the potential of mechanical stress to produce functional tissues.

Experimental conditions now need to be optimized in order to reach longer maturation times up to 7 days, approximative time at which myotubes are able to contract. More complex mechanical stimulations instead of a simple linear stretch, such as cyclic stimulations, could also be tested to improve differentiation in this 3D tissue model. Finally, this first proof of concept has been obtained with the most widely used cell line for skeletal muscle tissue engineering but the strategy could be adapted to more biologically relevant cell types such as human satellite cells. This tool could also contribute in the long term to the understanding of muscle disease by comparing control cells to diseased cells giving rise to myopathies or for instance desminopathies (see chapter 2 section 2.2).

The magnetic stretcher device opens many perspectives for a better understanding of the muscle but also for the study of differentiation under mechanical constraint. For instance, mapping the distribution of forces in the multicellular aggregate under constraint would enable to assess how differentiation depends on force distribution. To that end, Nicolas Borghi (Institut Jacques Monod) developed FRET (Fluorescence Resonance Energy Transfer) nanosensors based on fluorescence transfer : cadherin-TS [153]. These cadherins comprising the FRET sensors can be expressed in the cells thanks to plasmid transfection. The signal of fluorescence transfer depends on the distance between two fluorophores separated by a section with a known spring stiffness. Thus, from the fluorescence signal and therefore the tension of force nanosensors, the force distribution can be deduced. By coupling these nanosensors with 2-photon microscopy, we would be able to obtain a 3D distribution of forces in the mechanically stretched aggregate and look at the correlation with the differentiation pattern. First tests have been performed by standard transfection (lipofection or electroporation) to obtain stable C2C12 cell lines expressing the cadherin-TS. However, the obtained fluorescence signals were too low, and an alternative strategy by CRISPR/Cas9 is now considered.

Having access to the 3D force distribution in multicellular aggregates would also be

very interesting in terms of tissue mechanics. One could imagine to apply more complex mechanical stimulations to the multicellular aggregate and dissect how corresponding mechanical stresses propagate in the 3D tissue model. Besides, adapting the set-up to measure the force exerted by the aggregate itself with a dynamometer coupled to the mobile piece of the magnetic stretcher would also be of high interest to evaluate the pulling force and eventually the contraction of the tissue model if higher degrees of maturation were obtained. Indeed, in some experiments, glass slides not glued properly to the micromagnets were detached by the multicellular aggregates, evidencing a pulling force.

The formation of the cohesive aggregate during the first day could also be investigated more thoroughly to provide information on the mechanical properties of the multicellular aggregate. Indeed, the shape of the multicellular aggregate can be fitted by analogy with a drop of liquid with a given surface tension between two parallel plates also called capillary bridge [154]. From the capillary bridge theory, the shape of the liquid depends on an dimensionless number $C = \frac{\Delta P r_m}{\gamma}$ with $\Delta P$ the pressure difference in and outside the liquid, $r_m$ the haunck/neck radius and $\gamma$ the surface tension [154]. With the additional information of the pulling force F, we could therefore extract the effective surface tension of the multicellular aggregate upon formation by fitting the aggregate profile (see Figure 4.17) and extracting the corresponding dimensionless number. This formalism might also help to explain the experimental conditions leading to a stable or unstable multicellular aggregate as described section 4.2.2.

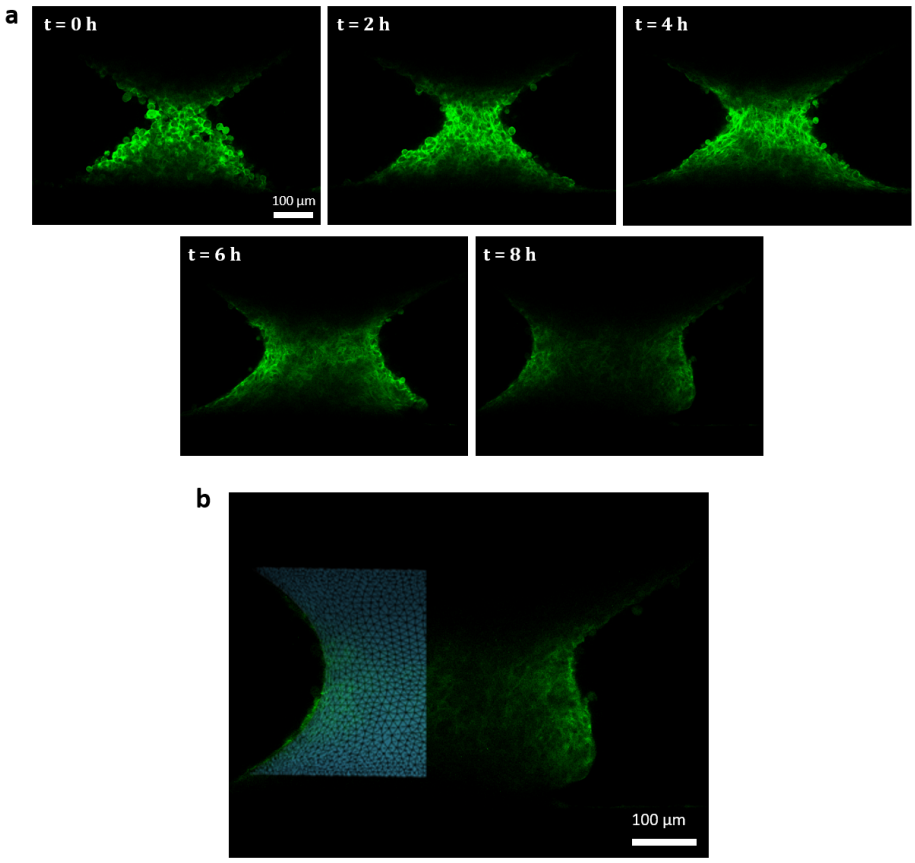


**Figure 4.17 Formation of the C2C12 cohesive multicellular aggregate during the first hours.** **a)** Representative images of the catenoid-like shaped cohesive multicellular aggregate formation. Actin is shown in green and images were taken every 2 hours at a constant depth. **b)** Cohesive aggregate formed after 8 hours with a superimposed simulation of a capillary bridge obtained with a finite element method (software Surface Evolver).

In conclusion, the magnetic stretcher is a promising tool for a wide range of applications, from tissue mechanics to cell differentiation under constraint or disease modelling. Overall, it should pave the way for a better understanding of the skeletal muscle and its differentiation.

# General conclusion

In this work, we took advantage of magnetic forces to apply external forces to tissue models and to remotely control cell organization. By incorporating superparamagnetic iron oxide nanoparticles to the cells, 3D tissue models of controlled shape and size and without any support matrix were formed and stimulated. This PhD is at the intersection between two major themes : tissue mechanics and tissue engineering of the skeletal muscle.

First, we focused on the macroscopic mechanical properties of these 3D tissue models and more specifically on the impact of microscopic properties of individual cells. Thanks to the magnetic signature of the tissue models, surface tension or Young's modulus were measured by flattening spheroids with a permanent magnet applying a constant magnetic field gradient. In a model of mouse muscle precursor cell spheroids, the role of intercellular adhesions and actin cytoskeleton structure and tension was investigated as well as the influence of the desmin intermediate filament network. While the mechanical role of intermediate filaments in biological tissues is still an open research question, our study evidenced the key role of desmin organization in the mechanics of this 3D muscle tissue model. Besides, we explored the interplay between tumor-related and mechanical properties in a model of human breast cancer cells through malignant transformation and EMT, suggesting that surface tension could act as a read-out of tumor aggressiveness and malignant transformation. Finally, magnetic rheometry, a magnetic approach developed in the team to probe the behavior of tissue models to a dynamical stimulation, was cross-validated with a novel microplate rheometer adapted to multicellular aggregates. These tools open new perspectives to investigate for instance ECM influence on mechanical properties of biological tissues by adapting the multicellular aggregate formation procedure or to conduct multiscale studies to explore rheology from the single-cell to the tissue scale.

Second, we developed a strategy to generate stretchable tissue models with no support matrix in the context of skeletal muscle tissue engineering. By using mouse muscle precursor cell multicellular aggregates formed and stretched between two micromagnets, we managed to induce an alignment of cells in the central part of the aggregate reminiscent of the muscle organization and to enhance myogenic differentiation in comparison to unstretched spheroids. The developed approach represents a first step to obtain reliable skeletal muscle constructs but is also a valuable tool for biophysical studies from cell deformation or tissue shape modelling under constraint to force distribution in 3D tissues.

In conclusion, this thesis investigated through magnetic approaches the mechanical properties of 3D tissue models and the differentiation under mechanical constraints aiming at a better understanding of the physics of complex biological tissues.

# Appendix A

# Simulation of the magnetic field

Magnetic field simulations were carried out with the software COMSOL Multiphysics (test trial) and the additional module AC/DC. For each configuration, the finite element problem was resolved with the following magnetostatics equations.

- Conservation of the magnetic flux:

  $\boldsymbol{\nabla}.\boldsymbol{B} = 0$

- Constitutive equations:

  **Water or air :** $\boldsymbol{B} = \mu_0\mu_r\boldsymbol{H}$ with $\mu_0$ the vacuum permitivity and $\mu_r$ the respective relative permitivity of water or air.

  **Neodymium magnet :**

  $\boldsymbol{B} = \mu_0\mu_r\boldsymbol{H} + \boldsymbol{B_r}$ with $\boldsymbol{B_r}$ the remanent flux density

  **Soft iron:**

  $\boldsymbol{B} = f(\mid \boldsymbol{H} \mid)\frac{\boldsymbol{H}}{\mid \boldsymbol{H} \mid}$ (see Figure A.1 for the BH curve)

- Boundary conditions:

  Magnetic isolation at the boundaries : $\boldsymbol{n}.\boldsymbol{B} = 0$

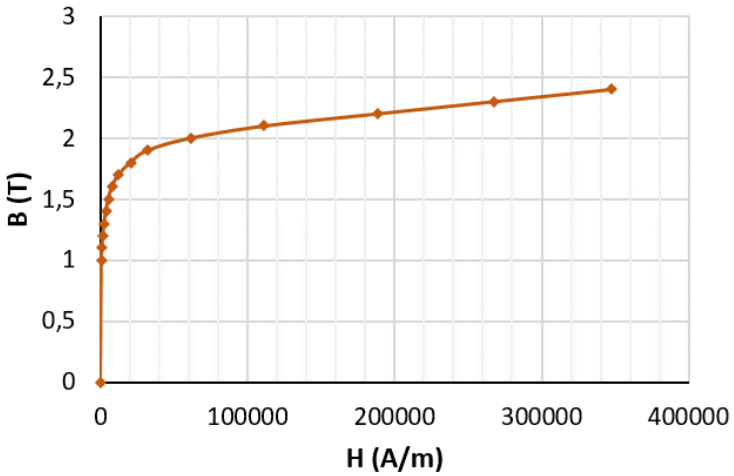


**Figure A.1 BH curve for soft iron used for the simulations in COMSOL Multiphysics.**

## A.1 Magnetic field gradient simulated for a permanent magnet

The magnetic field and the magnetic field gradient of a 6x6 mm permanent neodymium magnet immerged in water was simulated (Figure A.2 a) and compared to experimental data measured with a gaussmeter (Magnetometer Koshava5 Wuntronic) (Figure A.2 b). Experimental and simulated measurements are coherent and we measure an average magnetic field gradient of 170 T/m at a distance between 0.25 and 1.75 mm from the tip.

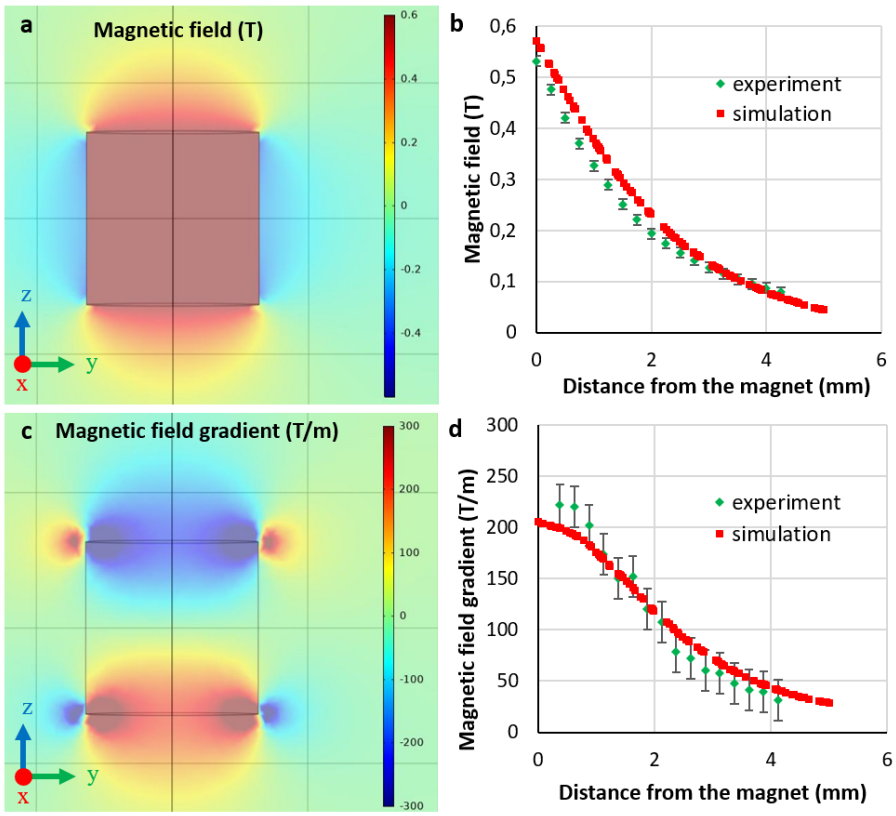


**Figure A.2 Simulated and experimental magnetic field and magnetic field gradient created by a 6x6 mm neodymium magnet.** **a-c)** 2D mapping of the simulated magnetic field and magnetic field gradient along the z axis. The yz plane cuts the magnet in its middle. **b-d)** Comparison between the simulated and experimental magnetic field measured with a gaussmeter and magnetic field gradient at the center of the magnet.

## A.2 Magnetic field gradient simulated in the magnetic stretcher device

One part of the magnetic stretcher is modeled by a 6x6 mm neodymium magnet in contact with a 9 mm long soft iron tip. Figure A.3 presents the quantification of the simulated magnetic field and magnetic field gradient (represented Figure 4.5) for varying soft iron needle diameters ranging from 250 to 750 µm.

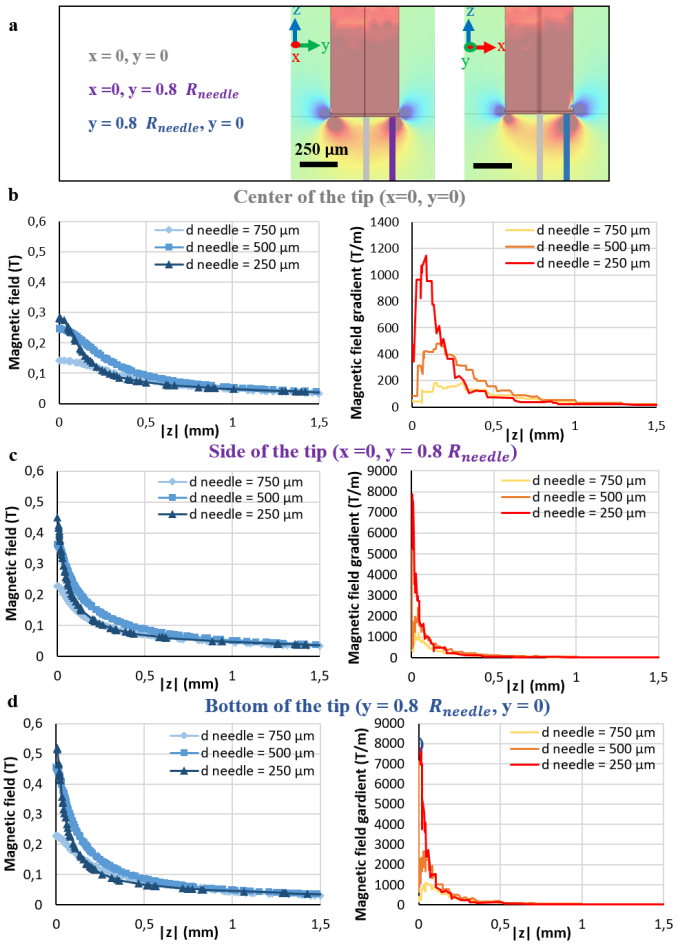


**Figure A.3 Simulated magnetic field and magnetic field gradient as a function of the distance to the tip $|z|$, at the center (gray), the lateral side (purple) and the bottom side (blue) of the tip for soft iron cylinder diameters varying from 250 to 750 µm**

Figure A.4 presents the quantification of the simulated magnetic field and magnetic field gradient in the magnetic stretcher composed of two identical pieces at a distance d and for varying diameters.

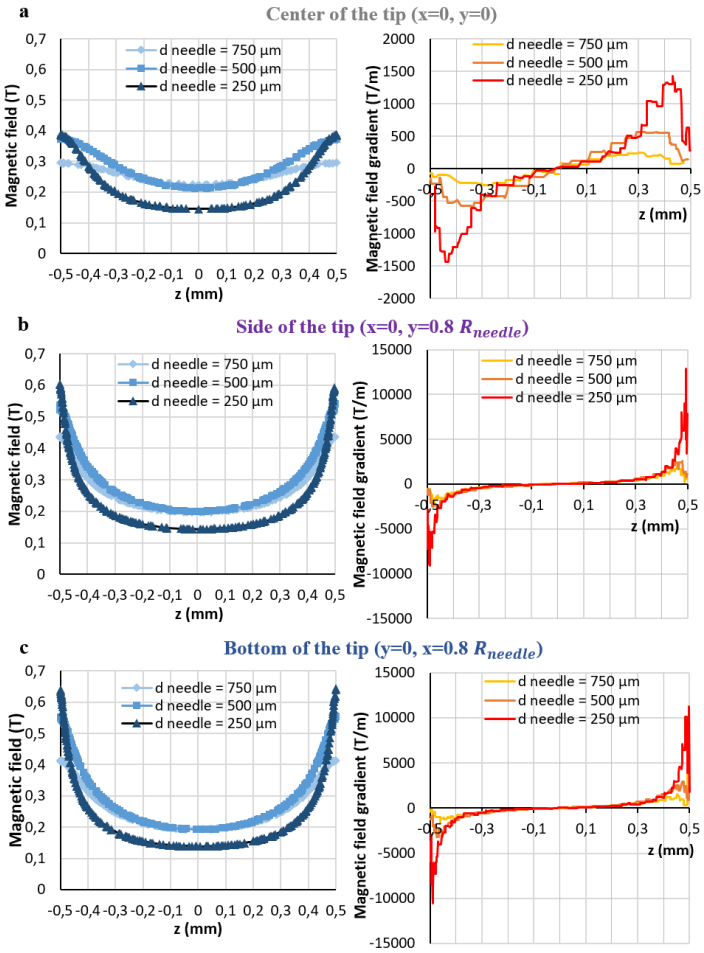


**Figure A.4 Simulated magnetic field and magnetic field gradient as a function of the position between the tips for a distance d= 1 mm, at the center (a), the lateral side (b) and the bottom side (c) of the tip.** The lines for the plot are positioned the same way as described Figure A.3.

Finally, Figure A.5 presents a mapping of the magnetic force in the magnetic stretcher for different distances d and for a needle diameter of 750, 500, and 250 µm. The magnetic force was approximated by $F_{mag} = M_{cell}^{sat} \times \frac{dB_z}{dz}$, since $\forall z,\ B_z > 0.11T$ and $M(B_z = 0.11) = 0.86M_{cell}^{sat}$ according to vibrating sample magnetometry (VSM) measurements. For an incubation with iron oxide nanoparticles for 30 min and with [Fe] = 2 mM, a magnetic moment of $M_{cell}^{sat} = 2 \times 10^{-13} A.m^2$ (corresponding to 3 pg of iron per cell) was measured for C2C12 cells by magnetophoresis. At a distance of 0.1 mm of the tip, no matter what the needle diameter is, the magnetic force reaches 200 to 250 pN at the edges of the tip. However, the impact of decreasing the diameter is more visible at the tip center where we have a magnetic force of 30 pN, 100 pN and 250 pN for a needle diameter of 750, 500 and 250 µm respectively at a distance of 0.1 mm. This result highlights the potential of increasing the magnetic force, by decreasing the needle diameter.

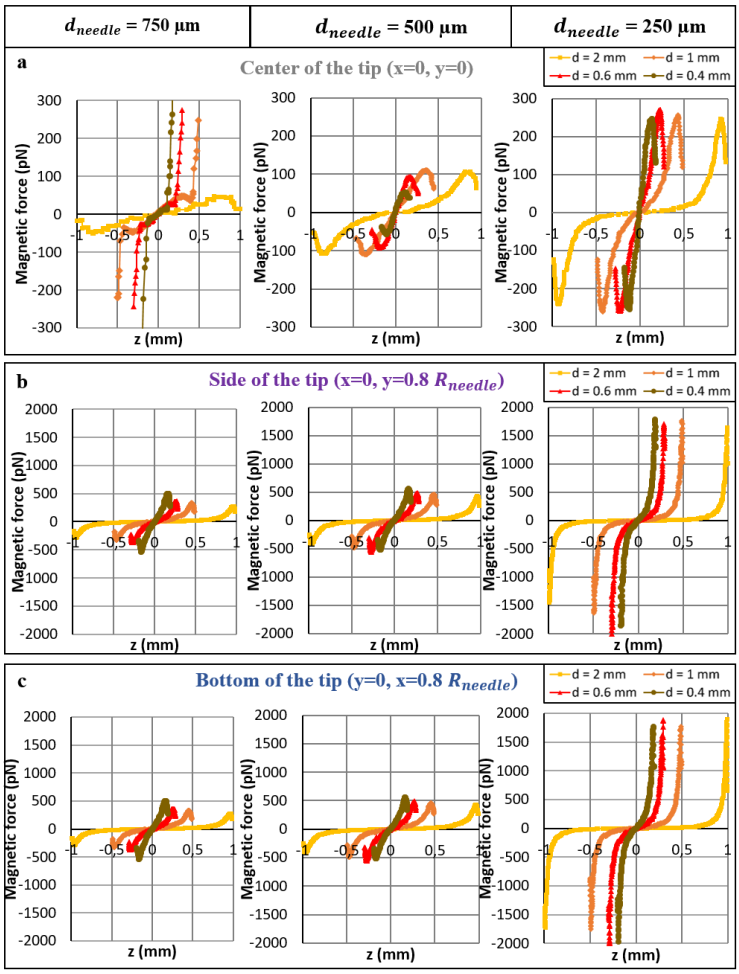


**Figure A.5 Magnetic force at the center (a), at the side (b) and at the bottom (c) of the tip as a function of the position in the magnetic stretcher, for a needle diameter of 750, 500 and 250 µm (left to right) and for different distances d.** The lines for the plot are positioned the same way as described Figure A.3 a. The magnetic force represented is averaged on about 0.02 mm and corresponds to a cell magnetic load of 3 pg per cell.

# Appendix B

# Shape profile calculation of a sessile drop

The classical Laplace equation of capillarity describes the mechanical equilibrium conditions for two homogeneous fluids separated by an interface: $\Delta P = \gamma(\frac{1}{R_1} + \frac{1}{R_2})$ with $R_1$ and $R_2$ the two curvature radii.

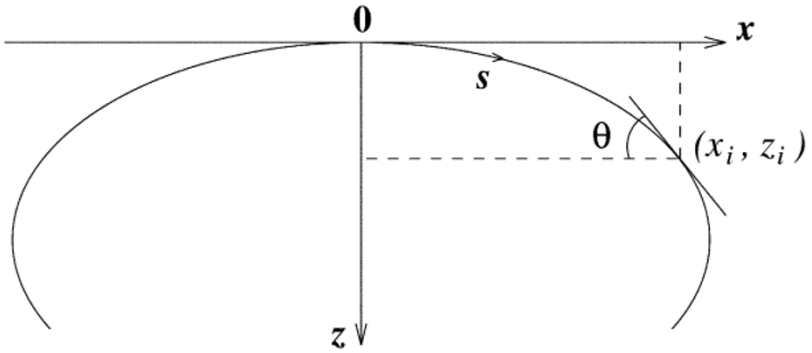


**Figure B.1 Profile of a pending drop.** Definition of the coordinate system used in the numerical solution of the Laplace equation for axisymmetric liquid–fluid interfaces. Illustration extracted form Neumann et al. [155].

For axisymmetric interfaces, it can be written as the following system of ordinary differential equations as a function of the arc length s, as defined in Figure B.1:

$$\frac{dx}{ds} = cos(\theta)$$
$$\frac{dz}{ds} = sin(\theta)$$
$$\frac{d\theta}{ds} = 2b + cz - \frac{sin(\theta)}{x}$$

where b is the curvature at the origin of coordinates (x=0, z=0) and $c = \frac{f_v}{\gamma} = \kappa^2$. b and c are the only two parameters that determine the shape of the profile. The above initial

value problem is integrated numerically, using the Matlab function ode45, to generate the Laplace profile. The computation of the profile is stopped when the angle $\theta$ becomes greater than 180°, to account for non-wetting conditions of the multicellular aggregate on the substrate.

To adjust the numerical profile to the experimental profile, the quadratic error $\mathcal{E}$ on the height $h$, the width $w$ and the volume $V$ were minimized with respect to the parameters b and c and with the Matlab function fminsearch.

$$\mathcal{E} = (1 - \frac{h_{th}}{h_{exp}})^2 + (1 - \frac{w_{th}}{w_{exp}})^2 + (1 - \frac{V_{th}}{V_{exp}})^2$$

# Appendix C

# Detailed material and methods related to chapter 4

### Cell culture

C2C12 Lifeact-GFP cells were cultured in Dulbecco's modified Eagle's medium (DMEM, Gibco), supplemented with 1% Penicillin-Streptomycin (P/S, Gibco), 2 $\mu$g/mL puromycin (P7255, Sigma) and 10% Fetal Bovine Serum (FBS, Gibco).

### Indirect immunofluorescence analysis

Cells in 2D were fixed for 15-20 min in 4% PFA at room temperature (RT). They were then permeabilized 15-20 min in 0.1% Triton X-100 at RT and non-specific interactions were prevented by an incubation with 5% BSA (#05479, Sigma-Aldrich) for 1h at RT. MHC was labelled thanks to the MF20 mouse primary antibody (dilution 1:200 in 0.5% BSA D-PBS 1x, DSHB) incubated for 2h at RT. Cells were then incubated for 2h at RT with a goat anti-mouse Atto550 antibody (dilution 1:500 in 0.5% BSA D-PBS 1x, 43394, Sigma). Nuclei were stained with Hoechst 33342 (dilution 1:1000 in D-PBS 1x, H3570, Invitrogen) for 15-20 min at RT. Images were obtained by confocal microscopy thanks to the LSM 780 Zeiss microscope equipped with a 20x water immersion objective (W Plan-Apochromat 20x/1.0 DIC, Zeiss). Represented images correspond to Z-projections on about 10 µm.

### Formation of C2C12 Lifeact-GFP spheroids

C2C12 Lifeact-GFP control spheroids were obtained as described in chapter 1 section 1.2.3. In summary, C2C12 Lifeact-GFP cells grown in 2D and at $70-80\%$ confluency were incubated for 30 min with a solution of iron oxide nanoparticles at [Fe]=2 mM supplemented with 5 mM citrate in RPMI 1640. After 2h of incubation in complete medium, cells were trypsinized, centrifuged and resuspended in a minimal volume (a few hundreds of µL). Suspended cells where then attracted in spherical agarose molds of 1.2 mm diameter, previously coated for 30 min with an anti-adhesive rinsing solution (07010, Stemcell Technologies), with permanent magnets placed below each mold. After an overnight incubation at 37°C, 5% $CO_2$, spheroids were removed from the molds by pipetting gently the surrounding medium.

### The magnetic stretcher adapted to 2-photon microscopy

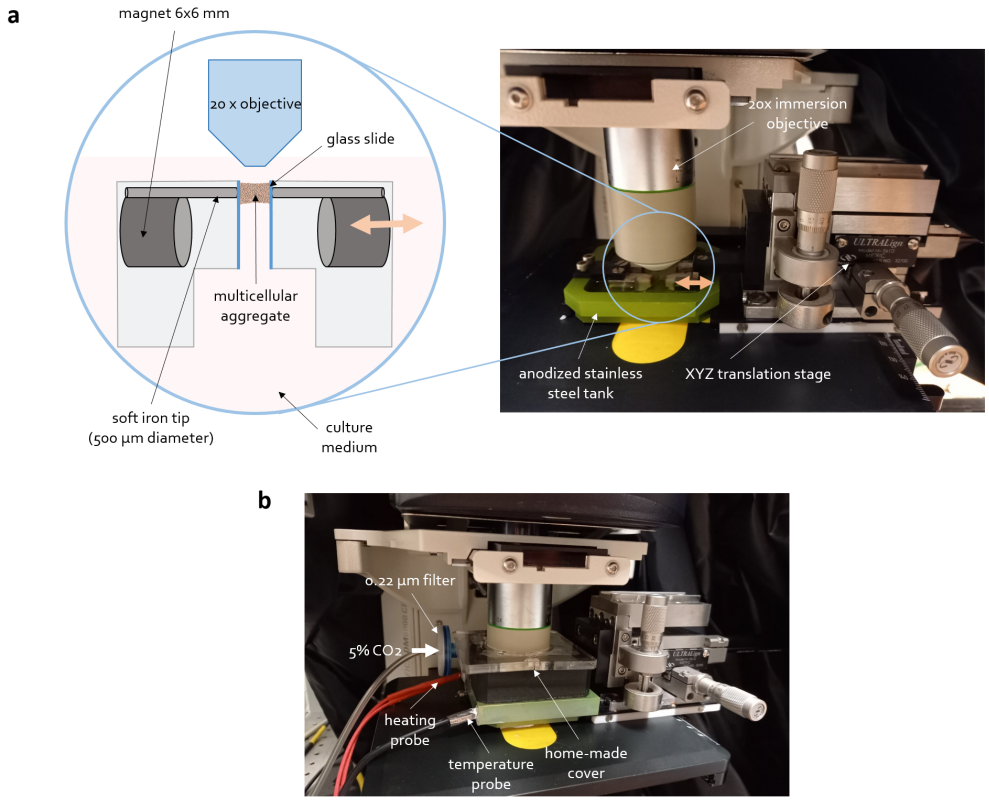


**Figure C.1 The magnetic stretcher device adapted to 2-photon microscopy.** **a)** Schematics and illustrative image of the magnetic stretcher device adapted to two-photon microscopy. **b)** Picture of the magnetic stretcher device showing the set-up to ensure a 37°C and 5% $CO_2$ regulation while being able to image the multicellular aggregate.

The initial device had to be reverted and adapted to be able to image the aggregate with 2-photon microscopy. As described chapter 4 section 4.2.1, we constructed a magnetic stretcher device that could fit under the 2-photon microscope while enabling the temperature and the atmosphere regulation at 37°C, 5% $CO_2$ (Figure C.1). In comparison to the device for bright field microscopy, the pieces are flipped up side down to allow observation with an immersion objective. A heating and a temperature probe are inserted in the tank made of anodized stainless steal to ensure temperature regulation. Thermal contact on the probes is guaranteed with thermal paste (Heat Sink Compound Plus, RS 217-3835, RS Pro). Finally, a homemade cover was built to enable the displacement of the immersed objective while keeping the box closed and allowing the flow of 5% $CO_2$ (8920, Messer) humidified air in the chamber.

**Aggregate formation in the magnetic stretcher**

To sterilize the magnetic stretcher set-up, the tank is rinsed several times with ethanol 70% and exposed to UV light for 30 min. After rinsing the tank several times with D-PBS 1x, the glass slides on each micromagnet are incubated with Matrigel (356234, Corning) diluted at 0.5 mg/mL in cold DMEM for 1h at room temperature. After rinsing the magnetic stretcher's tank, the tank is filled with white DMEM supplemented with 10% FBS, 1% P/S, 1% Amphotericin B, 2 µg/mL puromycin and 1x anti-oxydant supplement (A1345, Sigma).

C2C12 Lifeact-GFP cells are incubated for 30 min with a solution of iron oxide nanoparticles at [Fe] = 2 mM supplemented with 5 mM citrate. After 2h of incubation in complete medium, cells are trypsinized, centrifuged and resuspended at about 5 million cells/mL in complete medium. 15 µL of suspended cell solution (equivalent to 75k cells) are deposited on each micromagnet forming a hemisphere of non cohesive cells. The two micromagnets are then approached at a distance of 350 to 400 µm as shown Figure 4.14 d-e. After an overnight incubation at 37°C and 5% $CO_2$, the tank medium is changed for the differentiation medium composed of white DMEM with 2% HS, 1% P/S, 1% Amphotericin B and 1x anti-oxydant supplement. A linear stretch at 20 µm/h (1 µm step every 3 minutes) of the cohesive multicellular aggregate is started for 6 hours and the mobile piece is reapproached of about 40 µm at the end of the stretching. The medium is changed with fresh differentiation medium every 24 hours for the next two days.

### RT-qPCR measurements

Total RNA was extracted with the NucleoSpin RNA Kit (740955, Macherey-Nagel) following the manufacturer's protocol. For aggregate disruption, each aggregate was rinsed with D-PBS 1x and resuspended in 350 µL lysis buffer RA1 with 1% $\beta$-mercaptoethanol and disrupted with about 30 one-second pulses performed with a Biovortexer and a spiral pestle (918034 and 918044, Biospec). Complementary DNAs were obtained with the SuperScript II Reverse Transcriptase kit (18064022, Thermofischer Scientific) and random hexamers (C1181, Promega) according to the manufacturer's instructions. Quantitative PCR was performed with SYBR Green Master Mix (4309155, Thermofischer Scientific). The RPLP0 gene coding for the 60S acidic ribosomal protein P0 was used as a reference transcript. The primer sequences used for RPLP0, Myod1, Myog, Myf6, Tnnt1, Tnnt3, Myh1, Myh3, Myh4 and Ckm are presented Figure C.2.

| Gene | Primer sequence | |
|---|---|---|
| **RPLP0** | Fwd : | GCCAGCTCAGAACACTGGTCTA |
| | Rev : | ATGCCCAAAGCCTGGAAGA |
| **Myod1** | Fwd : | GCCGGTGTGCATTCCAA |
| | Rev : | CACTCCGGAACCCCAACAG |
| **Myog** | Fwd : | AGCATCACGGTGGAGGATATG |
| | Rev : | CAGTTGGGCATGGTTTCGT |
| **Myf6** | Fwd : | TGGCCAACCCCAACCA |
| | Rev : | GATGGCACTCCGCAGAATCT |
| **Tnnt1** | Fwd : | TGAAACTCCGGATTCTGTCTGA |
| | Rev : | TGGTCCTCCCCCATGTAGTC |

| Gene | Primer sequence | |
|---|---|---|
| **Tnnt3** | Fwd : | TGCCAGGGCCCCTTATTC |
| | Rev : | AGATGCCTGGGCGTGAAG |
| **Myh1** | Fwd : | TGGACCCACGGTCGAAGT |
| | Rev : | TGGTTGCAGCCCAGTGAGA |
| **Myh3** | Fwd : | GGCAAAGACCCGTGACTTCA |
| | Rev : | CTCACTCCTCGCTTTCATGGA |
| **Myh4** | Fwd : | AGAGCCGAGAGGTTCACACTAAA |
| | Rev : | TCTCCTGTCACCTCTCAACAGAAA |
| **Ckm** | Fwd : | GGTGGTGGATGGCGTGAA |
| | Rev : | TGGCCCTTTTCCAGCTTCT |

**Figure C.2 Primer sequences (5' to 3') used for real-time PCR analysis.**

### Protein extraction and Western Blot

For protein extraction, multicellular aggregates were rinsed with D-PBS 1x and put in an ice cold solution of 30 mM Tris-EDTA (pH adjusted with concentrated HCl to 7.4), 1 mM DTT (dithiothréitol), 1x anti-phosphatase cocktail (Roche, 04906837001) and 1x anti-protease cocktail (Roche, 11836170001). Multicellular aggregates were disrupted using lysing beads (Precellys lysing kit, P000912-LYSK0, Bertin) and the Precellys24 tissue homogenizer device (Bertin). Samples were then left for 30 min in ice and centrifuged for 20 min at 12 000 g and 4°C. The supernatant was retrieved and protein concentration was quantified by Bradford assay.

The multicellular aggregate protein extracts were then used for Western Blot analysis. They were separated on SDS-polyacrylamide 4-20% gels and transferred on PVDF membranes. After rinsing the membranes with TBST-Tween 20 buffer (TBST), the membranes

were blocked for 1h in the EveryBlot blocking buffer (12010020, Biorad) and incubated overnight at 4°C with primary antibodies anti-troponinT (SAB4200717, Sigma), rabbit anti-Myf6 (sc-301, Santa Cruz Biotechnology), or mouse anti-MHC (myosin heavy chain) (MF 20, DSHB) diluted at 1:1000 in 5% BSA TBST. Membranes were then washed 3 times with TBST and incubated for 1h with the anti-mouse (#7076, Cell Signaling) or anti-rabbit (#7074, Cell Signaling) horseradish peroxidase-linked secondary antibodies diluted at 1:2000 in the Everyblot blocking buffer. Peroxidase activity was revealed using a chemiluminescent detection kit (Amersham ECL Prime Western Blotting Detection Reagent, RPN2232, Cytiva) and the Syngene PXi device (Ozyme). Alpha-tubulin was used as the loading control and immuno-probed with the mouse anti-alpha tubulin antibody (T5168, Sigma) incubated overnight at 4°C and diluted at 1:2000 in 5% BSA TBST.

# Bibliography


[1] Hohmann and Dehghani. The cytoskeleton—a complex interacting meshwork. *Cells*, 8(4):362, April 2019.

[2] Anna V. Schepers, Julia Kraxner, Charlotta Lorenz, and Sarah Köster. Mechanics of single vimentin intermediate filaments under load. In *Optical Tweezers*, pages 677–700. Springer US, 2022.

[3] Charlotta Lorenz, Anna V. Schepers, and Sarah Köster. Quantifying the interaction strength between biopolymers. In *Optical Tweezers*, pages 701–723. Springer US, 2022.

[4] Anna V. Schepers, Charlotta Lorenz, Peter Nietmann, Andreas Janshoff, Stefan Klumpp, and Sarah Köster. Multiscale mechanics and temporal evolution of vimentin intermediate filament networks. *Proceedings of the National Academy of Sciences*, 118(27), June 2021.

[5] Huayin Wu, Yinan Shen, Suganya Sivagurunathan, Miriam Sarah Weber, Stephen A. Adam, Jennifer H. Shin, Jeffrey J. Fredberg, Ohad Medalia, Robert Goldman, and David A. Weitz. Vimentin intermediate filaments and filamentous actin form unexpected interpenetrating networks that redefine the cell cortex. *Proceedings of the National Academy of Sciences*, 119(10), March 2022.

[6] Kenneth M. Yamada, Andrew D. Doyle, and Jiaoyang Lu. Cell–3d matrix interactions: recent advances and opportunities. *Trends in Cell Biology*, 32(10):883–895, October 2022.

[7] R. O. Hynes. Cell adhesion: old and new questions. *Trends Cell Biol*, 9(12):M33–37, Dec 1999.

[8] Sally A. Kim, Chin-Yin Tai, Lee-Peng Mok, Eric A. Mosser, and Erin M. Schuman. Calcium-dependent dynamics of cadherin interactions at cell–cell junctions. *Proceedings of the National Academy of Sciences*, 108(24):9857–9862, May 2011.

[9] Keeley L. Mui, Christopher S. Chen, and Richard K. Assoian. The mechanical regulation of integrin–cadherin crosstalk organizes cells, signaling and forces. *Journal of Cell Science*, January 2016.

[10] Daniel A. Fletcher and R. Dyche Mullins. Cell mechanics and the cytoskeleton. *Nature*, 463(7280):485–492, January 2010.

[11] Robert M. Sutherland, W. Rodger Inch, John A. McCredie, and Jack Kruuv. A multi-component radiation survival curve using an in vitro tumour model. *International Journal of Radiation Biology and Related Studies in Physics, Chemistry and Medicine*, 18(5):491–495, January 1970.

[12] Robert M. Sutherland, John A. McCredie, and W. Rodger Inch. Growth of Multicell Spheroids in Tissue Culture as a Model of Nodular Carcinomas. *JNCI: Journal of the National Cancer Institute*, 46(1):113–120, 01 1971.

[13] Federica Foglietta, Roberto Canaparo, Giampiero Muccioli, Enzo Terreno, and Loredana Serpe. Methodological aspects and pharmacological applications of three-dimensional cancer cell cultures and organoids. *Life Sciences*, 254:117784, August 2020.

[14] Teruki Nii, Kimiko Makino, and Yasuhiko Tabata. Three-dimensional culture system of cancer cells combined with biomaterials for drug screening. *Cancers*, 12(10):2754, September 2020.

[15] David Gonzalez-Rodriguez, Karine Guevorkian, Stéphane Douezan, and Françoise Brochard-Wyart. Soft matter models of developing tissues and tumors. *Science*, 338(6109):910–917, November 2012.

[16] Joseph Ackermann, Martine Ben Amar, and Jean-François Joanny. Multi-cellular aggregates, a model for living matter. *Physics Reports*, 927:1–29, September 2021.

[17] Monika E Dolega, Sylvain Monnier, Benjamin Brunel, Jean-François Joanny, Pierre Recho, and Giovanni Cappello. Extracellular matrix in multicellular aggregates acts as a pressure sensor controlling cell proliferation and motility. *eLife*, 10, March 2021.

[18] Gaëtan Mary, Brice Malgras, Jose Efrain Perez, Irène Nagle, Nathalie Luciani, Cynthia Pimpie, Atef Asnacios, Marc Pocard, Myriam Reffay, and Claire Wilhelm. Magnetic compression of tumor spheroids increases cell proliferation in vitro and cancer progression in vivo. *Cancers*, 14(2):366, January 2022.

[19] Frank Sauer, Anatol Fritsch, Steffen Grosser, Steve Pawlizak, Tobias Kießling, Martin Reiss-Zimmermann, Mehrgan Shahryari, Wolf C. Müller, Karl-Titus Hoffmann, Josef A. Käs, and Ingolf Sack. Whole tissue and single cell mechanics are correlated in human brain tumors. *Soft Matter*, 17(47):10744–10752, 2021.

[20] Steffen Grosser, Jürgen Lippoldt, Linda Oswald, Matthias Merkel, Daniel M. Sussman, Frédéric Renner, Pablo Gottheil, Erik W. Morawetz, Thomas Fuhs, Xiaofan Xie, Steve Pawlizak, Anatol W. Fritsch, Benjamin Wolf, Lars-Christian Horn, Susanne Briest, Bahriye Aktas, M. Lisa Manning, and Josef A. Käs. Cell and nucleus shape as an indicator of tissue fluidity in carcinoma. *Physical Review X*, 11(1), February 2021.

[21] Marina Sanaki-Matsumiya, Mitsuhiro Matsuda, Nicola Gritti, Fumio Nakaki, James Sharpe, Vikas Trivedi, and Miki Ebisuya. Periodic formation of epithelial somites from human pluripotent stem cells. *Nature Communications*, 13(1), April 2022.

[22] Ali Hashmi, Sham Tlili, Pierre Perrin, Molly Lowndes, Hanna Peradziryi, Joshua M Brickman, Alfonso Martínez Arias, and Pierre-François Lenne. Cell-state transitions and collective cell movement generate an endoderm-like region in gastruloids. *eLife*, 11, April 2022.

[23] Xue Gong, Chao Lin, Jian Cheng, Jiansheng Su, Hang Zhao, Tianlin Liu, Xuejun Wen, and Peng Zhao. Generation of multicellular tumor spheroids with microwell-based agarose scaffolds for drug testing. *PLOS ONE*, 10(6):e0130348, June 2015.

[24] Tomita Vasilica Stirbat, Sham Tlili, Thibault Houver, Jean-Paul Rieu, Catherine Barentin, and Hélène Delanoë-Ayari. Multicellular aggregates: a model system for tissue rheology. *The European Physical Journal E*, 36(8), August 2013.

[25] Karoly Jakab, Brook Damon, Françoise Marga, Octavian Doaga, Vladimir Mironov, Ioan Kosztin, Roger Markwald, and Gabor Forgacs. Relating cell and tissue mechanics: Implications and applications. *Developmental Dynamics*, 237(9):2438–2449, September 2008.

[26] Kévin Alessandri, Bibhu Ranjan Sarangi, Vasily Valérïévitch Gurchenkov, Bidisha Sinha, Tobias Reinhold Kießling, Luc Fetler, Felix Rico, Simon Scheuring, Christophe Lamaze, Anthony Simon, Sara Geraldo, Danijela Vignjević, Hugo Doméjean, Leslie Rolland, Anette Funfak, Jérôme Bibette, Nicolas Bremond, and Pierre Nassoy. Cellular capsules as a tool for multicellular spheroid production and for investigating the mechanics of tumor progression in vitro. *Proceedings of the National Academy of Sciences*, 110(37):14843–14848, August 2013.

[27] Indra Van Zundert, Beatrice Fortuni, and Susana Rocha. From 2d to 3d cancer cell models—the enigmas of drug delivery research. *Nanomaterials*, 10(11):2236, November 2020.

[28] Nipha Chaicharoenaudomrung, Phongsakorn Kunhorm, and Parinya Noisa. Three-dimensional cell culture systems as an iin vitro/i platform for cancer and stem cell modeling. *World Journal of Stem Cells*, 11(12):1065–1083, December 2019.

[29] Francois Mazuel, Myriam Reffay, Vicard Du, Jean-Claude Bacri, Jean-Paul Rieu, and Claire Wilhelm. Magnetic flattening of stem-cell spheroids indicates a size-dependent elastocapillary transition. *Physical Review Letters*, 114(9), March 2015.

[30] Jose E Perez, Irène Nagle, and Claire Wilhelm. Magnetic molding of tumor spheroids: emerging model for cancer screening. *Biofabrication*, 13(1):015018, December 2020.

[31] A. Van de Walle, J.E. Perez, A. Abou-Hassan, M. Hémadi, N. Luciani, and C. Wilhelm. Magnetic nanoparticles in regenerative medicine: what of their fate and impact in stem cells? *Materials Today Nano*, 11:100084, August 2020.

[32] Vicard Du, Nathalie Luciani, Sophie Richard, Gaëtan Mary, Cyprien Gay, François Mazuel, Myriam Reffay, Philippe Menasché, Onnik Agbulut, and Claire Wilhelm. A 3d magnetic tissue stretcher for remote mechanical control of embryonic stem cell differentiation. *Nature Communications*, 8(1), September 2017.

[33] Yuri M. Efremov, Irina M. Zurina, Viktoria S. Presniakova, Nastasia V. Kosheleva, Denis V. Butnaru, Andrey A. Svistunov, Yury A. Rochev, and Peter S. Timashev. Mechanical properties of cell sheets and spheroids: the link between single cells and complex tissues. *Biophysical Reviews*, 13(4):541–561, July 2021.

[34] Aitziber L. Cortajarena, Daniel Ortega, Sandra M. Ocampo, Alberto Gonzalez-García, Pierre Couleaud, Rodolfo Miranda, Cristobal Belda-Iniesta, and Angel Ayuso-Sacido. Engineering iron oxide nanoparticles for clinical settings. *Nanobiomedicine*, 1:2, January 2014.

[35] Jeff W.M. Bulte, Trevor Douglas, Brian Witwer, Su-Chun Zhang, Erica Strable, Bobbi K. Lewis, Holly Zywicke, Brad Miller, Peter van Gelderen, Bruce M. Moskowitz, Ian D. Duncan, and Joseph A. Frank. Magnetodendrimers allow endosomal magnetic labeling and in vivo tracking of stem cells. *Nature Biotechnology*, 19(12):1141–1147, December 2001.

[36] Wensheng Xie, Zhenhu Guo, Fei Gao, Qin Gao, Dan Wang, Bor shuang Liaw, Qiang Cai, Xiaodan Sun, Xiumei Wang, and Lingyun Zhao. Shape-, size- and structure-controlled synthesis and biocompatibility of iron oxide nanoparticles for magnetic theranostics. *Theranostics*, 8(12):3284–3307, 2018.

[37] Ralf P. Friedrich, Iwona Cicha, and Christoph Alexiou. Iron oxide nanoparticles in regenerative medicine and tissue engineering. *Nanomaterials*, 11(9):2337, September 2021.

[38] Claire Wilhelm and Florence Gazeau. Universal cell labelling with anionic magnetic nanoparticles. *Biomaterials*, 29(22):3161–3174, August 2008.

[39] C. Rivière, C. Wilhelm, F. Cousin, V. Dupuis, F. Gazeau, and R. Perzynski. Internal structure of magnetic endosomes. *The European Physical Journal E*, 22(1):1–10, January 2007.

[40] François Mazuel. Agrégats multicellulaires magnétiques : mécanique des tissus et biodégradation des nanomatériaux., 2016.

[41] R Massart. Preparation of aqueous magnetic liquids in alkaline and acidic media. *IEEE Trans. Magn.*, 17(2):1247–1248, March 1981.

[42] François Mazuel, Ana Espinosa, Nathalie Luciani, Myriam Reffay, Rémi Le Borgne, Laurence Motte, Karine Desboeufs, Aude Michel, Teresa Pellegrino, Yoann Lalatonne, and Claire Wilhelm. Massive intracellular biodegradation of iron oxide nanoparticles evidenced magnetically at single-endosome and tissue levels. *ACS Nano*, 10(8):7627–7638, July 2016.

[43] Gaëtan Mary, François Mazuel, Vincent Nier, Florian Fage, Irène Nagle, Louisiane Devaud, Jean-Claude Bacri, Sophie Asnacios, Atef Asnacios, Cyprien Gay, Philippe Marcq, Claire Wilhelm, and Myriam Reffay. All-in-one rheometry and nonlinear rheology of multicellular aggregates. *Physical Review E*, 105(5), May 2022.

[44] Marziyeh Ajdary, Mohammad Moosavi, Marveh Rahmati, Mojtaba Falahati, Mohammad Mahboubi, Ali Mandegary, Saranaz Jangjoo, Reza Mohammadinejad, and Rajender Varma. Health concerns of various nanoparticles: A review of their in vitro and in vivo toxicity. *Nanomaterials*, 8(9):634, August 2018.

[45] Neenu Singh, Gareth J.S. Jenkins, Romisa Asadi, and Shareen H. Doak. Potential toxicity of superparamagnetic iron oxide nanoparticles (SPION). *Nano Reviews*, 1(1):5358, January 2010.

[46] Arun Balakumaran, Edyta Pawelczyk, Jiaqiang Ren, Brian Sworder, Aneeka Chaudhry, Marianna Sabatino, David Stroncek, Joseph A. Frank, and Pamela G. Robey. Superparamagnetic iron oxide nanoparticles labeling of bone marrow stromal (mesenchymal) cells does not affect their "stemness". *PLoS ONE*, 5(7):e11462, July 2010.

[47] Yiying Qi, Gang Feng, Zhongming Huang, and Weiqi Yan. The application of super paramagnetic iron oxide-labeled mesenchymal stem cells in cell-based therapy. *Molecular Biology Reports*, 40(3):2733–2740, December 2012.

[48] Ka-Wing Au, Song-Yan Liao, Yee-Ki Lee, Wing-Hon Lai, Kwong-Man Ng, Yau-Chi Chan, Mei-Chu Yip, Chung-Yee Ho, Ed X Wu, Ronald A Li, Chung-Wah Siu, and Hung-Fat Tse. Effects of iron oxide nanoparticles on cardiac differentiation of embryonic stem cells. *Biochemical and Biophysical Research Communications*, 379(4):898–903, February 2009.

[49] Aurore Van de Walle, Waïss Faissal, Claire Wilhelm, and Nathalie Luciani. Role of growth factors and oxygen to limit hypertrophy and impact of high magnetic nanoparticles dose during stem cell chondrogenesis. *Computational and Structural Biotechnology Journal*, 16:532–542, 2018.

[50] Aurore Van de Walle, Anouchka Plan Sangnier, Ali Abou-Hassan, Alberto Curcio, Miryana Hémadi, Nicolas Menguy, Yoann Lalatonne, Nathalie Luciani, and Claire Wilhelm. Biosynthesis of magnetic nanoparticles from nano-degradation products revealed in human stem cells. *Proceedings of the National Academy of Sciences*, 116(10):4044–4053, February 2019.

[51] Megane Beldjilali-Labro, Alejandro Garcia Garcia, Firas Farhat, Fahmi Bedoui, Jean-François Grosset, Murielle Dufresne, and Cécile Legallais. Biomaterials in tendon and skeletal muscle tissue engineering: Current trends and challenges. *Materials*, 11(7):1116, June 2018.

[52] Meagan E. Carnes and George D. Pins. Skeletal muscle tissue engineering: Biomaterials-based strategies for the treatment of volumetric muscle loss. *Bioengineering*, 7(3):85, July 2020.

[53] Stephan Lange, Nikos Pinotsis, Irina Agarkova, and Elisabeth Ehler. The m-band: The underestimated part of the sarcomere. *Biochimica et Biophysica Acta (BBA) - Molecular Cell Research*, 1867(3):118440, March 2020.

[54] Jacob L Krans. The sliding filament theory of muscle contraction. *Nature Education*, 3(9):66, 2010.

[55] Ivana Y. Kuo and Barbara E. Ehrlich. Signaling in muscle contraction. *Cold Spring Harbor Perspectives in Biology*, 7(2):a006023, February 2015.

[56] A. Ishijima, H. Kojima, H. Higuchi, Y. Harada, T. Funatsu, and T. Yanagida. Multiple- and single-molecule analysis of the actomyosin motor by nanometer-piconewton manipulation with a microneedle: unitary steps and forces. *Biophysical Journal*, 70(1):383–400, January 1996.

[57] Fábio C. Minozzo, Bruno M. Baroni, José A. Correa, Marco A. Vaz, and Dilson E. Rassier. Force produced after stretch in sarcomeres and half-sarcomeres isolated from skeletal muscles. *Scientific Reports*, 3(1), July 2013.

[58] Ricarda Haeger, Felipe de Souza Leite, and Dilson E. Rassier. Sarcomere length non-uniformities dictate force production along the descending limb of the force–length relation. *Proceedings of the Royal Society B: Biological Sciences*, 287(1937):20202133, October 2020.

[59] J. Gordon Betts. *Anatomy and Physiology*. 09 2022.

[60] Otger Campàs. A toolbox to explore the mechanics of living embryonic tissues. *Seminars in Cell &amp Developmental Biology*, 55:119–130, July 2016.

[61] Karine Guevorkian, Marie-Josée Colbert, Mélanie Durth, Sylvie Dufour, and Françoise Brochard-Wyart. Aspiration of biological viscoelastic drops. *Physical Review Letters*, 104(21), May 2010.

[62] H.M. Phillips, M.S. Steinberg, and B.H. Lipton. Embryonic tissues as elasticoviscous liquids. *Developmental Biology*, 59(2):124–134, September 1977.

[63] Sham Tlili, François Graner, and Hélène Delanoë-Ayari. A microfluidic platform to investigate the role of mechanical constraints on tissue reorganization. March 2022.

[64] Jonas Ranft, Markus Basan, Jens Elgeti, Jean-François Joanny, Jacques Prost, and Frank Jülicher. Fluidization of tissues by cell division and apoptosis. *Proceedings of the National Academy of Sciences*, 107(49):20863–20868, November 2010.

[65] Fabien Montel, Morgan Delarue, Jens Elgeti, Danijela Vignjevic, Giovanni Cappello, and Jacques Prost. Isotropic stress reduces cell proliferation in tumor spheroids. *New Journal of Physics*, 14(5):055008, May 2012.

[66] Morgan Delarue, Jean-François Joanny, Frank Jülicher, and Jacques Prost. Stress distributions and cell flows in a growing cell aggregate. *Interface Focus*, 4(6):20140033, December 2014.

[67] A. Bonfanti, J. Fouchard, N. Khalilgharibi, G. Charras, and A. Kabla. A unified rheological model for cells and cellularised materials. *Royal Society Open Science*, 7(1):190920, January 2020.

[68] L. Preziosi, D. Ambrosi, and C. Verdier. An elasto-visco-plastic model of cell aggregates. *Journal of Theoretical Biology*, 262(1):35–47, January 2010.

[69] Étienne Moisdon, Pierre Seez, François Molino, Philippe Marcq, and Cyprien Gay. Mapping cell cortex rheology to tissue rheology and vice versa. *Physical Review E*, 106(3), September 2022.

[70] Ramsey A. Foty and Malcolm S. Steinberg. The differential adhesion hypothesis: a direct evaluation. *Developmental Biology*, 278(1):255–263, February 2005.

[71] M. Lisa Manning, Ramsey A. Foty, Malcolm S. Steinberg, and Eva-Maria Schoetz. Coaction of intercellular adhesion and cortical tension specifies tissue surface tension. *Proceedings of the National Academy of Sciences*, 107(28):12517–12522, June 2010.

[72] Tomita Vasilica Stirbat, Abbas Mgharbel, Selena Bodennec, Karine Ferri, Hichem C. Mertani, Jean-Paul Rieu, and Hélène Delanoë-Ayari. Fine tuning of tissues' viscosity and surface tension through contractility suggests a new role for -catenin. *PLoS ONE*, 8(2):e52554, February 2013.

[73] Malcolm S. Steinberg. Reconstruction of tissues by dissociated cells. *Science*, 141(3579):401–408, August 1963.

[74] H.M. Phillips and M.S. Steinberg. Embryonic tissues as elasticoviscous liquids. i. rapid and slow shape changes in centrifuged cell aggregates. *Journal of Cell Science*, 30(1):1–20, April 1978.

[75] Jean-Léon Maître, Hélène Berthoumieux, Simon Frederik Gabriel Krens, Guillaume Salbreux, Frank Jülicher, Ewa Paluch, and Carl-Philipp Heisenberg. Adhesion functions in cell sorting by mechanically coupling the cortices of adhering cells. *Science*, 338(6104):253–256, October 2012.

[76] Albert K. Harris. Is cell sorting caused by differences in the work of intercellular adhesion? a critique of the steinberg hypothesis. *Journal of Theoretical Biology*, 61(2):267–285, September 1976.

[77] G. Wayne Brodland. The differential interfacial tension hypothesis (DITH): A comprehensive theory for the self-rearrangement of embryonic cells and tissues. *Journal of Biomechanical Engineering*, 124(2):188–197, March 2002.

[78] C. Norotte, F. Marga, A. Neagu, I. Kosztin, and G. Forgacs. Experimental evaluation of apparent tissue surface tension based on the exact solution of the laplace equation. *EPL (Europhysics Letters)*, 81(4):46003, January 2008.

[79] K. Guevorkian and J.-L. Maître. Micropipette aspiration. In *Methods in Cell Biology*, pages 187–201. Elsevier, 2017.

[80] Ali Kalantarian, Hiromasa Ninomiya, Sameh M.I. Saad, Robert David, Rudolf Winklbauer, and A. Wilhelm Neumann. Axisymmetric drop shape analysis for estimating the surface tension of cell aggregates by centrifugation. *Biophysical Journal*, 96(4):1606–1616, February 2009.

[81] Amy J. Jorgenson, Kyoung Moo Choi, Delphine Sicard, Karry M. J. Smith, Samantha E. Hiemer, Xaralabos Varelas, and Daniel J. Tschumperlin. TAZ activation drives fibroblast spheroid growth, expression of profibrotic paracrine signals, and context-dependent ECM gene expression. *American Journal of Physiology-Cell Physiology*, 312(3):C277–C285, March 2017.

[82] Robert Prevedel, Alba Diz-Muñoz, Giancarlo Ruocco, and Giuseppe Antonacci. Brillouin microscopy: an emerging tool for mechanobiology. *Nature Methods*, 16(10):969–977, September 2019.

[83] Sabrina Batonnet-Pichon, Anthony Behin, Eva Cabet, Florence Delort, Patrick Vicart, and Alain Lilienbaum. Myofibrillar myopathies: New perspectives from animal models to potential therapeutic approaches. *Journal of Neuromuscular Diseases*, 4(1):1–15, February 2017.

[84] Bertrand-David Segard, Florence Delort, Virginie Bailleux, Stéphanie Simon, Emilie Leccia, Blandine Gausseres, Fatma Briki, Patrick Vicart, and Sabrina Batonnet-Pichon. N-acetyl-l-cysteine prevents stress-induced desmin aggregation in cellular models of desminopathy. *PLoS ONE*, 8(10):e76361, October 2013.

[85] L. Kreplak and H. Bär. Severe myopathy mutations modify the nanomechanics of desmin intermediate filaments. *Journal of Molecular Biology*, 385(4):1043–1051, January 2009.

[86] Lev G. Goldfarb, Kye-Yoon Park, Larisa Cervenáková, Svetlana Gorokhova, Hee-Suk Lee, Olavo Vasconcelos, James W. Nagle, Christina Semino-Mora, Kumaraswamy Sivakumar, and Marinos C. Dalakas. Missense mutations in desmin associated with familial cardiac and skeletal myopathy. *Nature Genetics*, 19(4):402–403, August 1998.

[87] Elisabeth E. Charrier, Atef Asnacios, Rachel Milloud, Richard De Mets, Martial Balland, Florence Delort, Olivier Cardoso, Patrick Vicart, Sabrina Batonnet-Pichon, and Sylvie Hénon. Desmin mutation in the c-terminal domain impairs traction force generation in myoblasts. *Biophysical Journal*, 110(2):470–480, January 2016.

[88] Navid Bonakdar, Justyna Luczak, Lena Lautscham, Maja Czonstke, Thorsten M. Koch, Astrid Mainka, Tajana Jungbauer, Wolfgang H. Goldmann, Rolf Schröder, and Ben Fabry. Biomechanical characterization of a desminopathy in primary human myoblasts. *Biochemical and Biophysical Research Communications*, 419(4):703–707, March 2012.

[89] Catherine Even, Gilles Abramovici, Florence Delort, Anna F. Rigato, Virginie Bailleux, Abel de Sousa Moreira, Patrick Vicart, Felix Rico, Sabrina Batonnet-Pichon, and Fatma Briki. Mutation in the core structure of desmin intermediate filaments affects myoblast elasticity. *Biophysical Journal*, 113(3):627–636, August 2017.

[90] E Leccia, S Batonnet-Pichon, A Tarze, V Bailleux, J Doucet, M Pelloux, F Delort, V Pizon, P Vicart, and F Briki. Cyclic stretch reveals a mechanical role for intermediate filaments in a desminopathic cell model. *Physical Biology*, 10(1):016001, December 2012.

[91] Marina Spörrer, Delf Kah, Richard C. Gerum, Barbara Reischl, Danyil Huraskin, Claire A. Dessalles, Werner Schneider, Wolfgang H. Goldmann, Harald Herrmann, Ingo Thievessen, Christoph S. Clemen, Oliver Friedrich, Said Hashemolhosseini, Rolf Schröder, and Ben Fabry. The desmin mutation r349p increases contractility and fragility of stem cell-generated muscle micro-tissues. *Neuropathology and Applied Neurobiology*, 48(3), December 2021.

[92] Elisabeth E. Charrier, Lorraine Montel, Atef Asnacios, Florence Delort, Patrick Vicart, François Gallet, Sabrina Batonnet-Pichon, and Sylvie Hénon. The desmin network is a determinant of the cytoplasmic stiffness of myoblasts. *Biology of the Cell*, 110(4):77–90, February 2018.

[93] Cecilia Romagnoli, Teresa Iantomasi, and Maria Luisa Brandi. Available in vitro models for human satellite cells from skeletal muscle. *International Journal of Molecular Sciences*, 22(24):13221, December 2021.

[94] Mahmut Selman Sakar, Devin Neal, Thomas Boudou, Michael A. Borochin, Yinqing Li, Ron Weiss, Roger D. Kamm, Christopher S. Chen, and H. Harry Asada.

Formation and optogenetic control of engineered 3d skeletal muscle bioactuators. *Lab on a Chip*, 12(23):4976, 2012.

[95] Run Shi, Zhe Zhang, Ankai Zhu, Xingxing Xiong, Jie Zhang, Jiang Xu, Man-Sun Sy, and Chaoyang Li. Targeting type i collagen for cancer treatment. *International Journal of Cancer*, 151(5):665–683, March 2022.

[96] Nadia Harbeck, Frédérique Penault-Llorca, Javier Cortes, Michael Gnant, Nehmat Houssami, Philip Poortmans, Kathryn Ruddy, Janice Tsang, and Fatima Cardoso. Breast cancer. *Nature Reviews Disease Primers*, 5(1), September 2019.

[97] Jean Paul Thiery. Epithelial–mesenchymal transitions in tumour progression. *Nature Reviews Cancer*, 2(6):442–454, June 2002.

[98] Catalina Lodillinsky, Laetitia Fuhrmann, Marie Irondelle, Olena Pylypenko, Xiao-Yan Li, Hélène Bonsang-Kitzis, Fabien Reyal, Sophie Vacher, Claire Calmel, Olivier De Wever, Ivan Bièche, Marie-Lise Lacombe, Ana Maria Eiján, Anne Houdusse, Anne Vincent-Salomon, Stephen J. Weiss, Philippe Chavrier, and Mathieu Boissan. Metastasis-suppressor NME1 controls the invasive switch of breast cancer by regulating MT1-MMP surface clearance. *Oncogene*, 40(23):4019–4032, May 2021.

[99] P. S. Steeg, G. Bevilacqua, L. Kopper, U. P. Thorgeirsson, J. E. Talmadge, L. A. Liotta, and M. E. Sobel. Evidence for a novel gene associated with low tumor metastatic potential. *JNCI Journal of the National Cancer Institute*, 80(3):200–204, April 1988.

[100] Fred R. Miller, Steven J. Santner, Larry Tait, and Peter J. Dawson. MCF10dcis.com xenograft model of human comedo ductal carcinoma in situ. *JNCI: Journal of the National Cancer Institute*, 92(14):1185a–1186, July 2000.

[101] C Lodillinsky, E Infante, A Guichard, R Chaligné, L Fuhrmann, J Cyrta, M Irondelle, E Lagoutte, S Vacher, H Bonsang-Kitzis, M Glukhova, F Reyal, I Bièche, A Vincent-Salomon, and P Chavrier. p63/MT1-MMP axis is required for in situ to invasive transition in basal-like breast cancer. *Oncogene*, 35(3):344–357, April 2015.

[102] Anda Huna, Béatrice Nawrocki-Raby, Teresita Padilla-Benavides, Julie Gavard, Sylvie Coscoy, David Bernard, and Mathieu Boissan. Loss of the metastasis suppressor NME1, but not of its highly related isoform NME2, induces a hybrid epithelial–mesenchymal state in cancer cells. *International Journal of Molecular Sciences*, 22(7):3718, April 2021.

[103] Mathieu Boissan, Guillaume Montagnac, Qinfang Shen, Lorena Griparic, Jérôme Guitton, Maryse Romao, Nathalie Sauvonnet, Thibault Lagache, Ioan Lascu, Graça Raposo, Céline Desbourdes, Uwe Schlattner, Marie-Lise Lacombe, Simona Polo, Alexander M. van der Bliek, Aurélien Roux, and Philippe Chavrier. Nucleoside diphosphate kinases fuel dynamin superfamily proteins with GTP for membrane remodeling. *Science*, 344(6191):1510–1515, June 2014.

[104] Enrico Warmt, Steffen Grosser, Eliane Blauth, Xiaofan Xie, Hans Kubitschke, Roland Stange, Frank Sauer, Jörg Schnauß, Janina M Tomm, Martin von Bergen, and Josef A Käs. Differences in cortical contractile properties between healthy epithelial and cancerous mesenchymal breast cells. *New Journal of Physics*, 23(10):103020, October 2021.

[105] Jean-Léon Maître, Hervé Turlier, Rukshala Illukkumbura, Björn Eismann, Ritsuya Niwayama, François Nédélec, and Takashi Hiiragi. Asymmetric division of contractile domains couples cell positioning and fate specification. *Nature*, 536(7616):344–348, August 2016.

[106] François Gallet, Delphine Arcizet, Pierre Bohec, and Alain Richert. Power spectrum of out-of-equilibrium forces in living cells: amplitude and frequency dependence. *Soft Matter*, 5(15):2947, 2009.

[107] Valérie M. Laurent, Sylvie Hénon, Emmanuelle Planus, Redouane Fodil, Martial Balland, Daniel Isabey, and François Gallet. Assessment of mechanical properties of adherent living cells by bead micromanipulation: Comparison of magnetic twisting cytometry vs optical tweezers. *Journal of Biomechanical Engineering*, 124(4):408–421, July 2002.

[108] Martial Balland, Nicolas Desprat, Delphine Icard, Sophie Féréol, Atef Asnacios, Julien Browaeys, Sylvie Hénon, and François Gallet. Power laws in microrheology experiments on living cells: Comparative analysis and modeling. *Physical Review E*, 74(2), August 2006.

[109] Nicolas Desprat, Alain Richert, Jacqueline Simeon, and Atef Asnacios. Creep function of a single living cell. *Biophysical Journal*, 88(3):2224–2233, March 2005.

[110] Jochen Guck, Revathi Ananthakrishnan, Hamid Mahmood, Tess J. Moon, C. Casey Cunningham, and Josef Käs. The optical stretcher: A novel laser tool to micromanipulate cells. *Biophysical Journal*, 81(2):767–784, August 2001.

[111] Deny Hartono, Yang Liu, Pei Lin Tan, Xin Yi Sherlene Then, Lin-Yue Lanry Yung, and Kian-Meng Lim. On-chip measurements of cell compressibility via acoustic radiation. *Lab on a Chip*, 11(23):4072, 2011.

[112] Philip Kollmannsberger and Ben Fabry. Linear and nonlinear rheology of living cells. *Annual Review of Materials Research*, 41(1):75–97, August 2011.

[113] Pei-Hsun Wu, Dikla Raz-Ben Aroush, Atef Asnacios, Wei-Chiang Chen, Maxim E. Dokukin, Bryant L. Doss, Pauline Durand-Smet, Andrew Ekpenyong, Jochen Guck, Nataliia V. Guz, Paul A. Janmey, Jerry S. H. Lee, Nicole M. Moore, Albrecht Ott, Yeh-Chuin Poh, Robert Ros, Mathias Sander, Igor Sokolov, Jack R. Staunton, Ning Wang, Graeme Whyte, and Denis Wirtz. A comparison of methods to assess cell mechanical properties. *Nature Methods*, 15(7):491–498, June 2018.

[114] Yansheng Hao, Shaokoon Cheng, Yo Tanaka, Yoichiroh Hosokawa, Yaxiaer Yalikun, and Ming Li. Mechanical properties of single cells: Measurement methods and applications. *Biotechnology Advances*, 45:107648, December 2020.

[115] Andrew R. Harris, Loic Peter, Julien Bellis, Buzz Baum, Alexandre J. Kabla, and Guillaume T. Charras. Characterizing the mechanics of cultured cell monolayers. *Proceedings of the National Academy of Sciences*, 109(41):16449–16454, September 2012.

[116] Laura Casas Ferrer. Microfluidic flow of biomimetic tissues, 2022.

[117] Wolfgang H. Goldmann, Reinhard Galneder, Markus Ludwig, Weiming Xu, Eileen D. Adamson, Ning Wang, and Robert M. Ezzell. Differences in elasticity of vinculin-deficient f9 cells measured by magnetometry and atomic force microscopy. *Experimental Cell Research*, 239(2):235–242, March 1998.

[118] Philippe Marmottant, Abbas Mgharbel, Jos Käfer, Benjamin Audren, Jean-Paul Rieu, Jean-Claude Vial, Boudewijn van der Sanden, Athanasius F. M. Marée, François Graner, and Hélène Delanoë-Ayari. The role of fluctuations and stress on the effective viscosity of cell aggregates. *Proceedings of the National Academy of Sciences*, 106(41):17271–17275, October 2009.

[119] Anouchka Plan Sangnier, Aurore B. Van de Walle, Alberto Curcio, Rémi Le Borgne, Laurence Motte, Yoann Lalatonne, and Claire Wilhelm. Impact of magnetic nanoparticle surface coating on their long-term intracellular biodegradation in stem cells. *Nanoscale*, 11(35):16488–16498, 2019.

[120] Ian Janssen, Steven B. Heymsfield, ZiMian Wang, and Robert Ross. Skeletal muscle mass and distribution in 468 men and women aged 18–88 yr. *Journal of Applied Physiology*, 89(1):81–88, July 2000.

[121] Kevin P Campbell. Three muscular dystrophies: Loss of cytoskeleton-extracellular matrix linkage. *Cell*, 80(5):675–679, March 1995.

[122] Young-Bum Kim, Theodore P. Ciaraldi, Alice Kong, Dennis Kim, Neelima Chu, Pharis Mohideen, Sunder Mudaliar, Robert R. Henry, and Barbara B. Kahn. Troglitazone but not metformin restores insulin-stimulated phosphoinositide 3-kinase activity and increases p110 protein levels in skeletal muscle of type 2 diabetic subjects. *Diabetes*, 51(2):443–448, February 2002.

[123] R Lodi, A H Schapira, D Manners, P Styles, N W Wood, D J Taylor, and T T Warner. Abnormal in vivo skeletal muscle energy metabolism in huntington's disease and dentatorubropallidoluysian atrophy. *Ann. Neurol.*, 48(1):72–76, July 2000.

[124] Bruno Cadot, Vincent Gache, and Edgar R Gomes. Moving and positioning the nucleus in skeletal muscle – one step at a time. *Nucleus*, 6(5):373–381, September 2015.

[125] C. F. Bentzinger, Y. X. Wang, and M. A. Rudnicki. Building muscle: Molecular regulation of myogenesis. *Cold Spring Harbor Perspectives in Biology*, 4(2):a008342–a008342, February 2012.

[126] Hiroyuki Yamakawa, Dai Kusumoto, Hisayuki Hashimoto, and Shinsuke Yuasa. Stem cell aging in skeletal muscle regeneration and disease. *International Journal of Molecular Sciences*, 21(5):1830, March 2020.

[127] Oscar Hernández-Hernández, Rodolfo Daniel Ávila-Avilés, and J. Manuel Hernández-Hernández. Chromatin landscape during skeletal muscle differentiation. *Frontiers in Genetics*, 11, September 2020.

[128] Narendra Bharathy, Belinda Mei Tze Ling, and Reshma Taneja. Epigenetic regulation of skeletal muscle development and differentiation. In *Subcellular Biochemistry*, pages 139–150. Springer Netherlands, June 2012.

[129] Taimoor H. Qazi, David J. Mooney, Matthias Pumberger, Sven Geißler, and Georg N. Duda. Biomaterials based strategies for skeletal muscle tissue engineering: Existing technologies and future trends. *Biomaterials*, 53:502–521, June 2015.

[130] Pei Zhuang, Jia An, Chee Kai Chua, and Lay Poh Tan. Bioprinting of 3d in vitro skeletal muscle models: A review. *Materials &amp Design*, 193:108794, August 2020.

[131] DAVID YAFFE and ORA SAXEL. Serial passaging and differentiation of myogenic cells isolated from dystrophic mouse muscle. *Nature*, 270(5639):725–727, December 1977.

[132] Benjamin Langridge, Michelle Griffin, and Peter E. Butler. Regenerative medicine for skeletal muscle loss: a review of current tissue engineering approaches. *Journal of Materials Science: Materials in Medicine*, 32(1), January 2021.

[133] Guillaume Duclos, Christoph Erlenkämper, Jean-François Joanny, and Pascal Silberzan. Topological defects in confined populations of spindle-shaped cells. *Nature Physics*, 13(1):58–62, September 2016.

[134] Pau Guillamat, Carles Blanch-Mercader, Guillaume Pernollet, Karsten Kruse, and Aurélien Roux. Integer topological defects organize stresses driving tissue morphogenesis. *Nature Materials*, 21(5):588–597, February 2022.

[135] Mai T. Lam, Sylvie Sim, Xiaoyue Zhu, and Shuichi Takayama. The effect of continuous wavy micropatterns on silicone substrates on the alignment of skeletal muscle myoblasts and myotubes. *Biomaterials*, 27(24):4340–4347, August 2006.

[136] Sung Ho Cha, Hyun Jong Lee, and Won-Gun Koh. Study of myoblast differentiation using multi-dimensional scaffolds consisting of nano and micropatterns. *Biomaterials Research*, 21(1), January 2017.

[137] Alastair Khodabukus. Tissue-engineered skeletal muscle models to study muscle function, plasticity, and disease. *Frontiers in Physiology*, 12, February 2021.

[138] Sook Hee Ku, Sahng Ha Lee, and Chan Beum Park. Synergic effects of nanofiber alignment and electroactivity on myoblast differentiation. *Biomaterials*, 33(26):6098–6104, September 2012.

[139] V. Kroehne, I. Heschel, F. Schügner, D. Lasrich, J. W. Bartsch, and H. Jockusch. Use of a novel collagen matrix with oriented pore structure for muscle cell differentiation in cell culture and in grafts. *Journal of Cellular and Molecular Medicine*, 12(5a):1640–1648, September 2008.

[140] WonJin Kim and GeunHyung Kim. A functional bioink and its application in myoblast alignment and differentiation. *Chemical Engineering Journal*, 366:150–162, June 2019.

[141] Barbara Perniconi, Alessandra Costa, Paola Aulino, Laura Teodori, Sergio Adamo, and Dario Coletti. The pro-myogenic environment provided by whole organ scale acellular scaffolds from skeletal muscle. *Biomaterials*, 32(31):7870–7882, November 2011.

[142] Serge Ostrovidov, Sahar Salehi, Marco Costantini, Kasinan Suthiwanich, Majid Ebrahimi, Ramin Banan Sadeghian, Toshinori Fujie, Xuetao Shi, Stefano Cannata, Cesare Gargioli, Ali Tamayol, Mehmet Remzi Dokmeci, Gorka Orive, Wojciech Swieszkowski, and Ali Khademhosseini. 3d bioprinting in skeletal muscle tissue engineering. *Small*, 15(24):1805530, April 2019.

[143] Hironobu Takahashi, Tatsuya Shimizu, Masamichi Nakayama, Masayuki Yamato, and Teruo Okano. The use of anisotropic cell sheets to control orientation during the self-organization of 3d muscle tissue. *Biomaterials*, 34(30):7372–7380, October 2013.

[144] Eiji Nagamori, Trung Xuan Ngo, Yasunori Takezawa, Atsuhiro Saito, Yoshiki Sawa, Tatsuya Shimizu, Teruo Okano, Masahito Taya, and Masahiro Kino-oka. Network formation through active migration of human vascular endothelial cells in a multi-layered skeletal myoblast sheet. *Biomaterials*, 34(3):662–668, January 2013.

[145] Yasunori Yamamoto, Akira Ito, Masahiro Kato, Yoshinori Kawabe, Kazunori Shimizu, Hideaki Fujita, Eiji Nagamori, and Masamichi Kamihira. Preparation of artificial skeletal muscle tissues by a magnetic force-based tissue engineering technique. *Journal of Bioscience and Bioengineering*, 108(6):538–543, December 2009.

[146] Sarah M. Somers, Alexander A. Spector, Douglas J. DiGirolamo, and Warren L. Grayson. Biophysical stimulation for engineering functional skeletal muscle. *Tissue Engineering Part B: Reviews*, 23(4):362–372, August 2017.

[147] Cristian Pennisi, Stavros Papaioannou, John Rasmussen, and Vladimir Zachar. *The role of physical microenvironmental cues on myogenesis: Implications for tissue engineering of skeletal muscle*, pages 45–56. 12 2016.

[148] R. Rezakhaniha, A. Agianniotis, J. T. C. Schrauwen, A. Griffa, D. Sage, C. V. C. Bouten, F. N. van de Vosse, M. Unser, and N. Stergiopulos. Experimental investigation of collagen waviness and orientation in the arterial adventitia using confocal laser scanning microscopy. *Biomechanics and Modeling in Mechanobiology*, 11(3-4):461–473, July 2011.

[149] S. Ehrig, B. Schamberger, C. M. Bidan, A. West, C. Jacobi, K. Lam, P. Kollmannsberger, A. Petersen, P. Tomancak, K. Kommareddy, F. D. Fischer, P. Fratzl, and

John W. C. Dunlop. Surface tension determines tissue shape and growth kinetics. *Science Advances*, 5(9), September 2019.

[150] Qiyan Mao, Achyuth Acharya, Alejandra Rodríguez-delaRosa, Fabio Marchiano, Benoit Dehapiot, Ziad Al Tanoury, Jyoti Rao, Margarete Díaz-Cuadros, Arian Mansur, Erica Wagner, Claire Chardes, Vandana Gupta, Pierre-François Lenne, Bianca H Habermann, Olivier Theodoly, Olivier Pourquié, and Frank Schnorrer. Tension-driven multi-scale self-organisation in human iPSC-derived muscle fibers. *eLife*, 11, August 2022.

[151] Wesley R. Legant, Amit Pathak, Michael T. Yang, Vikram S. Deshpande, Robert M. McMeeking, and Christopher S. Chen. Microfabricated tissue gauges to measure and manipulate forces from 3d microtissues. *Proceedings of the National Academy of Sciences*, 106(25):10097–10102, June 2009.

[152] Jérome Chal and Olivier Pourquié. Making muscle: skeletal myogenesis in vivo and in vitro. *Development*, 144(12):2104–2122, June 2017.

[153] Nicolas Borghi, Maria Sorokina, Olga G. Shcherbakova, William I. Weis, Beth L. Pruitt, W. James Nelson, and Alexander R. Dunn. E-cadherin is under constitutive actomyosin-generated tension that is increased at cell–cell contacts upon externally applied stretch. *Proceedings of the National Academy of Sciences*, 109(31):12568–12573, July 2012.

[154] Boryan P. Radoev, Plamen V. Petkov, and Ivan T. Ivanov. Capillary bridges — a tool for three-phase contact investigation. In *Surface Energy*. InTech, December 2015.

[155] O.I.del Río and A.W. Neumann. Axisymmetric drop shape analysis: Computational methods for the measurement of interfacial properties from the shape and dimensions of pendant and sessile drops. *Journal of Colloid and Interface Science*, 196(2):136–147, December 1997.

# Résumé de la thèse en français

Les tissus biologiques sont des structures complexes et organisées. Une meilleure compréhension des processus dirigeant leur assemblage et leur organisation serait crucial dans de nombreux domaines allant de la modélisation des maladies à la biologie du développement en passant par l'ingénierie tissulaire qui vise à reproduire la fonction et la structure des organes pour la médecine régénérative ou la réparation tissulaire. Tandis que le rôle des signaux biochimiques a été largement étudié pendant de nombreuses années, les signaux biophysiques tels que les forces mécaniques ou les propriétés mécaniques des cellules sont désormais admises comme jouant un rôle essentiel dans les tissus matures et leur régulation, ainsi que dans le développement embryonnaire.

Etudier les propriétés mécaniques de tissus biologiques représente donc un problème majeur, à la fois pour une meilleure compréhension de leurs propriétés, et pour la reproduction d'organes complexes. Les tissus sont des matériaux complexes, hétérogènes, et actifs mais leurs propriétés peuvent être largement appréhendées à l'aide de concepts issus de la matière molle (viscoélasticité, tension de surface...). Leurs propriétés mécaniques émergent de leurs propriétés cellulaires microscopiques, cependant cette interaction n'est toujours pas entièrement comprise.

Les agrégats multicellulaires en tant que tissus modèles sont des outils utiles pour investiguer le rôle des propriétés cellulaires individuelles sur la mécanique des tissus, et pour reproduire la complexité tissulaire. En effet, les approches standards 2D sont éloignées de l'environnement tissulaire 3D, tandis que les sphéroïdes et les agrégats multicellulaires aident à reproduire plus fidèlement les conditions physiologiques des tissus concernant les adhésions cellule-cellule et cellule-matrice. Tandis que de nombreuses stratégies se concentrent sur l'obtention de tissus modèles 3D, la possibilité de stimuler les tissus via des forces extérieures est aussi fondamentale. Tout d'abord, pour mesurer ses propriétés mécaniques, des outils pour stimuler mécaniquement le tissu et enregistrer la déformation résultante sont nécessaires. Mais aussi, la stimulation mécanique a été démontrée comme essentielle pour la régulation et la maturation des tissus dans de nombreux types de tissus comme le cœur, le muscle ou l'intestin. Un des enjeux actuels de l'ingénierie tissulaire est en effet de contrôler l'organisation spatiale en 3D tout en étant capable d'appliquer des forces mécaniques. En particulier, le muscle squelettique possède une structure multi-échelle alignée et cette organisation et sa fonction dépendent des stimulations appliquées durant la maturation.

Les forces magnétiques sont de bonnes candidates pour contrôler à distance l'organisation cellulaire tout en appliquant des forces extérieures. L'équipe a développé une technique

basée sur l'incorporation de nanoparticules d'oxyde de fer dans les cellules leur conférant un moment magnétique et permettant leur manipulation à distance. Les nanoparticules d'oxyde de fer ont été d'abord introduites en tant qu'agents de contraste pour l'Imagerie par Résonance Magnétique (IRM), et elles sont désormais utilisées dans de nombreux domaines biomédicaux. La majorité des études ont démontré leur cytocompatibilité légitimant leur utilisation dans des applications *in vitro* et *in vivo*. Grâce à cette stratégie magnétique et sans l'ajout d'aucune matrice extérieure et d'aucun substrat, des agrégats multicellulaires de taille sans précédent et de forme contrôlée peuvent être formés puis stimulés à l'aide de forces magnétiques. Cette thèse vise à stimuler mécaniquement des tissus modèles grâce à des forces magnétiques (i) pour investiguer les propriétés mécaniques de tissus 3D et (ii) pour conduire l'organisation et la différenciation dans le contexte de l'ingénierie tissulaire pour le muscle squelettique.

---

Ce manuscrit de thèse est composé de deux parties indépendantes. Un premier chapitre d'introduction générale (**chapitre 1**) présente les éléments requis et communs aux deux parties. Les sphéroïdes et les agrégats multicellulaires en tant que modèles de tissus biologiques 3D sont introduits ainsi que les nanoparticules d'oxyde de fer et l'organisation du muscle squelettique.

La première partie (**partie I**) se concentre sur l'étude des propriétés mécaniques statiques et dynamiques d'agrégats multicellulaires formés et stimulés magnétiquement. Tout d'abord, les propriétés mécaniques et rhéologiques des agrégats multicellulaires sont introduites. Ensuite, dans le **chapitre 2**, les propriétés mécaniques macroscopiques de sphéroïdes telles que leur tension de surface effective sont mesurées et reliées aux propriétés microscopiques des cellules individuelles. Les propriétés mécaniques des sphéroïdes sont mesurées en écrasant et déformant l'agrégat à l'aide d'un gradient de champ magnétique constant. Dans le **chapitre 2 section 2.2**, la relation entre tension de surface macroscopique et propriétés microscopiques tels que la tension et l'organisation du cytosquelette d'actine, les adhésions intercellulaires ou les filaments intermédiaires est étudiée dans un modèle de sphéroïdes de cellules précurseurs de muscle de souris. Les résultats expérimentaux sont présentés sous forme d'un article accepté. Ensuite, dans le **chapitre 2 section 2.3** et avec un modèle de cellules humaines de cancer du sein, les propriétés tumorales telles que l'invasion, la migration ou l'adhésion sont corrélées à la tension de surface macroscopique. Les résultats expérimentaux sont présentés sous la forme d'un article publié. Enfin, le **chapitre 3** présente un outil magnétique pour explorer la rhéologie des agrégats multicellulaires en appliquant un champ magnétique variable grâce à un

électro-aimant. Les résultats expérimentaux obtenus avec ce rhéomètre magnétique sont validés de manière croisée avec un rhéomètre à plaques parallèles.

La deuxième partie de ce manuscrit (**partie II**) présente une approche magnétique pour appliquer des stimuli mécaniques afin de conduire l'organisation et améliorer la différenciation en 3D de tissus du muscle squelettique. Dans le **chapitre 4**, la myogenèse et les stratégies d'ingénierie tissulaire du muscle squelettique sont d'abord introduites. Puis, le dispositif de l'étireur magnétique utilisé pour obtenir des agrégats étirables composés de cellules précurseurs de muscle de souris entre deux micro-aimants est décrit ainsi que son optimisation. Les résultats expérimentaux démontrent que cet étireur magnétique conduit l'alignement des cellules et favorise la différenciation en cellules musculaires.